Renewable and Sustainable Energy Reviews 183 (2023) 113392

Contents lists available at ScienceDirect

Renewable and Sustainable Energy Reviews

journal homepage: www.elsevier.com/locate/rser

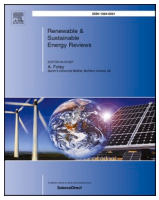

Evolution paths from gray to turquoise hydrogen via catalytic steam methane reforming: Current challenges and future developments

Samrand Saeidi [a,b,*], András Sápi [a], Asif Hussain Khoja [c], Sara Najari [a], Mariam Ayesha [d], Zoltán Kónya [a], Bernard Baffour Asare-Bediako [e], Adam Tatarczuk [f], Volker Hessel [g], Frerich J. Keil [h], Alírio E. Rodrigues [i]

[a] Department of Applied and Environmental Chemistry, Interdisciplinary Excellence Centre, University of Szeged, Rerrich Béla tér 1, Szeged 6720, Hungary
[b] Biotechnology Center, Silesian University of Technology, 8 Krzywousty St., 44-100 Gliwice, Poland
[c] Fossil Fuel Laboratory, Department of Thermal Energy Engineering, U.S.-Pakistan Centre for Advanced Studies in Energy (USPCAS-E), National University of Sciences & Technology (NUST), Sector H-12 Islamabad (44000), Pakistan
[d] School of Chemical and Materials Engineering (SCME), National University of Sciences & Technology (NUST), Sector H-12 Islamabad (44000), Pakistan
[e] Center for Renewable Carbon, University of Tennessee, Knoxville 37996, USA
[f] Department of Energy Transition – Institute of Energy and Fuel Processing Technology, 41-803 Zabrze, Poland
[g] School of Chemical Engineering, The University of Adelaide, North Terrace Campus, Adelaide, 5005, Australia
[h] Institute of Chemical Reaction Engineering, Hamburg University of Technology, Hamburg D-21073, Germany
[i] Laboratory of Separation and Reaction Engineering – Laboratory of Catalysis and Materials (LSRE-LCM), Associate Laboratory LSRE-LCM, Faculdade de Engenharia, Universidade do Porto, Rua Dr. Roberto Frias, 4200-465, Porto, Portugal

ARTICLE INFO

Keywords:
Conventional SMR
Blue/Turquoise H_2 production
Catalysis
Kinetic models
Operating conditions
Intensified SMR
Renewable energy
ESG

ABSTRACT

Fossil fuel depletion, global warming, climate change, and steep hikes in the price of fuel are driving scientists to investigate commercial and environmentally friendly energy carriers like hydrogen. Steam methane reforming (SMR), a current commercial route for H_2 production, has been considered the best remedy to fulfill the requirements. Despite the remarkable quantity of H_2 produced by the SMR, this technology still faces major challenges such as catalyst deactivation due to the sintering of metal nanoparticles, coking, and generation of a large quantity of CO_2. Firstly, the effects of catalyst types, kinetic models, and operating conditions on high-yield H_2 production, the evolution path from gray to blue, via the conventional SMR are comprehensively reviewed. Secondly, exploiting intensified techniques such as membrane technology, sorption, fluidization, and chemical looping for SMR to blue H_2 are discussed in detail. Further, a novel and sustainable path for the SMR process, hybridizing the use of novel materials and emerging technologies to produce turquoise H_2, is proposed. Finally, the critical points for steam reforming process technology that can help leverage environmental, social, and governance (ESG) profiling have been discussed.

1. Introduction

With the rapid growth of the world population and economic development, energy consumption is sharply rising. By 2050, fossil fuels are expected to meet 70% of global energy demand, maintaining their position as the market leader [1]. Nevertheless, environmental concerns about fossil fuels' worldwide consumption and emissions of greenhouse gases (GHG) have switched attention towards non-fossil fuel sources to achieve cleaner energy consumption [2–5]. Hydrogen (H_2), as a clean, renewable, and alternative energy carrier, offers certain advantages when compared with fossil fuels. While the formation of NOx during H_2 combustion is a concern, there are various methods for reducing or preventing NOx emissions, such as using catalysts or adjusting the combustion conditions. Overall, the advantages of H_2 as an energy carrier include; (i) near-zero or zero end-use emissions energy carrier (ii) ability to store it in gaseous or liquid form; (iii) simplicity of conversion to different energy sources; and (iv) a lower heating value (LHV) and a higher heating value (HHV) than most fossil fuels [6,7]. Moreover, the calorific value of H_2 is three times that of gasoline [8]. Contrarily, the flammability and low density of H_2 in storage are obstructing its extensive use as an energy-carrying source [9]. The advantages of H_2 as

* Corresponding author. Department of Applied and Environmental Chemistry, Interdisciplinary Excellence Centre, University of Szeged, Rerrich Béla tér 1, Szeged 6720, Hungary.
E-mail address: samrand.saeidi@chem.u-szeged.hu (S. Saeidi).

https://doi.org/10.1016/j.rser.2023.113392
Received 24 November 2022; Received in revised form 9 March 2023; Accepted 20 May 2023
Available online 22 June 2023

List of symbols

Abbreviations and Acronyms

H_2	hydrogen
CH_4	methane
CO_2	carbon dioxide
CO	carbon monoxide
S/C	steam to carbon
GHG	greenhouse gases
LHV	lower heating value
HHV	higher heating value
DRM	dry reforming of methane
SMR	steam methane reforming
SESMR	sorption-enhanced steam methane reforming
POM	partial oxidation of methane
ATR	auto-thermal reforming
TMR	tri methane reforming
TEM	Transmission electron microscopy
TPD	temperature-programmed desorption
TPR	temperature-programmed reduction
TG	glass transition temperature
TGA	thermogravimetric analysis
SEM	scanning electron microscope
FESEM	field emission scanning electron microscopy
XRD	X-ray powder diffraction
XPS	X-ray photoelectron spectroscopy
WGS	water-gas shift reaction
HT	high temperature
LT	low temperature
PSA	pressure swing adsorption
DFT	density functional theory
DFMs	dual function materials
LSCF	lanthanum strontium cobalt ferrite
CFD	computational fluid dynamics
DBD	dielectric-barrier discharge
GHSV	gas hourly space velocity
3DOM	three-dimensionally ordered macroporous
HTc	hydrotalcites
LOS	lithium orthosilicate
LDH	layered double hydroxides
CL-SMR	chemical looping steam methane reforming
CLC	chemical looping combustion
CSCM	combined sorption catalyst materials
MRs	membrane reactors
MOF	metal organic framework
OCs	oxygen carriers
CL-SESMR	chemical looping sorption enhanced steam methane reforming
SASMR	solar-assisted steam methane reforming
ESMR	electrified steam methane reforming
TZFBR	two-zone fluidized-bed reactor
TOS	time on stream
CCS	carbon capture and storage
ESG	environmental, social and governance
HB	Haber-Bosch
RECs	regional economic communities

Variables

r_1, r_2, r_3	rates of reactions (kmol/kg.cat.h.bar)
$K_{CO}, K_{H_2}, K_{CH_4}, K_{H_2O}$	adsorption constants of CO, H_2, CH_4, and H_2O
$p_{CH_4}, p_{H_2O}, p_{CO}, p_{H_2}$	partial pressure of components (N/m^2)
K_{eq}	equilibrium constant (m^3/kmol)
$R_{i=1,2}$	rate coefficient of reactions
E_{ak}	activation energy(J/mol)
s_x	net rate of reaction for x surface specie
K_s	number of surface reactions
$N_s and N_g$	number of surface and gas-phase species
$c_x{}^0$	reference concentration at normal pressure
R	ideal gas constant (kJ/kmol/K)
T	temperature
$T_{wall}, T_{flue}, T_{tube}$	temperature of wall (wall inside), flue gas (°C or K) and tube
A_k	Arrhenius constant
k_{fk}, k_{rk}	rate coefficients of forward and reverse reaction
h_f, h_g	coefficient of heat transfer (flue gas and reactor gas)
K_p	equilibrium constant for partial pressure
ΔH	heat of reaction (kJ/mol)
F_t	total molar flowrate (kmol.h)
X_i	fractional conversion of species
z	reactor length (axial coordinate) (m)
A	reactor cross-section area
R	rate of reaction ($kgm^{-3}s^{-1}$)
P_{TOT}	total pressure (N/m^2)
C_{ps}, C_{pg}	heat capacity of solid and gas (J/mol.K)
u	superficial space velocity (m/s)
S_i	heat source term ($Jm^{-3}s^{-1}$)
R_{cap}	capture reaction rate of CO_2 acceptor ($kgm^{-3}s^{-1}$)
U_{mf}	minimum fluidization velocity
g	gravitational acceleration
f	friction factor
d_p	diameter of particle (m)

Greek variables

ρ_g, ρ_s	density of gas and solid (kg/m^3)
λs	solid conductivity ($mL^2\ t^{-3}\ A^{-1}$)
ε_b	void fraction of bed
$\nu''_{xk} and \nu'_{xk}$	stoichiometric coefficients of reactants and products
ρ_b	density of catalyst (kg/m^3)
ε_{xk}	additional dependencies of activation energy
Θ_x	surface coverage of adsorbed species
μ	viscosity of inlet gas
ε_{mf}	void fraction under minimum fluidization
$Re_{p,mf}$	Reynolds number in the minimum fluidization
φ_s	sphericity of the solid particles
U_t	terminal velocity
U_t^*	dimensionless terminal velocity

a fuel are better realized if effective means of production are used with reduced GHG emissions. Methane (CH_4) and carbon dioxide (CO_2), with emissions of up to 16% and 76%, respectively, are the foremost contributors released from the industrial, agricultural, and transportation sectors [10].

Hydrogen production technologies differ regarding the state of development, the required feedstock and resources (coal, methane, and water), and the associated GHG emissions. Conventional, low-CO_2, CO_2-free, and carbon-free production routes are often referred to by the color descriptions “gray”, “blue”, “turquoise”, and “green”, respectively. The colors describe the H_2 production based on environmental friendliness as presented in Fig. 1 [11,12]. Brown H_2 is produced from the gasification of coal [13]. Gray H_2 is produced from fossil fuels and places a huge burden on the environment [14]. Blue H_2 is produced from fossil fuels as well, but it is followed by carbon capture techniques [15–17]. Turquoise hydrogen is produced from natural gas with an emphasis on

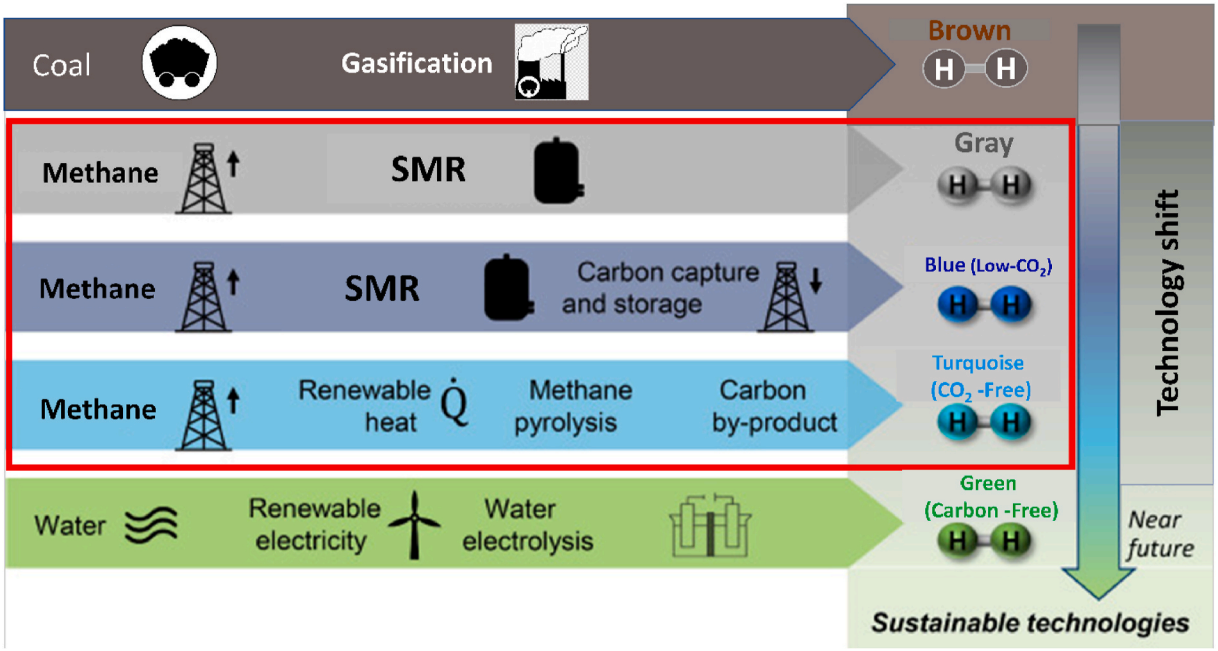

Fig. 1. General representation of H_2 production pathways describing environmental friendliness with special emphasis on the scope of this study (red paths). (Adapted with permission from Ref. [12]. Copyright (2022) Elsevier B.V.).

minimizing GHG. It involves the integration of carbon capture and storage (CCS) technologies as well as the utilization of renewable energy sources for process heating. The combination of these approaches aims to make the H_2 production process environmentally cleaner and CO_2-free [12]. Green H_2 is produced by utilizing renewable energy sources, typically through the process of electrolysis, where water is split into hydrogen and oxygen. Since the production relies on renewable sources of energy, such as solar or wind power, and does not involve fossil fuels, it is considered carbon-free and has a minimal environmental impact [12]. Presently, H_2 production on an industrial scale mainly includes 48% from reforming of natural gas, 30% from oil/-naphtha reforming in refineries or chemical industries, 18% from coal gasification, 3.9% from electrolysis of water, and 0.1% from other sources [18–20]. The utilization of CO_2 and CH_4 have received much consideration by means of gray and blue H_2 production techniques, such as steam reforming of methane (SMR) [21,22], partial oxidation of methane (POM) [23], CH_4 cracking [24], dry reforming of methane (DRM) [25], bi-reforming [26], tri-reforming of methane (TMR) [27], tri-reforming of methane (TMR) integrated with various water electrolysis systems [28], auto-thermal reforming (ATR) [29], and plasma [30]. Moreover, the conversion of hydrogen sulfide (H_2S) to hydrogen (H_2), which is called H_2S methane reforming, is widely used in the oil and gas industry for producing cleaner H_2 [31,32]. Among these technologies, SMR is currently the primary route for producing H_2 at the industrial level [33,34]. However, SMR produces approximately 9–11 kg CO_2/kg H_2, which is higher than other reforming techniques (POM and ATR) [35]. When providing the heat required to run the overall reaction, the process produces stoichiometric amounts of CO_2 from the combination of the steam reforming reaction and the water-gas shift (WGS) reaction, as well as combustion-based CO_2 [36]. On the other hand, CO_2 emissions from H_2 produced by coal gasification are nearly twice as high (23.7 kg CO_2/kg H_2) as SMR [36,37].

SMR represents the most common catalytic process for H_2 production from natural gas, despite its negative effect on the environment through GHG emissions [38]. Conventional SMR occurs by supporting Ni on various oxide supports. However, these catalysts usually undergo deactivation during operation, and this leads to lower selectivity [39]. To achieve a higher stability and purity of H_2, the advancement of catalyst preparation and proper selection of the support are very important. In addition to that, many different metal-based catalysts have been studied to minimize coke formation and increase H_2 yield [40–45]. Metal catalysts such as nickel (Ni) [46], cobalt (Co) [47], rhodium (Rh) [48], ruthenium (Ru) [49], and platinum (Pt) [50] were commonly used. Because of their low cost, Ni-based catalysts play the most important role in industrial reforming processes. However, Ni-based catalysts lead to coke formation and active site blockage, and they suffer from sintering, the agglomeration of smaller particles into bigger ones, which is associated with a decrease in available active sites [51,52]. To overcome these problems, modification of the catalyst by using promoters and examining various supports such as CeO_2 [53], ZrO_2 [54], SiO_2 [55], α-Al_2O_3 [56], γ-Al_2O_3 [57], TiO_2 [58], $MgAl_2O_4$ [59], MgO [60], La_2O_3 [61] and perovskite-type oxides have been reported [62,63]. Supported metal catalysts have gained focus due to significant progress in the metal dispersion over the supports, improving the catalytic performance and lowering the costs of the SMR process [64,65]. Proper selection of the support is crucial for achieving higher stability and purity of H_2. Therefore, various support systems have been synthesized to improve the performance of SMR that can be categorized according to their acidic or basic nature, structure, morphology, and chemical composition. It has been reported that in SMR, the Lewis basicity of the support plays a vital role in preventing the formation of coke because the base centers in the catalyst increase the chemisorption of CO_2. Adsorbed CO_2 interacts with the carbon species formed on the catalyst surface to generate CO, which inhibits coke deposition. Moreover, basic natural support materials promote surface carbon gasification to reduce coke deposition and increase stability [21,66]. While acidic supports promote polymerization and hydrocarbon cracking, which in turn assist the higher CH_4 conversion and other hydrocarbons (formed because of methyl radicals' recombination reaction) into the desired product. Based on structure and morphology, the support systems show various configurations, such as nanopowder, a grained catalyst, or structured forms like monoliths [67], honeycombs [68], or open-cell foams [69]. On the other hand, SMR makes use of nanostructures such as nanowires [70], nanorods [71], nanoflakes [72], nanotubes [73], nanofibers [74], and nanoclusters [75] to maximize metal dispersion and high stability.

Support systems can also be categorized according to their chemical composition, which includes single and mixed metal oxides [76], zeolites [77], perovskites [78], and hydrotalcites [79]. Furthermore, biomass-derived carbon-based support systems (activated carbon, carbon nanotubes) are also favorable for SMR due to their high surface area and economic synthesis. For instance, ceria as a support is used in SMR because of its different oxidation states and strong metal-support interaction, while in a recent study, mixed metal oxides, including $NiMgAl_2O_4$ and $NiCoMgAl_2O_4$, were also employed in SMR and showed better activity due to the formation of the desired structure. Additionally, the spinel structure can provide a high degree of structural stability, which can help maintain the catalytically active sites under harsh reaction conditions. Lee et al. [78] synthesized perovskite thin films ($LaFeO_3$ and $CaTiO_3$) with high activity due to better metal perovskite interaction, and Ni/Mg/Al catalysts known as hydrotalcite (HTc) exhibited the highest activity for SMR than Ni/Al_2O_3 owing to the high specific surface area and well-dispersed metal [79].

Coke formation in the SMR is caused by methane dissociation over the surface of the catalyst. It is a collective definition of various carbonaceous species formed during the SMR reaction. By rearrangements and polymerization reactions, carbonaceous species such as C_α, the most reactive form of carbon, are typically transformed into C_β, a less reactive form of carbon. The excessive formation of C_α in SMR could hinder the gasification of C_α or promote the formation of C_β that can be gasified or dissolved into metal crystallite due to high temperatures [80,81]. Furthermore, the dissolved C_β may disperse through the metal (i.e. Ni, Co) and start quick nucleation to form carbon whiskers, usually picking metal from support and resulting in fragmentation [82]. This type of coking encases carbon in a gum-like material and covers the active sites of metal. Over time, the carbon whiskers that are forming on the tip of the metal obstruct the catalyst bed and increase pressure drop to undesirable levels [83]. Consequently, the coking process reduces SMR activity.

Despite significant progress, industrial SMR suffers from inefficient energy integration [84], energy intensity, complex multistep processes, and GHG emissions [85]. Therefore, the development of current technologies to produce blue H_2 instead of gray H_2 by using carbon capture technology and making the process economically viable is highly demanded [86]. A series of new technologies have been proposed to improve the efficiency of SMR with reduced energy input and GHG emissions, including membrane technology [87], sorption-enhanced steam methane reforming (SESMR) [88], chemical looping steam methane reforming (CL-SMR) [89], chemical looping sorption-enhanced steam methane reforming (CL-SESMR) [90], solar-assisted steam methane reforming (SASMR) [91] and electrified steam methane reforming (ESMR) [92].

Several outstanding reviews have been reported on the SMR process, focusing on specific aspects of the reaction kinetics of SMR and comparison with its related technologies [93], the SMR process through membrane-based reactors [38], and the performance of Ni-based catalysts in the reforming processes [52]. However, a comprehensive picture from the basics to applied aspects of the SMR technology covering blue H_2 after the carbon-capturing techniques and the process intensifying techniques has not been reviewed yet.

In this work, the evolution route of the SMR process from gray to blue H_2 production has been thoroughly reviewed. First, the advancements in various catalyst systems such as transition metals, promoter-based, noble metals, bimetallic, and perovskite-based to enhance SMR activity while declining catalyst deactivation have been scrutinized. Secondly, kinetic models for simulating the SMR reaction emphasize the focus on enhancing catalyst performance via modifications in various types of reactors, and operating conditions are illustrated. Thirdly, the basics of SMR, which provide an in-depth view of controlling the process parameters such as reaction temperature, pressure, flow rate, and steam to carbon (S/C) ratio for H_2 production, are critically reviewed. At the end, the effects of reactor configurations such as membrane technology, sorption-enhancement, fluidization, and looping on blue H_2 production have been discussed. Moreover, future developments of industrial SMR and a novel sustainable path for the SMR, hybridizing the use of novel materials and emerging technologies to produce turquoise H_2, are proposed. Additionally, the critical points for process technology that can help leverage environmental, social, and governance (ESG) profiling have been listed. Finally, conclusive remarks, including the prospects for SMR focusing on cleaner H_2, have been presented.

2. Conventional SMR

SMR is a catalytic process that comprises a reaction between steam and light hydrocarbons or natural gas that produces a major quantity of H_2 [94]. At present, SMR of natural gas is carried out in packed-bed reactors using Ni-based catalysts, supported on ceramic oxides, due to the high efficiency of Ni and low cost. Sintering of metal particles and coking that usually occurs from side reactions, mainly during CH_4 cracking, are major problems of Ni-based catalysts [52,95–97]. The SESMR process occurs under harsh reaction conditions of high temperatures above 500 °C, high pressures, and multiple reaction and separation steps [98].

During the process, desulfurized natural gas is mixed with steam, generally at an S/C ratio in the range of 2.5–3.0 to lower coke formation, and fed to the reactor, where H_2 and CO are produced as a reaction (R1). The reaction is endothermic, and a significant amount of energy input is necessary to attain the reaction temperature and overcome the heat of the reaction. The reaction occurs on a catalyst bed inside furnace tubes, where additional energy is provided by the purge gas separated from the output of the SMR reactor. In commercial technology, high temperatures and pressure ranges for H_2 production are typically 800–1000 °C and 1.5–3.0 MPa, respectively [99,100]. The WGS then occurs to convert CO and H_2O to CO_2 and H_2, as shown in reaction (R2). This step is generally carried out in two reactors (high- and low-temperature WGS) to make use of the high-temperature and fast kinetics in the first step. Additionally, steam may be added to allow more H_2 production. A high-temperature (HT) shift reactor operating at 350–400 °C using a Cr/Fe_2O_3 catalyst and a low-temperature (LT) shift at 200 °C employing a copper-zinc catalyst were used to achieve enhanced equilibrium conversion of CO [101]. On a dry basis, the gas composition from a low-temperature shift reactor is about 76% H_2, 3% CO, 17% CO_2, and unconverted CH_4 [102]. Pressure swing adsorption (PSA) is a dominant process for H_2 separation. Multiple activated carbon or silica gel-packed beds provide constant off-gas and product composition. The adsorbent removes the impurities at high pressure and ambient temperature, whereas H_2 stays unchanged as it passes through the bed. Through this process, H_2 purity greater than 99% may be achieved [102,103]. The purge gas, with feed impurities and unconverted H_2, is sent to the reformer to supply a part of the energy to the unit [104]. A schematic view of the conventional SMR process is exemplified in Fig. 2.

The main reactions of SMR followed by WGS are described in reactions (R1)–(R3), respectively [107–109]:

$$CH_4 + H_2O \leftrightarrow CO + 3H_2 \left(\Delta H^0_{298}\right) = +206.2\ kJ/mol \quad \text{(R1)}$$

$$CO + H_2O \leftrightarrow CO_2 + H_2 \left(\Delta H^0_{298}\right) = -41.1\ kJ/mol \quad \text{(R2)}$$

$$CH_4 + 2H_2O \leftrightarrow CO_2 + 4H_2 \left(\Delta H^0_{298}\right) = +164.9\ kJ/mol \quad \text{(R3)}$$

The SMR reaction(s) as depicted in (R1)–(R3) can be tuned using various catalyst systems. Conventional and modern catalyst systems are used to control the reaction routes in order to optimize H_2 production while inhibiting coke deposition, which is a significant challenge in SMR. The reaction routes majorly depend on the composition, structure, and metal dispersion on the porous support [110]. The overall general mechanism for single metal, bimetal, and perovskites is presented in Fig. 3, which explains the relationship between catalyst type and

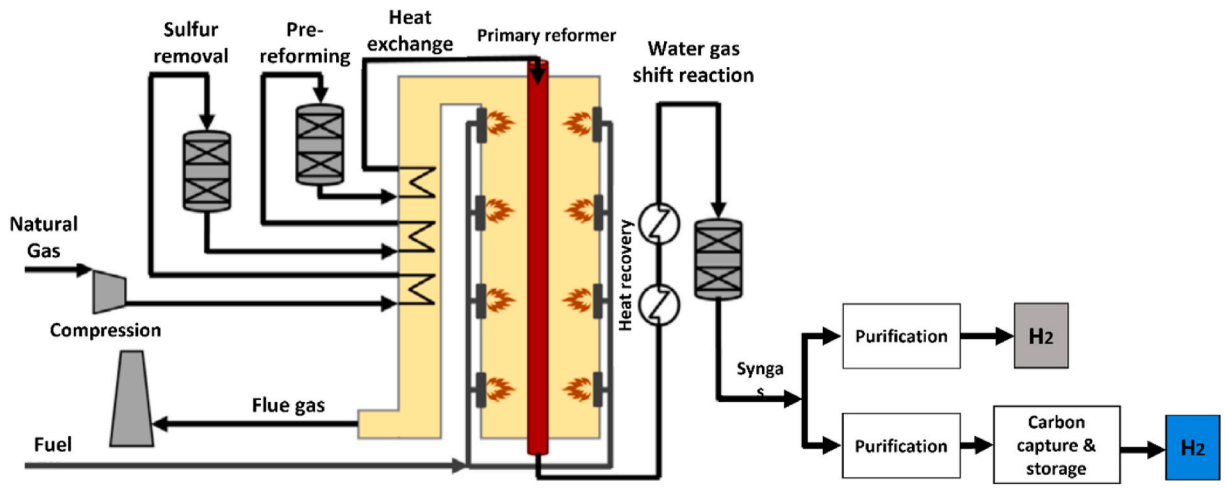

Fig. 2. Conventional multi-stages for H_2 production via SMR. (Adapted with permission from Refs. [105,106]. Copyright (2019) Technical University of Denmark).

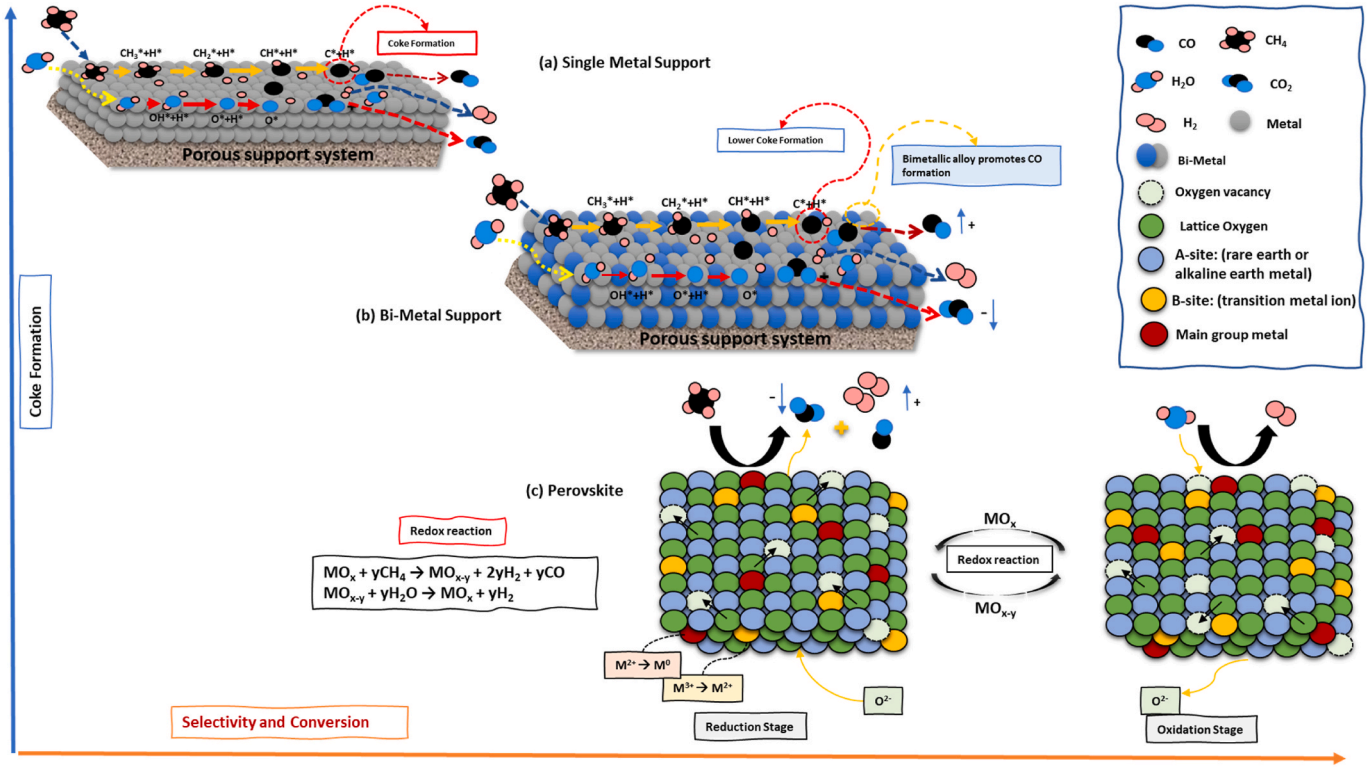

Fig. 3. The coke formation mechanism and performance of three types of catalysts for SMR (a) single metal, (b) bimetallic (Reconceptualized from this Ref. [130]. Copyright (2017) Elsevier B.V.), and (c) perovskite (Reconceptualized from this Ref. [131]. Copyright (2021) Elsevier B.V.).

performance analysis based on coke deposition, selectivity, and conversion.

Fig. 3(a) generally illustrates the mechanism of CH_4 being converted into CO and H_2, followed by WGS, which converts CO to CO_2, in the presence of steam on an active metal catalyst on a porous support. The reaction occurs in such a way that CH_4 is dissociated (CH_3*+H*, CH_2*+H*, CH*+H*, C*+H*) on adsorption onto an active metal site, while water is dissociated (OH*+H*, O*+H*) on adsorption onto the interface of metal and support to produce CO and H_2 [111–113]. Complete conversion of CH_4 and steam into H_2-rich syngas requires the minimum formation of coke and CO_2. In the use of single-metal catalysts, the size of metal particles and the strength of interaction between support and metal particles are important factors in reducing coke formation while following the targeted reaction routes. For the industrial sector, Ni-plated on α-Al_2O_3 is the most promising catalyst [75, 114–116]. Usually, the well-dispersion of Ni on a well-defined structure results in the best metal-support interactions. For SMR, various structures were synthesized for Ni in the form of both oxide and metallic states (e.g., LaNi–Fe, $NiAlO_3$, LaNi-Co) [114,117–119]. Encouraging results were reported, with better stability against the odds in SMR.

Another aspect to consider while selecting a catalyst for SMR is the metal particle size, which can significantly impact the reaction rate, selectivity, and stability of the catalyst. Smaller metal particle sizes result in higher catalytic activity due to their higher surface area and higher concentration of active sites. This increased activity can lead to higher reaction rates and faster conversion of CH_4 to H_2. However,

smaller particles may also be more susceptible to deactivation due to coking or sintering, which can decrease the lifetime of the catalyst. On the other hand, larger metal particle sizes can offer better stability and resistance to deactivation. But they may also have lower activity due to a lower concentration of active sites. Therefore, the extent of particle sintering depends on reaction conditions, metal loading, and crystallite size. The newly found mechanism for particle sintering is the aggregation of smaller particles and metal atom migration. Therefore, to prevent particle migration on the surface of a support, the metal-support interaction must be chosen properly. Furthermore, $Ru/Ni_xMg_{6-x}Al_2$ with x= 2, 4, and 6 M ratios were synthesized to study the catalytic performance and reduction in secondary reactions. It was found that even with a low Ru content of 0.5 wt%, the oxide particles were highly dispersed, which consequently showed better catalytic activity and fewer secondary reactions during the process [120].

Having said that, the single metal is susceptible to deactivation due to carbon formation, as indicated in Fig. 3(a), lowering the conversion efficiency and lifespan of the catalyst. This prompts the researcher to concentrate on single-metal catalyst alternatives [121]. The development of a bimetal catalyst for SMR has been extensively investigated to show its effectiveness regarding its performance in SMR.

The bimetal effect is significant in the SMR due to the additional integration of metal in the support system to improve the active sites and add more functionalities to the overall catalyst system. The addition of a second metal to the catalyst drastically modifies the metallic properties due to the formation of bimetallic alloys, i.e., Ni-M, on the surface [122]. Fig. 3(b) presents a general mechanism of SMR over bimetallic catalyst systems with possible reaction routes. H_2O and CH_4 react on the bimetallic catalyst surface to form H_2 via CH_4 dissociation route. The difference in comparison with monometallic catalysts occurs due to the bimetallic alloy, while CH_4 reforming reaction occurs with monoatomic carbon formation. However, the surface oxygen removes the monoatomic carbon, and the presence of a second metal changes the metal structure to block the graphite nucleation [123]. This formation of bimetallic alloys occurs during catalyst reduction, making the catalyst surface less prone to coke formation than single-site metal catalysts [124]. The proposed reaction mechanism (Fig. 3(b)) is targeted at the same category of metals, i.e., in the case of transition metals, both metals should be from the transition group or both from noble metals, or vice versa. The various groups can be integrated as bimetallic catalysts; however, the overall chemistry will be challenging to understand because of different surface functions [52]. The bimetallic catalysts offer a synergistic effect to enhance the performance of the C–H bond cleavages during CH_4 decomposition steps, altering the atomic and molecular adsorption energies [121]. It promotes CO formation rather than CO_2 formation and reduces carbon formation in SMR. The bimetallic catalysts also exhibit coke deposition but with better catalytic performance because of the synthesis optimization focusing on metal-support interaction. Hence the recent focus on perovskites, a promising alternative to single or bimetal catalysts. Perovskites offer a variety of metals (Ni, La, Sr, etc.) that integrate to form a unique crystal structure to optimize the SMR performance.

Different metals in perovskite-based catalysts tend to accelerate CH_4 activation and increase the number of oxygen vacancies. Fig. 3(c) shows the general mechanism of perovskite-based CL-SMR. The process involves reduction (MO_x) and oxidation stages (MO_{x-y}), as can also be seen in the inset reaction steps. Initially, for the POM, the redox catalyst is deprived of the lattice oxygen to produce syngas (H_2, CO) domination by a complete CH_4 oxidation [125]. This occurs when CH_4 gets adsorbed to the oxygen vacancy of perovskite and rapidly reacts with the active surface oxygen species. As the reaction proceeds, oxygen is consumed, generating more oxygen vacancies and H_2-rich syngas [126]. The excessive oxygen vacancies and carbon gasification reduce carbon formation and improve CO formation, while CO_2 production is also inhibited. In the oxidation stage, H_2O splitting occurs, where the reduced sample is re-oxidized back to perovskite along with H_2 production [127]. Oxygen vacancies formed in the reduction process provide active sites for H–O bond breakage in H_2O [126]. The double adjustment of different metals in the perovskite structure can help improve the coking resistance in the process along with the high stability in the redox cycles [128].

The spinel $MgAl_2O_4$ has been studied as a support in different chemical reactions due to its surface basicity and high chemical, thermal, and mechanical strength [129]. In comparison with generally used Al_2O_3 or SiO_2-based catalysts, Ni-loaded $MgAl_2O_4$ exhibited high coke resistance in DRM, SMR, and SESMR reactions. Control of $MgAl_2O_4$ composition to somehow achieve the desired performance is a tricky matter, as a high content of Mg leads to less coke formation and less mesopore formation, leading to smaller activity. However, low content of Mg presents vice versa effects [115]. It was reported that the catalytic performance of $MgAl_2O_4$ prepared from defect spinel structures in DRM was dependent on the Mg content, presenting a minimum coke formation at an Mg/Al molar ratio of 0.24 [132]. Similarly, the effect of Mg loading on the crystal size of Ni was studied to investigate the resulting catalytic performance and coke resistance of the synthesized Ni/$MgAl_2O_4$ in the SMR reaction. It was found that catalysts with higher Mg content showed greater resistance against coke deposition [133].

Similarly, Fonseca et al. [134] investigated HTc precursors to form Ni-based catalysts at 750 °C for 8 h in a quartz tube reactor for SMR. It was found that uniform active site distribution in the HTc structure reduced the carbonaceous deposit formation. In addition, Ni chelates have resulted in higher CH_4 conversion in comparison with other catalysts due to better active site dispersion. Supports including SiO_2 and Al_2O_3 allow surface oxidation of Ni-based catalysts at 500 °C during SMR, whereas ZrO_2 showed higher CH_4 conversion and stabilized the Ni particles, as ZrO_2 allows water accumulation that promotes SMR by the formation of hydroxyl groups [135]. At temperatures greater than 700 °C, Ni is incorporated into the alumina structure to form a solid solution of $NiAl_2O_4$–Al_2O_3 with NiO. Owing to the complex interactions between Ni-particles and Al_2O_3 support, their catalytic performance is still not well understood [136]. For example, even though the reduced $NiAl_2O_4$ is highly active during reforming reactions, it can still be re-oxidized with a source of oxygen, resulting in the inactivation and decay of $NiAl_2O_4$ [137]. Due to the redox and morphological properties (Ni dispersion, surface area) of supports, larger CH_4 conversion, reduction in coke formation, and superior catalytic properties were observed [52].

Several mechanisms have been proposed to better understand the reaction kinetics and the fundamentals of CH_4 dissociation and product formation [138,139]. The initially proposed reaction mechanism of SMR on Ni catalyst using an ab initio microkinetic model is shown in Fig. 4(a), where O*, CH_4*, CH_3*, CH_2*, CH_2O*, COH*, COOH*, CHO*, CO*, CO_2*, and H_2* represent the adsorbed species during the reaction over a multi-faceted Ni catalyst [140]. It is suggested that the oxygen concentration, among others, determines the reaction kinetics to a large extent and leads to the formation of H_2, CO, and CO_2 via various sequential routes [140]. Fig. 4(b) shows the reaction mechanisms, metal transitions, oxygen diffusion, and migration of the reaction boundary during the two-step reactions using X-ray powder diffraction (XRD), X-ray photoelectron spectroscopy (XPS), temperature-programmed reduction (H_2-TPR), and glass transition temperature (TG) technologies. It identifies three reaction stages and suggests that the synergistic effects between multi-metals in the double perovskite structure can effectively promote the POM and steam splitting. The decrease of the active metals and the increase of oxygen on the surface during the reaction demonstrate that the reaction boundary is fixed on the surface of the oxygen carrier (OC) particle. During the reduction stage, lattice oxygen transfers from the bulk to the boundary to take part in the CH_4 reduction reaction, while bits of them are transformed into chemically adsorbed oxygen with more stable properties. A large amount of syngas is generated due to the concordance of CH_4 dissociation with the lattice oxygen diffusion, and the resistance to coke formation is enhanced effectively. In the steam dissociation process, the deeply reduced metals

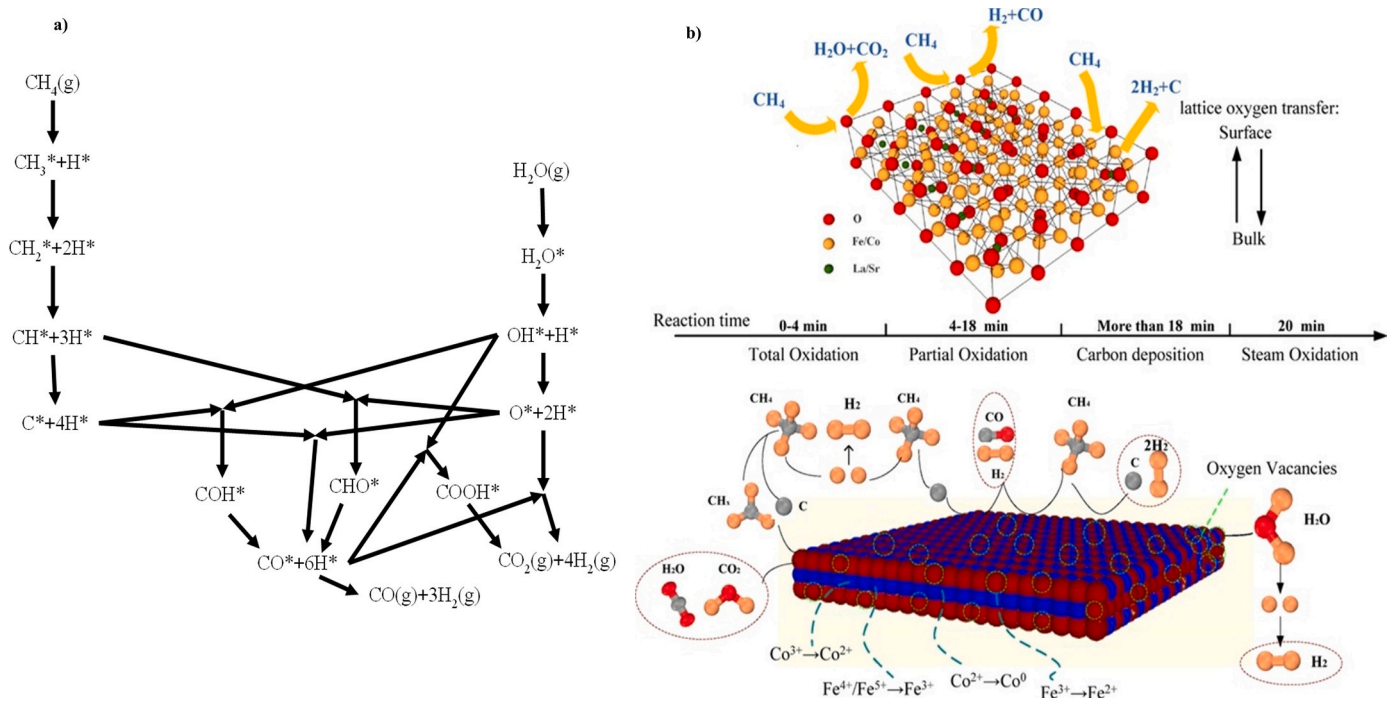

Fig. 4. a) The detailed mechanism of SMR over a multi-faceted Ni catalyst. (Recreated with permission from Ref. [140]. Copyright (2011) Springer Nature). b) Reaction mechanism model for CL-SMR over double perovskite oxides ($La_{1.6}Sr_{0.4}FeCoO_6$). (Adapted with permission from Ref. [141]. Copyright (2017) Elsevier B.V.).

combine with abundant oxygen vacancies to provide ample active sites for the breakage of the O–H bond of steam. The oxygen vacancies can be supplied directly by the O atom derived from H_2O [141]. The findings provide a potential way to develop a more active OC for CL-SMR to co-produce syngas and H_2 by comprehensively considering methane dissociation and lattice oxygen diffusion.

In most cases, surface active sites encourage cracking and subsequent polymerization of hydrocarbons, leading to coke formation on the surface of the catalyst during CH_4 cracking (R4) and the Boudouard reaction (R5). However, alkali metal addition can suppress carbonaceous deposition; however, the catalytic activity is also compromised. Proper acid-base balance (promoter role) and metal-support interaction should be considered to hinder coke formation [142]. Accordingly, to clarify the catalysis effects, kinetic models and process parameters on conventional SMR to gray H_2 production will be addressed in the following sections.

$$CH_4 \rightarrow C + 2H_2 \left[\left(\Delta H^0_{298}\right) = +75\ kJ\ /\ mol\right] \quad \text{(R4)}$$

$$2CO \rightarrow C + CO_2 \left[\left(\Delta H^0_{298}\right) = -172\ kJ\ /\ mol\right] \quad \text{(R5)}$$

2.1. Effect of catalyst

Generally, catalysts increase the rate of the SMR reaction and allow for greater H_2 production efficiency. Moreover, they allow for lower operating conditions compared to non-catalytic methods, reducing energy requirements and operating costs. Additionally, the catalyst can be designed to selectively promote the formation of H_2 over other byproducts, such as CO or CO_2, which can improve the overall yield and purity of the H_2 produced. In this section, the effect of catalyst type on SMR for H_2 production has been investigated according to previous experimental studies.

2.1.1. Supported Ni-based catalyst

The catalyst's properties and composition play a key role in the catalysis. The ideal catalyst is considered to have high stability, low cost, and high catalytic activity. SMR is performed using Ni over various support systems such as Al_2O_3, MgO, $MgAl_2O_4$, CeO_2, La_2O_3, TiO_2, ZrO_2, SiO_2, etc [135,143–145]. Ni is one of the most investigated and used catalysts for SMR due to its low cost and high activity in SMR reactions. Despite its widespread use in SMR reactions, Ni catalyst suffers from sintering and coking at low temperatures, though it performs better at higher temperatures. The possible elementary steps involved in CH_4 reforming and WSG are presented in Fig. 5, where C* and H* represent the chemisorption phenomena. To overcome the stated issues with the Ni catalyst, various approaches were followed, such as bimetal impregnation. For instance, Co–Ni over Al_2O_3 showed high stability against coke formation at different Co loadings [146]. The Ni catalyst performance in SMR and H_2 yield can be improved using noble metals. However, catalyst deactivation is mainly due to the loss of (active) surface area by the growth of crystals, pore collapse, and transformation of catalytic active phases to non-active phases [147]. Various approaches were adapted to overcome those issues. However, the question of elimination of the Ni catalyst deactivation in SMR remains unanswered.

Supported noble-metal catalysts such as Pd and Pt have shown superior stability and comparable reactivity over Ni-based supported catalysts in SMR [49,82,149,150]. The Ni catalysts perform better at moderate (600–900 °C) and high temperatures (>900 °C) and they exhibit lower catalytic performance at the lower temperatures (400–600 °C) as SMR is an endothermic reaction [151]. In comparison to the noble metal catalysts in SMR, Rh-perovskite catalysts presented higher activity than Ni-based catalysts in SMR by lowering the activation energy (69 vs. 96 kJ/mol) [152]. A tremendous amount of research has been conducted to improve catalytic performance and reduce coking and sintering by modifying the types and amounts of active metals, controlling support materials, and investigating preparation methods. In this regard, many research groups have examined the catalytic performance of noble metals in the SMR reaction. For instance, noble metals including Ru and Rh have exhibited higher catalytic activity in SMR reactions due to lower coke formation [93]. Norskov et al. reported that the activities of the examined metals were in the order of Ru ≈ Rh > Ni

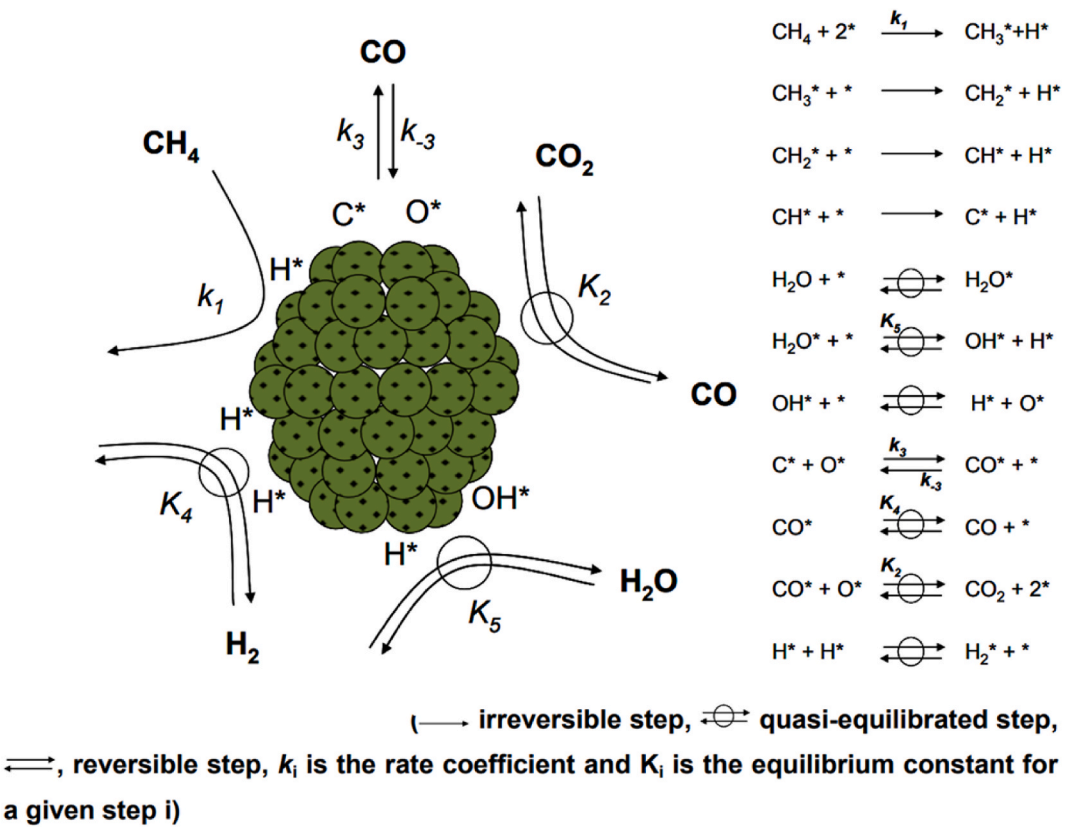

Fig. 5. The possible reaction mechanism and elementary reaction steps for CH_4 reforming and water gas shift reactions over Ni-supported catalyst. * represents the catalyst active site. (Adapted with permission from Ref. [148]. Copyright (2004) Elsevier B.V.).

≈ Ir ≈ Pt ≈ Pd, while the theoretical results showed somehow different results [153]. A study presented the reaction rate volcano projected by the microkinetic model on the surfaces of eight different transition metal catalysts for SMR at 500 °C and S/C of 3.5 [154]. The catalytic activities of transition metal catalysts in the following order were exhibited as; Ru ~ Rh > Ni ~ Pt > Pd ~ Co~>Fe > Cu. According to another study [153], Pt activated the C–H bond more efficiently than Rh, Ir, and Ru. Hence, it is not possible to form a specific order of selectivity and catalytic activity toward H_2 production due to the disagreement of results from different researchers [93].

Additives such as Ce, Zr, and La have been used to enhance the catalytic performance of conventional methane reforming catalysts. For instance, NiO/CeO_2 was tested for SMR at low temperatures and achieved stable operation for more than 25 h, the H_2 production of which was 5.0 mmol min^{-1} with an H_2/CO ratio of 4.3 [155].

The promoters improve the stability of the SMR; for instance, three different promoters, i.e., La, B, and Rh, were compared over $Ni/MgAl_2O_4$. The deactivation in unpromoted Ni catalysts is higher as compared to promoted catalysts. According to various studies, Ni particles are more prone to carbon growth on the tip and have a higher driving force for carbon diffusion [156,157]. Maluf & Assaf [158] investigated the use of Mo oxide as a promoter in Ni catalysts for SMR at various loadings and discovered stable catalytic performance due to the synergistic effect created by Mo electron transfer and enhanced catalytic sites. In another study, the Ce and calcium promoters were investigated in Fe_2O_3/Al_2O_3 catalyst for CL-SMR process. The addition of a 5% promoter shows a better CH_4 conversion as compared to the non-promoted catalyst. Xu et al. [159], investigated the effect of boron as a promoter on $Ni/\gamma\text{-}Al_2O_3$ for SMR, improving the catalytic performance as compared to a non-promoted Ni catalyst. The 1 wt% boron reduced the rate of deactivation by a factor of 3 and improved the coking resistance of the Ni-based catalyst. The anti-coking phenomena were investigated by DFT calculations, which concluded that the boron may reduce the nucleation of graphene islands while blocking the step sites. It also inhibits carbide formation while weakening the on-surface carbon binding energies [160,161].

Table 1 summarizes previous research and advancements for supported Ni-based catalysts for SMR, as well as operating conditions and performance. The Ni-supported catalysts synthesized via wetness impregnation and co-precipitation techniques were examined at temperatures between 500 and 600 °C for SMR. Ni–Zn–Al and Ni–Mg–Al catalysts synthesized via the co-precipitation method exhibited higher catalytic activity and more stability against sintering compared to $Ni/\alpha\text{-}Al_2O_3$ and Ni/SiO_2 prepared via wetness impregnation, owing to the enhanced metal-support interactions of the catalysts. The higher catalytic activity of Ni-based Zn–Al and Mg/Al was ascribed to the small particle size (3–6 nm) coming from increased metal-support interaction, which prevented the carbon dissolution to form nanofiber materials [162]. Various papers have described the enhanced characteristics of catalysts synthesized via the sol-gel method. For instance, Rodemerck et al. [163] reported mesoporous silica as a promising Ni-based candidate in SMR. In comparison with a catalyst prepared via the impregnation method, Ni/SiO_2 was prepared via the sol-gel method in the presence of a polymer to reduce the particle size of Ni. It was observed that the sol-gel method in the presence of polyethylene glycol produces smaller and finely dispersed Ni particles, presenting higher activity and enhanced stability against coking. Similarly, Ni was introduced into Ce-modified SBA-15 via a wetness impregnation technique. Catalysts with 10% Ni/CeO_2-SBA-15 proved more stable and enhanced H_2 yield by 30.5% (mol%) due to the oxygen storage capacity and redox property of CeO_2 [164]. An attempt to support Ni on alumina functionalized with silica via different impregnation techniques was reported. Compared with Ni supported on silica-alumina via conventional impregnation with sizes of 18–20 nm, the Ni nanoparticles prepared in ethylene glycol (5–8

Table 1
Summary of Ni-based catalysts for SMR.

Catalyst	Metal loading	Process conditions	CH_4 conversion (%)	H_2 yield (%)	CO selectivity (%)	H_2/CO ratio	Remarks	Ref
$NiAl_2O_4$ **$Ni_2Al_2O_5$**	34 wt% Ni 45 wt% Ni	T = 700 °C; GHSV = 65,500 h^{-1}	78% 82%	–	–	5.0 4.0	Both catalysts in the reduced state were found active for SMR without the deposition of carbon species due to the occurrence of sufficiently small Ni nanoparticles.	[166]
Ni/α-Al_2O_3 **Ni/SiO_2** **Ni/Zn/Al** **Ni/Mg/Al**	7-9 wt% Ni	T = 500 °C; T = 600 °C	–	–	0.1–0.3	–	Metal activity and resistance to sintering were more active at 600 °C. The interaction between Ni and support was stronger in Ni–Zn–Al and Ni–Mg–Al. Ni–Zn–Al showed the highest activity and the lowest formation of carbonaceous deposits.	[162]
Ni/Ce–ZrO_2/θ-Al_2O_3	12 wt% Ni	T = 700 °C; GHSV = 10,000 ml/g_{cat}; S/C = 3	97	–	–	–	The effect of steam treatment was studied over the synthesized catalyst. The catalyst was deactivated by steam treatment but regenerated via H_2 reduction, resulting in the formation of $NiAl_2O_4$ and further changes to Ni + Al_2O_3. The presence of more Al_2O_3 in the supported Ni catalyst facilitated the formation of inactive $NiAl_2O_4$.	[167]
Ni/m,t-ZrO_2	10 wt% Ni	T = 700 °C; S/C = 4	75	33	–	–	The amount of coke formation after the reforming reaction was dependent on the structure of ZrO_2 and the reaction conditions.	[168]
Ni/Al_2O_3 **Ni/MgO–Al_2O_3** **Ni/CeO_2** **Ni/$Ce_{0.4}Zr_{0.6}O_2$**	10 wt% Ni	T = 750 °C; S/C = 2; Catalyst loading = 100 mg	97.0 97.2 89.0 91.0	–	8.2 8.8 10.9 11.2	5.8 5.0 6.4 9.0	All catalysts exhibited excellent thermal stability with no loss for 50 h. Ni/$Ce_{0.4}Zr_{0.6}O_2$ showed the highest H_2/CO due to WGS, while the catalysts with Ni loading on MgO–Al_2O_3 and Al_2O_3 functioned best in SMR.	[143]
Ni/CaO–ZrO_2/γ-Al_2O_3 **NA** **NZA** **N20CZA** **N45CZA** **N55CZA**	10 wt% Ni;	T = 600 °C; S/C = 1; Catalyst loading = 100 mg	~60 ~45 ~60 ~45 ~45	– – – – 35	– – – – –	– – – – –	Various samples of 10 wt% Ni/Al_2O_3 modified with molar ratios of 0–0.55 were named NZA to N55CZA, respectively. $CaZrO_3$ prepared at a molar ratio of 0.55 CaO/ZrO_2 provided oxygen vacancies for water adsorption and showed the existence of a large quantity of whisker carbon. N55CZA showed the highest H_2 yield of 35%, followed by a decreasing order of NA, N45CZA, and N20CZA, respectively.	[169]
Ni/SiO_2-DBD	10% wt.% Ni	T = 700 °C; S/C = 1.5; GHSV = 26,000 ml/g_{cat}	63	–	47	–	Before calcination, Ni/SiO_2 was treated with DBD plasma. The catalyst prepared by this method revealed small particle sizes of Ni particles and low activity, which led to an improved balance between carbon gasification by H_2O and carbon deposition. Less carbon deposit formation at an S/C of 1.5.	[170]
Ni–MgO/Inorganic paper composite	NA	T = 800 °C; S/C = 3; Gas velocity = 18,000 h^{-1}	90	–	–	–	Two different preparation techniques, co-impregnation and sequential impregnation, were used to prepare the catalyst for SMR. Excellent catalytic performance and H_2 productivity are achieved from co-impregnated Ni/MgO.	[171]
NiO/SiO_2	10 wt% Ni	T = 700 °C; S/C = 3.5; Catalyst loading = 1.0 g	95.7	3.8 mol H_2/mol of CH_4 reacted	–	–	The crystallite size of NiO varied with the Ni loading and calcination temperature.	[55]
Ni/TiO_2	10 wt% Ni	T = 700 °C; S/C = 1.2; GHSV = 48,000 h^{-1}; Catalyst loading = 150 mg	92	–	77	–	The catalyst presented high resistance to coke formation and high activity at a low S/C ratio. For 96 h, stable conversions and selectivity were achieved. The catalyst was found favorable for use in industrial reformers considering there was no coke deposition and no significant changes in Ni particle size.	[172]
Ni/Mg-Aluminate (spinel)	15 wt% Ni	T = 800 °C; S/C = 3; GHSV = 16,000 h^{-1} Catalyst loading = 85 mg	100	–	–	>3	A catalyst with a higher Mg content showed high coke resistance. A catalyst with lower Mg content resulted in a larger surface area due to the difference between the exsolution of Ni particles and the sintering resistance.	[115]
Ni/$MgAl_2O_4$	15 wt% Ni	T = 600 °C; Calcination	50	–	–	5.1	Increasing calcination temperature decreased the surface area of metal and Ni crystal size but	[59]

(*continued on next page*)

Table 1 (*continued*)

Catalyst	Metal loading	Process conditions	CH_4 conversion (%)	H_2 yield (%)	CO selectivity (%)	H_2/CO ratio	Remarks	Ref
		temperature = 850 °C; S/C = 5; Pressure = 1 bar; Catalyst loading = 100 mg					enhanced the effective dispersion due to metal oxide formation. At 850 °C, the highest catalytic activity was observed.	
Ni/Ce–Gd	30 wt% Ni 10 mol% Gd	T = 700 °C; S/C = 3; Catalyst loading = 15 mg	60	–	–	11	The addition of gadolinium increased the metal-support interaction and provided better resistance to the sintering of metal particles.	[173]
Ni/SiO_2	10 wt% Ni	T = 500 °C; S/C = 1; Catalyst loading = 0.1 g	11	–	–	–	Low-temperature SMR was studied over Ni/TiO_2. The catalyst was able to maintain stable conversions for 96 h. The metal-support interaction was stronger in Ni/TiO_2 when compared with Ni/SiO_2.	[58]
Ni/TiO_2	10 wt%Ni		28	–	26			
NiO/SiO_2-DBD	10 wt% Ni	T = 800 °C; S/C = 0.5 GHSV = 2.4 × 10^4 $cm^3/g.h$	40	–	–	–	SMR at varying temperatures was investigated for Ni/SiO_2 prepared from DBD plasma. The catalyst increased CH_4 conversion from 25% to 40% when the temperature was raised from 600 °C to 800 °C.	[174]
$Ni/SiO_2/ZrO_2$	Varying quantities of Ni	T = 750 °C; S/C = 2.5 GHSV = 50,400 $mlg^{-1}h^{-1}$	>90	–	70	–	The porosity effect and stability of the catalyst were evaluated for SMR. The catalyst remained stable for 48 h with a CH_4 conversion of more than 90%.	[175]
Ni/Al_2O_3–Y_2O_3–ZrO_2	5 wt% Ni	800 °C; S/C = 1.25 Space time = 263 ms	95.6	67	87	3.7	The addition of Y_2O_3 to ZrO_2 was studied to develop kinetic data for SMR. It was observed that the introduction of Y_2O_3 increased the activity of the O_2 pumping component.	[176]

nm) improved dispersion, which consequently resulted in stable activity in SMR for 48 h, coming from less sintering and no coke formation [165]. In another study, Son et al. [57] investigated the impact of the MgO promoter on $CoNi/Al_2O_3$ catalytic performance. The $MgO–CoNi/Al_2O_3$ catalyst showed much higher activity and stability in the dry reforming of methane over 200 h in comparison with the MgO-free $CoNi/Al_2O_3$ catalyst. This excellent performance of $MgO–CoNi/Al_2O_3$ was attributed to the cumulative effects of a higher interaction of Ni with alumina, enhanced basicity of the surface lowering coke deposition, and a higher decomposition rate of adsorbed methane and CO_2. As apparent from the literature presented, the interaction of support and catalyst holds a crucial role in contributing to the catalyst's performance and stability due to its strong interaction with active metal. Hence, ZrO_2, CeO_2, and mixed oxides are mostly used as supports because of their redox properties, oxygen storage capacity, and sufficient resistance to coking, resulting in superior SMR catalytic performance as compared to conventional supports [52].

2.1.2. Promoters and noble metals

Metal promoters have been successfully incorporated into reforming catalysts to overcome the shortcomings of single metal (Ni) or (Co)-based catalysts and improve catalytic stability. These additives helped improve the reaction activity and reduce coke deactivation, thus increasing the H_2 yield [177]. Table 2 presents a summary of reported catalysts with promoters and noble metals for SMR. A sequence of noble metal catalysts supported on Al_2O_3 and $MgAl_2O_4$ prepared via the impregnation route was investigated for the SMR process. The 5%Rh and 5%Ir promoted $MgAl_2O_4$ recorded exceptionally high metal dispersions of around 50% and 100%, respectively, and proved to have the best stability and activity for SMR. Highly dispersed, fine nanosized Rh and Ir were identified on the spinel $MgAl_2O_4$ support with strong metal-support interaction [178]. The use of Pd as a promoter in a porous membrane enhanced the carbon resistance for low-temperature SMR. The addition of Pd upgraded the catalytic stability and activity of the Ni-YSZ membrane, thus increasing the H_2 yield and CH_4 conversion because of the equilibrium shift due to the difference in permeation rates between H_2 and other product gases as per Le Chatelier's principle. Pd clusters played a major role in reducing the carbon deposition on the catalyst surface during the SMR at 650 °C [179]. Furthermore, core-shell structured Ni@Pt significantly reduces carbon deposition without considerably reducing activity. Due to its comparison with Ni(111) and Pt (111), the core-shell Ni@Pt catalyst modified the surface Pt electron density and shifted the d-band center away from the Fermi level [180].

CeO_2 shows better characteristics for use as a support for Ni impregnation, but due to its beneficial impact, CeO_2 gives pronounced results when used as a promoter. CeO_2 support provides the role of an oxygen buffer for the catalyst. In this respect, CeO_2 was incorporated as a promoter of Pt/Al_2O_3 for the SMR and steam reforming of toluene to explore the impact of CeO_2. It was found that CeO_2 provided the source of oxygen needed to control the redox properties of the synthesized catalyst during the reforming reaction. However, due to the adsorption of both CH_4 and toluene in the same active sites, a slight deactivation of catalysts was observed, resulting in the accumulation of carbonaceous compounds on the surface [181]. Similarly, Duarte et al. [182] investigated the promotion of Al_2O_3 support with CeO_2 and $Sm_2O_3–CeO_2$ to disperse Rh to investigate the stability and activity of SMR at 500 °C. The $CeO_2–Al_2O_3$ support contributes to the partial stability of Rh, leading to the formation of nanosized and atomically dispersed particles of Rh. Because of the durable metal-support interaction, CeO_2 promotes the stabilization of atomically distributed small metal particles [183]. Rare earth metals and alkaline earth metals can provide a promising solution for the deactivation and sintering of catalysts [51]. Promoter(s) addition to supports changes the metal-support interactions, which frequently inhibit phase transformation and metal sintering while exposing more active sites to the reactants. However, the selection of a suitable co-metal can still be a difficult part, for which the reaction pathway is

Table 2
Summary of promoters and noble metals for SMR.

Promoter/ noble metal	Catalyst composition	Catalyst/ promotor loading	Process conditions	CH_4 conversion (%)	H_2 yield (%)	CO selectivity (%)	H_2/ CO ratio	Remarks	Ref
Alkali promoter (K_2O)	$NiO–Al_2O_3$	1-4 wt% K_2O	T = 550 °C S/C = 1.4–6; Catalyst loading = 25–100 mg	30–65	–	–	–	The addition of alkali to the reforming catalyst was studied and resulted in a reduction of reforming rates, but being highly coke-resistant, it was more efficient when used in the top portion of reformer pipes.	[184]
Ce-based	Ni–Ce/Al	13 wt% Ni 1.02 wt% Ce	S/C = 3; GHSV = 10,000 h^{-1}	90	–	–	–	Investigations into the effects of different Ce contents on the catalytic performance revealed that a small amount of Ce improved the Ni dispersion and inhabitation of carbon deposition. The optimum activity was achieved at 1.02 wt% Ce with 75% carbon conversion.	[177]
CeO_2-based	$Pt/CeO_2/Al_2O_3$	1.4 wt% Pt	T = 700 °C S/C = 4 Catalyst loading = 20 mg	74	–	~10	–	The effect of the reactant mixture (CH_4/toluene) on the activity of the catalyst for SMR, reforming of toluene, and mixture was observed. The catalyst underwent slight deactivation during the reforming of CH_4 or toluene. However, a strong deactivation was observed with the mixture of reactants.	[181]
Mo-based	$Mo–NiO/Al_2O_3$	0.05 wt% Mo	T = 700 °C S/C = 2	80	55	–	–	Mo addition increased the activity of active sites due to the electron transfer from Mo to Ni, enhancing the electron density of active sites. However, the metal's surface area decreased.	[158]
B-based	$B–Ni/\gamma Al_2O_3$	15 wt% Ni 1 wt% B	T = 800 °C GHSV = 330,000 cm^3/g.h Catalyst loading = 100 mg	61	–	–	–	The effect of boron addition on deactivation behavior was evaluated for SMR. The addition of boron enhanced the initial CH_4 conversion from 56 to 61% and reduced the deactivation rate by 3.	[159]
Pd-based	Pd–Ni-YSZ	0.5 wt% Pd	T = 650 °C S/C = 3 GHSV = 3800h^{-1}	94.6	3.94	–	–	Pd addition to the catalyst on the membrane in SMR was studied and resulted in higher catalytic activity and well-dispersed Pd particles. In addition, Pd addition exhibited increased adsorption capacity for H_2O.	[185]
Rh-based	$Rh/MgAl_2O_4$	5 wt% Rh	T = 850 °C S/C = 3 GHSV = 284,000 h^{-1} Catalyst loading = 9 mg	40	–	–	–	The addition of Rh to $MgAl_2O_4$ resulted in a highly stable spinal structure.	[178]
Rh-based	$Rh/Ce_{0.15}Zr_{0.85}O_2$	3 wt% Rh 10 wt% Ni	T = 500 °C	28.1	–	16.2	27.4	At low T = 500 °C, the catalyst demonstrated high stability and catalytic activity without coking.	[186]
			T = 600 °C	52.9	–	42.3	9.3		
			T = 700 °C	80.9	–	73.0	4.9		
			T = 800 °C	98.6	–	61.0	6.1		
			Catalyst loading = 100 mg						
Sm-based	Ni/SBA-15	3 wt% Sm 10 wt% Ni	T = 700 °C S/C = 3 Catalyst loading = 0.2 g	70	66	–	~3	Sm addition promoted the catalytic activity of the unpromoted catalyst from 31% to 70% for the Sm-promoted catalyst. The majority of carbon species deposited during the SMR stability test were filamentous carbon. However, none of the Ni nanoparticles were blocked by the carbon fibers.	[187]
M-based (M= Pt, Ru)	$M/ZnLaAlO_4$	3 wt% Pt 3 wt% Ru	T = 800 °C S/C = 3 GHSV = 10,500 h^{-1} Catalyst loading = 0.25 g	~95 ~99	~66 81.4	–	~5.5 ~6.5	As per the analysis by thermogravimetric analysis (TGA) and field emission scanning electron microscopy (FESEM), the Ru-promoted catalyst exhibited the best catalytic performance with almost no coke deposition.	[50]
Co-based	$Co–MgAl–CO_3$	–	T = 750 °C S/C = 2 Catalyst	80	–	–	4.8	Catalysts prepared by the traditional and anion-exchange methods showed stability for 6 h at an S/C of 2.	[188]

(*continued on next page*)

Table 2 (*continued*)

Promoter/ noble metal	Catalyst composition	Catalyst/ promotor loading	Process conditions	CH_4 conversion (%)	H_2 yield (%)	CO selectivity (%)	H_2/ CO ratio	Remarks	Ref
			loading = 100 mg						
Ru-based	Ru/Al_2O_3	8 wt % Ru	T = 800 °C S/C = 1.5 GHSV = 20,000 h^{-1}	88.7	–	–	~8.3	The Ru-modified catalyst exhibited higher yields of H_2 and CO. The H_2/CO ratio decreased with increasing temperature.	[189]
Ir-based	$Ir/MgAl_2O_4$	5 wt% Ir	T = 850 °C; S/C = 3; GHSV = 284,000 h^{-1} Catalyst loading = 9 mg	53	–	–	–	Ir addition, increasing the metal-support interaction and decreasing the tendency toward large particle sizes.	[178]
Pt-based	Pt/Al_2O_3	1 wt% Pt	T = 700 °C S/C = 4 Catalyst loading = 20 mg	~70	–	~10	–	Less carbon deposition on Pt addition was observed.	[181]

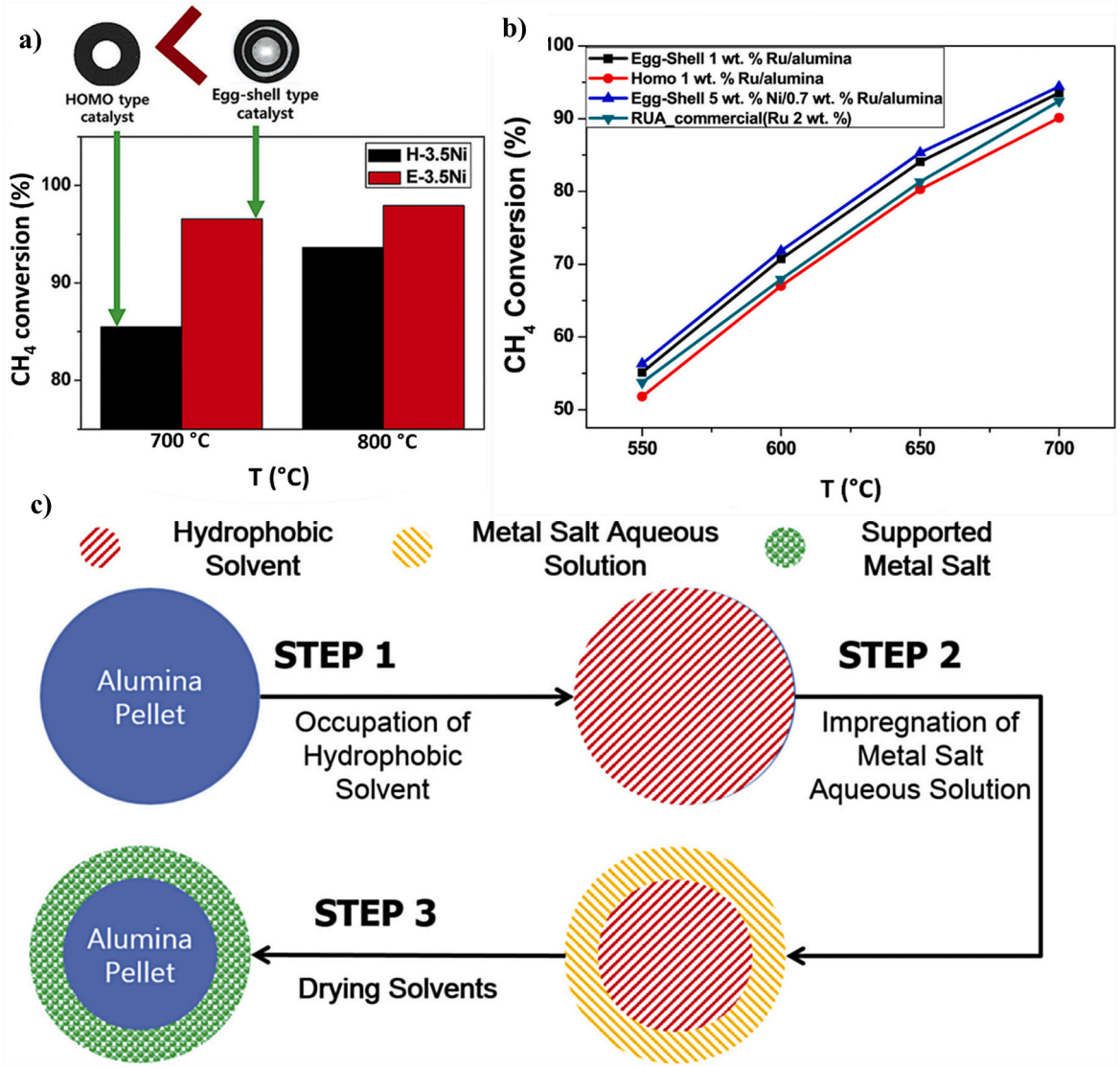

Fig. 6. (a) Influence of egg-shell type catalysts on CH_4 conversion. (Reprinted with permission from Ref. [192]. Copyright (2019) Elsevier B.V.); **(b)** influence of various catalysts depending on reaction temperature; RUA: commercial ruthenium pellet catalyst (Clariant, 2 wt% $Ru/\alpha\text{-}Al_2O_3$); **(c)** schematic illustration of bimetallic egg-shell type catalyst synthesis. (Reprinted with permission from Ref. [193]. Copyright (2017) Elsevier B.V).

Table 3
Bimetallic catalysts for SMR.

Catalyst/sorbent	Optimum loading	Process conditions	CH_4 conversion (%)	H_2 yield (%)	CO selectivity (%)	H_2/CO ratio	Remarks	Ref
Ni–La/α-Al_2O_3	7 wt% Ni 3 wt% La	T = 600 °C; Catalyst loading = 0.15 g GHSV = 32,000 ml/g_{cat}/hr	97	94	–	–	The addition of La increased the spacing between Ni active sites and inhibited sintering and agglomeration. Ni-interaction with support and La enhances dissociative adsorption of C-H_x species.	[201]
Co–Pt/Al_2O_3–ZrO_2–CeO_2	5 wt% Co–Pt 2.5%Ce–5%Zr	T = 750 °C; GHSV = 1000 hr^{-1}	95.4		–	4.0	The addition of ZrO_2 to Co–Pt/Al_2O_3 was studied for SMR and DRM. The synthesized catalyst enhanced the catalytic activity, stability, and selectivity for both processes.	[202]
Ru/La–Al_2O_3	1.5 wt% Ru/3 wt% La; 461 and 1367cpsi channel monolith	T = 800 °C; S/C = 3 GHSV = 20,000 h^{-1} Catalyst loading = 100–200 mg	>99.5%	–	~50	~8	The Ru/La–Al_2O_3 coated alumina monoliths were prepared by the wash coating technique, resulting in increased catalytic activity at lower temperatures.	[203]
Ni/La–Ca/Al_2O_3	21.6 wt% Ni	GHSV = 3.6×10^5 h^{-1} S/C = 3	88	–	–	–	Constant CH_4 conversion was obtained over 150 h of activity testing at GHSV = 1.2×10^5 h^{-1}. However, increasing the GHSV to 3.6×10^5 h^{-1} reduced the conversion in 150 h from 88% to 47%. The catalyst was not found suitable for SMR at higher GHSVs.	[204]
Ni/Ag/Al_2O_3 **Ni–Au/Al_2O_3**	8 wt% Ni	T = 700 °C; S/C = 4	49 96	–	–	–	The incorporation of Ag reduced the catalytic performance of Ni/Al_2O_3, while the addition of Au enhanced the catalytic stability and activity of the Ni catalyst for SMR.	[205]
Co–Ni/CeO_2	8 wt% Ni 12 wt% Co	T = 750 °C GHSV = 3000 h^{-1} Catalyst loading = 2 g	76.1	44.5	–	–	Co-based mono- and bimetallic catalysts were prepared via an impregnation technique to test for SMR. The bimetallic catalyst produced better results as compared to the monometallic catalyst. An increase in H_2 selectivity from 58.5% to 77.2% was observed with increasing Co–Ni loading.	[206]
Ru/Co_6Al_2	1 wt% Ru 0-6 wt% Co	T = 600 °C; S/C = 3	93	–	–	–	A highly active Ru- and Co-based catalyst was prepared for SMR. Ru/Co_6Al_2 exhibited the highest catalytic performance among varying Co loadings, with CH_4 conversion matching the equilibrium. Catalytic stability up to 100 h was observed.	[200]
Ni/(Pd/Rh)/$CeZrO_2$–Al_2O_3	0.09 wt%	T = 800 °C; S/C = 1.5 GHSV = 20,000 h^{-1}	92.7	–	–	~4.5	The Pd–Rh catalyst exhibited higher syngas production and lower coke formation.	[189]

required to be determined.

2.1.3. Bimetallic catalysts

To overcome the drawbacks of reforming catalysts, noble metals supported by various oxides have been extensively investigated. Yet, noble metals are quite expensive, which limits their utilization as promoters for SMR. Therefore, bimetallic catalysts were introduced where noble metals were added to transition metals such as Ni and Co to develop transition-noble metal alloys with improved and ultimate properties due to their higher catalytic activity and low cost [190]. A series of supported bimetallic catalysts with a 12% Ni loading but varying Co loadings were investigated for SMR [146]. The addition of Co to Ni/γ-Al_2O_3 improved the reaction stability and coke tolerance by enabling Ni–Co alloy formation on the surface while slightly losing activity. The formation of Ni–Co alloy causes blockage of the active low-coordinated Ni sites and lowers the metal dispersion, which consequently suppresses coking. Recently, the addition of varying quantities of Pt to Ni/$MgAl_2O_4$ was synthesized and studied for SMR. With 0.1% optimum Pt loading, Pt–Ni alloy formation on the surface of the catalyst increased the metal surface area, and hence higher catalytic activity was observed. However, Pt loading beyond 0.1 wt% resulted in lowering the catalyst stability, agglomeration, and activity of the active metals in the catalyst [191].

The active metal in the commercial SMR catalyst is evenly distributed in the Al_2O_3 pellets. Recently, egg-shell type Al_2O_3 pellets were prepared in which the active metal was selectively located on the outer region of the pellet to improve the mass transfer limitation and deactivation due to coke formation. A blocking solvent to minimize the penetration of active metal into the pores was used to form an egg-shell type catalyst. Despite the increase in temperature, Fig. 6(a) clearly shows that the egg-shell type catalyst exhibited higher CH_4 conversion even at lower Ni loading [192]. In addition to Ni metal, a bimetal of Ru/Ni supported on Al_2O_3 was tested for SMR. Maximum CH_4 conversion was observed at elevated temperatures for bimetal egg-shell type catalysts, which could be attributed to the effective utilization of active metal located on the pellet's outer surface (Fig. 6(b)). Fig. 6(c) [193] depicts the synthesis methods for the bimetal egg-shell type catalyst.

Bimetallic catalysts have been observed to increase overall catalytic performance in comparison to monometallic catalysts [146]. Summaries of the bimetal catalysts with CH_4 conversions for SMR are given in Table 3. The formation of Ni–Co alloy for CH_4 reforming has been investigated by several groups, which resulted in improving the coke resistance of the catalysts [194–196]. For instance, Yu et al. [197] and Zhang et al. [198] also reported the promotional effects of the higher metal dispersion on Co addition. Wang et al. [199] investigated the impact of Au, Ag, and Cu on Ni-based catalytic systems to inhibit carbon deposition. The results suggested the Ni–Cu catalyst as a promising bimetallic material with higher active carbon tolerance for SMR. Homsi

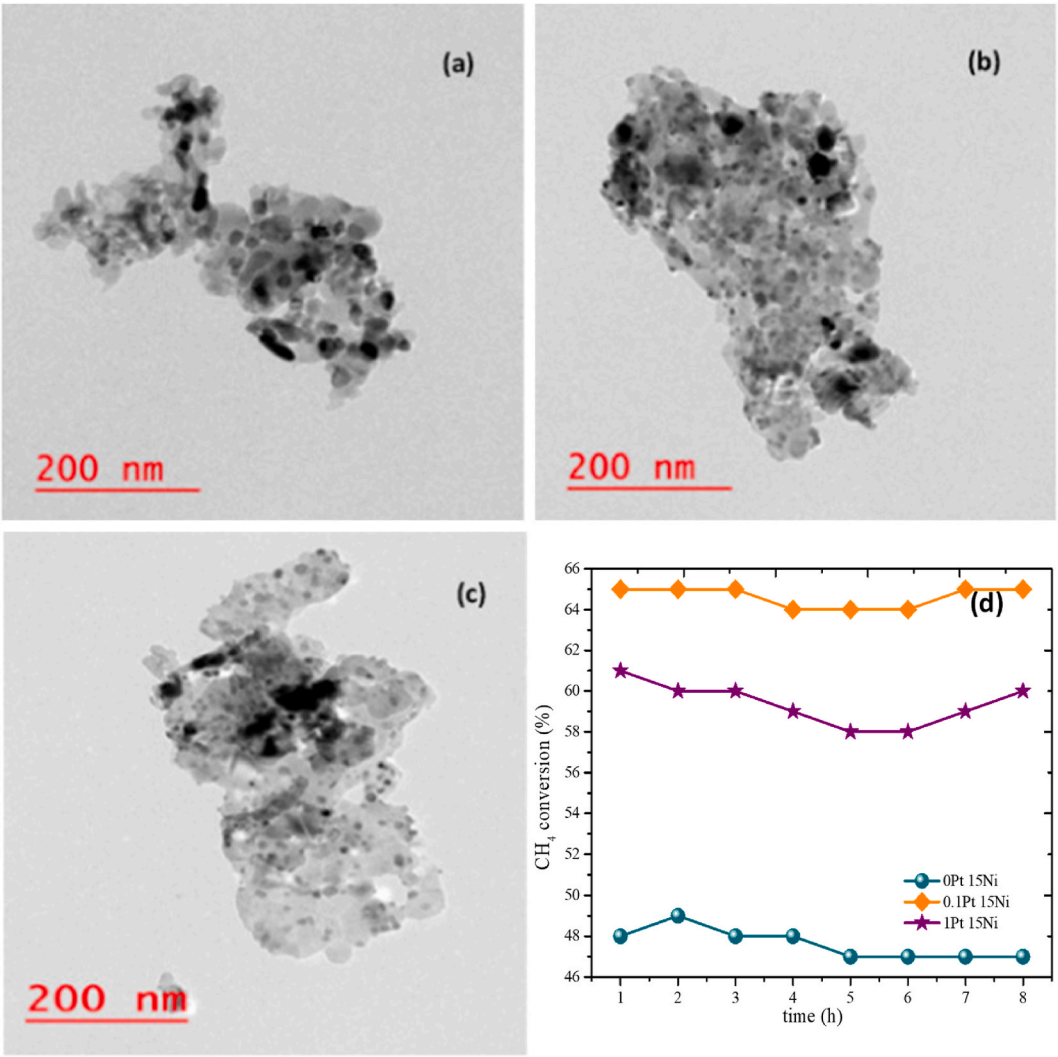

Fig. 7. Effect of Pt doping on the particle size distribution **(a)** 0% Pt 15% Ni **(b)** 0.1% Pt 15% Ni **(c)** 1% Pt 15% Ni **(d)** CH_4 conversion with time for different Pt concentrations at 600 °C, S/C = 5. (Reprinted with permission from Ref. [191]. Copyright (2017) Elsevier B.V.).

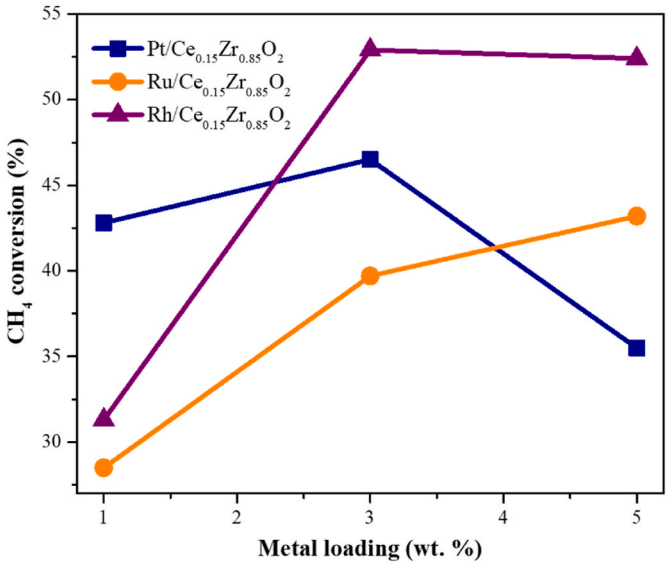

Fig. 8. Effect of metal loading on CH_4 conversion over $Ce_{0.15}Zr_{0.85}O_2$ supported by noble metal catalysts at a temperature of 600 °C. (Adapted with permission from Ref. [186]. Copyright (2004) Elsevier B.V.).

et al. [200] prepared a highly stable and reactive Co/Ru-based catalyst on a magnesium and aluminum mixed oxide support for H_2 production. It was found that an interaction between Co and Ru favored the formation of finely dispersed Co/Ru oxide species. The catalyst resulted in higher catalytic stability up to 100 h on stream and coke formation on the surface only at trace levels. Therefore, the presence of a second metal in the catalyst system results in a synergetic effect that increases the catalyst's activity and stability toward sintering. It modifies the properties of metallic particles by forming bimetallic surface alloys, considering that a bimetallic system can replace expensive noble metals and offer the ultimate properties of metal alloys [122].

2.1.4. Metal loading

Due to the tendency of Ni to form carbon over the surface, SMR performance is highly affected by this phenomenon. The doping of Ni-based catalysts with noble metals (Pd, Ag, and Rh) to enhance the Ni dispersion over the catalyst for the enhancement of the activity and stability of catalysts by reduction of carbon deposition has attracted many researchers [186,207,208]. However, it is required to determine the limits of metal loading, where the agglomeration of metal particles starts to appear once they exceed a certain limit [209]. The effect of Pt doping amount (0.01 wt% to 1 wt%) on the stability and activity in SMR of a 15 wt% Ni/$MgAl_2O_4$ catalyst has been investigated. It was found that CO selectivity increased with Pt addition. The increase in CO selectivity was due to an increase in noble metal content and CH_4 conversion. Hence, WGS equilibrium is affected, which favors the formation of CO. Also, Pt metal has a higher tendency to form CO in comparison to Ni. The smaller crystal size of active metal significantly changes the product distribution by increasing CO formation. The increase in CO formation may be attributed to the increase in active metal dispersion. Because of the maximum metal dispersion, Pt doping at 0.1 wt% produced the best catalytic activity, and increasing Pt doping did not affect metal dispersion. Fig. 7(a, b, c) shows transmission electron microscopy (TEM) images of the catalyst on Pt addition from 0 to 1 wt%. Active metal particles of smaller size were observed in the 0.1% Pt-catalyst, while larger agglomerated particles were formed in the 0% Pt-catalyst. The particle size of the 1% Pt-catalyst was smaller than 0% Pt, but larger than 0.1% Pt. The images also revealed the particle size distributions on Pt, which were 14.9 nm, 7.6 nm, and 9.3 nm, respectively, for 0, 0.1, and 1.0 wt% Pt. As can be observed from Fig. 7(d), 1% Pt/15% Ni exhibited a CH_4 conversion higher than 0% Pt/15% Ni but lower than 0.1% Pt/15% Ni. Thus, higher stability and activity of the catalyst were observed with increasing Pt content; 0.1% Pt and 15% Ni revealed the highest activity. However, higher Pt content resulted in the accumulation of the active metal on the surface, reducing the catalytic activity [191].

The impact of different metal (Ru, Pt, and Rh) loadings over a catalyst $Ce_{0.15}Zr_{0.85}O_2$ on the conversion of CH_4 was investigated. Fig. 8 summarizes the results at 600 °C and a space velocity of 9000 ml CH_4/g-cat.h. The results showed that maximum methane conversion occurred at a metal loading of 3 wt% in the case of Pt and Rh. However, increasing the metal loading in the case of Ru resulted in a further increase in CH_4 conversion. Even a 10% Ni loading in the catalyst resulted in lower activity when compared to the noble metal catalyst, although the former is more expensive [186].

In another study, the influence of Ag loading from 0.1 wt% to 0.6 wt % on the physicochemical properties of Ni–Al_2O_3 was investigated for SMR at 600 °C and S/C of 0.5. The catalytic study showed that Ag loading greater than 0.3 wt% presented higher resistance to coke

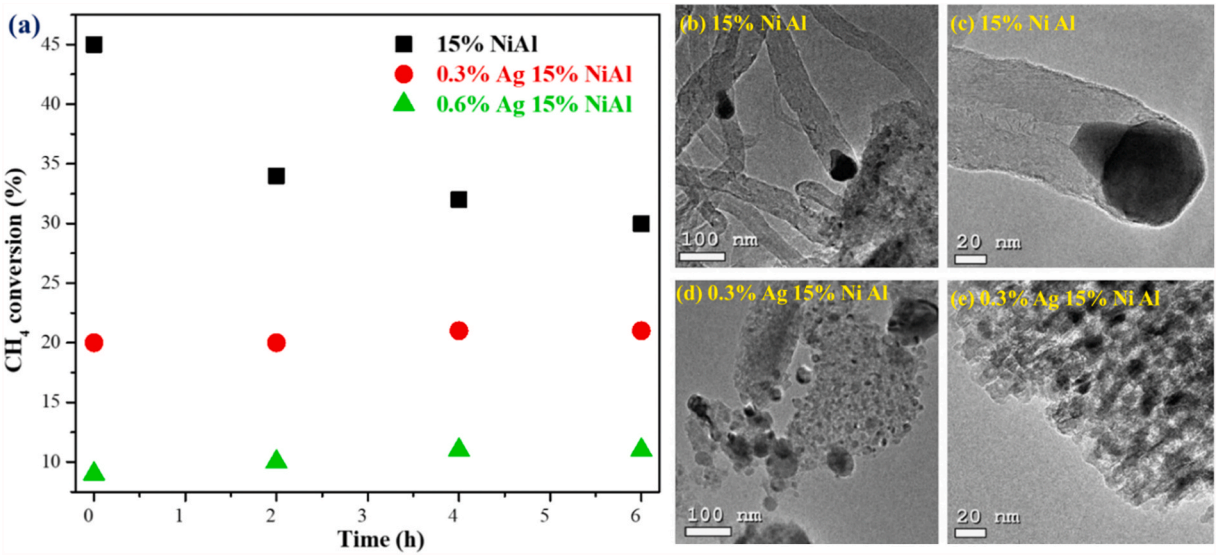

Fig. 9. (a) Effect of Ag (0–0.6 wt%) loading on CH_4 conversion for stability tests at 600 °C and for 6 h reaction time; **(b–c)** TEM images of 15%NiAl post-SMR exposing the coke formation; **(d-e)** TEM images of 0.3% Ag-loaded NiAl post-SMR. (Adapted with permission from Ref. [123]. Copyright (2007) Elsevier B.V.).

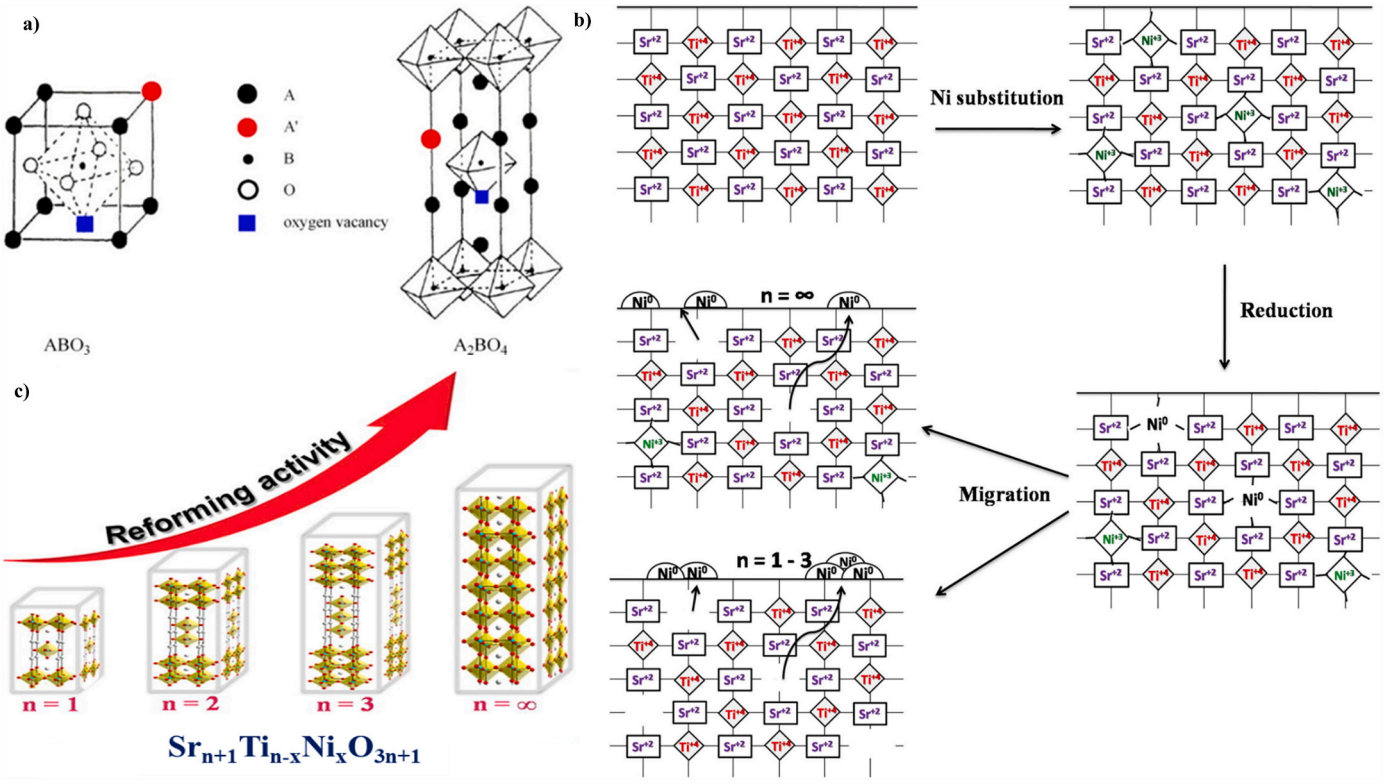

Fig. 10. a) Ideal structures of ABO_3 and A_2BO_4 perovskites. The red spheres signify the substitution of the A-site cation by another one. For the sake of simplicity, the oxygen mark is not illustrated in A_2BO_4. (Reprinted with permission from Ref. [63]. Copyright (2014) American Chemical Society.); **b)** Proposed mechanism of Ni metal migration in perovskites. **c)** Trend perovskite activity with the RP phase order of $Sr_{n+1}Ti_{n-x}Ni_xO_{3n+1}$ (n = 1 to ∞). (Reprinted with permission from Ref. [223]. Copyright (2018) Elsevier B.V.).

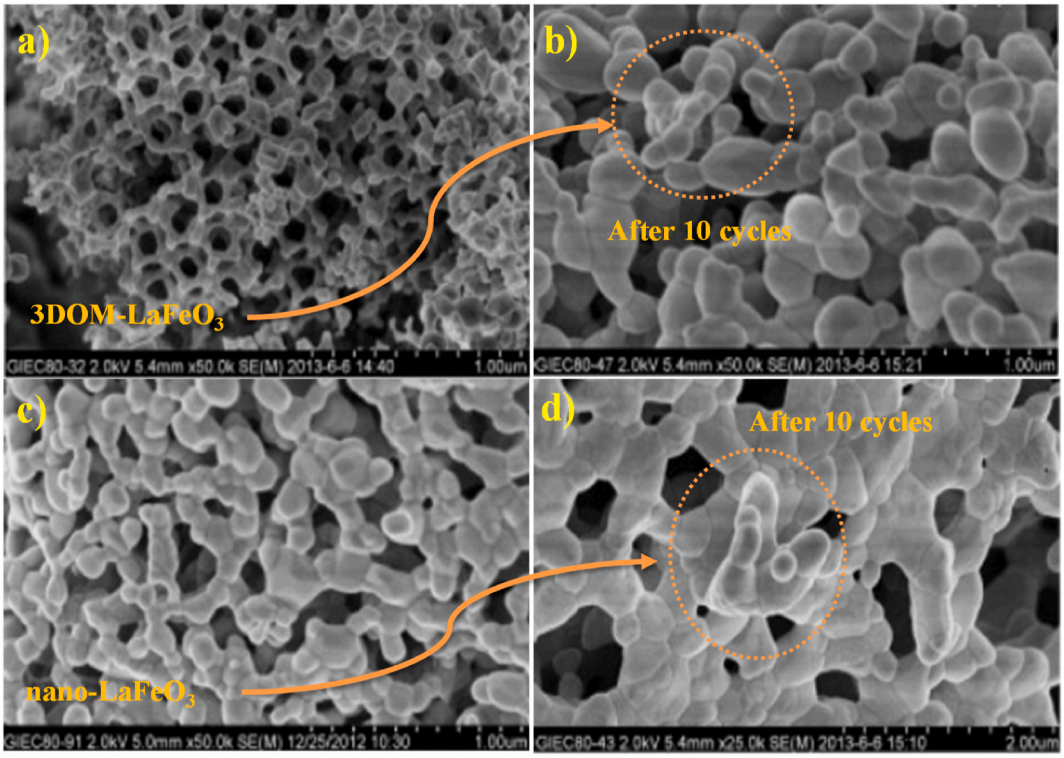

Fig. 11. SEM images of (a,b) freshly prepared and spent 3DOM-$LaFeO_3$ and (c,d) nano and spent $LaFeO_3$. (Reprinted with permission from Ref. [226]. Copyright (2014) Elsevier B.V.).

Table 4
Perovskite type catalysts for SMR and CL-SMR.

Catalyst	Application	Process conditions	CH_4 conversion (%)	H_2 yield (%)	CO selectivity (%)	H_2/CO ratio	Remarks	Ref
$LaNiO_3$	SMR	T = 850 °C; S/C = 2; GHSV = 1300 h^{-1} Catalyst loading = 0.3 g	86.86	88.15	–	–	Kinetic experiments at varying working conditions. At 500 °C and 900 °C, respectively, pressure had the greatest effect on H_2 yield and CO yield. Upon increasing GHSV, CH_4 conversion, CO, and H_2 yields are reduced.	[231]
$LaMn_{1-x}B_xO_{3+\delta}$ **(B= Co, Fe, Ni)**	CL-SMR	T = 850 °C; Oxygen carrier loading = 1 g	–	–	89.8 (Co doping) 90.6 (Fe doping) 87.3 (Ni doping)	2.0	Fe, Co, and Ni doping in $LaMnO_{3+\delta}$ enhanced the oxygen release rate in decreasing order of Ni, followed by Co and Fe, since the CH_4 activation and oxygen ion conduction were accelerated due to the incorporation of active sites, advancement of the perovskite structure, and oxygen vacancy formation. $LaMn_{0.8}Co_{0.2}O_{3+\delta}$ and $LaMn_{0.7}Fe_{0.3}O_{3+\delta}$ were found to be favorable OCs for CLSMR, considering the coke formation, H_2 and syngas yield.	[224]
$La_{1-x}Sr_xFeO_3$	CL-SMR	T = 850 °C; Catalyst loading = 2 g	~80	–	–	2.0	To investigate the effect of Sr doping on the properties of catalysts, a family of perovskites was prepared. Sr doping into the La-site upgraded the oxygen-carrying capacity of the catalyst. $La_{0.7}Sr_{0.3}FeO_3$ presented the best catalytic performance in 10 successive redox tests.	[232]
$LaMn_xFe_{1-x}O_{3+\delta}$	CLSMR	T = 850 °C	88 (x = 0) 97.3 (x = 0.3) 87.5 (x = 0.5)	–	–	>2.0 (x = 0) ~2.0 (x = 0.3) ~2.0 (x = 0.5)	The substitution of Mn for Fe in the oxygen carrier improved the mobility and amount of lattice oxygen. However, higher substitution proportions resulted in carbon deposition for CLSMR.	[233]
$Ba_{1-x}Sr_xCoO_{3-\delta}/CeO_2$	CL-SMR	T = 850 °C; Catalyst loading = 1 g	–	–	>90	~2.0	The Sr-doping in the catalyst exhibited higher syngas production as compared to $BaCoO_{3-\delta}/CeO_2$. CeO_2 increased gas production by providing an oxygen supply to the catalyst. The best catalytic performance was found with $Ba_{0.3}Sr_{0.7}CoO_{3-\delta}/CeO_2$.	[234]
$Sr_{n+1}Ti_{n-x}Ni_xO_{3n+1}$	SMR	T = 750 °C; S/C = 3; GHSV = 20,000 h^{-1}	97 (n = ∞) 89 (n = 3)	–	–	–	Oxygen defects and reforming activity increased as the dimensionality of perovskite layers increased. $SrTi_{0.8}Ni_{0.2}O_{3-\delta}$ revealed maximum oxygen defects, leading to the minimization of coke formation.	[223]
$BaCoO_{3-\delta}/CeO_2$	CL-SMR	T = 860 °C; Catalyst loading = 0.5 g	–	–	~90	~2.0	Because of the increased oxygen supply provided by CeO_2, the CeO_2-supported $BaCoO_{3-\delta}$ catalyst produced more syngas and H_2. The catalyst was found to be favorable for the cyclic experiments of CLSMR.	[235]

formation and higher stability owing to the variations in the structure of Ni sites. The high stability of the Ni catalysts was raised by the decrease of Ni particles, change in the nucleation of the graphite structure formation, and equilibration of different steps of reaction rate, decreasing the C formation rate. The addition of Ag to the catalyst stabilized CH_4 conversion (Fig. 9(a)), but at 0.1–0.6 wt% Ag loading, the conversion level was suppressed. The TEM image in Fig. 9(b) corresponds to a 15 wt % Ni–Al solution used in SMR stability tests and shows dark pear-shaped Ni particles as well as a significant amount of filament growth and coke formation. Fig. 9(c) depicts the inhibition of filament growth and carbon deposits caused by the addition of Ag to the catalyst. The catalyst revealed stable results for 6 h at 600 °C despite the large carbon deposition on the 15% Ni–Al catalyst. However, increasing the temperature to 660 °C after 1 h blocked the reactor. On the other hand, the promoted (>0.3 wt% Ag) catalyst exhibited stable results without filamentous coke formation, as presented in Fig. 9(d-e) [123].

Ni-supported α-Al_2O_3 with loadings varying from 0.2 to 10 wt% during the oxidative SMR was investigated. The conversion of CH_4 increased upon Ni loading, and it was found that the temperature of the catalyst bed is dependent on Ni loading. Since hotspot formation can be inhibited to some degree, 0.9 wt% Ni was chosen as a suitable loading for the reactor's performance [210]. The role of increasing Pt loading from 0.5 to 2 wt% over La_2O_3–Al_2O_3 support was investigated. Dispersing 0.5 wt% Pt over La_2O_3–Al_2O_3 support resulted in the best activity and higher stability coming from strong metal-support interaction as compared to higher loadings. Thus, due to the solid deactivation by coking and sintering of particles at higher loadings, a Pt loading of greater than 0.5 wt% could not alleviate the deactivation during the SMR reaction [211]. Also, the Ni crystallite size and its dispersion change upon metal loading [212]. Therefore, it is necessary to optimize the metal loading in catalyst systems to avoid agglomeration of metals, which often leads to poor stability and activity of catalysts. In most cases, the noble metal loading is limited to <1%, while Ni loading is optimum at 10–15% with porous alumina support.

2.1.5. Perovskite-based catalysts

Recently, perovskite-based catalysts have been explored in SMR and have attracted much attention. This type of material has shown promising results in emerging applications such as ceramic membranes [193, 213], heterogeneous catalysis [214], and solar cells [215,216]. As shown in Fig. 10 (a), the ideal framework of perovskite oxides ABO_3 and A_2BO_4 both consists of two cations (A and B). A is a larger cation located on the edge of the perovskite structure. A cation can be substituted by a foreign cation (A′) having a different oxidation state or radius. B is a smaller cation located in the center of an octahedron. For a perovskite structure to form, A must have cationic radii greater than 0.09 nm, while B must have cationic radii greater than 0.051 nm. Perovskites are mixed metal oxides that can hold 90% of the metal element at the A or B active

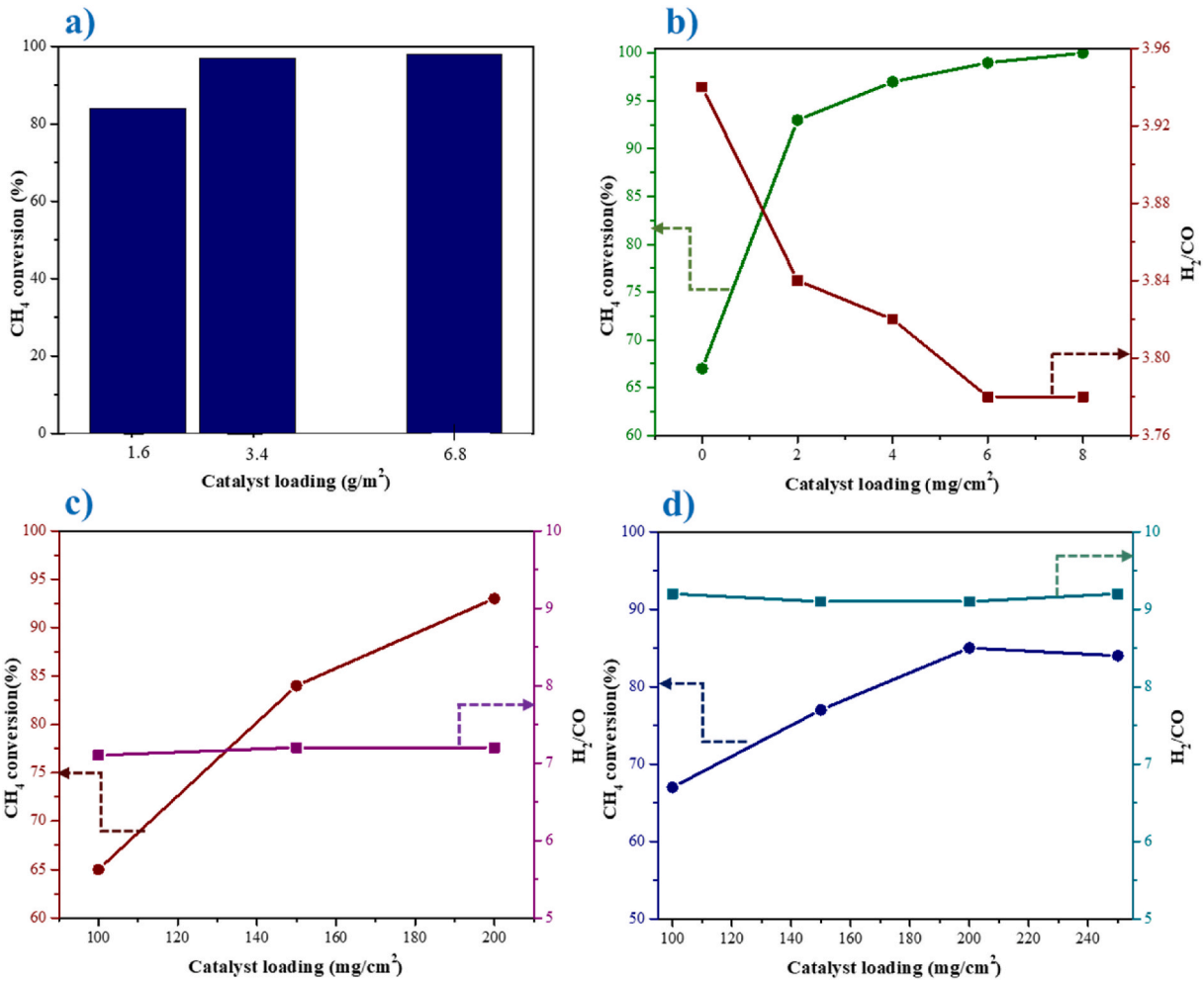

Fig. 12. Influence of catalyst loading on **(a)** CH_4 conversion over Ni catalyst at 900 °C reaction temperature and S/C ratio 3.0. (Adapted with permission from Ref. [236]. Copyright (2011) Elsevier B.V.); **(b)** CH_4 conversion on SMR catalyst at GHSV 30,000 h^{-1}. (Adapted with permission from Ref. [238]. Copyright (2009) Elsevier B.V.); **(c)** CH_4 conversion and H_2/CO ratio on Ru/La–Al_2O_3 catalyst at GHSV 20,000 h^{-1}. (Adapted with permission from Ref. [203]. Copyright (2018) Elsevier B.V.); **(d)** CH_4 conversion and H_2/CO on Ru/La–Al_2O_3 catalyst at GHSV 40,000 h^{-1}. (Adapted with permission from Ref. [239]. Copyright (2018) Elsevier B.V.).

sites without damaging the crystal structure. For instance, A-sites could be occupied with Sr, La, Ce, etc., while B-sites could be solely or partially occupied by Co and Ni [217]. This perovskite structure improves thermal stability, avoids coke formation, and reduces sintering, making them suitable candidates for gaseous reactions at elevated temperatures [152]. Initially, oxides like $LaFeO_3$ and $NaNbO_3$ were reported to catalyze CO oxidation [218]. The literature contains studies on perovskite-based catalysts for the reforming of CH_4, ethanol, and tar [214,219–221].

Therefore, perovskites may not only be used as catalysts but also as catalyst precursors. Since Ni metal can catalyze the SMR process, perovskite oxides containing Ni cations may act as precursors for the reforming process. After the reduction by H_2, Ni cations are reduced to real metal active sites for reforming [62]. Its widespread use in CH_4 reforming could be attributed to the fact that after reduction, catalysts with segregated active phases are attached uniformly onto unreduced oxide matrices [222]. A probable mechanism for Ni migration in the perovskite lattice is illustrated in Fig. 10(b). When reacting with $SrTi_{0.8}Ni_{0.2}O_{3-\delta}$ ($n = \infty$), the fine particles of metallic Ni on the surface have greater interaction with the support, while in lower-order perovskites there is weak interaction between the support and Ni particles. Ni^0 produced during the reduction, therefore, migrates fast to form agglomerates [223]. TPR and temperature-programmed desorption (TPD-O_2) showed Ni reducibility and estimated oxygen vacancies, which were found to influence catalytic activity during methane reforming. As depicted in Fig. 10(c), the catalytic activity increased with the order of the Ruddlesden-Popper (RP) phase of $SrTi_{0.8}Ni_{0.2}O_{3-\delta}$ ($n = 1$ to ∞).

Moreover, perovskite-based metal oxides are gaining more attention as OCs [224,225]. In this respect, three-dimensionally ordered macroporous $LaFeO_3$ (3DOM-$LaFeO_3$) and nano-$LaFeO_3$ perovskites were synthesized via an impregnation technique to test for the CL-SMR. The process proceeds based on POM, with the OC in the reactor producing the syngas, followed by the oxidation of the reduced OC by steam to produce H_2 in the reactor. The success of the process is dependent on appropriate OCs that are capable of producing H_2 with better activity for H_2O splitting, high CH_4 conversion, and resistance to agglomeration.

The 3DOM-$LaFeO_3$ catalyst resulted in a surface area of 8.08 m^2/g, more than the nano-$LaFeO_3$ (4.32 m^2/g). Compared with nano-$LaFeO_3$, 3DOM-$LaFeO_3$ presented a higher stable reactivity of CH_4 oxidation and improved endurance to carbon deposition, which was ascribed to the greater surface area of 3DOM perovskites. 3DOM-$LiFeO_3$ and nano-$LiFeO_3$ retained 63% and 45% of their initial surface area over 10 redox cycles, respectively, which is related to the higher textural stability of the former. Fig. 11(a-b) presents the scanning electron microscope (SEM) images of freshly prepared and spent (after 10 cycles) 3DOM-$LaFeO_3$ perovskite oxides. After 10 redox cycles, although the structure and skeleton of 3DOM perovskite partially collapsed due to the long thermal and chemical stresses during the reforming reactions, no agglomeration or sintering appeared on the sample surface. However, it still showed a higher surface area than that of nano-$LaFeO_3$. Fig. 11(c-d) shows the difference in the granular structure of nano-$LaFeO_3$ after 10 redox cycles. The particles, after a series of cycles, become larger due to sintering, which leads to a significant decrease in surface area and pore sizes [226].

The Cu^{2+} and Ca^{2+} substitutions are reported to improve the reactivity of the perovskite structure. Carrasco et al. [227] proved that the presence of Cu^{2+} at the $LaCu_{1-x}M_xO_3$ (M = Ti, Mn) surface was advantageous for the reactivity.

The redox property of perovskite plays a major role in reforming reactions, as carbon species produced on the surface of perovskites are detached from the surface reaction. Summaries of various perovskites used in SMR and CL-SMR are given in Table 4. A series of Ruddlesden-Popper (RP)-layered $Sr_{n+1}Ti_{n-x}Ni_xO_{3n+1}$ was prepared and used in reforming reactions. These catalysts enhanced the activity in syngas production at 20,000 h^{-1} GHSV (gas hourly space velocity) and an S/C of 3.0. In the temperature range of 600–750 °C, $SrTi_{0.3}Ni_{0.2}O_3$ demonstrated greater catalytic activity than $Sr_4Ti_{2.3}Ni_{0.7}O_{10}$. Lower conversions of CH_4 observed for lower values of n in layered $Sr_{n+1}Ti_{n-x}Ni_xO_{3n+1}$ perovskite were due to a decrease in the surface area of oxides and less dispersion of active Ni sites [223]. Zhang et al. [125] performed CL-SMR over cerium-doped perovskites ($La_{1-x}Ce_xFeO_3$) prepared via the sol-gel method. An appropriate amount of Ce^{3+} substitution in the A site of $LaFeO_3$ ($La_{0.5}Ce_{0.5}FeO_3$) promotes the lattice oxygen conversion rate in the POM step and boosts the reaction kinetics in the H_2O splitting step

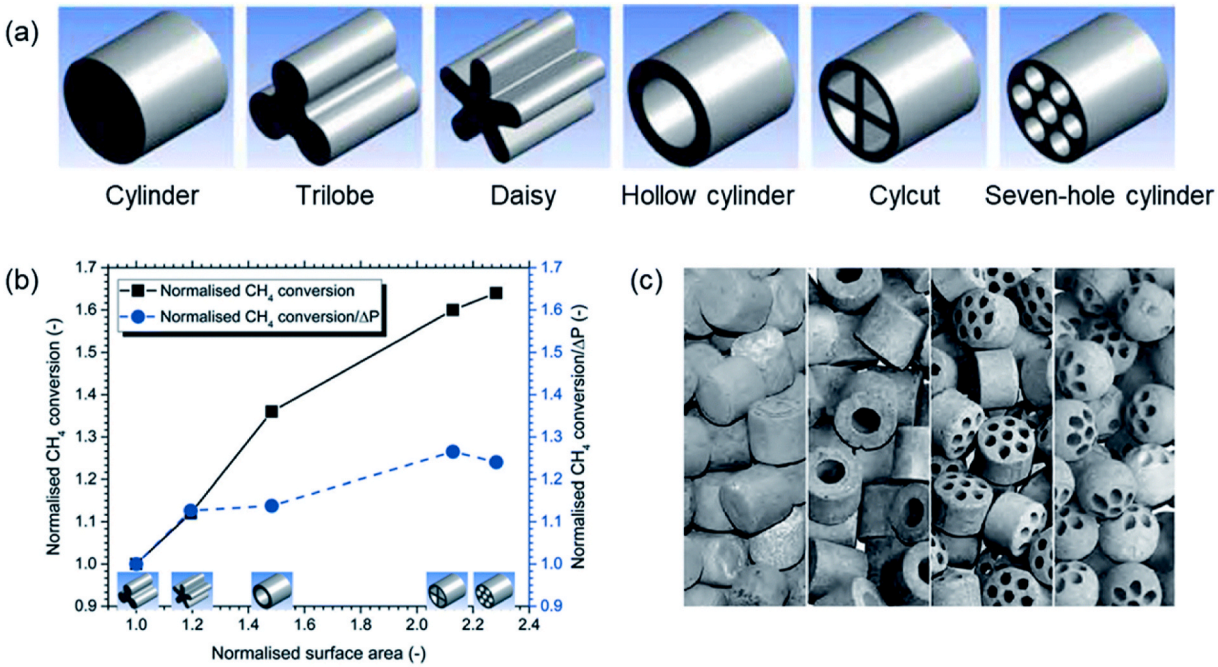

Fig. 13. a) Illustration of various catalyst particle shapes; **b)** effect of the CH_4 conversion and CH_4 conversion/ΔP on the surface area of the catalysts with various shapes; and **c)** illustration of various catalyst particle shapes in seven-hole spheres and cylinders. (Reprinted with permission from Ref. [243]. Copyright (2022) Royal Society of Chemistry.).

by enhancing the surface water activation and lattice oxygen mobility of the perovskite. This $La_{0.5}Ce_{0.5}FeO_3$ catalyst presented stability over 100 cycles of redox cycling with an average 90% CH_4 conversion. Recently, a Ni-based bimetallic catalyst anchored on a backbone material of $BaZr_{0.4}Ce_{0.4}Y_{0.1}Yb_{0.1}O_{3-\delta}$ was tested for SMR at reduced temperatures. Due to the formation of bimetallic alloys and coherent structural properties, the catalyst exhibited high catalytic performance and was less dependent on the flow rate of gas [228].

Ordered double perovskites are different in their properties and structure from simple perovskites, with rare earth and transition metals as A and B sites, respectively. These perovskites are less explored for SMR but have great potential for enhancing coking resistance because the perovskite structure supplies oxygen lattice to the metallic surface, converting carbon deposits to gaseous compounds. Huang et al. [229] used double perovskites, Sr_2CoMoO_6 and Sr_2NiMoO_6 for the SMR process. Sr_2CoMoO_6 performed better in reaction activity as compared to the other catalysts. Double perovskites (La_6NiTiO_6) were examined in the SMR reaction at a temperature ranging from 550 °C to 950 °C under different reduction conditions, resulting in 95% CH_4 conversion at 950 °C. The increased number of active sites and strong interactions of metal and support with higher oxygen vacancies are attributed to the increase in activity [230]. Therefore, it is undeniable that perovskite-based catalysts are an attractive approach to developing catalysts with higher activity and stability for SMR processes. However, the basic understanding of these catalysts with proper reaction mechanisms based on experimental results is still lacking, and it is necessary to extend the research to other applications of reforming with modified-structure perovskites.

2.1.6. Catalyst loading

Catalyst loading is defined as the weight of the catalyst loaded per the area of the plate that acts as a micro-channel wall [236]. Catalyst loading in a reforming reactor influences the CH_4 conversion and H_2/CO ratios because the higher the catalyst quantity loaded, higher the adsorption rate, catalytic activity, CH_4 conversion, H_2 yield, and reactor performance [237]. Increasing the quantity of catalyst in the reactor improves the catalytic activity while pushing the CH_4 conversion towards equilibrium. Furthermore, even as the catalyst loading increases, temperature and GHSV affect CH_4 conversion [203].

The effects of catalyst loading in the reactor by a few research groups are presented in Fig. 12. The reactor was tested with three different Ni metal loadings (1.6 g/m^2, 3.4 g/m^2, and 6.8 g/m^2) to observe the behavior of CH_4 conversion at 900 °C and an S/C of 1.0. The conversion increased upon Ni metal loading, which presented poor performance when catalyst loading was 1.6 g/m^2. However, the CH_4 conversion reached 98% at 6.8 g/m^2. Thus, higher catalyst loading is preferable for better reaction performance, as shown in Fig. 12(a) [236]. Azramendi et al. [238] performed SMR in a microchannel reactor and studied the influence of catalyst loading in the channel walls with an S/C of 2.0 and a GHSV of 101,460 h^{-1}. Fig. 12(b) shows the results where CH_4 increases with catalyst loading, which is similar to the previous finding. Depending on the mean temperature and GHSV, 2–4 mg/cm^2 of catalyst quantity is sufficient to obtain a CH_4 conversion of more than 97%. It was observed that the quantity of catalyst required reduces as the temperature increases, as at 930 °C, 4 mg/cm^2 was required to achieve 97% CH_4 conversion. Thus, 1000 °C is required to get the same conversion if catalyst loading is decreased to 2 mg/cm^2. H_2/CO is slightly reduced by increasing the catalyst loading. It was found that H_2/CO dependency on catalyst loading was also affected by an increase in temperature, as it was reduced from 3.82 to 3.65 from 930 °C to 1020 °C. Even at lower catalyst loadings, the selectivity for syngas is low despite higher temperatures. Metallic monolith-type catalyst loading effects (100–200 mg) on CH_4 conversion and H_2/CO with increasing GHSV based on catalyst loading were investigated. However, Fig. 12(c) demonstrates the conversion and H_2/CO ratios at 20,000 h^{-1}GHSV. The increase in CH_4 was seen at a particular value of GHSV since more loadings decreased the voidage in the monolithic structure, which influenced the transport and chemical processes. At constant temperature, however, catalyst loading made no difference in the H_2/CO ratio. Yet the experimental values obtained for H_2/CO were higher than the stoichiometric values due to WGS equilibrium [203]. Ashraf et al. [239] in another study described the impact of catalyst loading (100 mg–250 mg) on a higher GHSV of 40,000 h^{-1} and 800 °C. As shown in Fig. 12(d), CH_4 conversion increased as catalyst loading increased, whereas the H_2/CO ratio remained constant. However, conversion values decreased for all catalyst loadings, while the H_2/CO ratio started to increase gradually with increasing GHSV values up to 120,000 h^{-1}. In conclusion, the selection of catalyst loading is necessary for the high throughput per unit volume, along with an understanding of space velocity. Further, it is also understandable that keeping the flow rate constant and increasing the catalyst loading provides more active sites, and consequently, the CH_4 conversion can go beyond equilibrium. More catalyst loadings reduce the voidage of catalysts, which alters the volumetric flow rate per channel. This alteration influences the transport phenomena and chemical processes during the reaction. Therefore, it is crucial to consider the effect of space velocity on catalyst loading [203].

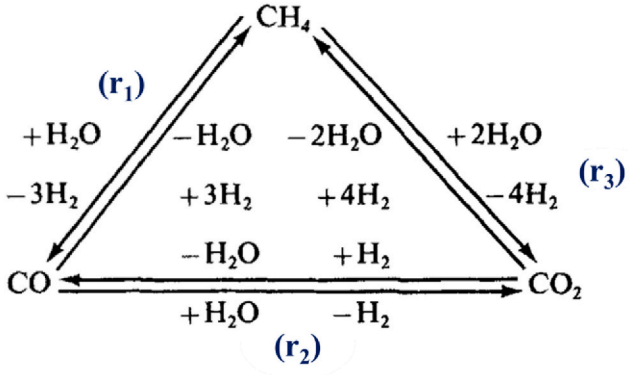

Scheme 1. A triangular scheme of three reactions (r_1, r_2 and r_3). (Reprinted with permission from Ref. [250]. Copyright (1989) Wiley).

Furthermore, industrial investigations show that the activity of a catalyst is dependent on many factors, including its composition, surface properties, and morphology (shape). In this section, the morphology/shape of the catalyst as an effective parameter in SMR are highlighted. Karthik and Buwa [240] investigated the heat transfer, pressure drop, and reaction performance of various catalyst shapes (cylinder, daisy, trilobe, cylcut, hollow cylinder, and seven-hole cylinder) via CFD, as shown in Fig. 13(a). Catalysts with smaller particle sizes have a higher effectiveness factor but can lead to an increase in pressure drop in industrial-scale facilities. Catalysts with internal shapes such as hollow cylinders provide larger surface areas and reduce diffusion limitations, while those with external shapes such as trilobal and daisy shapes have lower pressure drops. Monolithic structures also exhibit high efficiency due to their streamlined flow. The heat transfer and reaction performance per pressure drop were the highest for the trilobal particles.

As shown in Fig. 13(b), the methane conversion efficiency in SMR was compared for five catalyst shapes (hollow cylinder, daisy, cylcut, trilobe, and seven-hole cylinder), randomly arranged in several rows, via CFD [241]. Due to the large surface area, the methane conversion was higher for particles with an internal shape than for those with an external shape. The methane conversion per pressure drop was the highest for the cylcut particles. Pashchenko [242] experimentally investigated the effects of four different catalyst types on methane conversion and pressure drop: a cylinder, a ring, a convex cylinder with seven-holes, and a sphere with seven-holes, as shown in Fig. 13(c). The seven-hole sphere catalyst has a larger surface area and higher methane conversion efficiency than a cylinder. Future research should focus on

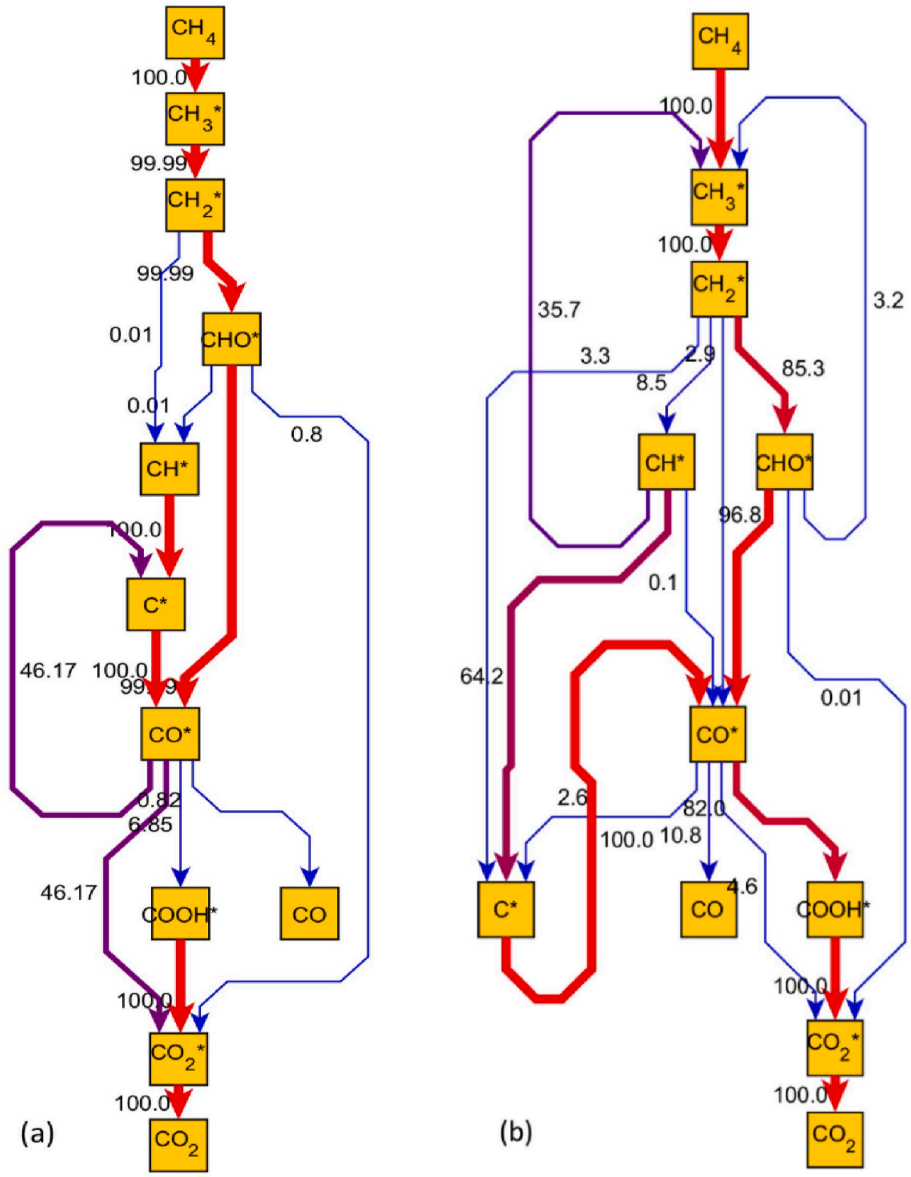

Fig. 14. Contribution analysis **(a)** Ni(10)-CeZrLa; **(b)** Rh (1)-CeZrLa; T= 450 °C, GHSV= 70,000 h^{-1}, Blue lines represent lowest conversion value (0%), and red lines indicate highest conversion value (100%). (Reprinted with permission from Ref. [254]. Copyright (2017) Elsevier B.V.).

the physical properties of catalysts and their performance under various operating conditions to improve efficiency and reduce maintenance issues in industrial-scale facilities.

2.2. Effective kinetic models

In the previous reports, the investigations into SMR reactions have been addressed with regard to the preparation and modification of catalysts, lacking a systematic overview of kinetic models for the process. The kinetic models give insight into the SMR reactions; transport studies; detailed distribution of products; CH_4 conversion; and coke formation. These models help in predicting the reaction conditions and performance limitations for H_2 production other than those investigated in experiments [244,245]. To evaluate the catalytic reactions and performance of reactor designs, various kinetic models have been studied and developed over different catalyst compositions [112,246–248]. A considerable effort has been put into kinetic studies of catalysts prepared under different conditions and preparation methods. Thus, many kinetic models and mechanisms were suggested based on different assumptions, operational conditions, and isotherms such as Langmuir-Freundlich (LF) and Langmuir-Hinshelwood (LH) that were well fitted to the experimental data [94,249]. Hence, it is impossible to form a generalized model that can apply to different catalysts with different parameters. The reasons might be two-fold: (i) the model and mechanism for each SMR catalyst are obtained experimentally under no diffusion limitations of species and no heat and mass transfer limitations; and (ii) changing the composition of the catalyst causes deviations in parameters and the structure of the kinetic model [112]. For instance, Xu and Froment [250] developed the well-known SMR model over an extensive temperature range, neglecting the CO_2 adsorption on the catalyst surface. The detailed mechanistic expression of the triangular scheme of three reactions can be found as follows (Scheme 1).

The model presented a reaction path with the following rate expressions (**Eqs. (1)–(3)**) [250]:

$$r_1 = \frac{\frac{k_1}{p_{H_2}^{2.5}} \cdot \left[p_{CH_4} \cdot p_{H_2O} - \frac{p_{H_2}^3 \cdot p_{CO}}{K_{eq1}} \right]}{\left(1 + K_{CO} \cdot p_{CO} + K_{H_2} \cdot p_{H_2} + K_{CH_4} \cdot p_{CH_4} + K_{H_2O} \cdot \frac{p_{H_2O}}{p_{H_2}} \right)^2} \quad (1)$$

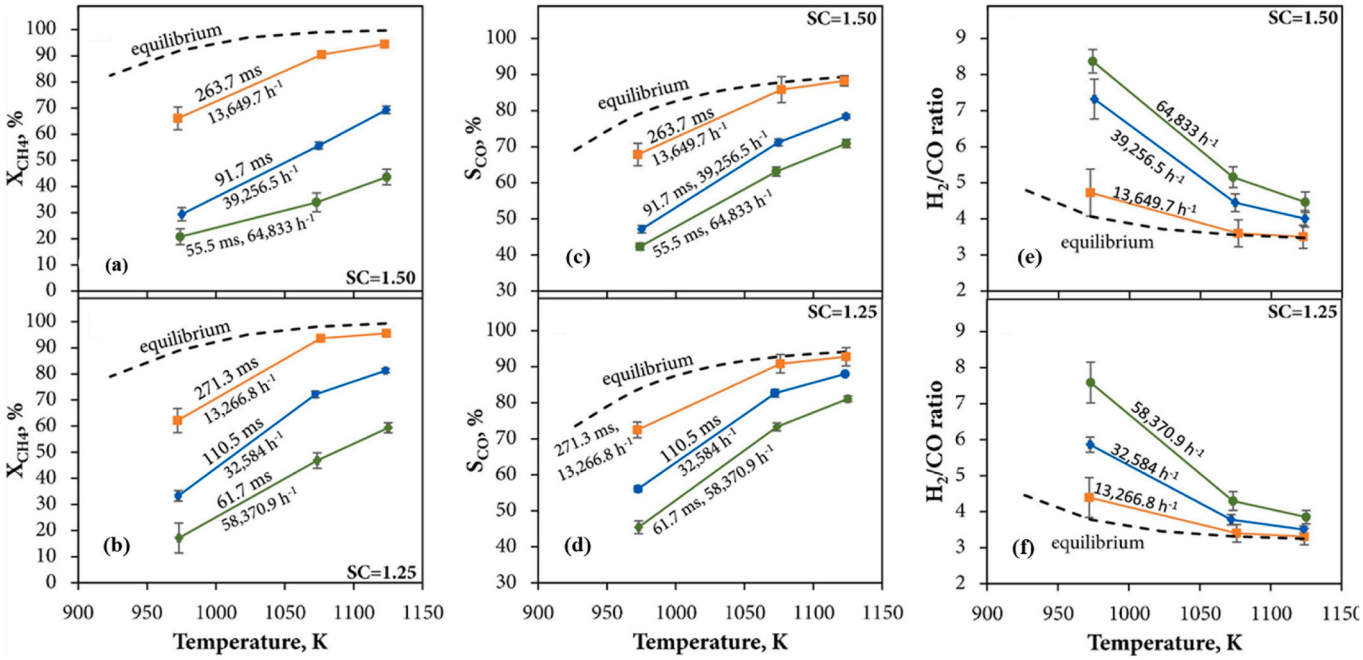

Fig. 15. (a–d) Experimental values of CH_4 conversion and CO selectivity (e–f) H_2/CO at S/C = 1.25 and 1.50 at varying values of GHSV (Reprinted with permission from Ref. [176]. Copyright (2017) Elsevier B.V.).

$$r_2 = \frac{\frac{k_2}{p_{H_2}} \cdot \left[p_{CO} \cdot p_{H_2O} - \frac{p_{H_2} \cdot p_{CO_2}}{K_{eq2}}\right]}{\left(1 + K_{CO} \cdot p_{CO} + K_{H_2} \cdot p_{H_2} + K_{CH_4} \cdot p_{CH_4} + K_{H_2O} \cdot \frac{p_{H_2O}}{p_{H_2}}\right)^2} \quad 2$$

$$r_3 = \frac{\frac{k_3}{p_{H_2}^{3.5}} \cdot \left[p_{CH_4} \cdot p_{H_2O}^2 - \frac{p_{H_2}^4 \cdot p_{CO_2}}{K_{eq3}}\right]}{\left(1 + K_{CO} \cdot p_{CO} + K_{H_2} \cdot p_{H_2} + K_{CH_4} \cdot p_{CH_4} + K_{H_2O} \cdot \frac{p_{H_2O}}{p_{H_2}}\right)^2} \quad 3$$

Where K_i is the adsorption constant, $K_{eq,i}$ equilibrium constants, k_i rate coefficients of reactions, and p_i are the partial pressures. The following models presented more detailed measured results than equilibrium values due to the modifications in the process.

2.2.1. Microkinetic model

Microkinetic model is frequently employed because it can offer thorough insights into reaction pathways, adsorption and desorption phenomena, and interactions between surface species. It is suitable for examining catalyst performance and design since it takes into consideration the molecular-level kinetics of specific elementary stages. The microkinetic model developed for SMR over Ni-based catalysts predicts the thermodynamic consistency during the surface mechanisms and the exit flow rates of chemical species for the entire reactor volume between the flow guide tube and the reactor tube. It is an effective technique to obtain a detailed understanding and information about the reaction pathways, intermediates, rate-determining steps, and surface reactions, as it makes no assumption of a rate-determining step for elementary reactions [251]. The model comprises oxidation and partial oxidation reactions, WGS, methanation reactions, and coke formation reactions. The combination of density functional theory (DFT) calculations with microkinetic modeling is a popular tool to gain a better understanding of catalytic reactions [252]. DFT is applied to develop a microkinetic model for SMR over a Ni multi-faceted catalyst. A reaction pathway was developed for a multi-faceted catalyst by using DFT, transition state theory, and thermodynamics of different surfaces. This model helps to investigate the relative activity of each Ni facet and the primary reaction mechanism [140]. Similarly, a microkinetic model to thoroughly understand the activity trends of different Ni sites was developed. Compared to DRM, the rates of SMR were more pronounced on the surfaces of transition metals (Co and Ru) [253].

To elucidate the importance of reaction pathways for low-temperature SMR, a recent study conducted a contribution analysis at the outlet of the catalyst, as shown in Fig. 14, and step-by-step reaction pathways can be seen in previous research [254]. The net formation rates of all surface species and gas-phase molecules involved in the reaction over Ni(10)-CeZrLa and Rh (1)-CeZrLa are presented. The microkinetic model for this study identified the dehydrogenation of CH_3* as the rate-determining step. The model predictions suggested that Rh catalysts yielded better catalytic activity than Ni catalysts on account of stable surface intermediates.

The molar production rate of the surface species s_x is given by Eq. (4) [255].

$$s_x = \sum_{k=1}^{K_s} \left(\nu''_{xk} - \nu'_{xk}\right) k_{fk} \prod_{y=1}^{N_s+N_g} c_y^{\nu'_{yk}} \quad 4$$

Where, s_x is the net rate of reaction for x surface species, the number of surface reactions is K_s, ν''_{xk} and ν'_{xk} are the stoichiometric coefficients of products and reactants, respectively. N_s, N_g are the number of surfaces and gas-phase species. The modified Arrhenius equation describes the temperature dependence of the rate coefficients k_{fk} as in Eq. (5) [255].

$$k_{fk} = A_k T^{\beta k} \, exp\left[\frac{-E_{ak}}{\mathrm{RT}}\right] \prod_{x=1}^{Ns} exp\left[\frac{\varepsilon_{xk}\Theta_x}{RT}\right] \quad 5$$

Using the parameters, ε_{xk} this expression considers the additional dependencies of activation energy, whereas Θ_x is defined as the surface coverage species. To observe the equilibrium of reactions, the following Eq. (6) was used for the rate coefficients for forward (k_{fk}) and reverse (k_{rk}) reactions [255].

$$\frac{k_{fk}}{k_{rk}} = K_{pk} \prod_x \left(c_x^{\,0}\right)^{\nu_{xk}} \quad 6$$

Where $c_x^{\,0}$ are the reference concentrations at normal pressure, and K_{pk} is the equilibrium constant. The detailed surface reaction path was

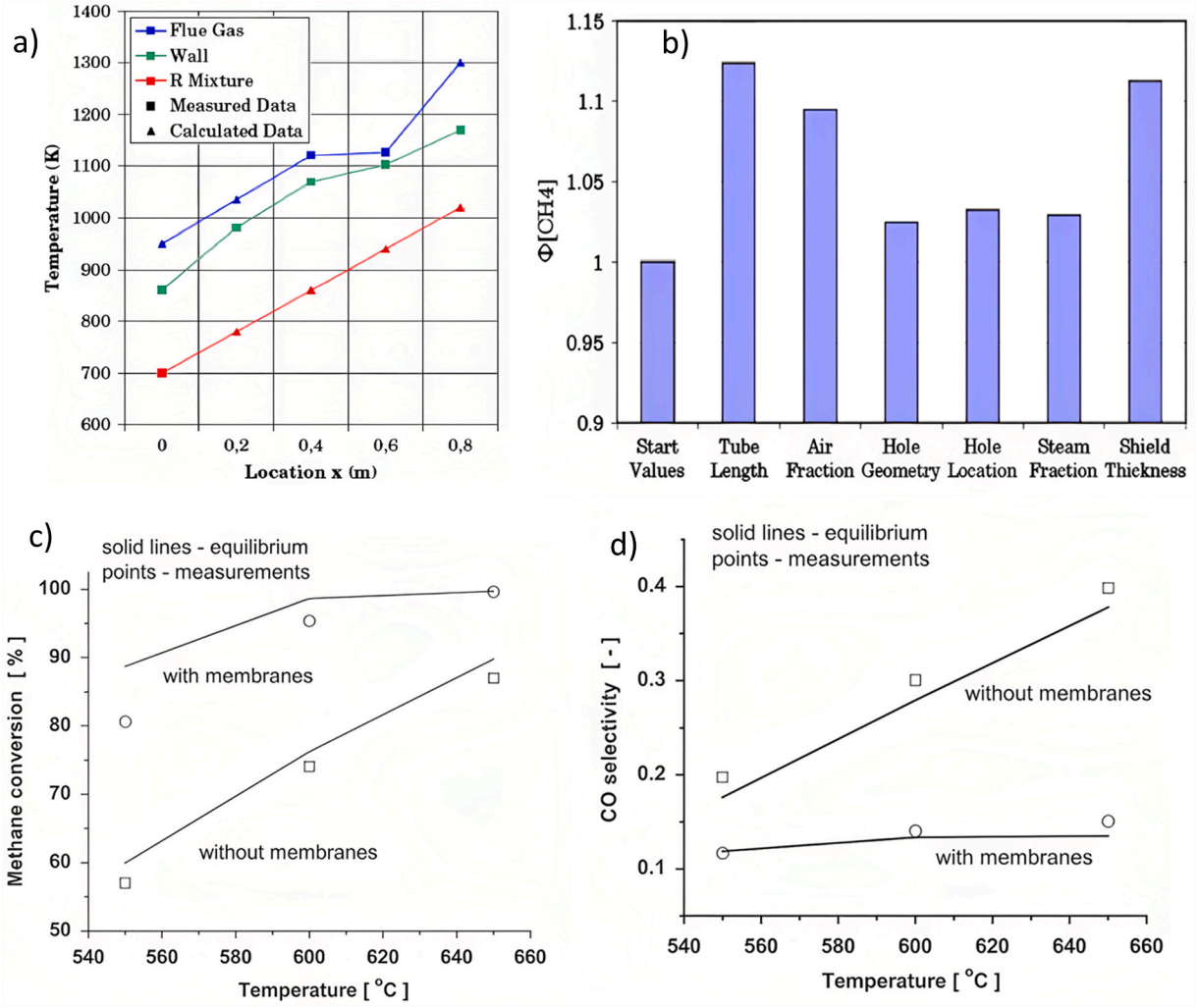

Fig. 16. (a) Measured and predicted temperatures at different points in a reactor as a function of axial position **(b)** CH_4 conversion efficiencies with different modifications and compared without modifications. (Reprinted with permission from Ref. [260]. Copyright (2009) Elsevier B.V); **(c)** measured and equilibrium CH_4 conversions with and without membrane **(d)** measured and equilibrium CO selectivity with and without membrane in the fluidized bed reactor. (Reprinted with permission from Ref. [261]. Copyright (2007) Elsevier B.V.).

presented by 42 equations, while the conversion and selectivity were measured experimentally by numerical simulations using mass transport models and developed mechanisms. The numerically predicted and experimentally measured CH_4 conversion and H_2 and CO yield as a function of temperature. CH_4 conversion and H_2 yield exhibited lower experimental values as compared to equilibrium values at lower temperatures. However, increasing temperatures enhanced the values up to the equilibrium values. It was observed that lower temperatures resulted in a higher calculated H_2/CO ratio as compared to the equilibrium values [255].

Various researchers worked on modifying the microkinetic model by changing the parameters for CH_4 reforming reactions [247,254,256,257]. To simulate the SMR process over Ni spinel catalyst, the model was optimized under isothermal conditions in a plug flow reactor at 17.5 psi. The results reported an average 19% increase in the coverage of H_2 species as compared to the original model due to changing the parameter value of CH_4 conversion. Fig. 15(a-d) presents equilibrium and experimental results for S/C = 1.25 and 1.50, with increasing temperature at three different values of GHSV. Like in the previous case, the experimental values were below equilibrium for CH_4 conversion and CO selectivity. Therefore, any noticeable deactivation of the catalyst can be identified readily. Because CO production is favored at elevated temperatures, CO selectivity also increases with increasing temperature. H_2/CO reduced at elevated temperatures, and for the two S/C ratios, increased steam content improved the H_2 production and resulted in higher H_2/CO at 1.50 as compared to 1.25 as presented in Fig. 15(e-f) [176]. Salciccioli et al. [246] presented their result for the microkinetic model, stating that a remarkable change in the thermodynamic consistency can be observed with a minor change in activation energy. Conclusively, the microkinetic model gives an understanding of the rate-limiting steps and the dominant surface species on each surface [140].

Microkinetic models develop generalized kinetic behavior of catalysts within broader parts of the steam reforming system [258]. The approaches based on microkinetic modeling provide advantages in catalyst design, such as diffusional limitations, parameter optimization, and structural modification of the catalyst particle during the SMR process [259]. For each surface of the catalyst, this model offers the opportunity to investigate the activity, considering the coverage information, resulting in an accurate estimation of the catalytic activity [154]. The application of this model involves assumptions about the homogeneity of the catalyst surface. However, such assumptions can lead to significant non-uniformities in the catalyst surface that affect the catalyst performance and SMR process [259]. These non-uniformities can be accounted for by advances in simulation and multiscale modeling.

2.2.2. Lumped parameter model

Lumped parameter models provide a more straightforward method by combining several reaction steps into a single rate expression. It provides a basic understanding but lacks the intricacies and complexities of the actual reactions. A lumped parameter thermodynamic model predicts the chemical reactions occurring in the reformer tubes and heat transfer from the flue to the reactant gas. The main element of this model is the interaction between chemical reactions and heat transfer. A lumped model was presented with the heat transfer simulations inside the reactor, at the reactor wall, in the reactor space, and in the reactions occurring in the reformer tubes. The measured and predicted temperatures of the tube wall, flue gas, and reformer gas are considered. The wall temperature is taken as the average temperature of the reactor mixture and flue gas multiplied by each fraction of the heat transfer coefficient **Eq. (7)** [260].

$$T_{wall} = \frac{h_f}{h_g + h_f} T_{flue} + \frac{h_g}{h_g + h_f} T_{tube} \quad 7$$

Where, h_f and h_g are the heat transfer coefficients for flue and reformer gas. Besides, T_{wall}, T_{flue} and T_{tube} are the temperatures of wall, flue gas, and tube, respectively.

The simulated temperatures at different points (flue gas, reformer gas, and the reformer tube wall) were validated with measured data from a prototype reactor. The results showed that the measured wall temperature was between the predicted flue and reformer gas temperatures, as shown in Fig. 16(a). For the equilibrium reactions (SMR and WGS), the rate of reaction depends on the kinetics (speed of reaction occurring) and thermodynamics (distance to the equilibrium position). The values for the equilibrium constant for partial pressure (K_p) and heat of reaction (ΔH) were calculated using the Van't Hoff equation Eq. (8) [260]:

$$K_p = K_{p,298}\ exp\left(\frac{\Delta H}{R}\left[\frac{1}{298} - \frac{1}{T}\right]\right) \quad 8$$

The model was also used to evaluate the impact of design modifications on the performance of the reactor. Fig. 16(b) shows the conversion efficiency of CH_4 to H_2 with various modifications, and the values are compared to the values without modifications. The results exhibited that up to 9.5% and 11.2% more H_2 were produced by increasing the fraction of air in the burner fuel and the thickness of the insulation shield, respectively, by 50% [260]. Similarly, various researchers worked on the lumped parameters for simulation-based SMR [261–263]. A two-phase reactor model was developed for a fluidized-bed Pd-based membrane reactor. The model developed a lumped flux expression for the H_2 permeation rate through the membranes in the reactor and demonstrated experimentally that the thermodynamic equilibrium limitations can be improved by the insertion of membranes in the reactor, leading to increased CH_4 conversion and H_2 yield while reducing the CO selectivity. Fig. 16(c) shows that without membranes, the measured CH_4 conversions are close to equilibrium (96%) at all temperatures, whereas with membranes, the approach to equilibrium improves with increasing temperature. In the case of CO selectivity, a reduction is observed when membranes are used, as presented in Fig. 16(d). Unlike commercial SMR catalysts at 650 °C, the use of noble metal-based catalysts ensures that operation can take place in a regime without kinetic rate limitations [261].

The lumped parameter thermodynamic model helps to design the steam reformers for H_2 production at optimal efficiency. The model presents a uniform performance of the system in each domain [264]. It considers the heat transfer phenomena in the reactor by simulating different domains of the reactor and the overall heat production. Assembling all the model parts led to the temperature gradient differential equations. Apart from heat transport, the model also evaluates the design modifications of the process. However, the physical domain of the lumped parameter model is restricted to the volume between the reactor tubes, the flow guide tubes, and the reactor tubes themselves [260]. Still, the application of this model can have beneficial effects on the efficiency of the SMR system.

2.2.3. Isothermal model

Calculations are made easier by the use of isothermal models, which assume a constant temperature throughout the reactor. They give a clear grasp of how temperature impacts reaction rates and are especially helpful for steady-state simulations. A steady-state, one-dimensional, isothermal model for the simulation of a membrane-based fixed-bed reactor to obtain H_2 was developed and compared the maximum conversions with that of a conventional reactor. The model was developed to explore the opportunity of enhancing the CH_4 conversion using a membrane reactor via metallic, ceramic, or metallic/ceramic composite membranes. As produced H_2 is selectively separated from the membrane reactor, a shift in the chemical reaction equilibrium occurs towards the product. Thus, increasing the CH_4 conversion to syngas increases and enhances H_2 purity after separation due to the membrane-based system. The approach can be represented by Eq. (9):

$$\frac{dX_i}{d_z} = \frac{\rho_b A R_i}{F_t} \quad 9$$

Where, F_t is the total molar flowrate, ρ_b is the density of the catalyst, X_i is the conversion of species i, z is the reactor length, A is the area of the cross-section of the reactor, and R_i is the reaction rate of species i [265]. Singh and Saraf [266] worked on the kinetic model, and the following rate equations, (10) and (11), were developed:

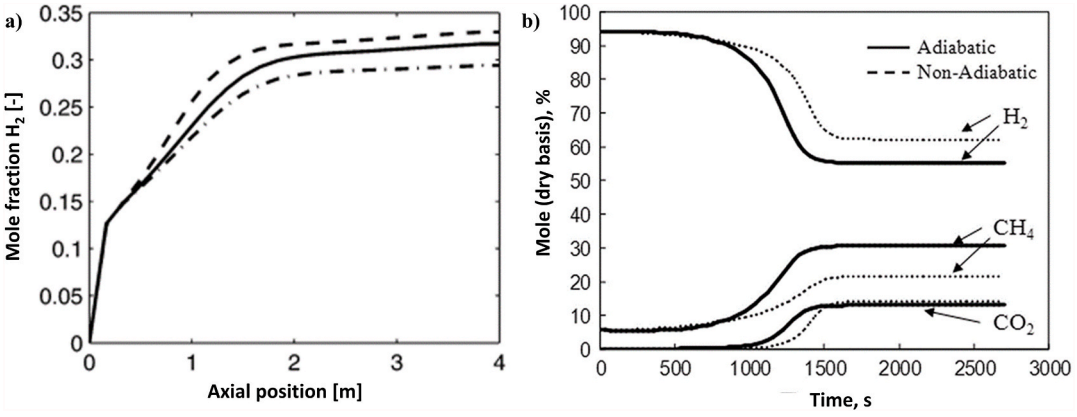

Fig. 17. (a) H_2 mole fraction as a function of axial position in the reactor using varying approaches. (Reprinted with permission from Ref. [272]. Copyright (2007) American Chemical Society); **(b)** Reactor performance under adiabatic and non-adiabatic conditions. (Reprinted with permission from Ref. [274]. Copyright (2012) Elsevier B.V.).

$$R_1 = k_1^0 e^{-Ea1/RT}\left(P_{CH_4} - P_{CO}P_{H_2}^3 \Big/ K_{eq1} \Big/ P_{H_2O}\right) \Big/ P_{TOT}^{0.5} \quad 10$$

$$R_2 = k_2^0 e^{-Ea2/RT}\left(P_{CO} - P_{H_1}P_{CO_2} \Big/ K_{eq2} \Big/ P_{H_2O}\right) \Big/ P_{TOT}^{0.5} \quad 11$$

Where, $R_{i=1,2}$ is the rate of reaction coffecient (refer to the major reactions, SMR and WGS for first-order kinetic expression), $k_i{}^0$ is the reaction rate coefficient, R is the ideal gas constant, T is the temperature, Ea is the activation energy, P_i is the partial pressure, $K_{eq,i}$ is the equilibrium constant and P_{TOT} is the total pressure.

The CH_4 conversion with a membrane reactor is higher at all temperatures as compared to a fixed-bed reactor. In a temperature range of 600–900 °C, a 16% increase in the yield of the process was exhibited as compared to the conventional reactor. Higher equilibrium conversion was observed at elevated temperatures. The isothermal model, like the previous works based on membrane reactor (MR) modeling, was reported by many researchers [267–269]. Recently, an optimization study recommending the operating conditions for improved efficiency in the case of MRs over packed bed reactors, was developed. An optimization study was conducted by dividing the length of the reactor into isothermal segments, resulting in higher process efficiency. Results showed higher CH_4 conversion with the membrane in the reactor, with temperature playing a major role in the CH_4 conversion [270].

This model assumes steady-state and isothermal conditions throughout the reactor. A comparison of isothermal and non-isothermal simulations for SMR indicates that the former simulation gives better performance with higher CH_4 conversion and H_2 production. It indicates a limited number of adjustments in the parameters are available to practically improve the reactor's performance [271]. Additionally, the model helps to observe the potential of using a membrane reactor for SMR. It develops the ordinary differential equations for the flow variations of components as the reaction occurs in the SMR reactor. The model can also help predict the diffusive permeation mechanism of the membrane used in the membrane reactor for SMR [265]. The isothermal model in the SESMR application contributes to quantitative identification in sorption enhancement and process equilibrium conversion [98]. Thus, the isothermal model highlights the significance of parameter control during the SMR process.

2.2.4. *Transient model*

Transient kinetic models encompass the time-varying characteristics

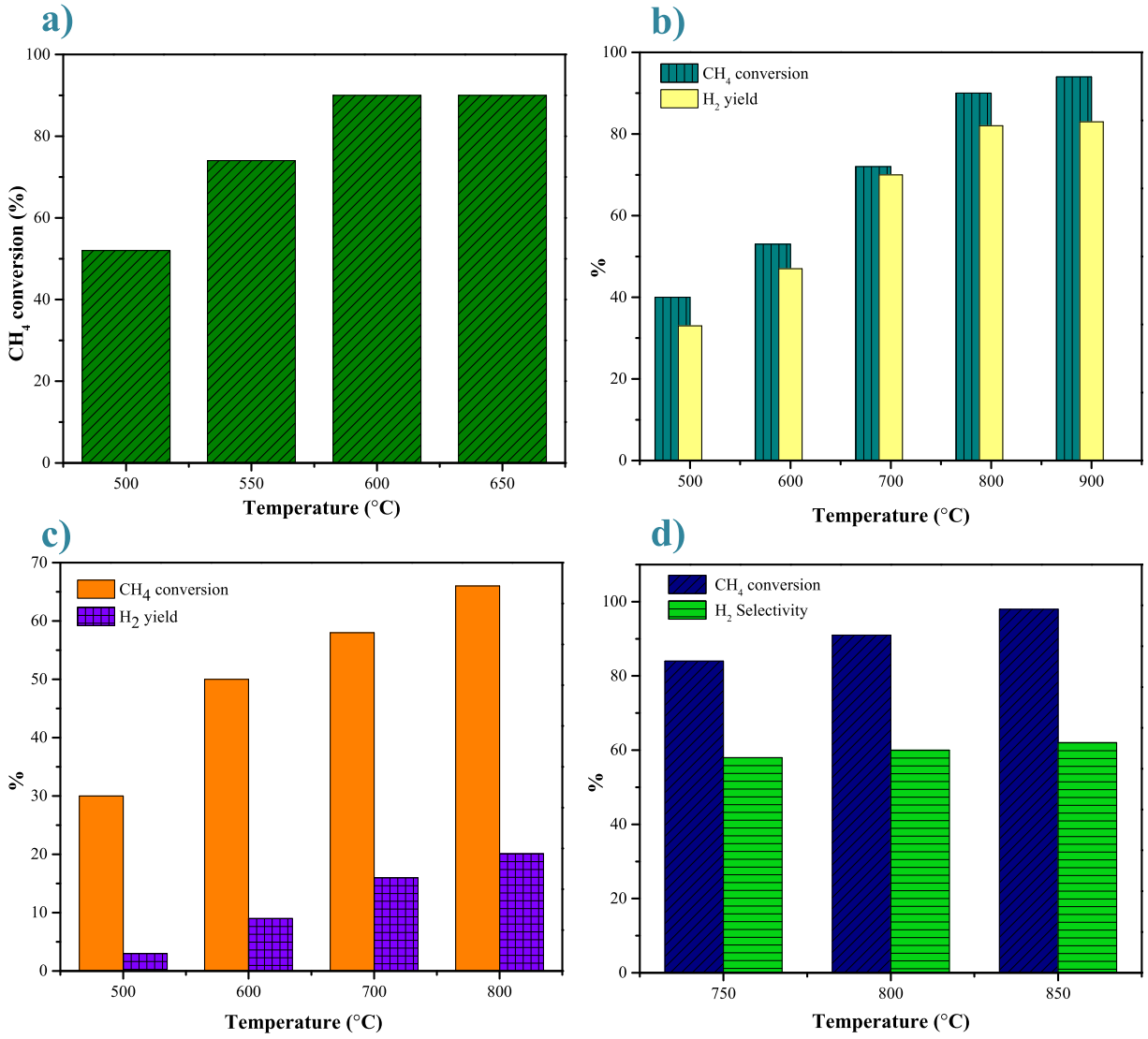

Fig. 18. Influence of temperature on **(a)** CH_4 conversion on CaO–Ni/Al_2O_3 catalyst. (Adapted with permission from Ref. [286]. Copyright (2021) Elsevier B.V.); **(b)** CH_4 conversion and H_2 yield over $LaNiO_3$ catalyst. (Adapted with permission from Ref. [231]. Copyright (2020) John Wiley & Sons Ltd); **(c)** CH_4 conversion and H_2 yield over Ni–CaO/Al_2O_3 catalyst. (Adapted with permission from Ref. [287]. Copyright (2015) American Chemical Society); **(d)** CH_4 conversion and H_2 selectivity on Ni/Al_2O_3 catalyst. (Adapted with permission from Ref. [282]. Copyright (2013) Elsevier B.V.).

of the SMR process, accounting for fluctuations in temperature, reactant concentrations, and other factors. These models are well-suited for simulating the startup and shutdown operations and enable a thorough examination of transient phenomena like heat and mass transfer. A transient one-dimensional reactor model was developed to simulate SMR with an enhanced sorption process over Li_2ZrO_3 as a sorption agent [272]. The model was established for the CO_2 capture process because of its time-dependent nature. From three different transient models, the selection of a specific model was dependent on the sorbent installation method in the reactor. One of the models considers that a single particle contains the properties of both a reforming catalyst and a sorbent, while the other suggests that both are separated into different particles. In terms of temperature, the one-dimensional energy equation (12) was formulated as [272]:

$$\left(\rho_g C_{pg}\varepsilon_b + \rho_s C_{ps}\right)\frac{\partial T}{\partial t} + \rho_g\, u C_{pg}\frac{\partial T}{\partial z} = \frac{\partial}{\partial z}\left(\lambda_s \frac{\partial T}{\partial z}\right) + S_i \qquad 12$$

Where ρ_g and ρ_s are the densities of gas and solid; ε is the void fraction; S_i is the source term (different for various models); and C_p is the heat capacity of the gas mixture; u is superficial velocity (m/s); γ_s is conductivity of solid; C_{pg} and C_{ps} are the heat capacity of the gas mixture and solid.

A continuity **Eq. (13)** for the transient model to evaluate the pressure and velocity coupling in the reformer was formed as [272]:

$$\varepsilon_b \frac{\partial \rho_g}{\partial t} + \frac{\partial}{\partial z}\left(\rho_g u\right) = -R_{cap} \qquad 13$$

Where $-R_{cap}$ are the capture kinetics, as mass is removed from the gaseous phase, in terms of CO_2. The average momentum equation, **Eq. (14)**, for the reforming reactor was given as [272]:

$$\frac{\partial}{\partial t}\left(\rho_g u\right) + \frac{\partial}{\partial z}\left(\frac{\rho_g u u}{\varepsilon_b}\right) = \varepsilon_b \frac{\partial p}{\partial z} - \varepsilon_b f \frac{\rho_g |u|\, u}{d_p} \qquad 14$$

For SMR heterogeneous models, an efficiency factor has been used for the simulation of the process. Heterogeneous models for SESMR have been developed to check if the process is diffusion-controlled or not, as in the case of SMR [273]. As reported, the CO_2 capture step was the limiting step of SMR. Therefore, no advantages of heterogeneous models were seen under standard conditions. Thus, a pseudo-homogeneous model showed satisfactory results for the particles, with an efficiency factor of >87% of the dry H_2 mole fraction obtained in the process with a CO_2 acceptor [272]. The H_2 mole fraction is compared in Fig. 17(a)

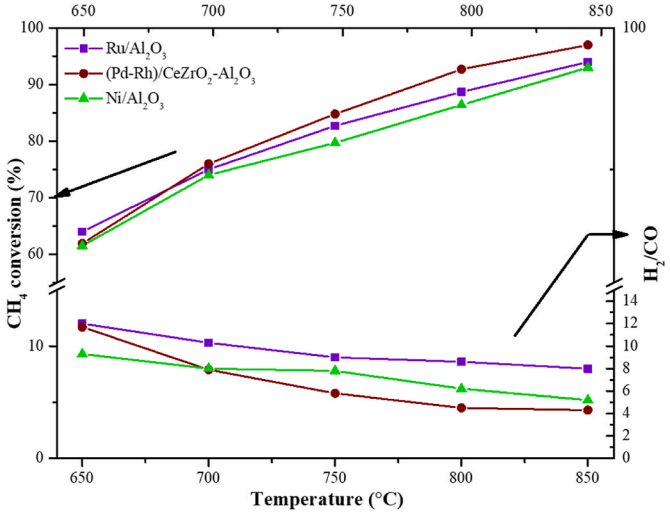

Fig. 19. Effect of temperature on CH_4 conversion and H_2/CO ratio on Ru/Al_2O_3, NiAl_2O_3, and Pd–Rh/$CeZrO_2$–Al_2O_3 at GHSV 20,000 h^{-1}. (Recreated with permission from Ref. [189]. Copyright (2015) Elsevier B.V.).

using different approaches that assume constant velocity and mass flux, as well as momentum and continuity equations. These approaches influence the solution of other transport equations. For mole fractions in the output, a 10–15% discrepancy was observed between the model prepared and the others. Similarly, Fernandez et al. [274] reported the development of a transient model to analyze the sorption-based SMR process and investigate the reactor conditions and material parameters for optimum performance. The model validated that adiabatic conditions resulted in more favorable reactor performance as compared to non-adiabatic conditions. The product gas has a higher temperature under adiabatic conditions during the breakthrough period (from 720 to 1080 s), as shown in Fig. 17(b). The 85% CH_4 conversion and 95% H_2 purity were achieved under optimal conditions of 650 °C and a GHSV of 3.5 kg/m^2 s. In recent years, much attention has been paid to the modeling of sorption-based SMR processes [275–277].

In summary, numerous studies have been conducted to better understand and develop SMR kinetics using various catalysts and supports. Different kinetic expressions and rate-limiting steps have been developed. However, according to the literature, the differences in kinetic mechanisms have been caused by the various types of supports, metal dispersion, and diverse particle sizes in each study [38].

The transient model describes the importance of SMR under transient conditions, as the process is highly nonlinear and involves a chemical reaction, heat and mass transfer, and flow. The transient model can evaluate the diffusion flux models that include reaction conditions, flow, and heat and mass transfer within the pellets [278]. It considers the transport characteristics of the process by establishing mathematical models. However, heat and mass transfer become more complex in the transient state as compared to the steady-state [279]. Thus, it is important to consider the investigation of transport mechanisms in a transient state. Application of the transient model in SESMR gives the analysis of the interaction between the chemical reactions, the effect on temperature, H_2 production, and CaO conversion [279]. The analysis suggests that higher CO_2 yield is obtained under adiabatic reaction conditions during the transition period. Furthermore, examining the transient behavior of the SESMR process indicates that carbonation kinetics play a limiting role, necessitating lower space velocities compared to SMR [274].

2.3. *Effective processing parameters*

The strong influence of changing temperature, pressure, flow rate, and S/C ratio on the products' selectivity has been studied [115,191,203,280]. Even though the preparation techniques, composition, and structure were different for each synthesized catalyst as observed in this section, they exhibited almost similar trends in the case of changing process parameters. Thus, the study of process parameters is necessary for understanding efficient reactor output and minimizing energy sources [281]. This section covers various investigations of the performance of synthesized catalysts by changing the process parameters to explore better options for optimum process conditions for SMR.

2.3.1. *Effect of temperature*

The reformer reaction in SMR is highly endothermic (R1). Therefore, this is desirable under low pressure and high temperatures. It has been observed that coke deposition occurs at lower reaction temperatures, while CH_4 conversion increases with an increase in temperature. H_2 selectivity also decreases with increasing temperature at equilibrium [282]. Therefore, it is feasible to run the process at temperatures higher than 700 °C to maintain adequate reaction activity. Recently, a lanthanum strontium cobalt ferrite (LSCF)-supported Ni catalyst was investigated for SMR at various operating temperatures (750–850 °C), which resulted in a significant rise in CH_4 conversion (up to 89.77%) [283]. It was observed that the experimental results and equilibrium trends can also vary with temperature and metal loading. The prepared 10% NiO/$NiAl_2O_4$ exhibited CH_4 conversion close to that of equilibrium

beyond 650 °C and an S/C of 4.4, while 5% NiO/$NiAl_2O_4$ revealed lower CH_4 conversions in the range of 400–650 °C [284].

CH_4 conversion was observed as a function of temperature at operating temperatures ranging from 600 to 800 °C, with CH_4 conversion increasing significantly with increasing temperature. Even at a fixed temperature, CH_4 conversion correspondingly increased with an increase in residence time, with a conversion close to that of equilibrium beyond a residence time of 4 kg_{cat}. s/mol at all temperatures [285]. Ni/Ce–ZrO_2 and Ni/YSZ were investigated to analyze the influence of temperature on product distribution and carbon deposition. The H_2 production yield increased from 70.9% to 84.9% as temperature increased from 900 to 1000 °C, while coke formation decreased significantly due to increased reforming reactivity of CH_4 at high temperatures. The H_2 yield and CO fraction increased, whereas the CO_2 fraction decreased. Changes in the fraction of H_2, CO, and CO_2 were a result of mildly exothermic WGS, while due to further reforming reactions to CO and H_2, CH_4 production decreased [280].

Various reports were published investigating the impact of temperature on CH_4 conversion, H_2 yield, and selectivity, as presented in Fig. 18. As shown in Fig. 18(a), increased temperatures on CaO–Ni/Al_2O_3 at S/C of 3.0 promoted the reforming process, with CH_4 conversion increasing from 52% to 90% in the 500 °C–650 °C range [286]. Similarly, a perovskite-based $LaNiO_3$ was tested for SMR in the range of 500–900 °C, GHSV = 900 h^{-1}, and S/C = 1, as shown in Fig. 18(b). Higher temperatures stimulated H_2 formation and CH_4 conversion during the SMR reaction, significantly relying upon the other reaction conditions, including GHSV, S/C, and pressure [231]. Fig. 18(c) shows that increasing the temperature from 500 °C to 800 °C maximizes H_2 yield and CH_4 conversion to 20.1% and 66%, respectively, over Ni/Al_2O_3 [287]. Similarly, Monero et al. [282] reported the influence of reaction temperature on CH_4 conversion and H_2 selectivity. The Ni/Al_2O_3 catalyst was tested for SMR from 750 to 850 °C, as presented in Fig. 18(d). An increase in CO selectivity and almost constant H_2 selectivity at equilibrium were experimentally observed due to the contact mode of gas flow in a fluidized-bed reactor.

Roy et al. [189] investigated the temperature influence (650–850 °C) on CH_4 conversion and H_2/CO ratio on different noble metals over Al_2O_3, as shown in Fig. 19. When the temperature was raised to 850 °C, three different types of noble metal catalysts increased CH_4 conversion. However, the Pd–Rh catalyst exhibited better CH_4 conversion, which was not substantially higher as compared to other catalysts. For all catalysts, the H_2/CO ratio decreased with increasing temperature. Below 700 °C, ratios exhibited the order Ni < Pd–Rh < Ru, while above 700 °C, the order changed to Pd–Rh < Ni < Ru as presented in Fig. 19.

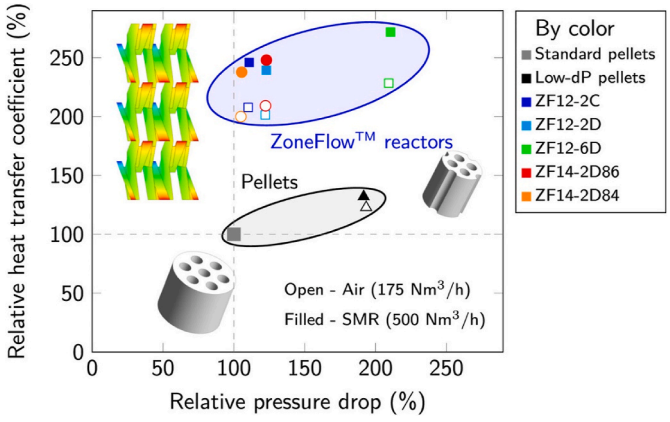

Fig. 20. Relative heat transfer coefficient vs. relative pressure drop of the ZoneFlow™ reactors of various designs and for two commercial reference pellets. Filled: typical commercially applied SMR conditions (SMR mixture @ 30 bar and 700 °C) at a flow rate of 500 Nm^3/h; Open (air @ atm pressure and 300 °C) at a flow rate of 175 Nm^3/h. (Reprinted with permission from Ref. [299]. Copyright (2021) Elsevier B.V.).

Recently, a numerical study was performed for a composite grille-sphere packed bed instead of a conventional packed bed reactor for SMR [288]. On investigating the influence of inlet temperature in the range of 527–677 °C, the numerical methods (solid particle and equivalent medium method) both exhibited the same tendencies. CH_4 conversion and H_2 fraction increased with increasing temperature. The study was based on numerical methods for H_2 production. The solid particle method was able to show the details of the simulation. However, the equivalent medium method presented the macro situation of the simulation. The values obtained from the equivalent medium were greater than those obtained from the solid particle method while studying the influence of temperature rise.

Evidently, high operating temperatures (>700 °C, as mentioned earlier) hold a decisive role in contributing to the performance of the catalyst because of the endothermic nature of the reaction, which requires elevated temperatures for methane activation [51]. Lower temperatures will cause low catalytic activity along with coke deposition, whereas severe conditions caused at elevated temperatures will cause the sintering of the catalyst, high energy consumption, high operation costs, lower energy efficiency, and higher GHG emissions [289]. In addition, the reaction temperature is a key factor in reforming processes, leading to kinetic limitations. The equilibrium can be achieved at high temperatures as compared to lower reaction temperatures, indicating a kinetically limited process [290]. Therefore, intensification processes have been proposed in the literature aiming at the reduction of operating temperatures for reforming processes, as will be discussed in **section 3**.

2.3.2. *Effect of pressure*

As mentioned in the above section, industrial SMR operates in a pressure range of 1.5–3 MPa. However, the main SMR reaction favors low pressure due to the greater number of product moles, and thus the process is operated at elevated temperatures (>800 °C). That can benefit the SMR reaction for improved CH_4 conversion and simultaneously reduce the extent of the WGS reaction to produce a lower CO_2 amount in the products [95]. On the other hand, due to the equal number of moles in the WGS reaction, it is not sensitive to changes in pressure. Therefore, at a fixed temperature and S/C ratio, the conversion of CH4 decreases as the pressure increases. However, it can show a positive effect when the reaction is controlled by catalyst kinetics, extending the contact time [291]. The longer the contact time, the more the reaction is usually thermodynamically controlled, and high pressure inhibits the CH_4 conversion due to the nature of the SMR reaction [95]. The pressure effect has an effect in both directions, but it is dependent on the other experimental conditions, most notably contact time. It is necessary to gain insights into the pressure effect on SMR while keeping the other parameters constant. For example, SMR reactions at low pressure (0.5–1.0 MPa) for Ni-based catalysts were investigated and reported to have lower CH_4 conversion compared to equilibrium conversion and industrial SMR [59].

Generally, the higher reaction pressure is thought to result in faster reaction rates while increasing the concentration of reactants, increasing the collision frequency of molecules, and enhancing the formation of product molecules. It also helps to overcome the thermodynamic barrier to reactions and promotes faster reactions while maintaining high concentrations of active species. However, higher reaction pressure gives lower reaction rates at constant temperature and a fixed S/C ratio for SMR because the number of moles of products is greater than the reactant species [292]. Additionally, in a micro-channel reactor, the active reaction zone is dependent on the reaction pressure and the catalyst properties. The active reaction zone can provide important information needed for the design of the Ni catalyst for SMR. In the case of increasing pressure, the active reaction zone thickness of endothermic SMR gradually increases with reduced equilibrium CH_4 conversion [264]. The contact time of feed with the Ni-catalyst in a micro-channel reactor also increases when the system is compressed, which favors the

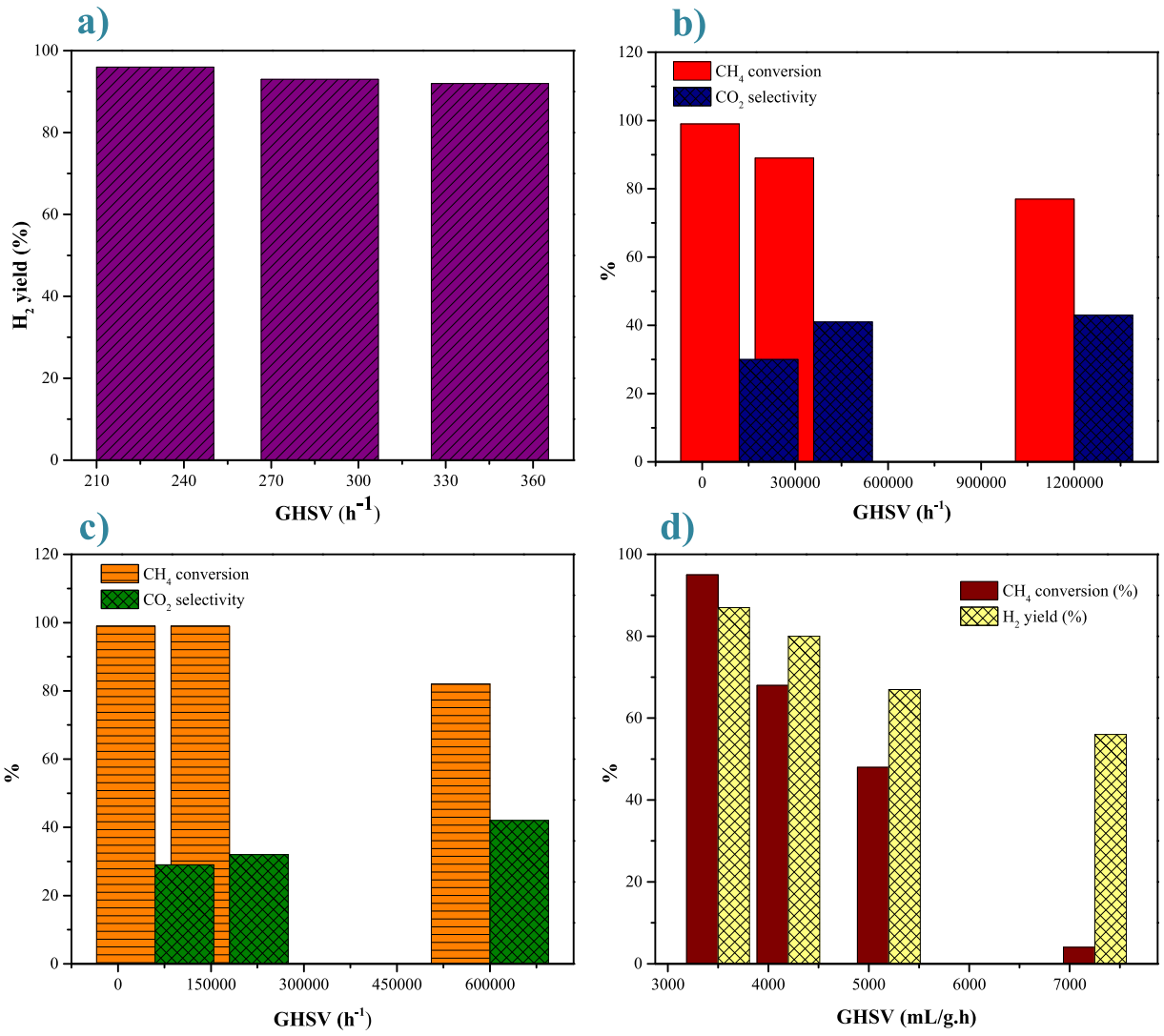

Fig. 21. Effect of GHSV on **(a)** CH_4 conversion on $Ni0_{.50}/Mg_{2.50}Al$ (1 g), CC-AN-80 (3 g) catalyst. (Adapted with permission from Ref. [307]. Copyright (2012) Elsevier B.V.); **(b)** CH_4 conversion and CO_2 selectivity on $Ni_{0.5}$/La–Ca/Al_2O_3 catalyst. **(c)** CH_4 conversion and CO_2 on $Ni_{0.5}Mg_{2.5}AlO_9$ catalyst. (Adapted with permission from Ref. [204]. Copyright (2011) Elsevier B.V.); **(d)** CH_4 conversion and H_2 yield on Ni–CaO/Al_2O_3 catalyst. (Adapted with permission from Ref. [287]. Copyright (2015) American Chemical Society.).

CH_4 conversion. Still, the CH_4 conversion is inhibited at higher pressure due to an increase in the total number of moles [95]. However, in the case of SESMR, low pressure is more suitable than high pressure due to the higher gas mole formation and subsequent steam reforming and carbonation of the sorbent [102]. The quality of the H_2 produced in SESMR at medium-low pressure is greater than the quality obtained in SMR at conventional pressure. This means that little effort is required to separate H_2 for downstream processes [293]. Fernandez et al. [294] modeled SESMR for Ca/Cu for H_2 yield under high pressure (0.5–3.5 MPa), and the results show the lower pressure is better for H_2 purity and CH_4 conversion.

Moreover, the gradient of fractional CH_4 conversion with W_{cat}/F_{CH4} was investigated at different pressures. The results showed that the gradient decreased as the pressure increased, indicating that the reaction is close to equilibrium at enhanced pressures and far from equilibrium at reduced pressures. Thus, to reach equilibrium at low pressure, more contact time is required [295]. Similarly, the effect of pressure on SMR is investigated at 830 °C, an S/C of 3.0, and a constant GHSV of 4.8 L/(h.g). It clearly depicts that the decrease in CH_4 conversion increases with pressure to some extent, which means that the reaction rate is limited thermodynamically under these reaction conditions [292,296]. It is observed that high pressure is not favored in SMR thermodynamically due to a net increase in the product mole side [297]. Besides opposing the methane conversion, high pressure also enhances the WGS reaction by increasing the H_2 yield and is favorable for the permeation rate.

In the case of employing the MRs for SMR, pressure increases have the following effects on the reactant conversion: (i) A negative effect related to the thermodynamics of SMR causes an increase in the number of moles, as discussed. (ii) The positive effect is related to the H_2 permeation through the membrane, i.e., the H_2 permeation driving force is increased with increasing pressure. The higher the pressure, the more H_2 is removed through the membrane, which favors the reaction toward product formation. (iii) Another positive effect is related to the concentration of CO, which is decreased by increasing pressure due to the beneficial effect on the WGS reaction [298].

Furthermore, Minette et al. [299], investigated experimentally the heat transfer of ZoneFlow™ reactors with different designs as well as low-pressure drops and standard reference pellets and established correlations for their heat transfer coefficients. Different designs of the ZoneFlow™ reactors were provided by varying the annulus width and the number of collars. Fig. 20 shows a comparison between standard

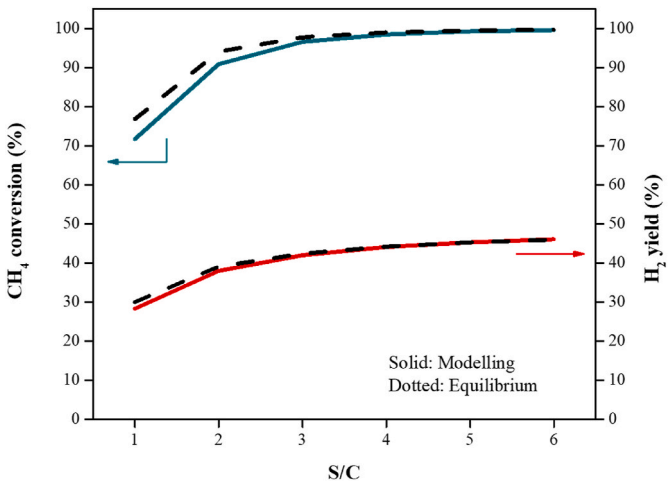

Fig. 22. Effect of S/C ratio on the CH_4 conversion and H_2 yield at 700 °C, Solid lines: Modeling, Dotted lines: Equilibrium. (Adapted with permission from Ref. [309]. Copyright (2021) Elsevier B.V.).

pellets and ZoneFlow™ reactors in terms of heat transfer coefficient and pressure drop. The standard pellets have a higher heat transfer coefficient than low-dP pellets but a much higher pressure drop. The ZoneFlow™ reactors have slightly higher pressure drops than low-dP pellets but significantly higher heat transfer coefficients, with some reactors providing more than double the heat transfer coefficient of low-dP pellets. However, the ZF12-6D reactor has a pressure drop that is around 2 times higher than that of low-dP pellets and around 1.1 times higher than that of standard reference pellets, but improved heat transfer allows for a shorter reactor length depending on catalyst activity. Finally, Fig. 20 clearly shows that at equivalent pressure drop, heat transfer is two-to three-times more efficient with the ZoneFlow™ reactors compared to the reference pellets.

Conclusively, in SMR reactions, at lower pressure, the equilibrium composition of syngas is shifted to yield a higher H_2 concentration, and the energy consumption can also be decreased. This shift is in accordance with the Le Chatelier's Principle [300]. The increase in pressure shows a negative equilibrium effect on H_2 yield due to the non-zero stoichiometric molar balance between the gas products and reactants in the SMR [293]. Therefore, Le Chatelier's principle will favor the reactants with lower partial pressures owing to their lower molar

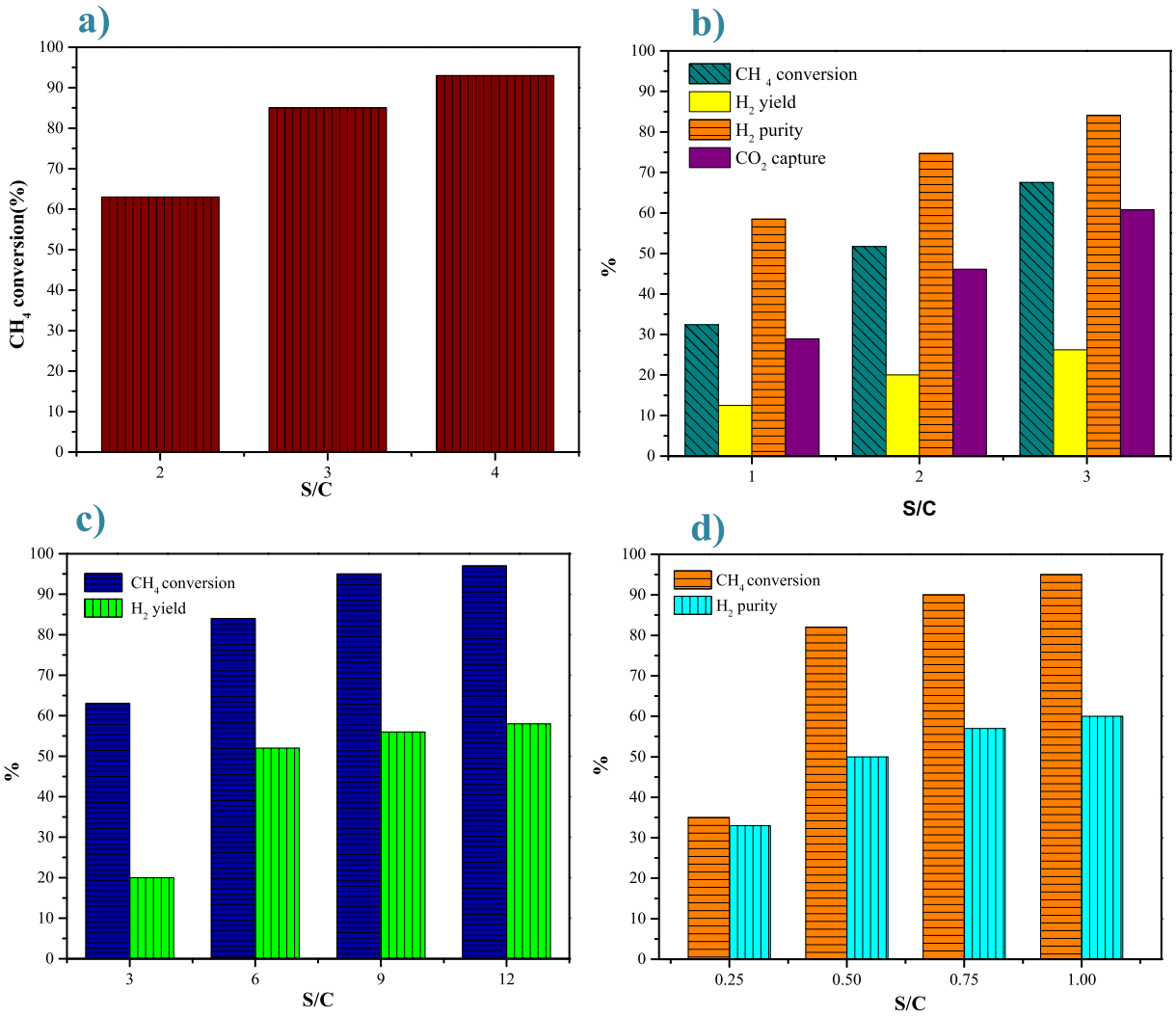

Fig. 23. Influence of S/C ratio on **(a)** CH_4 conversion on a 20 wt% Ni–Ca/Al_2O_3 catalyst at 600 °C. (Adapted with permission from Ref. [286]. Copyright (2021) Elsevier B.V.); **(b)** CH_4 conversion, H_2 yield, H_2 purity, and CO_2 capture on an 18% Ni/Al_2O_3 catalyst at 650 °C, modeled catalytic performance. (Adapted with permission from Ref. [310]. Copyright (2017) Elsevier B.V.); **(c)** CH_4 conversion and H_2 yield on Ni/Al_2O_3 catalyst. (Adapted with permission from Ref. [287]. Copyright (2015) American Chemical Society); **(d)** Product composition of Y-doped Rh substituted zirconates for SMR at 850 °C. (Adapted with permission from Ref. [311]. Copyright (2020) Elsevier B.V.).

concentration. While high pressure in SMR favors CH_4 conversion only when the contact time is extended, Overall, parametric correlation, particularly contact time, is critical in SMR and WGS pressure analysis for product formation.

2.3.3. Effect of space velocity

The effect of increasing the volumetric flow rate of feed in terms of GHSV is one of the most important processing parameters. GHSV is defined as the ratio of the volumetric flow rate of CH_4 to the weight of the catalyst (GHSV (ml/(h.g_{cat})= volumetric flow rate (ml/h)/catalyst weight (g_{cat})) [301]. As per previous reports, lower values of GHSV favor the production of H_2 with increasing residence time [204,302]. This is due to the fact that GHSV is not only dependent on the flow rate but also the catalyst loading. Therefore, with increasing the GHSV, the conversion of both steam and CH_4 is reduced owing to the shorter contact time between catalyst and reactant [303]. However, at lower GHSV, the contact time is increased, and that starts several side reactions, affecting the H_2/CO ratio to a greater extent. The effect of the flow rate of CH_4 on Ni–CaO for SMR was studied at an S/C ratio of 4.0 and 650 °C. On increasing the flow rate of CH_4, the production efficiency of H_2 decreased. While a decrease in the pre-breakthrough period was observed on increasing CH_4 flow rate due to the rapid saturation of CaO working as a sorbent [304]. The longer contact time in the sorption-enhanced SMR process exhibits maximum H_2 purity along with extremely low molar fractions of CO_2 in the product stream [305]. An increase in GHSV will limit heat and mass transfer due to higher flow rates [306]. During SMR, an effect of boron promotion on Ni stability, 20 mg of catalyst, was tested at a GHSV of 330,000 cm^3/h.g_{cat}. To reduce the mass transfer limitations, catalyst loading was reduced to 10 mg and GHSV increased to 660,000 cm^3/h.g_{cat} [159].

Various investigations on the influence of increasing GHSV on CH_4 conversion, H_2 yield, and H_2/CO ratio are presented in Fig. 21. Xie et al. [307] synthesized a CaO-based catalyst and analyzed the effect of GHSV by varying the inlet flow rate of CH_4 but keeping the S/C ratio constant at 4.2. It was observed that a reduction in GHSV slightly improved H_2 purity. As presented in Fig. 21(a), improved H_2 yield (>90% dry basis) was observed at the pre-breakthrough stage at lower GHSV. Moreover, the increase in the pre-breakthrough period was also observed at low GHSV as the process was sorption enhanced. However, with increasing reaction time, the H_2 yield was reduced to approximately 77%. Therefore, a lower GHSV is preferable for the SMR process. However, it also depends on the catalyst's characteristics. Conversely, experiments can be performed at elevated GHSV to avoid the effect of external mass transfer limitations, and the utilization of lower reactor volumes leads to a decrease in the capital cost of the reformer. A high GHSV is advantageous in reducing the metallic sintering during the reaction. Thus, even though a high contact frequency is offered between the catalyst and the reactants, the residence time is shortened, lowering the overall CH_4 conversions.

The effect of increasing GHSV on the catalytic performance of Ni/La–Ca/Al_2O_3 is shown in Fig. 21(b). Ni/La–Ca/Al_2O_3 demonstrated a decrease in CH_4 conversion while increasing CO_2 selectivity. However, an increase in residence time reduced the CH_4 conversion from 88% to 47% in 150 h at a GHSV of 3.6×10^5 h^{-1}. At a GHSV of 1.2×10^6 h^{-1}, however, the CH_4 conversion decreased from 77% to 29% [204]. Similarly, $Ni_{0.5}Mg_{2.5}AlO_9$ showed a similar trend to Fig. 21(b), with CH_4 conversion decreasing and CO_2 selectivity increasing when GHSV was increased. However, for GHSV of 6×10^5 h^{-1}, initial 82% CH_4 conversion was reduced to 62% in 150 h of reaction time. This behavior could be ascribed to the fact that the catalyst was not able to supply enough active sites in a short residence time, and interaction with reactant molecules was reduced. Nonetheless, near 100% CH_4 conversions were observed at a lower GHSV of 1.8×10^5 h^{-1} in a residence time of 20 ms, as illustrated in Fig. 21(c) [204]. CH_4 conversion and H_2 yield over Ni–CaO/Al_2O_3 were studied by increasing GHSV from 3600 to 7200 ml/(g.h). As illustrated in Fig. 21(d), both CH_4 conversion and H_2 yield were reduced with increasing GHSV [287].

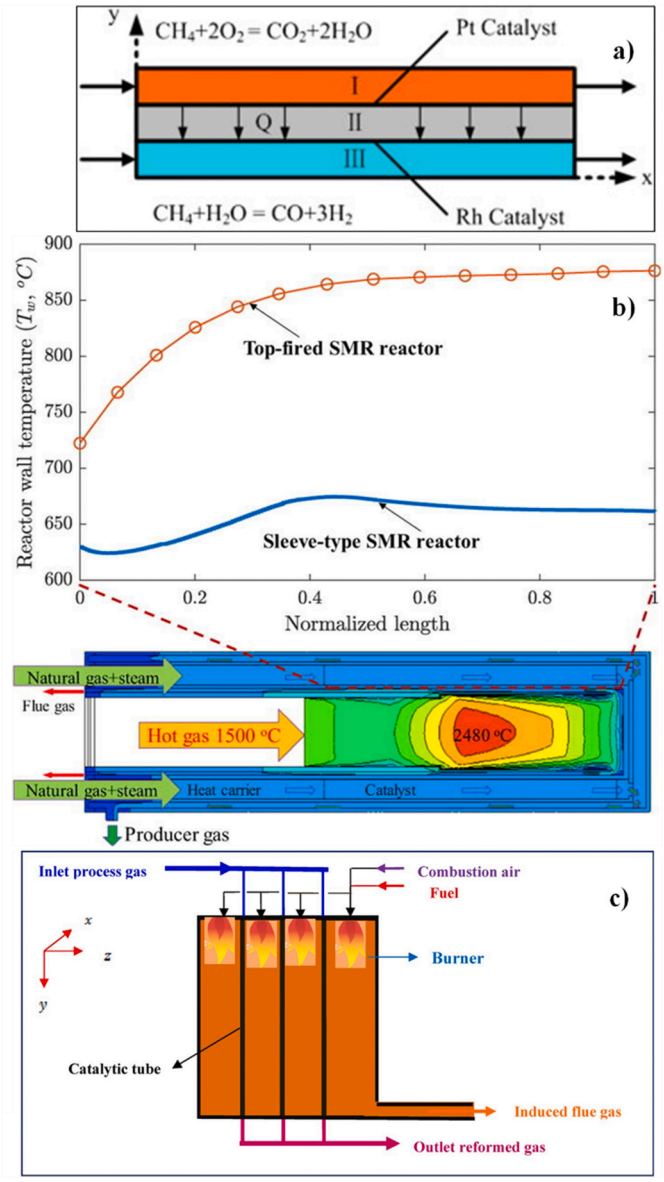

Fig. 24. (a) Geometric structure of SMR micro-reactor. (Recreated with permission from Ref. [315]. Copyright (2010) Elsevier B.V.); **(b)** Comparison of temperature profiles for sleeve-type and top-fired SMR reactors. (Recreated with permission from Ref. [316] Copyright (2019) Elsevier B.V.); **(c)** Top-fired reactor for SMR. (Recreated with permission from Ref. [317] Copyright (2017) Elsevier B.V.).

Therefore, to understand the GHSV effect, one must consider the catalyst loading and the structure geometry, along with knowledge of space velocity, to describe the conversion of CH_4 in SMR [239]. As per the literature, it is infeasible for the reaction to reach equilibrium if the space velocity is too high for the catalyst to contribute efficiently to the reaction pathways. This means that the penetration of feed gases through the catalyst pellet is not sufficient, and the active part of the catalyst is not completely utilized [296]. Hence, a thorough assessment of the effect of GHSV can help identify the conditions for the formation of desired products.

2.3.4. Effect of S/C ratio

Steam is a principal reactant in SMR that is recognized to have an impact on the H_2 yield. Therefore, the S/C ratio is considered a key parameter to study in SMR. The S/C ratio in SMR significantly affects the

CH_4 conversion and H_2 yield. The feed mixture in the reactor must contain enough steam (ca. more than the stoichiometric amount) to inhibit coke formation and thermal cracking of hydrocarbons. Coke deposition is a major issue at low S/C ratios (<1.3) due to unwanted reactions; therefore, higher S/C ratios (2.5–4.0) are favorable for higher H_2 yield and CH_4 conversion due to enhanced WGS reaction [203]. On the other hand, high S/C favors higher conversion but requires excess steam production, which has an energy disadvantage [308]. For instance, Radfarnia and Iliuta [304] investigated the effect of S/C ratios in the range of 2.0–5.0 on H_2 yield in a composite containing Ni catalyst and CaO sorbent. It was observed that the H_2 yield was favored by increasing the steam quantity following the thermodynamic analysis. However, for S/C ratios of 4.0 and 5.0, H_2 yield and CH_4 conversion were almost unchanged. Over 900 °C, Laosiripojana and Assabumrungrat [280] investigated the effect of S/C on H_2 yield and coke formation over Ni/Ce–ZrO_2 and Ni/YSZ. The amount of carbonaceous product formation significantly decreased, while H_2 yield and CO_2 fraction increased with an increasing S/C ratio from 3.0 to 5.0 due to enhanced reforming of CH_4 at higher inlet steam concentrations. Recently, the kinetics of various catalysts were investigated in a developed model, and the results were analyzed and validated with the modeling results. As presented in Fig. 22, a comparison between equilibrium and modeling results revealed that higher S/C improved H_2 production by shifting the reforming reaction (R1) in the forward direction, leading to improved CH_4 conversion [309].

Fig. 23 demonstrates the effect of the S/C ratio on various investigations to analyze CH_4 conversion, H_2 yield, and H_2 and CO selectivity. Chen et al. [286] prepared a CaO-based Ni/Al_2O_3 catalyst and varied S/C from 2.0 to 4.0 at 600 °C. The higher S/C ratio led to encouraging performance in the process. CH_4 conversion of more than 90% was attained at an S/C ratio of 4.0, as shown in Fig. 23(a). The result was according to the Le Chatelier's principle, as higher reactant concentrations favored the reforming reaction in the forward direction. Modeling of H_2 production in a packed bed reactor was performed via SESMR. According to the results, a higher steam fraction can improve H_2 purity and yield, as shown in Fig. 23(b), with maximum CH_4 conversion at S/C of 3.0. On further enhancement of S/C to 6.0, increased H_2 purity to 97.5% and a lower CO_2 concentration in the product were noticed with an increased pre-breakthrough period [310]. A similar trend was reported over Ni/Al_2O_3, with an increasing S/C ratio. The CH_4 conversion remained constant, and almost insignificant H_2 selectivity was observed. However, as the S/C ratio increased, CO selectivity decreased due to the extension of the WGS reaction, in which CO is consumed. Even at an S/C of 0.5, the system achieved steady-state, and CH_4 conversions were close to equilibrium [282]. Hoe and Hughes [112] and Zeppieri et al. [152] observed similar trends in the reduction of CO selectivity.

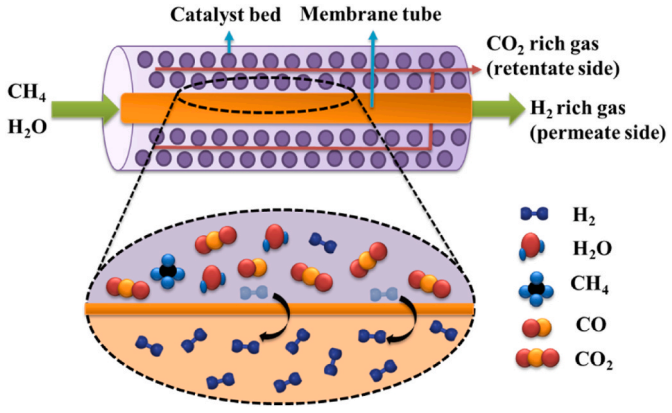

Fig. 25. Schematic diagram of MR for SMR. (Recreated with permission form [325]. Copyright (2020) Elsevier B.V.).

As shown in Fig. 23(c), H_2 yield and CH_4 conversion increased significantly as S/C increased from 3.0 to 12. It was observed that at higher S/C, catalyst deactivation as a result of coking was suppressed, yet the higher steam requirements increased the cost of H_2 production [287]. Fig. 23(d) presents the low S/C effect on Y-doped Rh-substituted zirconates for SMR. On increasing S/C from 0.25 to 1.0, the activity of the catalyst increased and also remained stable at each condition for 3 h each [311].

Thus, it is necessary to investigate the S/C ratio effect as SMR reactions, including WGS reaction, are influenced by the amount of steam entered into the reformer. This is because the S/C ratio has a significant impact on the efficiency of the SMR system owing to the substantial heat required for the conversion of water to steam [312]. However, it is also necessary to consider the reaction temperature while selecting the S/C ratio for a system. Even though higher S/C promotes the CH_4 conversion and H_2 yield, the promotion becomes weaker with an increase in the reaction temperature. Moreover, CO_2 formation is positively related to the steam concentration in the system, and higher S/C promotes CH_4 conversion to CO_2. While CH_4 conversion to CO is not affected by increasing S/C. At higher reaction temperatures, increasing S/C has little effect on the conversion and yield. At lower temperatures (500 °C), the increase in S/C is more beneficial to the conversion of CH_4 to CO_2. As a result, the CO_2 amount increases while the CO amount decreases [313]. Thus, S/C plays a key role in the overall performance of SMR. Higher S/C will result in increased CH_4 conversion, H_2 yield, and lower carbon deposition on the catalyst surface. However, the WGS reaction will be influenced by the quantity of steam entering the reformer because higher energy is required to convert water into steam, which influences the operational cost of the system.

3. Intensified SMR process

Process intensification is considered to be one of the most promising progress paths for SMR due to its being highly endothermic [314]. SMR requires a set of tubes and catalysts placed inside the heating chamber for reforming [44]. The heat supply and the transfer rate to the system play a dominant role in the performance of the reactor. Such a system influences the operational and capital costs of the SMR process, which requires innovative modifications to the process. In recent years, a micro-reactor concept with enhanced integration of an endothermic reforming channel and an exothermic combustion channel has been developed. The simplified structure of a micro-reactor is illustrated in Fig. 24(a) [315]. The three zones of the micro-reactor are as follows: (i) fuel gas is introduced into zone I, where the CH_4 combustion reaction occurs over a Pt catalyst; (ii) zone II contains the catalyst, which acts as the wall medium on both sides; and (iii) conduction occurs from the heat of zone I to zone III, where the SMR reaction occurs on Rh coated channel walls. This concept follows a comprehensive computational fluid dynamics (CFD) model that considers chemistry and physics processes to understand the flow and heat conduction between the two channels. Similarly, a CFD model of the annulus reactor for SMR was developed that considered the effect of the sleeve between the reactor and the combustor on heat transfer [316]. This type of reactor is equipped with a burner in the core for the combustion of the feed gas. The outside annulus area contains the catalyst bed and heat carrier zone, as shown in Fig. 24(b). The SMR reactor with a sleeve presented a flat temperature profile as compared to the top-fired SMR reactor along the length of the reactor. The flatter wall temperature results in a reduced risk of hot-spot formation and is beneficial in terms of fixed and operating costs. A top-fired reactor is a primary reformer with a large number of tubes and burners placed on top to burn feed gas, as shown in Fig. 24 (c) [317].

It is specified for the reactor based on annular and top-heating using burners; the catalyst and flow dynamics are separately discussed. The process efficiency can be enhanced using modified catalysts, but the equilibrium conversion would decrease based on the Le Chatelier's

Table 5
Membrane/catalyst systems for SMR.

Membrane/catalyst system	Process conditions	CH_4 conversion (%)	H_2 permeance/H_2 purity ($mol/m^2/s/Pa^{-0.5}$)/%	Remarks	Ref
Pd–Ag/Ni–Al_2O_3	T = 450 °C S/C = 2 P = 3.0 bar GHSV = 3710 h^{-1}	50	-/70	A noticeable difference in CH_4 conversion with high H_2 purity was seen with the membrane reactor as compared to the conventional reactor. The H_2 in the product was totally CO_2 and CO-free.	[331]
Pd/NiO/YSZ/NiO/PSS	T = 560 °C; GHSV = 1000 h^{-1}	75.1	3.81×10^{-3}/93.1 vol%	Higher H_2 permeance through the membrane was observed than in studies without a Pd membrane. The membrane reactor was efficient for H_2 production.	[333]
Pd–Ru/Ni–Al_2O_3	T = 500 °C; S/C = 3 GHSV = 837 h^{-1}	~77.5	3.46×10^{-3}/-	The Pd–Ru membrane for SMR exhibited moderate selectivity and improved permeability. The membrane revealed a stability test of 100 h under mild processing conditions. Only ~2% CO concentration in the product stream diminished the need for a series of WGS reactors.	[320]
Pd/Al_2O_3	T = 580 °C P = 28 bar; GHSV = 950 h^{-1}	86	-/>80	The Pd-MR working under realistic process conditions for H_2 production yielded high-purity H_2 with a maximum 98% CH_4 conversion and continuous 86% CH_4 conversion for 1100 h, showing great potential for SMR.	[343]
Pd–Au/Ru-PSS	T = 511 °C S/C = 3 GHSV = 185 L/h/kg	94	2.39×10^{-3}/>99.2	Under 500 h, the equilibrium shift for MR improved by 35%. The stable performance of the alloy makes it a potential candidate for SMR.	[334]
Pd–Ag/Ni/$CaAl_2O_4$	T = 500 °C S/C = 3	~50	1.38×10^{-8}/-	No interaction of membrane and catalyst was noticed in the fluidized-bed mode for MR, resulting in constant permeance. The ideal perm-selectivity was reported to decrease at higher temperatures (600 °C).	[344]
Pd–Ag	T = 500 °C S/C = 3	55.5	4×10^{-6}/>99.98%	Stable performance of a thin Pd membrane was observed for 900 h in a bubbling fluidized-bed regime.	[345]
Pd–Au/Ni-based	T = 450 °C; P = 300 kPa GHSV = 2600 h^{-1}	48	1.3×10^{-3}/99.99	The bi-layer metallic membrane exhibited good stability and high H_2 purity at lower temperatures over a longer period of 1000 h. The alloy developed for MR was a good candidate for SMR with no coke formation at low process conditions.	[346]

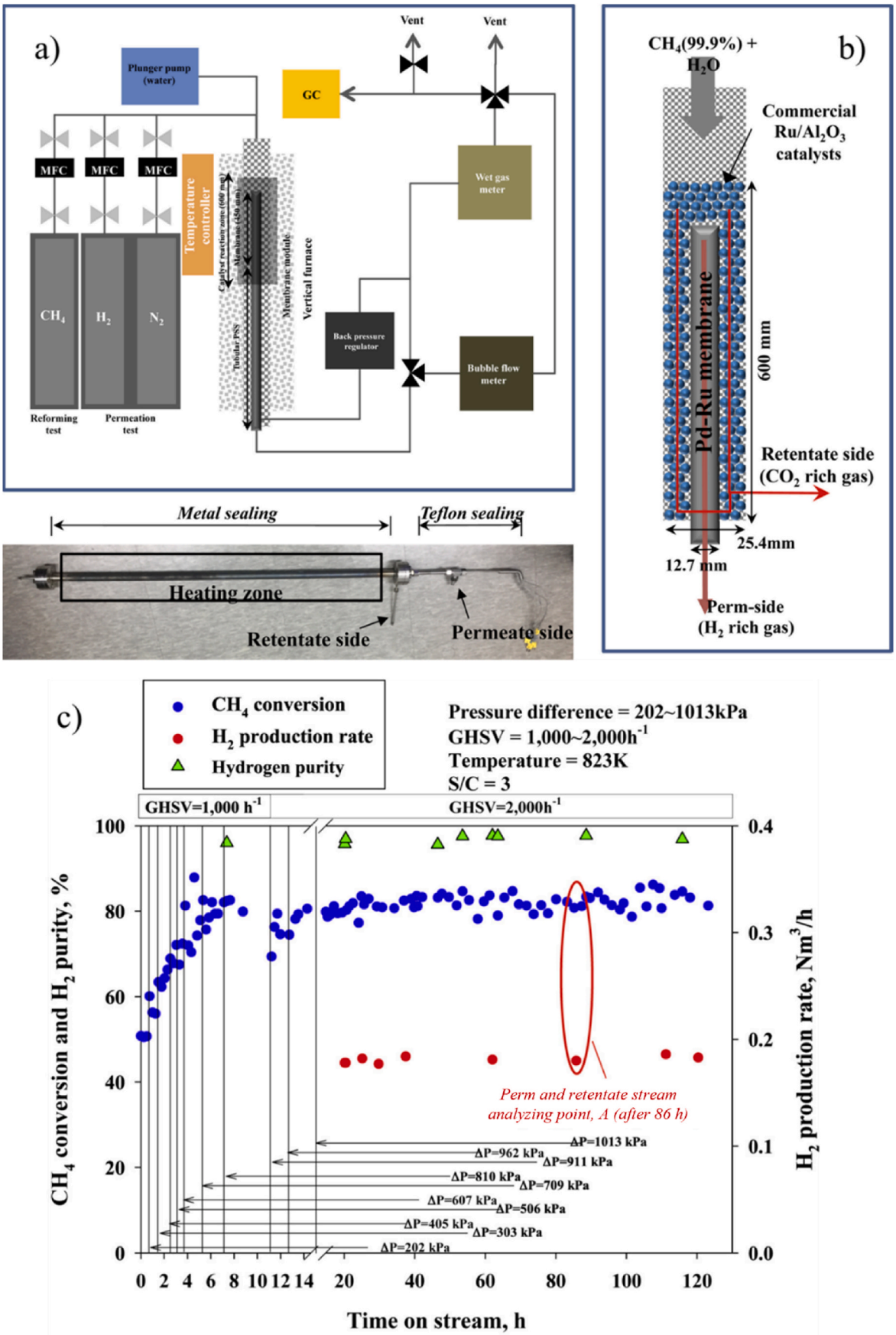

Fig. 26. (a) Schematic of a Pd composite-based membrane SMR setup **(b)** Membrane reactor graphical illustration **(c)** SMR catalytic and stability analysis at various pressure differences for 120 h reaction time. (Reprinted with permission from Ref. [333]. Copyright (2018) Elsevier B.V.).

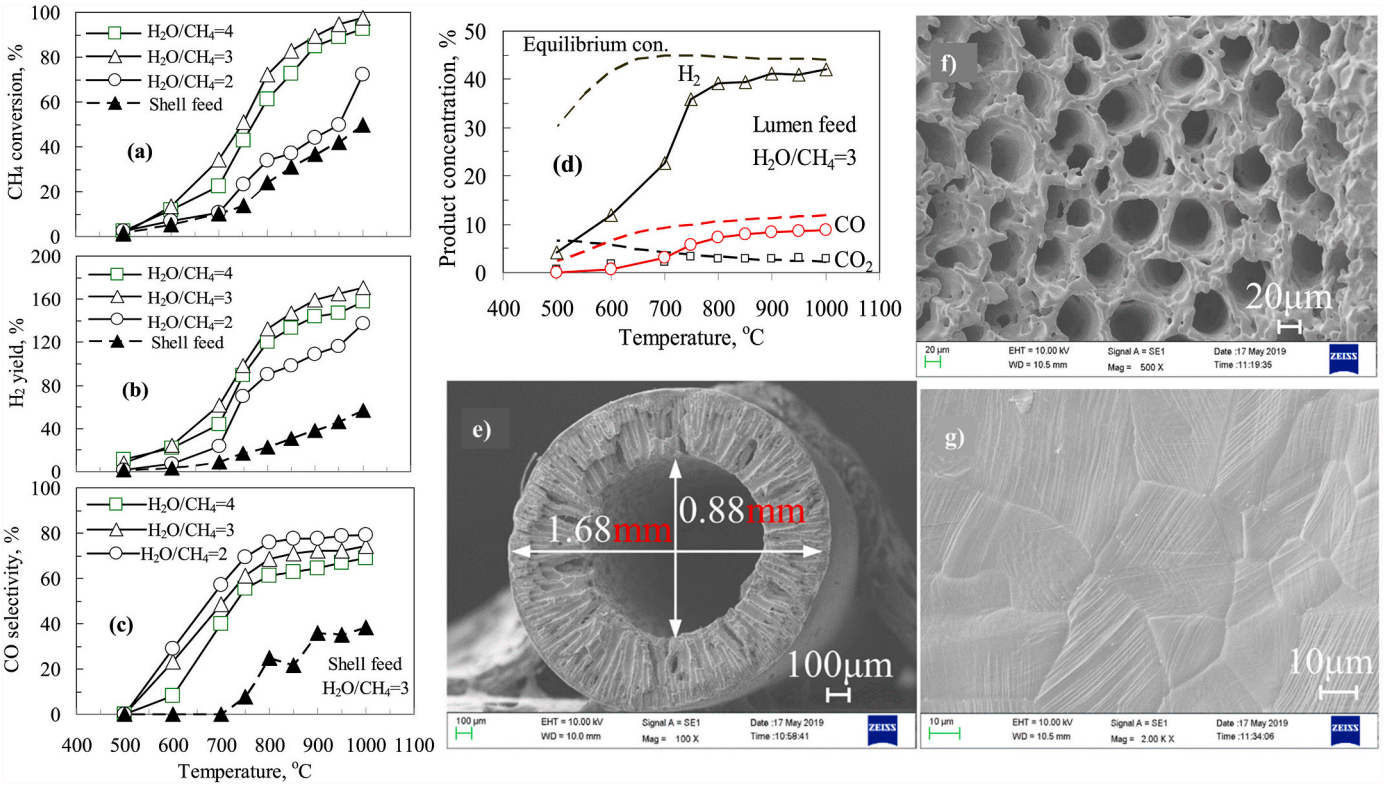

Fig. 27. Catalytic performance of SMR over hollow fiber membrane **(a)** CH_4 conversion, **(b)** H_2 yield, **(c)** CO selectivity, **(d)** gas concentration at S/C = 3, SEM images of Ni-based hollow fiber membranes **(e)** cross-section, **(f)** inner surface, **(g)** outer surface. (Reprinted with permission from Ref. [339]. Copyright (2021) Elsevier B.V.).

principle. Therefore, process intensification is practiced and achieved via coupling various techniques such as in-situ CO_2 removal [274], membrane technology, and chemical looping [318] with SMR. Hence, using the idea of process intensification by using multifunctional reactors coupled with various applications, the thermodynamic limitations as well as heat and mass transfer limitations can be minimized for better performance of SMR reactor systems [319]. The literature-reported effects of using sorption, membrane technology, fluidization, and looping on intensifying the conventional SMR to produce H_2 are presented in the following sections.

3.1. *Effect of membrane technology*

Conventionally, SMR is operated at higher temperatures in a fixed-bed reactor to convert maximum CH_4 into H_2, requiring expensive materials to bear the thermal stress. In addition, coke formation and high energy consumption are critical issues in SMR [44]. Lowering the reaction temperature while keeping the CH_4 conversions high is an attractive path to overcome these issues. In this respect, the employment of MRs is a feasible approach to achieving the aforementioned purpose [320,321]. Using the MRs for SMR allows the H_2 produced to be removed via permeation through the walls of the reactor. This results in shifting the equilibrium conversion to enhanced values in accordance with the Le Chatelier's principle [322]. Using the MRs causes H_2 to be produced at the same reaction rate but with increased purity and conversion as compared to the conventional reactor [323]. As shown in Fig. 25, feed gases flow into the membrane reactor under controlled conditions. The reactor consists of two zones: (i) reaction zone and (ii) the permeate zone. The reaction zone contains a membrane module packed around the catalyst bed, over which the reaction will occur. The product from this zone will come out of the retentate stream. While the permeate zone allows H_2 molecules to be separated from other species via membranes that are highly selective for H_2, the result is a permeate or H_2-rich stream [322]. The main features of MR for SMR must be high selectivity towards H_2, high flux, and stability, and cost is also one of the key parameters [324].

MRs, such as inorganic [325], polymer [259], and metal alloyed [326], are being synthesized because of their thermal, mechanical, and chemical properties for the selective permeation of targeted molecules. Considering the suitability of membranes for SMR, it is important to consider the impact of process conditions on the stability of the membrane, factors causing membrane fouling, and membrane material [259]. Chompupun et al. [322] reported the effect of process parameters in MR on SMR. They proposed that above 700 °C in MR, a maximum CH_4 conversion of up to 100% is possible, whereas above 900 °C in conventional SMR. An increase in the S/C ratio in MR dilutes the concentration of the mixture and reduces the H_2 partial pressure difference between the permeation and the reaction zones. This leads to improved CH_4 conversion, but H_2 recovery is reduced. Therefore, an optimum S/C ratio must be considered. In the SMR process, conversion shows an inverse relationship with the pressure in the reactor. Contrarily, enhanced pressure increases the CH_4 conversion [322].

The performance of membranes in MR has been assessed in terms of thermal stability, H_2 permeability, and perm-selectivity [298]. Pd and its alloys with Ru [327], Cu [328], and Pt [329] are the most widely used materials in MRs due to their high perm-selectivity towards H_2 and ability to run SMR at milder operative conditions than conventional SMR [330–332]. These membranes are highly expensive, thus mostly composite membranes with a Pd layer on porous substrates have been synthesized at low temperatures. Various reports of SMR in MR are summarized in Table 5. SMR was performed at 550 °C in the presence of Pd membranes packed with a Ru/Al_2O_3 catalyst in order to produce H_2 with high conversion. The composite exhibited 82% CH_4 conversion in a 120-h stability test [333]. As suggested by the sources, the addition of active catalysts like Au can help to enhance the performance of MR compared to the conventional process. Pd–Au membranes exhibit

Table 6
Sorbent-catalyst systems for SESMR.

Sorbent	Catalyst/ sorbent composition	Optimum loading	Process conditions	CH_4 conversion (%)	H_2 yield/H_2 purity (%)	Remarks	Ref
CaO-based	Ni/CaO	12.5 wt% Ni/CaO	T (HM1) = 400 °C; S/C = 3 Catalyst loading = 0.8 g	>80	-/80	CaO and HTc were replaced with Al_2O_3 support for the Ni catalyst. A 12.5 wt% Ni loading with CaO resulted in an 80% H_2 concentration. The catalytic activity of Ni/CaO was less than that of Ni/Al_2O_3.	[396]
CaO-based	Ni/HTc (HM1) $Ni–CaO/Al_2O_3$ (HM2)	10 wt% Ni	T (HM1) = 400 °C; S/C = 6 T (HM2) = 550 °C; S/C = 5 GHSV = 3600 ml/g.h Catalyst loading = 3 g	~97 ~95	~88/- ~87/-	Ni/Al_2O_3 showed lower adsorption capacity but high cyclic stability, while Ni–CaO/Al_2O_3 showed higher adsorption capacity but regeneration temperature affected the stability of the catalyst for SESMR. HM1 exhibited stability for 16 cycles and adsorbed 1.1 mol/kg. Conversely, HM2 adsorbed 12.3 mol/kg of CO_2/sorbent and was stable for 11 cycles.	[287]
CaO-based	$Ni_{0.5}/Mg_{2.5}Al$ $CaO–Ca_9Al_6O_{18}$	Ni:Mg:Al = 0.5:2.5:1	T = 600 °C S/C = 4.2 Catalyst loading = 3 g	>95	-/>95	The effects of process conditions on the SESMR were studied. Results revealed that high S/C and low temperature favored high purity but a lower yield of H_2. The sorbent/catalyst ratio had no effect on H_2 purity. However, almost 83% of the initial sorption capacity of the sorbent was retained after 50 consecutive cycles of carbonation/calcination at 650 °C.	[307]
CaO-based	CaO/NiO	18.5 wt% NiO	T = 650 °C; S/C = 3	~91	90.9/93.3	A thermodynamic analysis of CL-SESMR and SESMR was conducted. The analysis revealed significant advantages for SESMR over SMR. Sorbing agents increased the performance of the reformer at lower temperatures. However, on comparison between CL-SESMR and SESMR, it was found that using pure O_2 for regeneration reduced the energy needs by up to 26% for CL-SESMR as compared to SESMR.	[99]
CaO-based	Al-stabilized CaO–NiO	25 wt% NiO	T = 650 °C; S/C = 4	99.1	97.3/-	The synthesized hybrid catalyst was tested for SESMR. The efficient results of the catalyst verified its potential for use in the process. CaO molar conversion at the 25th sorption cycle was 41.2%.	[304]
CaO-based	$CaO–NiO/NiAl_2O_4$	10 wt% NiO	T = 650 °C; S/C = 4	94 vol%	-/96 (vol%)	A CaO-based sorbent and catalyst were prepared and tested for SESMR. A simulation model was executed to evaluate the operating conditions of the process. The system was able to run at lower S/C ratios, although increased CO and CH_4 concentrations were obtained.	[397]
CaO-based	Ni/CaO–Zr	20.5 wt% NiO	650 °C; S/C = 4 Sorbent-catalyst loading = 2 g	~99	~91/-	The synthesized bi-functional sorbent/catalyst for the SESMR process revealed a higher H_2 yield after 10 cycles than the equilibrium yield of H_2 from SMR.	[398]
MgO-based	Ni/MgO	NA	T = 700 °C; S/C = 1.5 F^{in}_{CH4} = 400 NmL/min	86	-/-	A stable and active MgO-based catalyst was prepared by coating a monolithic powder. The catalyst exhibited higher activity due to NiO–MgO formation and presented better results compared to the conventional $Ni–Al_2O_3$.	[399]
Zr-O_3 based	Ni/Na_2ZrO_3	NA	T = 500 °C; S/C = 3; GHSV = 1120 h^{-1}	>95	-/80.79 (mol%)	A CFD model to simulate CH_4 reforming using a sorbent-catalyst system was developed for the sorption-enhanced process in a membrane reactor and compared with a traditional membrane reactor. The results suggested enhanced H_2 production, yield, and CH_4 conversion.	[400]

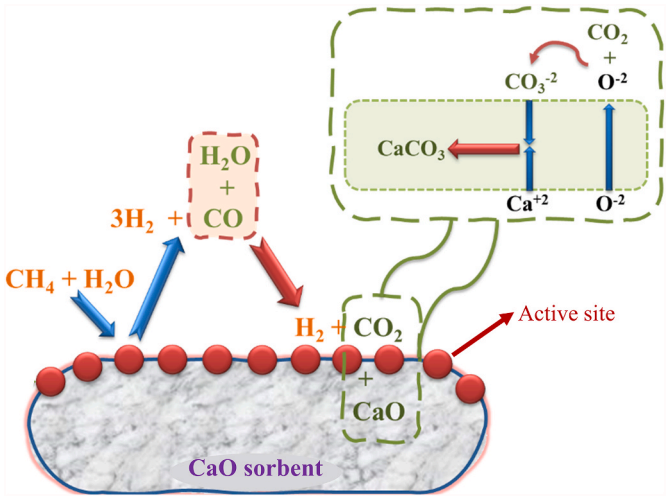

Fig. 28. Mechanism of CaO-based catalyst for SESMR ($CaCO_3$ deposition on the catalyst surface on reaction of CO_2 released with CaO particle. (Reprinted with permission from Ref. [368]. Copyright (2015) Elsevier B.V.).

increased tolerance to carbon deposition and are easier to exploit over a wide temperature range compared to pure Pd [334]. Similarly, the Pd-membrane with Ru/Al_2O_3 was decorated on NiO/YSZ/NiO-layered treated stainless steel. The SMR at 610 °C yielded 75.1% CH_4 conversion with 93.1 (vol%) H_2 in permeate stream [335]. Much higher CH_4 conversions at lower temperatures were observed for MR as compared to conventional SMR. A Pd–Ag membrane was tested for SMR at 450 °C over a Ni catalyst. A 50% CH_4 conversion was yielded in a membrane reactor, while only a 6% CH_4 conversion was achieved in a fixed-bed reactor at the same reaction conditions. Furthermore, a comparison of CO selectivity for both reactors as a function of temperature and pressure revealed lower selectivity in MR with respect to fixed-bed at specific conditions, probably due to the shift of WGS reaction (R2) [331]. Extremely low concentrations of CO in the gas composition of MR have been observed in the studies. That means enhancement of WGS due to selective removal of H_2 via membrane [320]. For this reason, two specific columns of CO selectivity and H_2/CO have been excluded in Table 5. The CH_4 conversion and H_2 yield are targeted as the most important outcomes of SMR. It is noticed that the Pd-based membrane is due to its capacity to remove H_2 from the products. For instance, Kim et al. [333] utilized a gas permeation and SMR test system that contained a membrane module, furnace, temperature controller, pressure controller, digital soap-bubble flow meter, and wet gas meter. The system included a metal ferrule and a Teflon ferrule for sealing the permeate side of the membrane reactor. A bubble leakage test was conducted before the SMR test to ensure gas tightness (Fig. 26(a)). The SMR test was conducted at 823 K, and a commercial Ru/Al_2O_3 catalyst was packed between the membrane module and the Pd-based composite membrane Fig. 26(b). The GHSV was increased from 1000 to 2000 h^{-1}, and the steam-to-carbon ratio was set at 3 for the overall SMR test. A stability test was conducted for around 120 h at a GHSV of 2000 h^{-1} and a pressure difference of 1013 kPa to obtain an efficient methane conversion under rough operating conditions. The hydrogen recovery, production rate, and compositions of the gas streams were periodically measured during the stability test. The gas compositions were analyzed using a gas chromatograph equipped with a thermal conductivity detector.

As shown in Fig. 26(c), the stability of SMR was tested at different pressure differences and GHSVs at 823 K for about 120 h. Methane conversion and hydrogen production rate were measured periodically during the stability test. Results showed that CH_4 conversion and H_2 production rate were approximately 82% and 0.18 $Nm^3\ h^{-1}$, respectively, at a pressure difference of 1013 kPa and a GHSV of 2000 h^{-1}. The

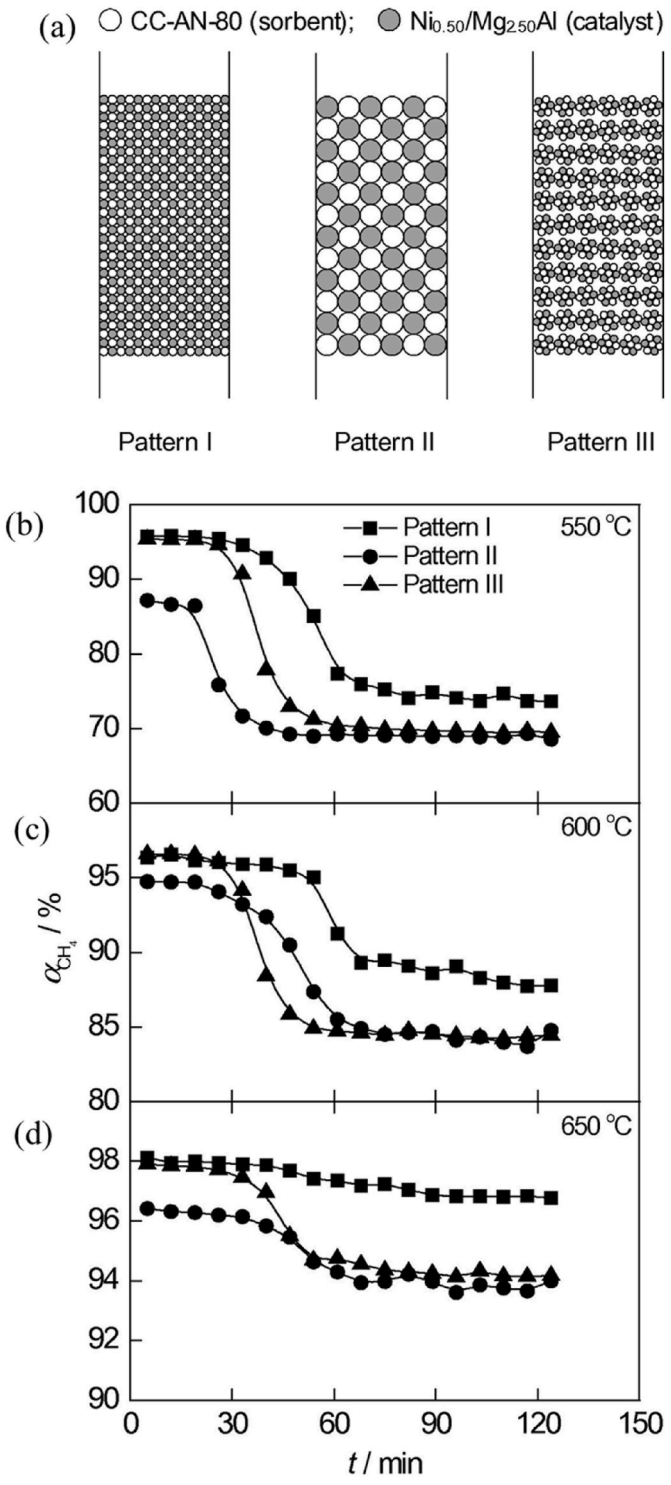

Fig. 29. (a) Different employment patterns of catalyst and sorbent **(b–d)** effect of catalyst and sorbent loading patterns on CH_4 conversion at various temperatures. $Ni_{0.50}/Mg_{2.50}Al$ (1 g), CC-AN-80 (3 g), 1 atm, H_2O/CH_4 (molar ratio) = 4.2, FCH4, in = 14.7 ml/min (Reprinted with permission from Ref. [307]. Copyright (2012) Elsevier B.V.).

H_2 recovery and purity remained at around 92.4% and 97%, respectively, during the stability test.

The membrane configuration can be developed in various shapes and geometries, i.e., planar and tubular, which include hollow-fibers, spiral wound, and frame. The most commonly used membranes are tubular in shape, which offers a high active surface area to the total volume [324].

The two main concepts of unsupported and supported membranes are widely practiced in H_2 permeance. The supported membranes are composed of a selective film deposited on the porous support, which is usually metallic or ceramic. Due to the high purity of H_2, dense metal membranes are more common. More details about the commercial membranes and their performance are reported by Gallucci et al. [324]. Based on the material size, the microporous membranes consisting of zeolite membranes, Metal organic framework (MOF) membranes, silica membranes, and carbon membranes are being utilized for H_2 purity in SMR [336,337]. The dense ceramic membranes were also used for H_2 purity in SMR due to their proton transport mechanism. The operating temperature is generally >900 °C. The dense membranes consist of perovskite-based materials, but this type of utilization is very limited in SMR [338].

Recently, H_2 production has also been carried out using hollow fiber membranes consisting of a dense layer on a porous Ni substrate [339]. The porous surface played the role of catalyst, while the external skin layer worked as a membrane for SMR reaction, yielding high stability in product (reformate) gases with enhanced resistance to carbon deposition at >800 °C. At 1000 °C and GHSV = 25,937 h^{-1}, the CH_4 conversion was 98.58% and H_2 production rate was 50.84 mmol $m^{-2}s^{-1}$. Fig. 27 (a-d) shows the performance results as a function of temperature, where a noticeable increase in CH_4 conversion and H_2 yield can be seen above 500 °C due to the favorable endothermic SMR reaction at higher temperatures. An increase in S/C from 2.0 to 3.0 enhanced the CH_4 conversion and H_2 yield, but further enhancement of S/C to 4.0 caused a reduction in performance, suggesting that SMR on Ni-based membranes followed an adsorption mechanism. Similarly, CO selectivity increased from 500 to 800 °C with an insignificant change above 1000 °C, as shown in Fig. 27(d). The H_2 concentration in the product gas rose with temperature and became constant above 800 °C because of the thermodynamic equilibrium at such temperatures. Fig. 27(e-g) presents the SEM images of the hollow fiber membrane prepared for H_2 permeation. The outside diameter of the membrane was 1.68 mm, with a porous substrate of finger-like pores. A smooth surface with grain boundaries between Ni particles was seen on the outer surface [339].

A novel concept of CO_2 perm-selective MR allows CO_2 along with the promoted H_2. Such a type of MR is made of a dual-phase ceramic carbonate membrane. Due to the in-situ CO_2 removal, the concentration of H_2 in the retentate can be significantly enhanced in a single-stage MR. This method will lead to a reduced reactor footprint with no extra requirement for the WGS unit [340,341].

Various kinetic models have been developed to understand the kinetics and performance of MR using CFD [87,322]. A study developed a global kinetic model and introduced source and sink formulations for the H_2 permeation through the membrane. The developed model efficiently captured the trends observed experimentally and suggested an optimum temperature range of 400–700 °C to achieve a good balance between reaction performance and permeation through the membrane [342]. Various kinetic models have already been discussed in the previous section regarding MRs for SMR.

In conclusion, the recent advancements in MR technology give benefits to membrane technology in the SMR process, including enhanced heat and mass transfer, separation in one stage, and higher selectivity for H_2. The potential of the already established technology of the membranes is already in the market. Nevertheless, there are still many challenges from an industrial point of view, such as the stability of time on stream and the cost of membranes. Moreover, microporous and carbon membranes need more attention to make them commercially viable in SMR for H_2 production.

3.2. Effect of sorption

For the past few years, the focus on H_2 production has shifted towards the technologies that support the reduction of GHG emissions, i.e., to turn the H_2 from gray to blue [347,348]. Yet fossil fuels as a feedstock for H_2 will remain for the foreseeable future. Various investigations have reported advanced technologies in the process that use modified catalysts to overcome the limitations of SMR [39,349,350]. One way is to remove either CO_2 or H_2 continuously, thereby shifting the thermodynamic equilibrium towards H_2 production. As shown in the previous studies, there is a possibility to replace the complex multistep reactions with a single-step reaction that utilizes a mixed bed of catalyst matrix and solid sorbent operating in an intermediate temperature range [351]. The process, known as SESMR, is an intensification of reactions (R1) and (R2) via a high-temperature solid-sorbent, hence, coupling the

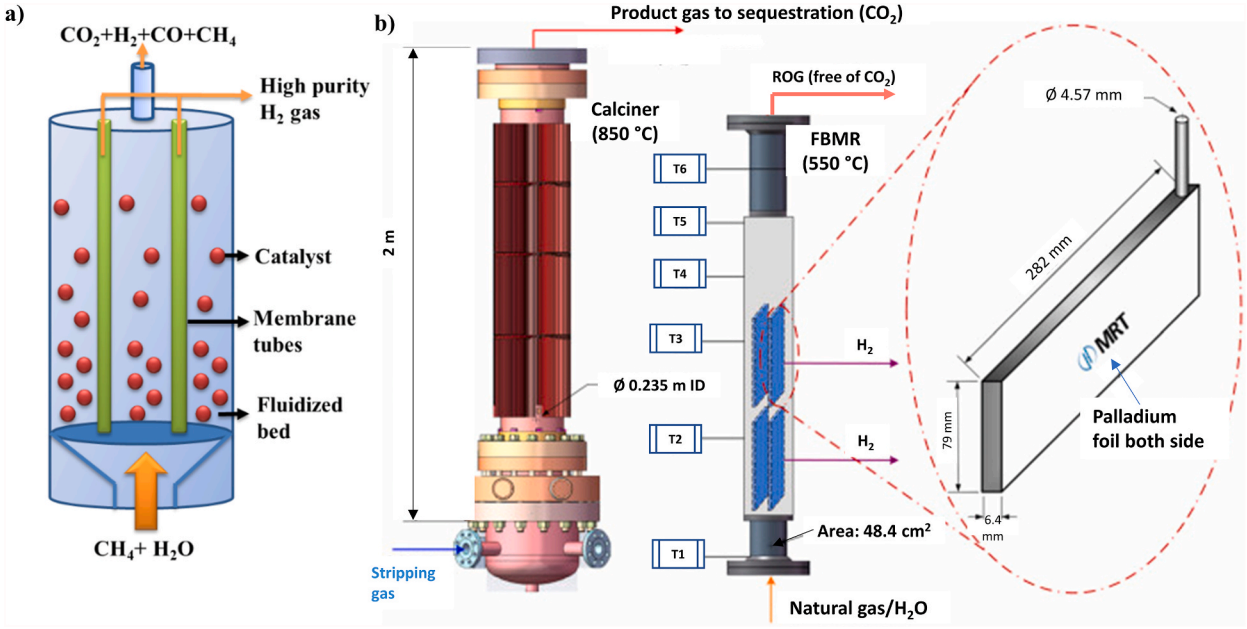

Fig. 30. (a) Schematic diagram of a membrane-assisted fluidized-bed reactor for SMR. (Reprinted with permission from Ref. [403]. Copyright (2021) Taylor & Francis.); **(b)** Fluidized-bed membrane reactor (FBMR) and calciner configurations with special emphasis on palladium membrane dimensions; ROG: reactor off-gas. (Reprinted with permission from Ref. [409]. Copyright (2011) Elsevier B.V.).

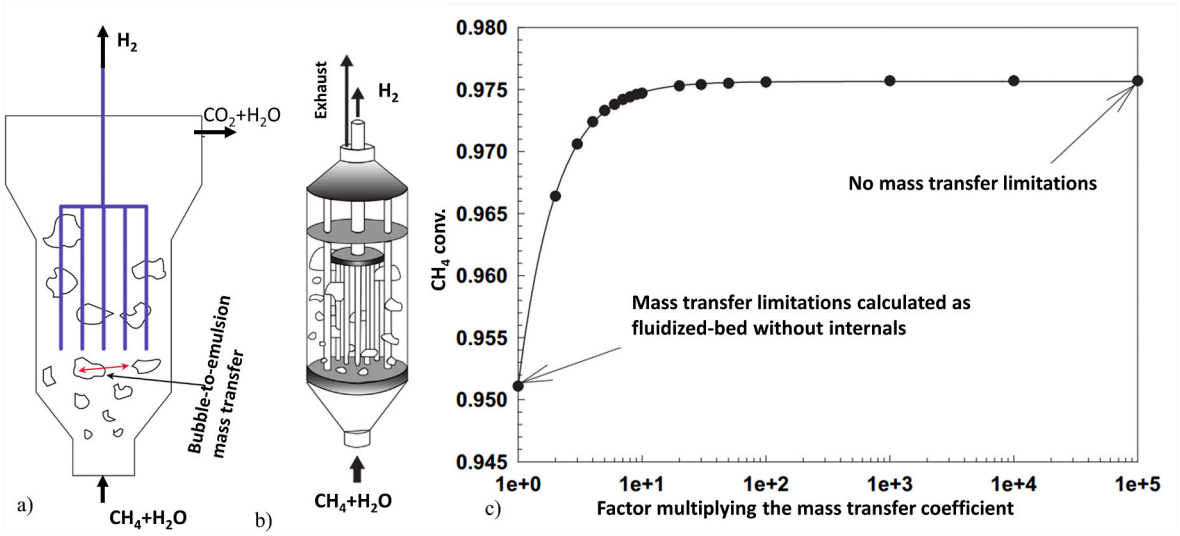

Fig. 31. (a) Bubbling regime in fluidized-bed reactor; **(b)** concept of membrane reactor with increasing bubble size; **(c)** impact of mass transfer limitations of bubble-to-emulsion regime on CH_4 conversion in fluidized-bed reactor. (Recreated with permission from Ref. [411]. Copyright (2010) Elsevier B.V.).

commercial SMR with in-situ CO_2 capture [352,353]. Using this technique, the equilibrium of the reforming reaction is shifted towards H_2 production from 80% to 95%, based on Le Chatelier's principle [354]. The concept behind the SESMR process is centered around the utilization of a reforming catalyst and a solid regenerable sorbent to capture in-situ CO_2 from the reaction zone [65].

The enhanced sorption process allows for lower reaction temperatures and reduces the coking and sintering of the catalyst. In addition, the heat needed for the endothermic reforming reactions is provided by the heat released from the exothermic carbonation reaction. Hence, approximately 15%–20% of CO_2 in the outlet gases can be captured from SMR. The yield of H_2 produced is dependent on the properties of the reforming catalyst and the sorbing agent used for CO_2 capture, leading to a higher product yield of H_2 [355,356].

However, the process requires a sorbent regeneration stage to reuse the sorbent once it becomes saturated with CO_2. After saturation, the sorbent can be regenerated at higher temperature conditions that depend on the partial pressure of CO_2, producing pure CO_2 and being ready for storage as chemical feedstock [357]. The reaction temperature and pressure in SESMR are much lower than in conventional SMR, at 400–600 °C and 0.1–0.3 MPa, respectively. The lower operating temperatures suggest the need for a very active reforming catalyst [162]. SESMR is favored at reduced pressures owing to the increase in the number of gas moles in the overall reaction involving reforming and carbonation. A GHSV lower than required for SMR is preferable because of the rate-limiting effect of the carbonation reaction [294]. Accordingly, the process has been investigated in various configurations, including fluidized-bed and fixed-bed under atmospheric or high pressure [307,358–364]. Extensive studies on low-cost H_2 production systems have been carried out, including SESMR [365–367].

The reactor system consists of a reforming catalyst and sorbent that remove CO_2 as soon as it is produced through reforming and WGS. Indeed, the CaO carbonation shifts the equilibrium of the WGS [368]. An ideal CO_2 sorbent should have high cyclic stability, adequate adsorption characteristics, satisfactory adsorption/desorption kinetics, and high mechanical strength. In recent years, numerous sorbents have been studied, e.g., mixed oxides such as magnesium oxide [369,370] and calcium oxide [371], HTc-based materials [372,373], lithium orthosilicate (LOS) [374,375], and multifunctional sorbent-catalyst materials [363,376]. Table 6 presents different sorbent-catalyst systems for the SESMR process, with CH_4 conversion and H_2 yield in the pre-breakthrough times where the sorbent is highly active. However, CO selectivity and H_2/CO ratio have not been reported for the SESMR, as an extremely low concentration of CO in the product gas is exhibited due to the sorptive removal of CO_2 [377]. Among these, CaO-based sorbents have a strong chemical interaction with CO_2 to form $CaCO_3$ (R6), resulting in the highest adsorption capacity, fast calcination/carbonation cycles, and adequate reversibility [378–380]. Fig. 28 illustrates the mechanism of CaO-based sorbents and catalysts for SESMR. The CaO particle helps to react with the CO_2 produced during the reforming reaction over an active metal site, depositing $CaCO_3$ on the surface of the catalyst.

$$CaO + CO_2 \leftrightarrow CaCO_3[(\Delta H_{298}) = -178\ kJ/mol] \quad \text{(R6)}$$

However, the major drawbacks of CaO sorbents are the decay in the adsorption capacity throughout the multicycle operation and low conversions due to the formation of the $CaCO_3$ layer that covers and fills the pores of CaO, thus hindering the CO_2 diffusion to the reaction interface [381]. For this reason, attention has been paid to modifying CaO-based sorbents either by changing the calcium precursors, steam reactivation, modification of pore structure, or by incorporating a variety of metal oxides such as ZrO_2, MgO, Al_2O_3, and La_2O_3 into the CaO system [382–385]. This group of synthetic CaO-based modified sorbents has shown a decrease in sintering phenomena because the metal oxides may behave as spacers between the CaO particles, protecting them from the accumulation of sintered grains during multiple cycles. As a result of this phenomenon, a noticeable improvement in active surface area and mechanical and thermal stability may be observed [386].

The effect of CaO dispersion on a highly porous γ-Al_2O_3 was studied to compare the stability and kinetics of bulk CaO as a sorbent. The synthesized catalyst/sorbent was tested at 650 °C for 84 cycles and demonstrated long-term stability when compared to bulk CaO as a sorbent. This sorbent was a candidate for SESMR with a CO_2 uptake efficiency of up to 15% [387]. The improvement in sorption (CaO-based $CaTiO_3$ coated adsorbents) of CO_2 during the SMR was analyzed. Due to the $CaTiO_3$ coating, a sorption capacity of up to 5.3 mol/kg was observed after 40 cycles of carbonation/calcination reaction, whereas a capacity of up to 3.7 mol/kg was observed without coating [388]. CO_2 sorbents derived from Al and Ca precursors are expected to be applied in the SESMR process. Among various precursors, CaO–$Ca_9Al_6O_{18}$ with 80 wt% CaO content showed the best performance for sorption and stability over multiple cycles [389]. Similarly, a bi-functional catalyst from the HTc precursor containing calcium as a sorbent and Ni as a reforming catalyst was also developed. The CO_2 sorption capacity observed over 10 cycles was 0.074 g CO_2/g sorbent and stabilized over 7 cycles with a 0.3% average decay rate per cycle. The material with Ca developed a

larger quantity of high-purity H_2 than with Ni–SiO_2 [390].

HTc promotes CO_2 capture sorbents known as layered double hydroxides (LDH) from the anionic clay family, with the general chemical formula $[M^{II}_{1-x}M^{III}_{x}(OH)_2]^{x+}[A^{n-}_{x/n}.yH_2O]^{x-}$, where A^{n-} represents n-valent anions, M^{II} and M^{III} are the divalent cations (e.g., Mg^{+2}, Cu^{+2}, Mn^{+2}, Zn^{+2}) and trivalent metal cations (e.g., Fe^{+3}, Co^{+3}, Al^{+3}, Cr^{+3}). For example, it consists of layers of Al and Mg with exchangeable interlayers of carbonate ions and H_2O molecules. The layers have a brucite-type structure, i.e., $Mg(OH)_2$, in which Mg accelerates CO_2 selective adsorption. The cations Mg^{+2} are octahedrally linked with OH^- and arranged in sheets held together by H-bonds. The Mg^{+2} cations in this structure are partially replaced by Al^{+3}, resulting in a positive charge that is compensated due to the presence of CO_3^{-2} ions that can exist in conjunction with H_2O molecules between two brucite-type sheets [391]. Calcination of such LDH gives a homogenous mixture of M^{II} and M^{III} oxides that are finely dispersed and associated with high thermal stability and surface area. HTc-based catalysts have shown promising results owing to the uniform dispersion of active metal on the catalyst surface, large surface area, and memory effect, which enables HTc to return to its original form after contact with an aqueous solution. Lately, Ni-loaded calcined HTs have been promising for the catalytic reforming of different hydrocarbons [392,393].

HTc has an acceptable CO_2 capture capacity of 0.45–1 mol/kg at elevated temperatures of 400–450 °C. Dewoolkar et al. [287] produced 98.5% H_2-rich gas from Ni-based HTc for SESMR. Prepared HTc adsorbed almost 1.1 mol CO_2/kg of sorbent and showed stability up to 16 cycles. Similarly, cerium promoted HTc for SESMR, improved H_2 production, and offered strong basic sites for the adsorption of CO_2. Adsorption capacity up to 12.3 mol/kg sorbent was observed with stability up to 11 cycles [372].

Based on the diameter of the catalyst particle, there are three major approaches to introducing catalyst and sorbent, as shown in Fig. 29(a) [307]. Pattern I depicts the small particle size catalyst and sorbent with a diameter of 0.16 mm, premixed uniformly and pelletized by applying 20

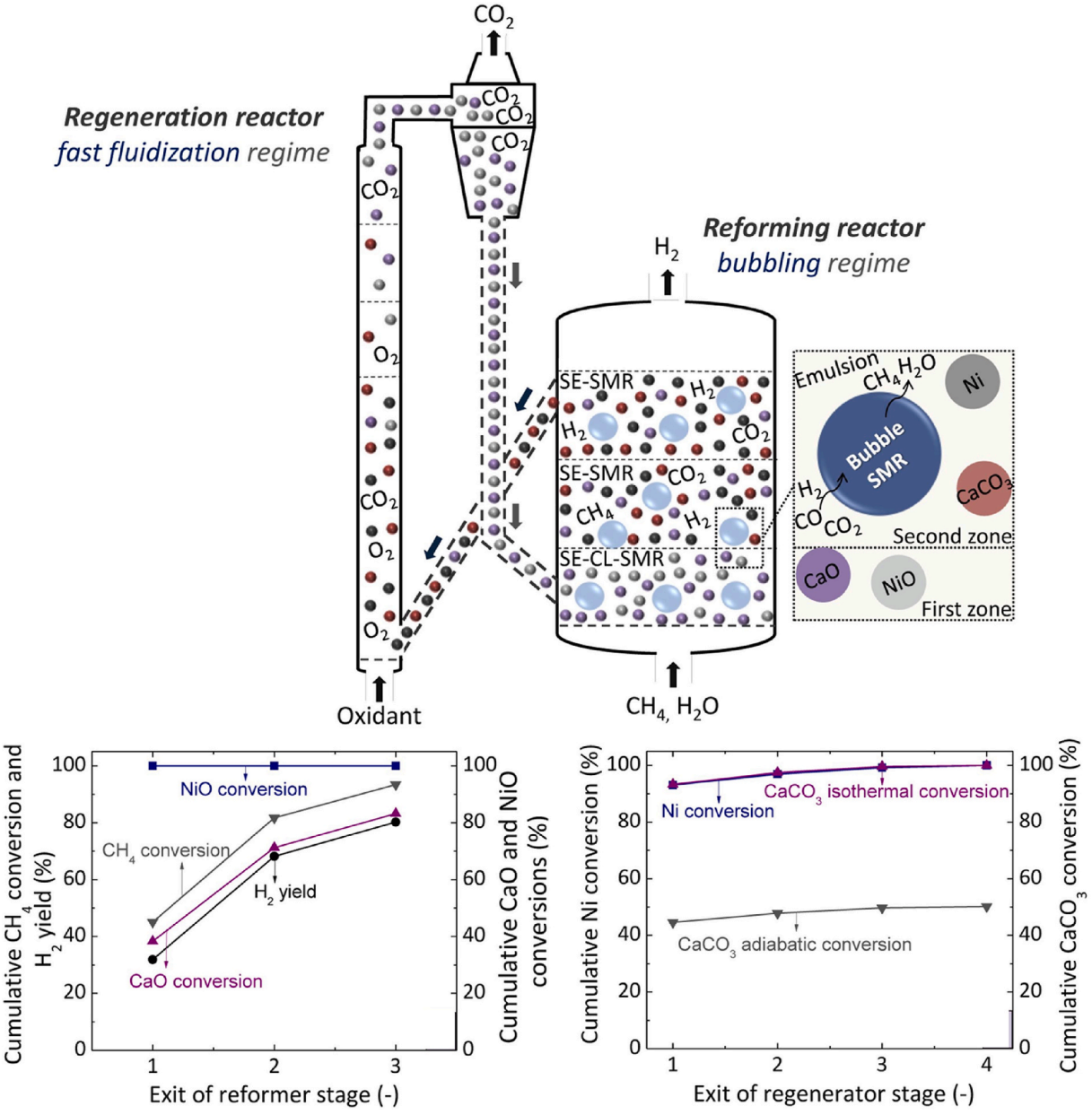

Fig. 32. Dual fluidized-bed reactor scheme, conversion and H_2 yield at the exit of reformer and regenerator. (Reprinted with permission from Ref. [416]. Copyright (2020) Elsevier B.V.).

MPa pressure into cylindrical pellets. Patterns II and III have relatively larger particle diameters of 1.42 mm. The particle size of the catalyst and sorbent is important because it is closely related to the internal diffusion limitations, and the applied patterns can present a comparative analysis. The performance analysis of these applied patterns for various temperature ranges is shown in Fig. 29(b-d). The integration of catalyst and sorbent into one particle (pattern III), namely the combined catalyst, can improve the mass transfer of CO_2 between catalyst and sorbent compared to pattern II, because in pattern III the CO_2 formed over the catalyst can be directly captured by the sorbent in the same particle, while in pattern II the CO_2 has to diffuse from the catalyst particle to the bulk phase first and then into the sorbent particle [307].

The sorbent and catalyst interactions play a key role in the mass transfer limitations and post-breakthrough period of SESMR. The interaction between catalyst and sorbent is always complex, so the kinetics of the SESMR focus on adsorption-desorption under transient conditions. CO_2-sorbent surface interactions with diffusion limitations via carbonate formation. Various kinetic models were presented for SESMR and thoroughly presented in the literature [356]. The time-dependent models are being employed due to CO_2-capturing behavior and diffusion limitations. The reforming and WGS reactions were modeled using classical Langmuir-Hinshelwood equations [250]. However, the set of operating conditions may influence the equilibrium limitations. During the design phase of the reactor, the length of the reactor, gas velocity, and interaction between catalyst/sorbent, and reactants must be carefully selected to achieve the maximum performance with the least pressure drop. Consequently, the reactor can be modeled and validated via theoretical approaches.

CFD played a significant role in understanding the fluidized-bed reactor systems in SESMR. SESMR kinetics have been studied in a fluidized bed using CFD [394]. CFD simulations can help with the kinetics of SESMR with a fluidized-bed especially in the case of a modified configuration of the reactor, as in the work of Herce et al. [395]. This study investigated the feasibility of SESMR for higher H_2 production in a riser reactor and upsized a bubbling reactor from a laboratory to a larger scale. Similarly, simulations for a pilot-scale riser were developed for SESMR in a circulating fluidized-bed reactor and suggested a riser height of 7.0 m to give the distribution of solids without the segregation of catalyst and sorbent [394]. The effects of fluidization on SMR and SESMR are discussed in detail in a separate section.

Based on the available studies related to the CO_2 sorbents in the SESMR process, blue H_2 can potentially be obtained in a single step. The required reaction temperature range is between 450 °C and 650 °C; the stability and mass ratio between sorbent and catalyst, and the regeneration of catalyst and sorbent (cyclic tendency) are key components in SE+SMR, along with the low-cost synthesis of catalyst and sorbent with

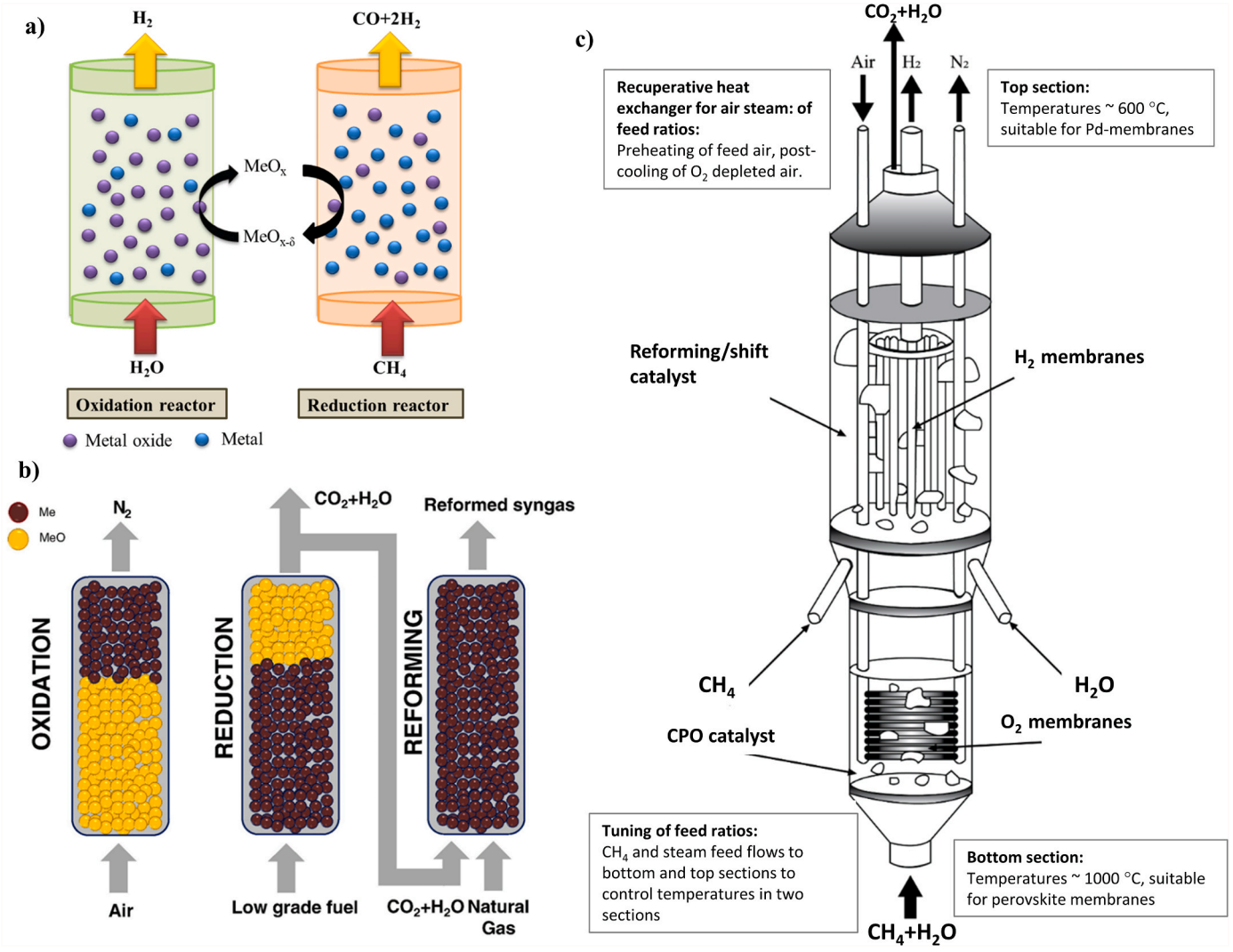

Fig. 33. Schematic illustration of **(a)** CL-SMR. (Recreated with permission form [410]. Copyright (2012) Elsevier B.V.); **(b)** schematic illustration of chemical looping reforming in fixed bed reactor. (Reprinted with permission from Ref. [428]. Copyright (2017) Elsevier B.V.); **(c)** the novel bi-membrane fluidized-bed reactor for producing pure H_2 and CO_2. CPO: catalytic partial oxidation, (Recreated with permission form [321]. Copyright (2006) Elsevier B.V.).

Table 7
Summary of OCs for CL-SMR

Oxygen carriers	Process conditions	Reactor type	Number of redox cycles	CH_4 conversion (%)	H_2 yield	CO selectivity (%)	H_2/CO	Remarks	Ref
$Mg_{0.1}(Cu_{0.3}Ni_{0.3}Mn_{0.4})_{0.9}$ Fe_2O_4	T = 650 °C; S/C = 2.5	Fixed-bed	24	99.4	84.4%	–	5.9	Metal oxides combined for OC yielded spinel structures. High stability and the lowest coke formation were observed during 24 redox cycles.	[433]
La–Mn–Fe–O	T = 850 °C OC loading = 1.8 g	Fixed-bed	9	–	–	–	2.0	Four samples of OC exhibited high syngas production and CH_4 conversion, while two samples showed ideal values. $La_{0.85}MnFe_{0.15}O_3$ presented enhanced structural stability and excellent activity during the redox cycles.	[435]
$LaMn_{0.5}Fe_{0.5}O_3$	T = 850 °C	Fixed-bed	5	87.5	–	–	~2.0	Variable substitutions of Mn yielded varying results for CL-SMR. Less coke formation was observed in $LaMn_{0.5}Fe_{0.3}O_3$ and $LaMn_{0.3}Fe_{0.7}O_3$, while $LaMn_{0.7}Fe_{0.3}O_3$ was not found suitable for CL-SMR owing to reduced H_2 generation capacity.	[233]
CeO_2–Fe_2O_3	T = 875 °C OC loading = 4 g	Fixed-bed	16	52.49	5.99 mmol/g	~100	~2.0	Fe@Ce provided selective oxygen from CeO_2 that facilitated oxygen ion transport. Enhanced CO selectivity, syngas production, and high-purity H_2 were all exhibited.	[429]
Ce–Fe–Zr–O–MgO	T = 800 °C OC loading = 2 g	Fixed-bed	50	63.2	1.14 mol/kg	>90	2.0	Monolithic OC exhibited high stability and enhanced activity for water splitting and CH_4 oxidation. Resistance to coke formation was observed using honeycomb support, which prolonged the running cycle of the process.	[70]
$Fe_2O_3/MgAl_2O_4$ Fe_2O_3/ZrO_2 Fe_2O_3/YSZ Fe_2O_3/Al_2O_3 Fe_2O_3/SiO_2	T = 900 °C OC loading = 12 g	Fluidized-bed	10	–	~1.1/L ~0.8/L ~0.75/L ~0.5/L ~0.2/L	–	–	Various supports with Fe_2O_3 were tested to observe the effect on H_2 yield. 99.5% H_2 purity is exhibited by Fe_2O_3 on $MgAl_2O_4$, YSZ, or ZrO_2. However, 98.8% and 99.3% H_2 purity were seen for SiO_2 and Al_2O_3 on Fe_2O_3. The Fe_2O_3/supports exhibited H_2 yield in the following order: $MgAl_2O_4$>ZrO_2>YSZ > Al_2O_3>SiO_2.	[458]
NiO/CaO	T = 650 °C	Fluidized-bed	–	98.1	–	–	2.13	An internal circulation reactor configuration was proposed for the CL process. Enhanced CH_4 conversion to syngas was observed with 93.0% syngas purity.	[459]
Fe_2O_3/Al_2O_3	T = 900 °C OC loading = 20 mg	Fluidized-bed	10	–	~0.25 mol	–	–	Fe_2O_3 on Al_2O_3 was more reactive than TiO_2. Deeper Fe_2O_3 reduction and higher H_2 production (97%) were observed at temperatures ranging from 600 to 900 °C, whereas suppression of carbon deposition during the reduction period was observed at higher temperatures. The highest H_2 yield was observed for Fe60Al40, with few differences in yields for Fe90Al10.	[460]

the highest sorbent capacity [145]. A configuration such as a fixed-bed reactor system has been considered by various groups, but due to mass transfer and diffusion limitations, a fluidized-bed configuration with solid recirculation is a more important and practicable approach. Even though the concept is not novel, extensive studies are still needed to develop highly efficient hybrid systems with stable cyclic operation to reach commercial scale.

3.3. Effect of fluidization

Conventionally, fixed-bed reactors are used for SMR. But, considering the drawbacks of fixed-bed reactors, including hotspot formation in the reactor due to higher temperatures, pressure drop, and lower efficiency, fluidized-bed reactors are an alternate configuration for SMR [319]. These reactors have advantages over conventional reactors, including: (i) fewer temperature gradients, hence cheaper reactor material for the reformer; (ii) despite the fast solid mixing of feed and solids in the fluidized bed, temperatures can easily be controlled; (iii) extremely high solid-gas contact happens in these reactors, allowing an impressive usage of catalysts [401,402]. Fig. 30(a) [403] depicts a general schematic diagram of a membrane-assisted fluidized-bed reactor. Various experimental and theoretical studies have been performed using fluidized-bed reactors for SMR coupled with SESMR or MR [342,404,405]. Fluidized-bed is preferable for H_2 production, as this approach is used where there is a need for a catalyst to be regenerated continuously owing to its higher capability for solid handling and facilitating heat and mass transfer [406].

As shown, CO_2 sorption is regarded as an efficient enhanced-reforming approach for blue H_2 production. On one hand, the gas product CO_2 is removed to improve the purity of hydrogen . On the other hand, additional heat can be provided for the reforming reaction owing to the exothermic CO_2 sorption reaction [407]. Thus, the integrated technology of H_2 membrane permeation and CO_2 in-situ sorption as well as its application in the catalytic reforming process has attracted researchers' interests [408]. Andrés et al. [409] investigated the effect of H_2 permeation through a perm-selective Pd membrane and CO_2 sorption through limestone sorbent on SMR performance in a pilot-scale fluidized-bed reactor, as shown in Fig. 30(b). They showed that removing the CO_2 in-situ causes a shift in the thermodynamic equilibrium to boost blue H_2 production.

A fluidized-bed reactor operates in a bubbling regime or fast fluidization. Concerning the feasibility of these reactors, process conditions can be assured by means of requirements for the circulation rate of solids, solid regeneration, and solid particle makeup, which are applicable in reforming technologies [405,410]. The SMR in a bubbling-regime fluidized-bed reactor is depicted in Fig. 31(a). The H_2 recovery through the membrane shifts both reforming and WGS reactions towards higher CH_4 conversion and H_2 yield as compared to conventional SMR. A pressure difference is applied between the reaction and permeation sides to enhance H_2 permeation. The application of membrane inside the reactor reduces the bubble diameter, reduces the chances of back mixing, and increases the bubble-to-emulsion mass transfer. One of the concerning factors that affect the reactor's performance is the limitation of mass transfer between the emulsion phase and bubble phase [411]. As shown in Fig. 31(b), increasing the bubble diameter, which is itself increased by the reactor length, increases the mass transfer limitation. The increase in bubble size results in a reduction in CH_4 conversion. According to Fig. 31(c), the CH_4 conversion decreases as the mass transfer limitations increase. It also shows that enhancing the mass transfer by a factor of 10 gives a conversion that is

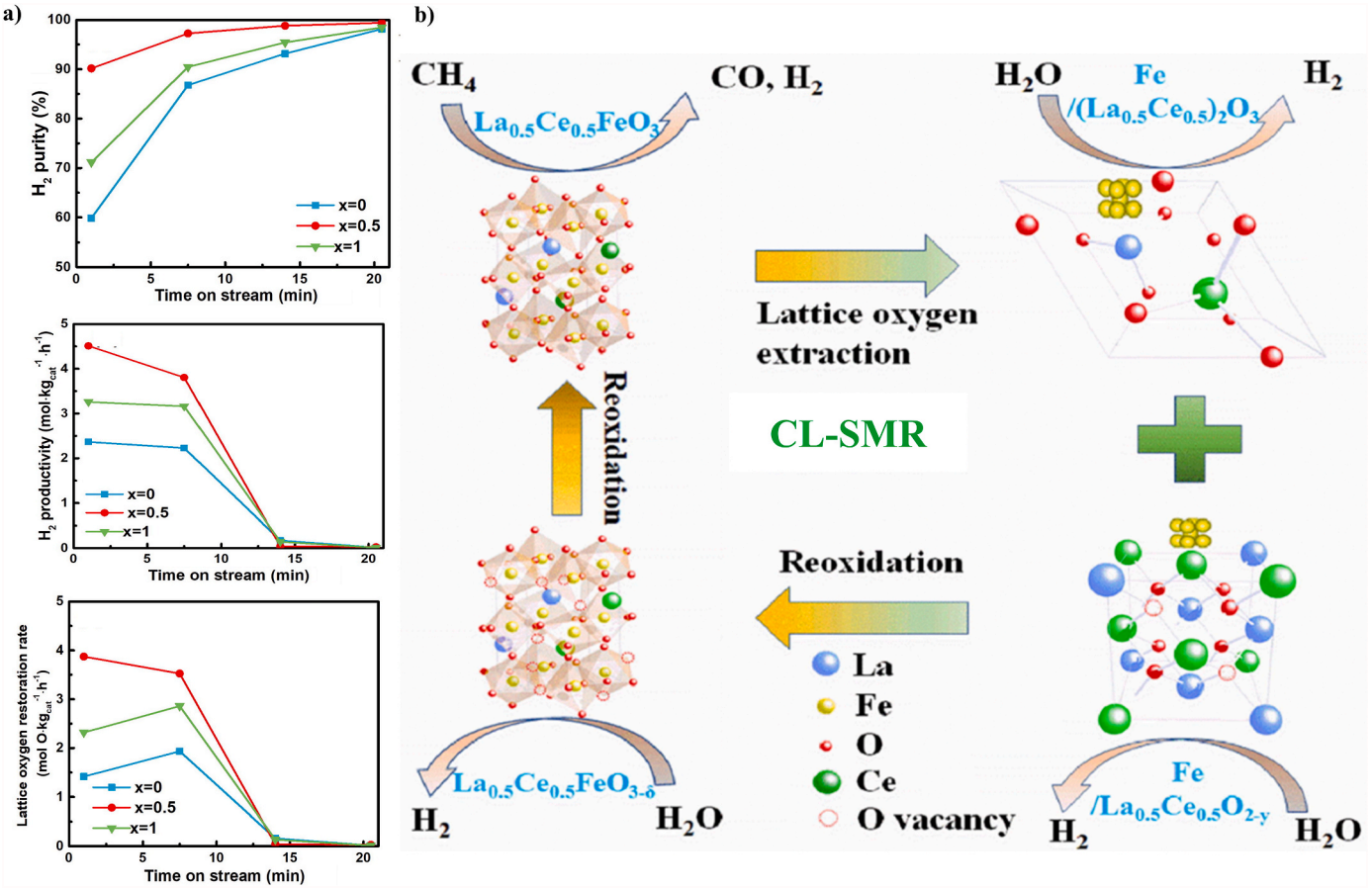

Fig. 34. CL-SMR reaction performance during H_2O splitting step over $La_{1-x}Ce_xFeO_3$ catalyst, (x = 0, 0.5, 1) in terms of **(a)** H_2 purity, productivity, and rate of oxygen restoration; **(b)** proposed mechanism of CL-SMR over $La_{0.5}Ce_{0.5}FeO_3$ for H_2 production. (Reprinted with permission from Ref. [125]. Copyright (2020) Elsevier B.V.).

nearly ideal without the mass transfer limitations. Therefore, the use of membranes inside the reactor bed leads to a reduction in the bubble size due to the bubble break-up by membrane tubes [411].

SESMR was performed in a bubbling regime to investigate the mixing flow behavior of the catalyst and sorbent, yielding a H_2 product of >0.95 mol purity. The superficial gas velocity played a key role in the fluidized-bed. In the case of the bed operating at a lower velocity of 0.15 m/s, segregation of catalyst and sorbent was observed, with the sorbent sinking towards the bottom while the catalyst rose in the upper section of the reformer. However, increasing the velocity to 0.3 m/s expanded the bed, and well-mixed sorbent and catalyst occurred [412]. H_2 production via SESMR was performed in a fast fluidization scheme, resulting in 98.58% H_2 purity and good mixing with no segregation of catalyst and sorbent [394].

Fluidized-bed reactors are highly dependent on the fluidization conditions. Very high feed rates can cause the H_2 yield to be lower in the SMR process due to gas slip. Furthermore, under fluidization conditions, the maximum flow would result in increased bubble-to-emulsion limitations [413]. Industrial systems are typically designed for specific process conditions, though the output changes when varying the flow rates of feed into the reactor. This results in a change in fluidization velocity too. Therefore, industrial reactors are designed so that the fluidization regime falls within an appropriate production capacity range of 40%–100% of nominal to minimal capacity [413]. Bubble size is also considered a crucial point in a fluidized-bed. This is because the rate of phenomena in a fluidized-bed (heat transfer, catalytic reaction, interphase reaction, and gas dispersion) is highly dependent on the bubble size in the fluidization regime. An increase in bubble diameter may cause bubbling fluidization to change into slugging fluidization. In the case of a slugging regime, large-sized bubbles inhibit the reaction, resulting in the fluctuation of the outlet concentration of SMR product gas and CH_4 conversion [414].

Two different configurations of FBMRs were proposed by Adris et al., [415]. The configurations differ in the streams passing through the Pd membrane to permeate hydrogen. The product stream is passed through the membrane after passing through a cyclone for removing the entrained solids, followed by a valve that creates a driving force for H_2 permeation across the membrane. The second configuration involves feeding part of the feed into the reactor and the remaining feed into the membrane. In this case, the driving force is the difference in H_2 concentration between the feed and product. The focus in both configurations is to generate an H_2 partial pressure difference to enhance permeation [415].

Another study proposed the concept of a two-zone fluidized-bed reactor (TZFBR) integrated with catalyst regeneration. Oxidative SMR was tested on the fixed-bed, fluidized-bed, and TZFBR. Oxidative SMR overcomes the SMR limitations of the high S/C ratio and external heating source required for the endothermic reaction. This process is more efficient than conventional SMR. However, it has the drawback of hotspot formation in the initial bed section and coke formation in the final section. In oxidative SMR, it is necessary to supply oxygen with steam so that the endothermic SMR is combined with CH_4 combustion and POM. The fixed-bed configuration depicts a reactor with the catalyst supported on inert glass wool. The fluidized-bed reactor and TZFBR

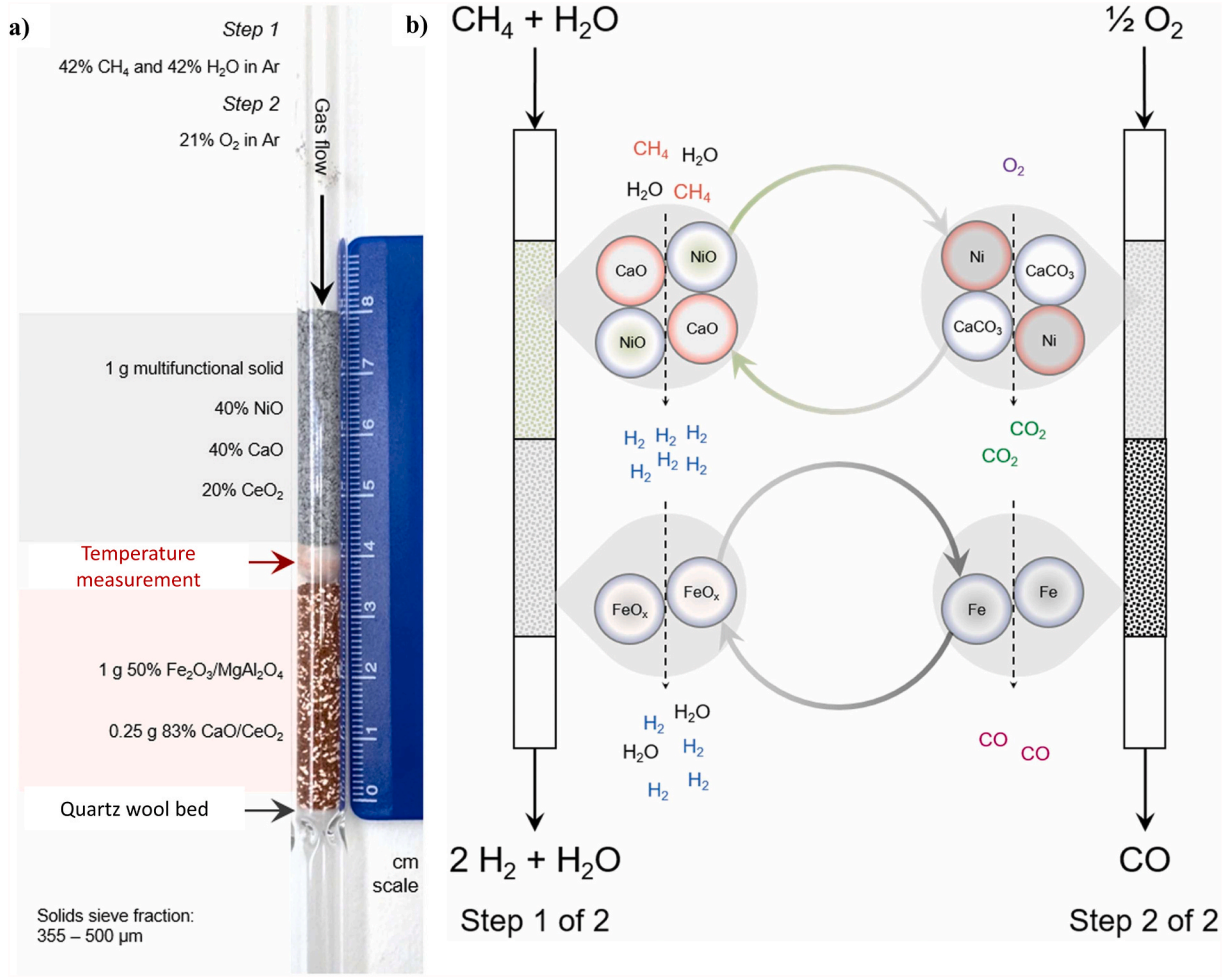

Fig. 35. a) The reactor configuration for CO and H_2 rich streams in two-step CL-rWGS; **b)** The schematic presentation of two CL-rWGS steps; 1: H_2 production; 2: CO production. (Reprinted with permission from Ref. [445]. Copyright (2022) Elsevier B.V.).

configurations consist of a fluidized-bed made of quartz. In TZFBR, the quartz tube is placed in the reactor to feed CH_4 at the point of bed height while steam and oxygen pass through the lower part. The influence of reactor type on product distribution shows that H_2 selectivity in the TZFBR was slightly higher than in the fluidized-bed reactor. No coke formation was observed in the TZFBR as compared to the fluidized-bed reactor, which had a 10% coke selectivity. However, higher CO selectivity was observed in TZFBR. This happened because gasification and coke combustion are favored at the bottom of the reactor. The comparison of fluidized-bed reactor and TZFBR performances with reactor temperature shows that CH_4 conversion in the latter was stable and higher than in the fluidized-bed reactor during a TOS (time on stream) of 190 min at a very low S/C ratio of 0.75 [282].

Intrinsic kinetic models have been developed for fluidized-bed reactors. A study suggested that micro fluidized-bed reactors exhibited enhanced heat and mass transfer as compared to fixed-bed reactors without having uneven temperature distribution or issues in heat and mass transfer performance [313]. Micro fluidized reactors have shown superior heat and mass transfer properties in which the fluidized medium and catalyst particles are suspended due to an upward-flowing gas that allows temperature uniformity and rapid heat transfer. This property makes fluidized-bed reactors more suitable for temperature-sensitive reactions, removing the need for back-mixing and external diffusion [313]. The application of a micro fluidized reactor can provide accurate intrinsic kinetic equations in SMR. A kinetic model suggested two mechanisms for SMR. A series reaction mechanism in which steam and CH_4 first react to form CO, which further reacts with steam to form H_2 and CO_2. Also, a parallel reaction mechanism in which steam and CH_4 simultaneously react to form CO_2 and CO. The kinetic equations for the two different mechanisms take the following forms, as represented in Eqs. (15) and (16):

$$\text{Parallel reaction mechanism } r_{CO} = k_1 . p_{CH_4}^{a_1} . p_{H_2O}^{b_1} . p_{H_2}^{c_1} \; r_{CO_2} = k_2 p_{CH_4}^{a_2} . p_{H_2O.}^{b_2} . p_{H_2}^{c_2} \quad 15$$

$$\text{Series reaction mechanism } r_{CO} = k_3 . p_{CH_4}^{a_3} . p_{H_2O}^{b_3} . p_{H_2}^{c_3} \; r_{CO_2} = k_4 . p_{CH_4}^{a_4} . p_{H_2O}^{b_4} . p_{H_2}^{c_4} \quad 16$$

Where k_1 and k_2 are the Arrhenius rate constants, i.e., $k_1 = A_1 e^{-E1/RT}$ and $k_2 = A_2 e^{-E2/RT}$, respectively. p_{CH4}, p_{H2O}, and p_{H2} are the partial pressures of CH_4, H_2O, and H_2, respectively. The r_{CO} and r_{CO2} are the rate constants of CO and CO_2. The model concluded that the series reaction mechanism gives negative activation energy for the WGS reaction, which is unrealistic. However, the results of the parallel reaction mechanism were consistent with the experimental data, with more than 95% CH_4 conversion at 700 °C and a 0.2 m/s inlet velocity [313].

Another study presented a conceptual design of SMR coupled with CO_2 capture and CL-SMR in two interconnected fluidized reactors using NiO/ZrO_2 as a catalyst and $CaO/CaZrO_3$ as a sorbent [416]. Fig. 32

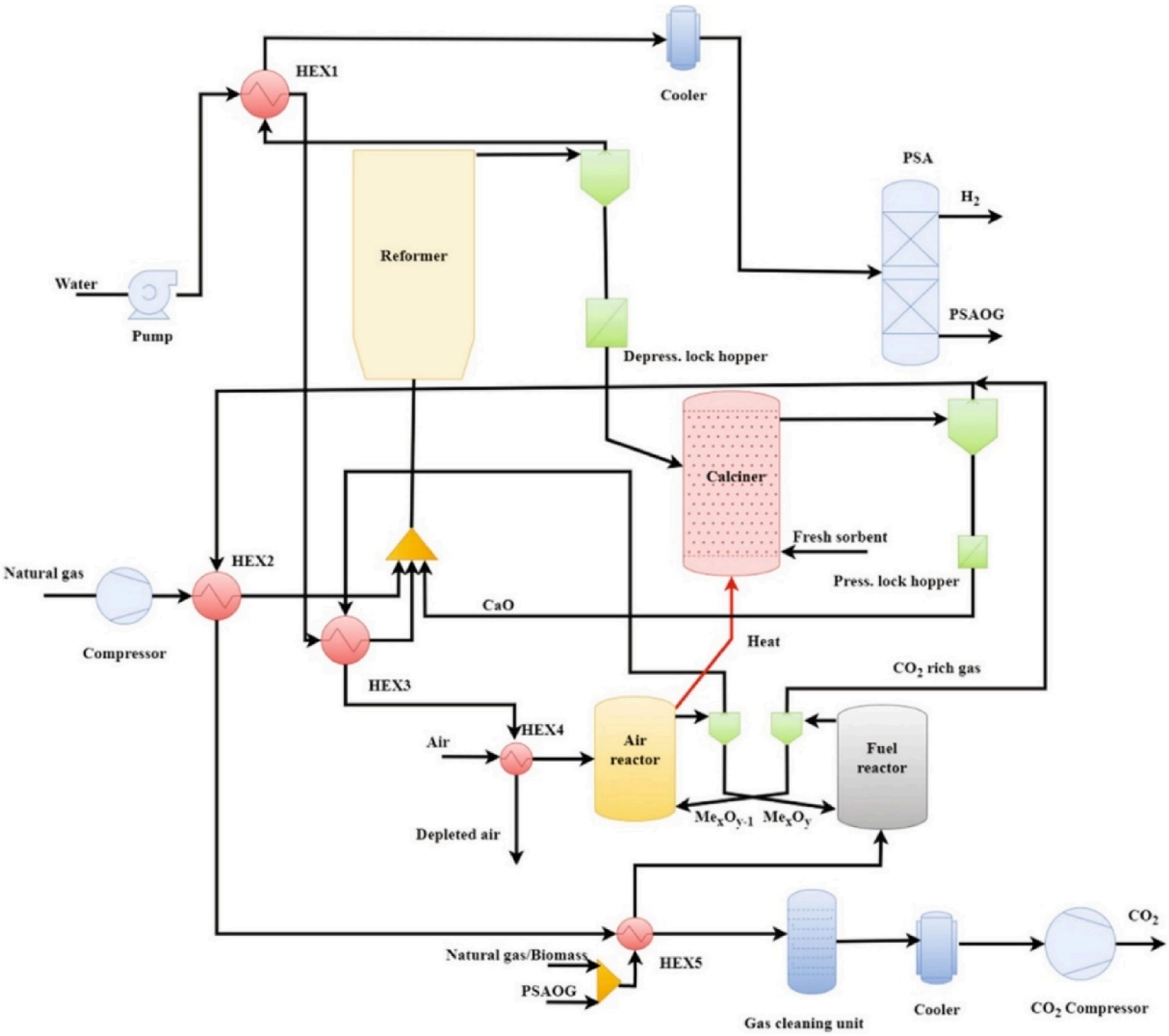

Fig. 36. Process flow diagram for CLC-SESMR. (Reprinted with permission from Ref. [88]. Copyright (2020) Elsevier B.V.).

shows a schematic illustration of the system with H_2 yield and reactant conversions at the exit of each reactor stage. Reforming occurs in a bubbling reactor; however, a fast fluidization reactor is used for regeneration. As shown in Fig. 32, solid particles from the gas product stream of the reformer containing Ni, $CaCO_3$, and CaO enter the regenerator with a pure O_2 stream. External heat is required for the regeneration of the sorbent and a temperature of 900 °C to drive calcination. The hydrodynamics and reaction rates for the fluidized-bed reactor were calculated using kinetic models. The minimum fluidization velocity (U_{mf}) was analyzed using the following theory by Wen and Yu (**Eq. (17)**) [417].

$$U_{mf} = \frac{d_p^2 \times (\rho_s - \rho_g) \times g}{150 \times \mu} \frac{\varepsilon_{mf}^3 \times \varphi_s^2}{1 - \varepsilon_{mf}}, Re_{p,mf} < 20 \quad 17$$

Where d_p is the diameter of the particle, ρ_s, and ρ_p are the densities of solid and gas particles, μ is the viscosity of inlet gas, g is the gravitational acceleration, ε_{mf} is the void fraction under minimum fluidization, φ_s is the sphericity of the solid particles, and $Re_{p,mf}$ is the Reynolds number in the minimum fluidization condition. The terminal velocity (U_t) is calculated by the following **Eq. (18)**.

$$U_t = U_t^* \times \left[\frac{\rho_g^2}{\mu \times (\rho_s - \rho_g) \times g}\right]^{-1/3} \quad 18$$

Where U_t^* is the dimensionless terminal velocity, the reactor is assumed to operate in a bubbling regime that occurs when the superficial velocity of the gas is greater than the minimum bubbling velocity but less than the terminal velocity. The simulation results were close to the equilibrium values for H_2 production with 95% purity, 93.4% CH_4 conversion, and an 80.2% H_2 yield in a bubbling reactor. The results were in agreement with those of fixed-bed reactors, where both were found close to equilibrium [416].

It is suggested that a fluidized-bed reactor integrated with membrane technology be used to overcome the limitations of the conventional process, including heat transfer limitations and higher intraparticle resistance. The advantage of temperature uniformity in a fluidized-bed also reduces the thermal stresses on the material of the membrane. It also offers the possibility to limit coking by using circulating fluidized-bed reactors. However, considering the industrial point of view, issues are still to be addressed before commercialization, including the membrane cost and the stability of membranes under harsh fluidization conditions. Although these issues are solved by the fluidized-bed reactor, when SESMR is applied in a fluidized-bed reactor, there is a drawback of higher energy requirements in the regeneration step. This leads to the application of oxygen-transferring material in the reactor, as in chemical looping, as an attractive process for H_2 production.

3.4. Effect of chemical looping

To overcome the inefficiency of heat supply to endothermic reforming reactions and inhibit coke formation, oxygen is successfully introduced into a fluidized-bed for oxidative reforming (or partial oxidation) so that the auto-thermal condition can be achieved [418,419]. All strategies of chemical looping conversion of methane, including chemical-looping combustion, chemical-looping partial oxidation, chemical-looping dry reforming, and chemical-looping steam reforming were scrutinized by Li et al. [420–422]. However, this research only focuses on CL-SMR. In CL-SMR, CH_4 is partially oxidized to H_2 and CO without the utilization of elemental oxygen and substituted with lattice oxygen of the OCs [423]. CL-SMR is a novel blue H_2 production technique that combines SMR with inherent CO_2 separation while consuming no additional energy [294,424,425]. The process is favored under an S/C of 4.0. Under these conditions, the process yields high H_2 purity, up to 92.6%, without the need for any purification process. Compared to the energy efficiency of SMR and CL-SMR, the latter process exhibits approximately 17.48% greater energy efficiency as compared to SMR [426]. The process involves the formation of syngas from CH_4 in the first step via solid metal oxide OC, converting it into reduced OC as in reaction (**R7**). In the second step, H_2 is produced by the decomposition of H_2O over the reduced OC as in reaction (**R8**). The reactions in CL-SMR are illustrated in Fig. 33(a) [427].

CL-SMR occurs in a fixed-bed reactor with a dual-step that cyclically changes the feed to a reactor containing oxygen transfer material, as illustrated in Fig. 33(b) [428]. Three phases occur in three parallel reactors in sequence. The oxidation reactor forms NiO by reacting Ni in the air stream and releasing N_2. The OC is reduced in the reduction reactor, forming H_2O and CO_2. The final reactor contains the reduced OC and is fed with CH_4, recirculated CO_2/H_2O, and additional steam to form syngas. Each reactor operates in oxidation, reduction, or reforming mode by switching the inlet streams. Furthermore, Patil et al. [321] designed a type of combined membrane-assisted fluidized-bed reactor for blue H_2 production using light hydrocarbons as fuel, as illustrated in Fig. 33(c) [107]. The H_2 separation membrane was located at the upper reactor, while the oxygen addition membrane was at the bottom. The autothermic operation with a high fuel conversion and H_2 yield could be achieved with a low catalyst load. In addition, the temperature in these two zones could be effectively controlled to achieve optimum reforming performance by adjusting the feed ratio from the bottom to the top zone.

Reduction reaction (**R7**):

$$MeO_x + \delta CH_4 \leftrightarrow MeO_{x-\delta} + \delta(2H_2 + CO) \quad (R7)$$

Oxidation reaction **(R8)**:

$$MeO_{x-\delta} + \delta H_2O \leftrightarrow MeO_x + \delta H_2 \quad (R8)$$

Overall reaction **(R9)**:

$$CH_4 + H_2O \leftrightarrow 3H_2 + CO \quad (R9)$$

Where MeO_x and $MeO_{x-\delta}$ are the metal oxides and reduced metal oxides (carriers), respectively, whereas **(R9)** represents the overall SMR process.

The CL-SMR process is dependent on the metal oxide selected as an OC. A suitable OC must have a high capacity for oxygen storage, high reactivity under alternating processes of oxidation and reduction, good thermal and mechanical stability, and appropriate reactivity under changing oxidation and reduction processes [429]. Recently, a number of OCs, including Ni-ferrites [430,431], Cu ferrites [432,433], CeO_2 [434], and perovskite-based [435], have been studied for CL-SMR. The Ni-based OCs are unselective for the POM, but the reaction favors the total oxidation of CH_4 even with a small quantity of NiO. However, the Ni-based OCs may trigger environmental concerns [436]. For H_2 production, Fe-based OCs are highly active in water-splitting reactions but have a higher selectivity for the total oxidation of CH_4, which is undesirable for syngas production [437].

CeO_2 has been significantly investigated for CL-SMR owing to its syngas selectivity, resistance to carbon deposition, and outstanding ion conductivity [234,430,438]. Table 7 presents various OCs with catalysts for CL-SMR. In the reduction and oxidation steps, respectively, CeO_2 can partially oxidize CH_4 directly into syngas without CO_2 formation in CL-SMR, giving high-quality syngas and pure H_2 in the reduction and oxidation steps [429].

The process was investigated over Fe_2O_3 and CeO_2. The combination resulted in enhancing the reducibility of CeO_2 and the redox activity of the process due to Fe_2O_3 addition, revealing a strong interaction between Ce and Fe [439]. The calcined CeO_2–Fe_2O_3 at 800 °C was tested for CL-SMR. It exhibited high selectivity and conversion due to its higher lattice oxygen activity [440]. The high performance of Ce–Fe mixed oxides can be ascribed to the solid interaction between CeO_2 and Fe_2O_3 and the formation of a solid solution of Ce–Fe–O. The thermal stability and oxygen storage capacity of CeO_2 are greatly improved due to the creation of oxygen vacancies in CeO_2 by Fe^{3+} [441]. CeO_2-promoted Ni-based was used as an OC for the process. It was found that CeO_2 in

NiO improved the nanoparticle distribution with 100% CH_4 conversion and 86.98% H_2 yield at 700 °C (reduction temperature) [442]. A Ce–Fe–Zr-based monolithic OC was tested to produce syngas. It was observed that monolithic OC promoted the activity of water splitting, CH_4 oxidation, and also improved the resistance to coke formation [70].

Perovskites can be optimized to adjust the performance of the reaction by changing the cations [443]. The enhanced reactivity of the redox property of $LaFeO_3$-based perovskites due to the excellent oxygen conduction and availability of larger concentrations of oxygen vacancies has received lots of attention in CL-SMR [232,444]. However, Fe, Ni, and other cations facilitate carbon deposition due to methane cracking, which can be a negative factor leading to the deactivation of OCs, impure H_2 production, and incomplete utilization of fuel [437]. It occurs in cases where the supplied oxygen available from the internals is not sufficient to meet the oxygen needs on the surface of OCs. As an active site, Co is highly efficient at regulating the reactivity of $LaMnO_{3+\delta}$ as compared to Fe. To overcome this limitation, Sr and Co were double-adjusted to match the oxygen supply from bulk and the oxygen needed on the surface of OCs. The catalyst exhibited the best reaction performance and high stability in redox tests in a range of 0.2–0.4 and 0.4–0.5 substitution proportions of Sr and Co [128]. The kinetic behavior of the $La_{1-x}Ce_xFeO_3$ catalyst (x = 0, 0.5, 1) during the H_2O splitting step is depicted in Fig. 34(a). Initially, the H_2 purity is less than 100% due to the deposited carbon during the partial oxidation step. $La_{0.5}Ce_{0.5}FeO_3$ showed the highest purity, productivity, and oxygen restoration rate. It can also be seen that the H_2 production is negligible after 21 min, which shows that the water and oxide reaction achieves thermodynamic equilibrium.

Moreover, an extensive reaction mechanism of CL-SMR over the $La_{0.5}Ce_{0.5}FeO_3$ catalyst is presented in Fig. 34(b) [125]. This study examines the potential of Ce^{3+} promoted $LaFeO_3$ redox catalysts for H_2 production via the CL-SMR mechanism. The study finds that during the POM step, the catalyst is deprived of lattice oxygen and produces syngas, while the perovskite structure gradually collapses and reduces to composites of $Fe^0/(La_{0.5}Ce_{0.5})_2O_3$ and $Fe^0/(La_{0.5}Ce_{0.5})O_{2-x}$ owing to the exhausting of lattice oxygen. In the H_2O splitting as a subsequent step, the reduced sample is re-oxidized back to $La_{0.5}Ce_{0.5}FeO_3$ perovskite via $La_{0.5}Ce_{0.5}FeO_{3-\delta}$ with the H_2 production. The study finds that $La_{0.5}Ce_{0.5}FeO_3$ exhibits the highest surface exchange coefficient and lattice oxygen migration ability among all the $La_{1-x}Ce_xFeO_3$ redox catalysts, and with the promotion of an adequate quantity of Ce^{3+} substitution, $La_{0.5}Ce_{0.5}FeO_3$ exhibits a better potential in CL-SMR for H_2 production compared to other catalysts.

Recently, a novel method for a two-step SMR for blue H_2 was proposed. Fig. 35(a) presents the experiment using a fixed-bed quartz reactor with a multifunctional material and oxygen and CO_2 carriers. The materials were pelletized, crushed, and sieved before being placed in the reactor, before loading them in the reactor, aggregates between 355 and 500 μm in size should be obtained. The reactor type is electrically operated with three heating zones and operates at 650–725 °C. The feed gases do not have direct contact between CH_4 and O_2, thereby reducing the safety risks. This temperature range ensures that the kinetics of reaction steps are fast and thermodynamically favored in the direction of the carbonation reaction. The proposed reaction mechanism is presented in Fig. 35(b). It is set to shift the equilibrium in the desired direction, ultimately improving the heat management of the system using 3 solid intermediates [445]. NiO is an OC that replaces the O_2 used for POM, a CO_2 carrier to favor the reaction in the direction of H_2 production. In step 1, NiO is reduced to Ni, which catalyzes the SMR reaction, and any CO_2 produced is captured by the CaO (sorbent). However, in step 2, O_2 is used for the exothermic oxidation of $CaCO_3$. To enhance the heat distribution, an adequate number of oxygen carrier pairs can be introduced to the reactor bed, such as CuO/Cu [446]. Another OC, FeO_x, is placed downstream of the solids for in-situ utilization of the CO_2 released [447]. In the first step, a fraction of the produced H_2 reduces FeO_x, followed by CO_2 released in the second step and oxidizing Fe back to FeO_x. The implication of such a system can be named chemical looping-reverse water gas shift (CL-rWGS). Therefore, heat management occurs by splitting the heat of POM to syngas into 2 steps that form separate streams of high-purity H_2, CO, and energy carriers (CaO, FeO_x).

This concept differs from the CL-SMR, which requires heat supply in

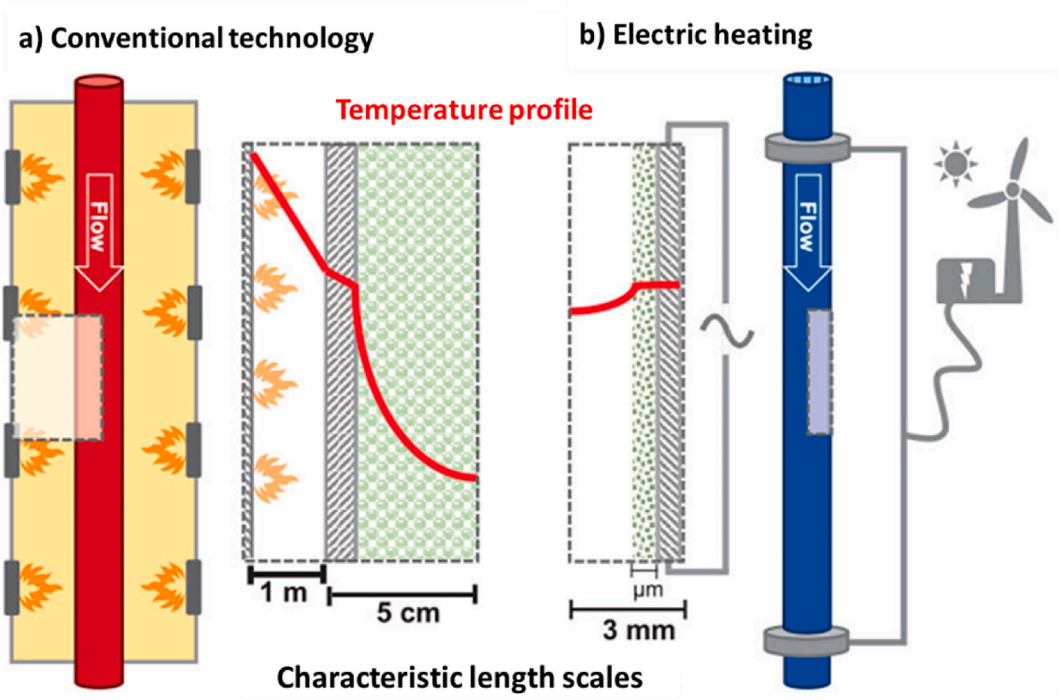

Fig. 37. Schematic of reactor scale and temperature profiles in **a)** conventional reformers and **b)** the electrified reformer. (Recreated with permission from Ref. [485]. Copyright (2019) Science.).

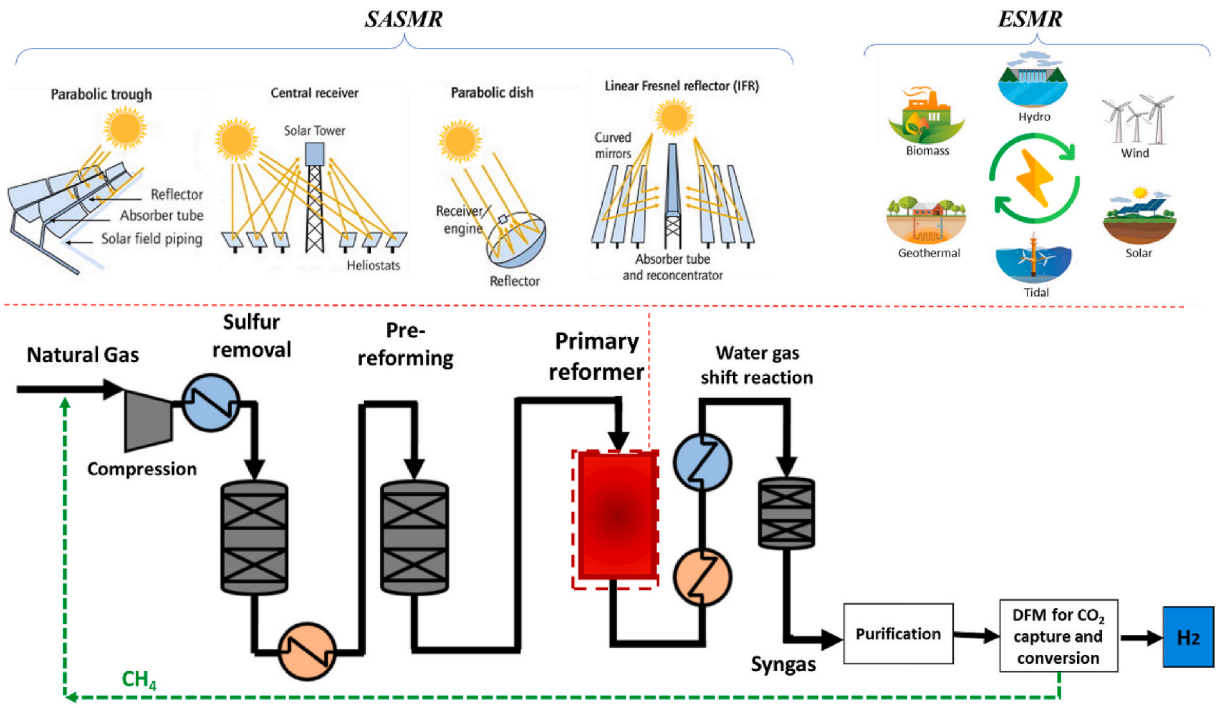

Fig. 38. Schematic of a sustainable path for the SMR by hybridizing renewable energy as a heat source and exploiting smart materials like DFMs, zeolite, and MXenes. (Recreated with permission from Refs. [480,486,487,493]. Copyright (2021, 2014) Elsevier B.V.).

the steps and forms mixed steam of syngas in one step of the process [448]. It also differs from CL-partial oxidation, which forms syngas in one step and an O_2 stream in the second step [449]. This method can be seen as producing blue H_2 with in-situ CO_2 capture and conversion to CO in a two-step process. The additional energy demand is reduced by coupling exothermic and endothermic reactions and lowering the reaction temperature as compared to conventional SMR.

To attain an increase in reaction rate and catalyst regeneration, a novel circulating fast fluidized-bed membrane reformer was suggested [450,451], where an H_2 separation membrane and an oxygen addition membrane were simultaneously introduced into a fluidized-bed reactor. Another novel configuration for chemical looping combustion (CLC) technology for blue H_2 production is to combine it with SESMR technology, as shown in Fig. 36 [311]. The CLC-SESMR consists of two units. The first unit involves the SESMR process, where feed gases are sent to the reformer containing the CaO sorbents. The $CaCO_3$ is decomposed to CaO in the calciner by using the heat released from the CLC process [310]. The second unit is the CLC process, which consists of an air and fuel reactor. Metal oxide is used to combust the feed gas in the fuel reactor to produce CO_2 and H_2O. The metal oxide from this reactor is then regenerated in the air reactor [452]. Such a type of process is optimized by taking into consideration the operating conditions, including temperature, S/C, reformer, air and fuel reactor, calciner, and CaO/H_2O ratios [453]. A higher quantity of metal oxide in the system leads to higher CH_4 consumption during the reduction reaction. This occurs as the higher quantity of metal oxide circulating in the reactor increases the temperature and favors the endothermic SMR reaction [454]. The use of Fe and Ni-based materials as OCs has been investigated for CLC-SESMR and CLC processes with biomass fuel [455]. Additionally, the thermodynamic analysis of Fe-based oxides exhibits similarity in H_2 purity, energy, and process efficiency. However, it differs in terms of CH_4 conversion and CO_2 capture, while Fe-based OCs have shown 100% fuel conversion [88].

Kinetic models for CL-SMR depend on the evaluation of both oxidation and reduction steps during the process, with the concept that the nature of the support can affect the kinetic performance. This study developed a shrinking core model to evaluate the reduction profiles of NiO/TiO_2 and NiO/Al_2O_3, and used the "Avrami-Erofeev" model for the reduction profiles of ZrO_2 and NiO/SiO_2. The study on oxidation profiles revealed a slow diffusion-controlled regime and a fast chemical reaction-controlled regime. The "Avrami -Erofeev" and "Prout Tompkins" models resulted in an optimal fit [456]. The kinetic parameters for the SMR, WGS reaction, and oxidation degree of two OCs were determined [436]. It was found that the performance of SMR and WGS reactions was similar to the two OCs but lower than the Ni-based conventional catalyst. The performance of OCs depends on their degree of oxidation or reduction. This increases the reduction conversion of OCs, thus increasing the catalytic activity. Moreover, Dai et al. [457] stated that models including the power law model, shrinking core model, and nucleation and nuclei growth models can interpret the kinetics in the reduction step over $LaFeO_3$.

Conclusively, in CL-SMR, the redox catalyst plays the role of an intermediate for storing and then delivering oxygen ions. Therefore, the kinetic and thermodynamic properties of the redox catalyst play a key role in defining the feasibility of this technology. Still, the transport kinetics of the lattice oxygen in catalysts for CL-SMR are lacking. Moreover, concerning the catalyst structures for CL-SMR, $LaFeO_3$ is the most investigated perovskite, mainly due to its high oxygen mobility and the capability to host a huge concentration of vacancies at elevated temperatures.

4. Future developments of industrial SMR

SMR is a highly energy-intensive process that relies on the combustion of fossil fuels, mainly natural gas, to achieve a high yield of product and a high conversion of feedstock. Industrial SMR consists of large furnaces containing several hundred tubular reactors, heated via fossil fuel combustion. Gas fire heaters for combustion require extensive fuel and also account for 1% of the CO_2 emissions globally [461]. There are several future developments required to mitigate the environmental impact of SMR, some of them are discussed as follows.

4.1. Advanced catalyst development

There is a critical need to design advanced catalysts that require lower operating conditions in order to reduce the energy requirements of the SMR process. The development of such catalysts should target improving the selectivity and efficiency of the SMR process. The details have been explained in the section on “2.1. Effect of catalyst".

4.2. Multi-functional materials development for CO_2 capture and conversion

Multi-functional materials like dual-function materials (DFMs) [462], zeolites [463], and two-dimensional (2D) transition-metal (groups IV, V, VI) carbides (MXenes) have unique properties that can improve the efficiency and productivity of the SMR process by capturing CO_2 and converting it to methane simultaneously. Zeolites are one type of DFM that has been extensively studied in the context of SMR. Zeolites are microporous materials with a unique structure that provides them with a high surface area and catalytic properties. In SMR, zeolites act as catalysts, capable of breaking the C–H bonds in methane and facilitating the formation of H_2 and CO. Moreover, MXenes have recently gained significant attention due to their unique physical and chemical properties, including high electrical conductivity, thermal stability, and tunable surface chemistry. MXenes are recommended for CO_2 capture and/or conversion. For instance, the Cr_3C_2 and Mo_3C_2 MXenes exhibit the most promising CO_2 to CH_4 selective conversion capabilities [464]. However, exposure to oxygen and/or steam at a high temperature can also change the lattice structure and morphology of MXenes, leading to amorphous structures. The risk of oxidation of 2D catalysts in oxygen-rich environments also makes catalyst calcination and regeneration processes quite challenging. Therefore, new calcination and regeneration methods are required to preserve the 2D structure.

4.3. Process intensification

The implementation of process intensification techniques such as heat integration, process integration, and process optimization can improve the energy efficiency of the SMR process. Recently, researchers are exploring hybrid processes that combine SMR with other technologies, such as electrolysis or photovoltaics, to produce cleaner hydrogen more efficiently and with a lower environmental impact [422]. These techniques can also reduce the capital and operating costs of the process.

4.4. Decentralized and modular SMR

While most industrial SMR takes place in large, centralized facilities, there is potential for smaller, decentralized production systems that can be located closer to the sources of raw materials and energy. This strategy could use a small-scale SMR process or alternative technologies to produce hydrogen on-site, reducing logistics costs and increasing efficiency [243]. Small modular chemical plants have many benefits, including low financial risks, flexibility, and rapid response to changes in demand. Additionally, smaller facilities may find it easier to meet stricter safety regulations, leading to potential economic and safety advantages [465].

4.5. Renewable energy-powered SMR

Renewable energy sources can be used to generate the heat and steam required for SMR instead of fossil fuels. In this case, the heating method will shift from combustion to electricity and renewable energy-powered systems [466,467]. This process can reduce carbon emissions and make hydrogen production more sustainable. Among all renewable energies, solar energy is an abundant source, and the energy mix is a very appealing phenomenon in all commercial activities [468,469].

4.5.1. Solar-assisted SMR

Recent technologies are focusing on alternatives to fossil fuels that can create possibilities for supplying heat using renewable and carbon-free sources such as solar energy, which is termed SASMR [429, 470–473]. The solar irradiance is available at 1 kW/m^2, but such flux is not sufficient for direct utilization in SMR. The SMR process, heated by solar energy, allows a 34–53% CO_2 reduction and a 34% decrease in CH_4 consumption compared to the conventional plant [474]. Thus, SASMR has been recognized as an attractive option as it is capable of reducing fossil fuel consumption and upgrading solar to chemical energy [475].

The SASMR is categorized into three temperature ranges: low-temperature range (300–600 °C), middle-temperature range (600–900 °C), and high-temperature range (>900 °C). The catalyst requirement for SASMR has the same requirements as conventional SMR, i.e., stability, high activity, and optimal particle size to avoid mass transfer limitations. However, at low temperatures, SASMR has catalyst activation issues, while in the middle and high-temperature ranges, sintering and thermal crackdown are the primary issues. Specifically, in SASMR, continuous cooling and heating due to the cyclic nature of solar irradiation can cause several thermal stresses in the catalyst [476]. The Ni-based catalysts are commercially acceptable on Al_2O_3 support for SMR; however, for SASMR in a low-temperature range, the Ni-based catalyst is less suitable due to its deficient intrinsic properties and promotion of oxidative routes, which further leads to deactivation [477]. In general, Ni-based catalysts show lower catalytic activity and coking in low and medium-temperature SASMR, while in high-temperature SASMR, the Ni-based catalysts show high catalytic performance while coking and sintering resistance capacities are lower. While platinum group-based catalysts show better performance in terms of catalytic and coking resistance, they show fair resistance to sintering and oxidation. The metal carbides show mixed performance in the low, medium, and high-temperature SASMR. The direct comparison is still difficult due to the stability and activation issues of the catalyst in SASMR. The bimetallic approach seems much more suitable due to the mixed properties of the Ni–Pt-based catalyst on ZrO_2 and CeO_2 support systems. The complexity of the catalyst’s performance has remained a challenge as a result of variations in the solar energy source due to weather conditions and high process endothermicity.

A major challenge in solar-based reforming is achieving the integration between the concentrating solar method and SMR. Solar energy can be integrated in both direct and indirect ways. The indirect utilization is subject to the system fluid for indirect heating of reactants, whereas solar irradiation is directed to the catalytic system for reaction and is typically used for both low and high-temperature SASMR [478].

An approach to this challenge is to use solar reactors/receivers to directly capture and convey the concentrated solar rays through quartz windows to the reforming reactor operating at conventional conditions [479]. All types of solar concentration systems, such as parabolic trough collectors, linear Fresnel reflector systems, dish–engine systems, and power towers, also known as central receiver systems, can be employed in the reforming process [480]. The parabolic trough and linear Fresnel reflector are limited to low-temperature SAMR, while the solar tower and parabolic dish engines can be effectively utilized for medium and high-temperature SAMSR because the reformer is heated directly by irradiating it with sunlight. Considering the operating temperatures for SASMR, the increase in the process temperature depends directly on the input solar heat of the SMR process. Increasing the input solar heat results in higher operating performance but should be limited to 900 °C to ensure long-term stability and durability of the catalysts in the reactor. However, high temperatures and low pressure were favorable operating conditions for SAMSR [473]. It is challenging to select a solar energy utilization option; direct utilization is more favorable for high-temperature SASMR with PSA and carbon capture and storage (CCS) technology to produce blue H_2, with lower emissions than conventional SMR.

4.5.2. Electrified SMR

In electrified SMR (ESMR), the energy is supplied by renewable electricity sources such as wind, hydro, tidal, geothermal, biomass, and solar power. This makes the process much more environmentally friendly, as it reduces GHG emissions and the use of non-renewable energy sources. The primary reformer of the conventional process is altered by removing the burners and replacing them with an electrical heating system, such as Joule heat, Ohmic heating, or resistive heating [481,482]. With Joule heating or Ohmic heating, the energy is directly applied to the process feed without generating flue gas that carries energy out of the system [461]. Despite the higher electricity cost compared to natural gas, the significant benefits of the process, including the reduced volume of the reformer by two folds, no temperature gradient across the wall of the reactor, and reduced GHG emissions, have been discussed [92]. Recently, Balzarotti et al. [483] investigated the development of a highly conductive structure, which supports the intensification of non-adiabatic SMR. Rieks et al. [484] applied direct joule heating to the CH_4 reforming process. Specifically, the high thermal duty of the dry reforming process was fulfilled by directly washcoating heating components consisting of a FeCrAl alloy with a $LaNi_{0.95}Ru_{0.05}O_3$ catalyst at different washcoat thicknesses. Moreover, Wismann et al. [485] employed the same strategy in a more novel manner by directly incorporating an electrically heated catalytic structure into a SMR reactor. A 50 cm long and thin FeCrAl tube was used, and its inner walls were rendered catalytically active by depositing a catalytic washcoat layer. Current flow was then forced into the tube's walls [486]. In Fig. 37 (a), the limitations of conventional SMR technology have been illustrated, including the low thermal conductivity of the SMR catalyst and reactor walls, which creates steep temperature gradients across the catalyst and reduces catalyst utilization, increasing the risk of carbon formation. Besides, in Fig. 37 (b), a fully electrically driven reformer has been introduced based on direct resistive heating, which removes thermal limitations and enables energy to be supplied directly to the catalytic sites, allowing well-defined control of the reaction front. Electrification reduces reactor volume, CO_2 emissions, and waste-heat streams, which provides a disruptive advantage to existing industrial reformers, enabling the production of "greener" hydrogen for the large-scale synthesis of essential chemicals [487]. Furthermore, it has been proved that induction heating of nanoparticles using magnetic hysteresis inside chemical reactors is an attractive approach for electrified heating of endothermic reactions like SMR. Induction heating heats up from the inside and supplies where needed while avoiding the huge temperature gradients throughout the catalyst bed [486]. Recently, a rapid interest has grown in using magnetic nanoparticles for the induction heating of reactions [488,489] (see Fig. 38).

A most recent novel heat pipe tubular reactor was proposed based on the hybrid technologies of electric heat supply and concentrated solar methods for SMR. The performance of the SASMR reactor was tested by a device providing high-frequency induction and a solar simulator, respectively. The reactor exhibited outstanding uniformity of temperature throughout the catalyst zone, with 100% CH_4 conversion. The high thermal conductivity of the reactor was able to supply energy to the endothermic SMR and promote the turquoise H_2 yield [475,490].

Finally, based on the above-mentioned discussion, a novel and sustainable path (Fig. 38) for the SMR process drastically reduces CO_2 emissions by hybridizing renewable energy as a heat source and exploiting smart materials like DFMs [491], zeolites [463], and MXenes [492]. In this path, the produced methane can be recycled into the process as feed, which leads to the production of turquoise H_2 in the output. The sustainable path can be considered a decentralized system for SMR and integrated with places with easily available renewable energy resources. Several places such as the Sihwa Lake Tidal Power Station in South Korea, Nesjavellir Geothermal Power Station in Iceland, the Alholmenskraft biomass plant in Alholmen-Jakobstad, Finland, the Polaniec biomass plant in Staszów, Poland, etc could take advantage of the abundance of renewable energy resources to produce the turquoise H_2 on-site in these locations.

4.6. Environmental, social, and governance (ESG) profiling

Environmental, social, and governance (ESG) profiling is a framework used to evaluate the sustainability and social responsibility of an organization's business practices. When applied to the SMR process for H_2 production, ESG profiling can help identify and address potential environmental and social impacts associated with the production process.

Global events have shown limitations of the classical production model that ask for complementary measures in technological innovation, motivated by societal demands [494]. The Covid-19 pandemic has emphasized vulnerabilities in global supply chains, and the declining resources raised criticality in elements, minerals, and resources. On top is the climate change-related problems. SMR process generates hydrogen for the Haber-Bosch (HB) process, to globally produce ammonia (NH_3), which contributes to nearly 2% of global carbon emissions. This limitation in meeting societal and environmental demands necessitates alternative ways of production. The current supply chain revolves around large-scale, centralized production that exports ammonia to local markets across large geographic distances. The solution may be a regional production with decentralized supply chains, being idealized as a self-sufficient 'at-farm' supply [494]. The 'societal-environmental limitation' requires chemical processes with low emission of carbon dioxide and more resilient production via converting new abundant resources such as biomass, water, and air. Plasma processing is an emerging technology that can use renewable energy and activate renewable, hardly otherwise reactive molecules, in the context of electrochemistry [494,495]. Excessive transportation can lead to increased prices due to the cost of fuel, labor, and other associated expenses. Additionally, transportation contributes to environmental impacts through GHG emissions, air pollution, and other negative effects. Therefore, it is important to consider new supply chain strategies that can reduce transportation needs and minimize environmental impact. For example, this limits the development of rural, smallholder farmers in Africa.

To exemplify the emission issue, the carbon footprint of centralized production is up to 2.96 kg. CO_2- eq/kg. NH_3, where 29.3% corresponds to transport [495]. Local plants using electrolysis and HB loops obtained rates of 0.12, −0.52, and −1.57 kg. CO_2-eq/kg.NH_3 using solar, wind, and biogas sources, respectively [3]. Regional plants using high-temperature plasma instead of electrolysis obtained their best rate of −0.65 kg. CO_2-eq/kg.NH_3 using biogas. At farm electrolysis-based plants feeding novel, non-thermal plasma NH_3 synthesis reached a rate of −1.07 kg. CO_2-eq/kg.NH_3, using solar energy. Accordingly, the coming blue/turquoise hydrogen and ammonia economy will consider the internationalization of these (environmental) costs [496]. This can largely change the economic calculation of the chemical and steam reforming industry. Carbon tax, as considered, e.g., in South Africa, will have future impact costs of hydrogen and ammonia and therefore determine the SMR technology choice.

Nonetheless, cost internalization is only part of the bigger picture of ESG [497], which determines global investment and technology selection. Social factors relevant to SMR process, e.g., skilled labor, food security, and national security have a critical impact. Africa is a future marketplace appropriate for the SMR process; therefore, ESG learning should be given crucial consideration. Africa established regional economic communities (RECs) via recognized groups of African nations' governance to promote economic integration through factors such as free trade, free movement of people, and integrated infrastructure [498]. African importation tariffs are a critical factor influencing ammonia's market price.

For the SMR process technology, small-scale modular units can help to leverage advanced chemical processing and internalized cost and ESG opportunities [499]. Hessel et al. [499], summarized some critical

considerations as follows.

1. Utilities: Access to essential utilities such as water, electricity, etc. at remote sites.
2. Pressurized operation: Avoid pressurized conditions when possible, as it will need compressors which add capital investment.
3. Gas preconditioning: Avoid or simplify when possible.
4. Transience: Plan for relocation of the plant and longer operational lifetime by multiple uses (and locations).
5. Location: Consider local climate, access to skilled personnel, and legislation.
6. Accessibility limitation: Consider the transportation of the chemical plant.
7. Flexible feed: Permit processing to be flexible with local resources.
8. Process robustness: Reduce human interaction, e.g. in start-up and shutdown of the plant operation.
9. Environmental control: A technology game changer is needed to address climate and other environmental demands.
10. Product quality: This is an asset that can promote the internalization of costs. For example, local-tuned fertilizers may address local soil and climate demands with controlled release of nutrients to decrease their loss.

5. Concluding remarks and future perspectives

Conventional SMR is an industrial-scale technology widely used for gray H_2 production worldwide, despite being an energy-intensive and complex process. The CO_2 emissions during the process make it questionable for the modern world. Despite its commercial prospects, special attention is paid to reducing CO_2 emissions and producing blue and turquoise H_2. This review describes insights into the catalyst systems, kinetic models, and process conditions for the SMR process. The particular emphasis is on the novel and sustainable evolution path, focusing on the efficient production of cleaner H_2 (blue or turquoise) via catalytic SMR. This production relies on conventional and intensified configurations that utilize renewable energy as a heating source for the reformer instead of fossil fuel. Additionally, the proposed path includes the use of DFMs to simultaneously capture and convert CO_2 to methane. Finally, the critical points for SMR process that can help leverage ESG profiling have been discussed. The conclusive remarks based on the review are as follows.

1. As the most researched and widely applied catalyst in commercial SMR applications, Ni-based catalysts have been synthesized and applied by using/tuning novel supports, promoters, and noble metals. Notably, the addition of promoters such as Ce and Co has resulted in a remarkable catalytic improvement of Ni-based SMR catalysts. Despite the excellent activity of noble metals, their application is restricted by their high cost. However, the combination of Ni-based catalysts and adsorbents to decrease GHG still faces stability issues. Further improvement of Ni-based catalysts is expected through the utilization of advanced characterization techniques and a deeper understanding of the structure-activity relationship in catalyst design and preparation. For example, the efficient SMR can be achieved by finely anchoring Ni particles at the single-atom level using various preparation strategies.
2. Developing a kinetic model presents a challenge in various conventional reactor systems. Among the kinetic models, the generalized microkinetic model, as the most common kinetic model, offers the potential to tune up the SMR process. It addresses catalyst design considerations by providing insights into diffusional limitations, structural changes, and reaction mechanisms, thus revealing the favorable pathways for enhanced H_2 production. A simplified depiction of the SMR process can be provided by the lumped-parameter kinetic model, which might not adequately depict the complexities and intricacies of the real reaction mechanism. Isothermal models are suitable for steady-state simulations, while transient models capture dynamic behavior. Transient kinetic models are more suitable for sorption-enhanced and chemical looping SMR due to their transient nature and ability to investigate the diffusion flux, reactant flow, heat, and mass transfer. Scientists are actively engaged in exploring and refining the kinetic models to enhance their accuracy in predicting the performance of intensified SMR with new smart materials to efficiently produce blue or turquoise H_2.
3. The performance of SMR is greatly influenced by key processing parameters, including reaction temperature, pressure, GHSV, and S/C ratio. The reaction temperature plays a crucial role in activating the Ni-Pt catalyst, while adjusting the S/C ratio allows for tuning H_2 and CO_2 production and suppressing the RWGS reaction. Plus, adjusting the S/C ratio is necessary to prevent the formation of coke during the SMR process. Additionally, diffusion and mass transfer limitations can be adjusted by varying the flows of reactants while maintaining a constant catalyst loading.
4. Process intensification, accomplished through the utilization of membranes, adsorbents, and chemical looping, has a significant impact on the performance of SMR when heated using fossil fuel combustion. This impact encompasses various aspects, including H_2 separation, catalyst stability, CO_2 capture techniques, and energy integration, ultimately leading to the enhanced production of blue H_2.
5. The consideration of using renewable energy as a heating source for the SMR reformer has led to the establishment of a proof of concept. Previous reports have explored the use of highly conductive alloy-based tubes for indirect heating through electric furnaces, resulting in enhanced heat transfer and quick catalyst activation. Systems assisted by renewable electricity offer easy handling during start-up and shutdown of the SMR system, along with compactness and flexibility in reformer configuration. By harnessing renewable energy sources and DFMs, the simultaneous capture and conversion of CO_2 to methane can be achieved, effectively reducing CO_2 emissions while promoting the production of turquoise H_2.

The outcomes of this review can create incentives for further research into exploiting renewable energy as a heat source and smart materials like DFMs, zeolites, and MXenes to enhance turquoise H_2 production, along with methods to enhance catalyst stability in the SMR process based on ESG profiling.

Declaration of competing interest

The authors declare that they have no known competing financial interests or personal relationships that could have appeared to influence the work reported in this paper.

Data availability

No data was used for the research described in the article.

Acknowledgements

AS gratefully acknowledges the support of the Bolyai Janos Research Fellowship of the Hungarian Academy of Science and the "UNKP-21-5-SZTE-586" New National Excellence Program as well as the funding provided by the Indo-Hungarian TÉT project (2019-2.1.13-TÉT_IN-2020-00015) and FK 143583 of NKFIH and Project no. RRF-2.3.1-21-2022-00009, titled National Laboratory for Renewable Energy has been implemented with the support provided by the Recovery and Resilience Facility of the European Union within the framework of Programme Széchenyi Plan Plus. ZK is grateful for K_21 138714 and

TKP2021-NVA-19 under the TKP2021-NVA funding scheme of the Ministry for Innovation and Technology.

References

[1] Capurso T, Stefanizzi M, Torresi M, Camporeale S. Perspective of the role of hydrogen in the 21st century energy transition. Energy Convers Manag 2022;251:114898.

[2] Saeidi S, Najari S, Hessel V, Wilson K, Keil FJ, Concepción P, et al. Recent advances in CO_2 hydrogenation to value-added products — current challenges and future directions. Prog Energy Combust Sci 2021;85:100905.

[3] Saeidi S, Amin NAS, Rahimpour MR. Hydrogenation of CO_2 to value-added products—a review and potential future developments. J CO2 Util 2014;5:66–81.

[4] Saeidi S, Najari S, Fazlollahi F, Nikoo MK, Sefidkon F, Klemeš JJ, et al. Mechanisms and kinetics of CO_2 hydrogenation to value-added products: a detailed review on current status and future trends. Renew Sustain Energy Rev 2017;80:1292–311.

[5] Najari S, Saeidi S, Gróf G, Keil FJ, Rodrigues AE. Kinetic parameters estimation via dragonfly algorithm (DA) and comparison of cylindrical and spherical reactors performance for CO_2 hydrogenation to hydrocarbons. Energy Convers Manag 2020;226:113550.

[6] Dincer I, Acar C. Review and evaluation of hydrogen production methods for better sustainability. Int J Hydrogen Energy 2015;40:11094–111.

[7] Nikoo MK, Saeidi S, Lohi A. A comparative thermodynamic analysis and experimental studies on hydrogen synthesis by supercritical water gasification of glucose. Clean Technol Environ Policy 2015;17:2267–88.

[8] Nicoletti G, Arcuri N, Nicoletti G, Bruno R. A technical and environmental comparison between hydrogen and some fossil fuels. Energy Convers Manag 2015;89:205–13.

[9] Zhang F, Zhao P, Niu M, Maddy J. The survey of key technologies in hydrogen energy storage. Int J Hydrogen Energy 2016;41:14535–52.

[10] Khoja AH, Tahir M, Amin NAS. Cold plasma dielectric barrier discharge reactor for dry reforming of methane over Ni/ϒ-Al_2O_3 -MgO nanocomposite. Fuel Process Technol 2018;178:166–79.

[11] Newborough M, Cooley G. Developments in the global hydrogen market: the spectrum of hydrogen colours. Fuel Cell Bull 2020;2020:16–22.

[12] Hermesmann M, Müller T. Green, turquoise, blue, or grey? Environmentally friendly hydrogen production in transforming energy systems. Prog Energy Combust Sci 2022;90:100996.

[13] Bartlett J, Krupnick A. Decarbonized hydrogen in the US power and industrial sectors: identifying and incentivizing opportunities to lower emissions. Public Utilities Commission; State of California; Report 20-25, Dec 2020.

[14] Moon S, Lee Y, Seo D, Lee S, Hong S, Ahn Y-H, et al. Critical hydrogen concentration of hydrogen-natural gas blends in clathrate hydrates for blue hydrogen storage. Renew Sustain Energy Rev 2021;141:110789.

[15] Yu M, Wang K, Vredenburg H. Insights into low-carbon hydrogen production methods: green, blue and aqua hydrogen. Int J Hydrogen Energy 2021;46:21261–73.

[16] Antzaras AN, Lemonidou AA. Recent advances on materials and processes for intensified production of blue hydrogen. Renew Sustain Energy Rev 2021;155:111917.

[17] Howarth RW, Jacobson MZ. How green is blue hydrogen? Energy Sci Eng 2021;9:1676–87.

[18] Singh R, Dutta S. A review on H_2 production through photocatalytic reactions using TiO_2/TiO_2-assisted catalysts. Fuel 2018;220:607–20.

[19] Nikolaidis P, Poullikkas A. A comparative overview of hydrogen production processes. Renew Sustain Energy Rev 2017;67:597–611.

[20] Nazir H, Louis C, Jose S, Prakash J, Muthuswamy N, Buan MEM, et al. Is the H_2 economy realizable in the foreseeable future? Part I: H_2 production methods. Int J Hydrogen Energy 2020;45:13777–88.

[21] Noh YS, Lee K-Y, Moon DJ. Hydrogen production by steam reforming of methane over nickel based structured catalysts supported on calcium aluminate modified SiC. Int J Hydrogen Energy 2019;44:21010–9.

[22] Ou Z, Zhang Z, Qin C, Xia H, Deng T, Niu J, et al. Highly active and stable Ni/perovskite catalysts in steam methane reforming for hydrogen production. Sustain Energy Fuels 2021;5:1845–56.

[23] de C, Roseno KT, Schmal M, Brackmann R, Alves RMB, Giudici R. Partial oxidation of methane on neodymium and lanthanium chromate based perovskites for hydrogen production. Int J Hydrogen Energy 2019;44:8166–77.

[24] Wang B, Albarracín-Suazo S, Pagán-Torres Y, Nikolla E. Advances in methane conversion processes. Catalyst 2017;285:147–58.

[25] Abdulrasheed A, Jalil AA, Gambo Y, Ibrahim M, Hambali HU, Hamid MYS. A review on catalyst development for dry reforming of methane to syngas: recent advances. Renew Sustain Energy Rev 2019;108:175–93.

[26] Santos DBL, Noronha FB, Hori CE. Bi-reforming of methane for hydrogen production using $LaNiO_3$/$Ce_xZr_{1-x}O_2$ as precursor material. Int J Hydrogen Energy 2020;45:13947–59.

[27] Chein R-Y, Hsu W-H. Thermodynamic analysis of syngas production via tri-reforming of methane and carbon gasification using flue gas from coal-fired power plants. J Clean Prod 2018;200:242–58.

[28] Lim D, Lee B, Lee H, Byun M, Lim H. Projected cost analysis of hybrid methanol production from tri-reforming of methane integrated with various water electrolysis systems: technical and economic assessment. Renew Sustain Energy Rev 2022;155:111876.

[29] Araújo PM, da Costa KM, Passos FB. Hydrogen production from methane autothermal reforming over $CaTiO_3$, $BaTiO_3$ and $SrTiO_3$ supported nickel catalysts. Int J Hydrogen Energy 2021;46:24107–16.

[30] King B, Patel D, Zhu Chen J, Drapanauskaite D, Handler R, Nozaki T, et al. Comprehensive process and environmental impact analysis of integrated DBD plasma steam methane reforming. Fuel 2021;304:121328.

[31] Spatolisano E, De Guido G, Pellegrini LA, Calemma V, de Angelis AR, Nali M. Process sensitivity analysis and techno-economic assessment of hydrogen sulphide to hydrogen via H_2S methane reformation. J Clean Prod 2022;330:129889.

[32] Spatolisano E, De Guido G, Pellegrini LA, Calemma V, de Angelis AR, Nali M. Hydrogen sulphide to hydrogen via H_2S methane reformation: thermodynamics and process scheme assessment. Int J Hydrogen Energy 2022;47:15612–23.

[33] Ali Khan MH, Daiyan R, Neal P, Haque N, MacGill I, Amal R. A framework for assessing economics of blue hydrogen production from steam methane reforming using carbon capture storage & utilisation. Int J Hydrogen Energy 2021;46:22685–706.

[34] Al-Qahtani A, Parkinson B, Hellgardt K, Shah N, Guillen-Gosalbez G. Uncovering the true cost of hydrogen production routes using life cycle monetisation. Appl Energy 2021;281:115958.

[35] Khojasteh Salkuyeh Y, Saville BA, MacLean HL. Techno-economic analysis and life cycle assessment of hydrogen production from natural gas using current and emerging technologies. Int J Hydrogen Energy 2017;42:18894–909.

[36] Parkinson B, Tabatabaei M, Upham DC, Ballinger B, Greig C, Smart S, et al. Hydrogen production using methane: techno-economics of decarbonizing fuels and chemicals. Int J Hydrogen Energy 2018;43:2540–55.

[37] Sadeghi S, Ghandehariun S, Rosen MA. Comparative economic and life cycle assessment of solar-based hydrogen production for oil and gas industries. Energy 2020;208:118347.

[38] Iulianelli A, Liguori S, Wilcox J, Basile A. Advances on methane steam reforming to produce hydrogen through membrane reactors technology: a review. Catal Rev Sci Eng 2016;58:1–35.

[39] LeValley TL, Richard AR, Fan M. The progress in water gas shift and steam reforming hydrogen production technologies – a review. Int J Hydrogen Energy 2014;39:16983–7000.

[40] Wang Y, Peng J, Zhou C, Lim Z-Y, Wu C, Ye S, et al. Effect of Pr addition on the properties of Ni/Al_2O_3 catalysts with an application in the autothermal reforming of methane. Int J Hydrogen Energy 2014;39:778–87.

[41] Acha E, Requies J, Barrio VL, Cambra JF, Güemez MB, Arias PL. Water effect in hydrogen production from methane. Int J Hydrogen Energy 2010;35:11525–32.

[42] Özdemir H, Faruk Öksüzömer MA, Ali Gürkaynak M. Preparation and characterization of Ni based catalysts for the catalytic partial oxidation of methane: effect of support basicity on H_2/CO ratio and carbon deposition. Int J Hydrogen Energy 2010;35:12147–60.

[43] Jiménez-González C, Boukha Z, de Rivas B, Delgado JJ, Cauqui MÁ, González-Velasco JR, et al. Structural characterisation of Ni/alumina reforming catalysts activated at high temperatures. Appl Catal A-Gen 2013;466:9–20.

[44] Mbodji M, Commenge JM, Falk L, Di Marco D, Rossignol F, Prost L, et al. Steam methane reforming reaction process intensification by using a millistructured reactor: experimental setup and model validation for global kinetic reaction rate estimation. J Chem Eng 2012;207–208:871–84.

[45] Dantas SC, Resende KA, Rossi RL, Assis AJ, Hori CE. Hydrogen production from oxidative reforming of methane on supported nickel catalysts: an experimental and modeling study. J Chem Eng 2012;197:407–13.

[46] Viorel C, Karl S, Monica D, Maria M, Alexandru RB, Petru M, et al. Supported nickel catalysts for low temperature methane steam reforming: comparison between metal additives and support modification. React Kinet Mech Catal 2011;105:173–93.

[47] Vinum MG, Almind MR, Engbæk JS, Vendelbo SB, Hansen MF, Frandsen C, et al. Dual-function cobalt–nickel nanoparticles tailored for high-temperature induction-heated steam methane reforming. Angew Chem Int Ed Engl 2018;130:10729–33.

[48] Katheria S, Deo G, Kunzru D. Rh-Ni/$MgAl_2O_4$ catalyst for steam reforming of methane: effect of Rh doping, calcination temperature and its application on metal monoliths. Appl Catal A-Gen 2019;570:308–18.

[49] Soria MA, Mateos-Pedrero C, Guerrero-Ruiz A, Rodríguez-Ramos I. Thermodynamic and experimental study of combined dry and steam reforming of methane on Ru/ZrO_2-La_2O_3 catalyst at low temperature. Int J Hydrogen Energy 2011;36:15212–20.

[50] Khani Y, Shariatinia Z, Bahadoran F. High catalytic activity and stability of $ZnLaAlO_4$ supported Ni, Pt and Ru nanocatalysts applied in the dry, steam and combined dry-steam reforming of methane. J Chem Eng 2016;299:353–66.

[51] Farooqi AS, Yusuf M, Mohd Zabidi NA, Saidur R, Sanaullah K, Farooqi AS, et al. A comprehensive review on improving the production of rich-hydrogen via combined steam and CO_2 reforming of methane over Ni-based catalysts. Int J Hydrogen Energy 2021;46:31024–40.

[52] Meloni E, Martino M, Palma V. A short review on Ni based catalysts and related engineering issues for methane steam reforming. Catalysts 2020;10: 1-38.

[53] Kabasaeed AE, Al-Fatesh AS, Naeem MA, Ibrahim AA, Fakeeha AH. Catalytic performance of CeO_2 and ZrO_2 supported Co catalysts for hydrogen production via dry reforming of methane. Int J Hydrogen Energy 2015;40:6818–26.

[54] Fan M-S, Abdullah AZ, Bhatia S. Hydrogen production from carbon dioxide reforming of methane over Ni–Co/MgO–ZrO_2 catalyst: process optimization. Int J Hydrogen Energy 2011;36:4875–86.

[55] Bej B, Pradhan NC, Neogi S. Production of hydrogen by steam reforming of methane over alumina supported nano-NiO/SiO_2 catalyst. Catalyst 2013;207:28–35.

[56] de Souza VP, Costa D, dos Santos D, Sato AG, Bueno JMC. Pt-promoted α-Al_2O_3-supported Ni catalysts: effect of preparation conditions on oxi-reduction and catalytic properties for hydrogen production by steam reforming of methane. Int J Hydrogen Energy 2012;37:9985–93.

[57] Son IH, Lee SJ, Roh H-S. Hydrogen production from carbon dioxide reforming of methane over highly active and stable MgO promoted Co–Ni/γ-Al_2O_3 catalyst. Int J Hydrogen Energy 2014;39:3762–70.

[58] Kho ET, Scott J, Amal R. Ni/TiO_2 for low temperature steam reforming of methane. Chem Eng Sci 2016;140:161–70.

[59] Katheria S, Gupta A, Deo G, Kunzru D. Effect of calcination temperature on stability and activity of Ni/$MgAl_2O_4$ catalyst for steam reforming of methane at high pressure condition. Int J Hydrogen Energy 2016;41:14123–32.

[60] Lu Q, Hou Y, Laraib SR, Khalifa O, Li K, Xie W-l, et al. Electro-catalytic steam reforming of methane over Ni-CeO_2/γ-Al_2O_3-MgO catalyst. Fuel Process Technol 2019;192:57–64.

[61] Bicki R, Antoniak-Jurak K, Michalska K, Franczyk E, Konkol M, Kowalik P, et al. The effect of La_2O_3 and CeO_2 modifiers on properties of Ni–Al catalysts for LNG prereforming. Int J Hydrogen Energy 2021;46:11664–76.

[62] Bian Z, Wang Z, Jiang B, Hongmanorom P, Zhong W, Kawi S. A review on perovskite catalysts for reforming of methane to hydrogen production. Renew Sustain Energy Rev 2020;134:110291.

[63] Zhu J, Li H, Zhong L, Xiao P, Xu X, Yang X, et al. Perovskite oxides: preparation, characterizations, and applications in heterogeneous catalysis. ACS Catal 2014;4:2917–40.

[64] Pompeo F, Nichio NN, Ferretti OA, Resasco D. Study of Ni catalysts on different supports to obtain synthesis gas. Int J Hydrogen Energy 2005;30:1399–405.

[65] Soltani R, Rosen MA, Dincer I. Assessment of CO_2 capture options from various points in steam methane reforming for hydrogen production. Int J Hydrogen Energy 2014;39:20266–75.

[66] Choudhary V, Uphade B, Mamman A. Simultaneous steam and CO_2 reforming of methane to syngas over NiO/MgO/SA-5205 in presence and absence of oxygen. Appl Catal A-Gen 1998;168:33–46.

[67] Vita A, Italiano C, Ashraf MA, Pino L, Specchia S. Syngas production by steam and oxy-steam reforming of biogas on monolith-supported CeO_2-based catalysts. Int J Hydrogen Energy 2018;43:11731–44.

[68] Hiramitsu Y, Demura M, Xu Y, Yoshida M, Hirano T. Catalytic properties of pure Ni honeycomb catalysts for methane steam reforming. Appl Catal A-Gen 2015;507:162–8.

[69] Roy PS, Park N-K, Kim K. Metal foam-supported Pd–Rh catalyst for steam methane reforming and its application to SOFC fuel processing. Int J Hydrogen Energy 2014;39:4299–310.

[70] Long Y, Li K, Gu Z, Zhu X, Wei Y, Lu C, et al. Ce-Fe-Zr-O/MgO coated monolithic oxygen carriers for chemical looping reforming of methane to co-produce syngas and H_2. J Chem Eng 2020;388:124190.

[71] Ligthart D, Van Santen R, Hensen E. Influence of particle size on the activity and stability in steam methane reforming of supported Rh nanoparticles. J Catal 2011;280:206–20.

[72] Wu Y, Wang W, Wang K, Zeng Y, Dong D, Shao Z, et al. Morphology and catalytic performance of flake-shaped NiO-Yttria-stabilized zirconia (YSZ) particles with nanocrystalline YSZ grains. Ind Eng Chem Res 2012;51:6387–94.

[73] Chaichi A, Sadrnezhaad S, Malekjafarian M. Synthesis and characterization of supportless Ni-Pd-CNT nanocatalyst for hydrogen production via steam reforming of methane. Int J Hydrogen Energy 2018;43:1319–36.

[74] Silva T, Chaghouri M, Tidahy LH, Gennequin C, Abi-Aad E, Cesario M, et al. Methane reforming reactions for hydrogen production using hydrotalcite precursors and nanofibers based catalysts. 2021 12th International Renewable Energy Congress (IREC): IEEE; 2021. p. 1–4.

[75] Lai G-H, Lak JH, Tsai D-H. Hydrogen production via low-temperature steam–methane reforming using Ni–CeO_2–Al_2O_3 hybrid nanoparticle clusters as catalysts. ACS Appl Energy Mater 2019;2:7963–71.

[76] Etminan A, Sadrnezhaad S. A two step Microwave-assisted coke resistant mesoporous Ni-Co catalyst for methane steam reforming. Fuel 2022;317:122411.

[77] Lopes FV, Grande CA, Ribeiro AM, Vilar VJ, Loureiro JM, Rodrigues AE. Effect of ion exchange on the adsorption of steam methane reforming off-gases on zeolite 13X. J Chem Eng Data 2010;55:184–95.

[78] Lee S, Monai M, Shen K, Chang J, Vohs JM, Gorte RJ. A study of how $LaFeO_3$ and $CaTiO_3$ supports affect the oxidation, hydrogenation, and methane steam reforming activity of Pt and Ni catalysts. J Phys Chem C 2022;126:11619–28.

[79] Qi Y, Cheng Z, Zhou Z. Steam reforming of methane over Ni catalysts prepared from hydrotalcite-type precursors: catalytic activity and reaction kinetics. Chin J Chem Eng 2015;23:76–85.

[80] Bartholomew CH. Carbon deposition in steam reforming and methanation. Catal Rev Sci Eng 1982;24:67–112.

[81] Trimm DL. Catalysts for the control of coking during steam reforming. Catalyst 1999;49:3–10.

[82] Zhang H, Sun Z, Hu YH. Steam reforming of methane: current states of catalyst design and process upgrading. Renew Sustain Energy Rev 2021;149:111330.

[83] Rostrup-Nielsen J, Trimm DL. Mechanisms of carbon formation on nickel-containing catalysts. J Catal 1977;48:155–65.

[84] Chen Z, Po F, Grace JR, Jim Lim C, Elnashaie S, Mahecha-Botero A, et al. Sorbent-enhanced/membrane-assisted steam-methane reforming. Chem Eng Sci 2008;63:170–82.

[85] Silvester L, Antzara A, Boskovic G, Heracleous E, Lemonidou AA, Bukur DB. NiO supported on Al_2O_3 and ZrO_2 oxygen carriers for chemical looping steam methane reforming. Int J Hydrogen Energy 2015;40:7490–501.

[86] Nazir H, Muthuswamy N, Louis C, Jose S, Prakash J, Buan MEM, et al. Is the H_2 economy realizable in the foreseeable future? Part III: H_2 usage technologies, applications, and challenges and opportunities. Int J Hydrogen Energy 2020;45:28217–39.

[87] Alrashed F, Zahid U. Comparative analysis of conventional steam methane reforming and PdAu membrane reactor for the hydrogen production. Comput Chem Eng 2021;154:107497.

[88] Yan Y, Manovic V, Anthony EJ, Clough PT. Techno-economic analysis of low-carbon hydrogen production by sorption enhanced steam methane reforming (SE-SMR) processes. Energy Convers Manag 2020;226:113530.

[89] Lee M, Lim HS, Kim Y, Lee JW. Enhancement of highly-concentrated hydrogen productivity in chemical looping steam methane reforming using Fe-substituted $LaCoO_3$. Energy Convers Manag 2020;207:112507.

[90] Antzaras AN, Heracleous E, Lemonidou AA. Sorption enhanced–chemical looping steam methane reforming: optimizing the thermal coupling of regeneration in a fixed bed reactor. Fuel Process Technol 2020;208:106513.

[91] Yu X, Yang L, Xuan Y, Liu XL, Zhang K. Solar-driven low-temperature reforming of methanol into hydrogen via synergetic photo- and thermocatalysis. Nano Energy 2021;84:105953.

[92] Bukkholm IS. Electric steam methane reforming-Economical and environmental implications of replacing methane with electricity for heating in a steam methane reformer. NTNU; 2021.

[93] Chen L, Qi Z, Zhang S, Su J, Somorjai GA. Catalytic hydrogen production from methane: a review on recent progress and prospect. Catalysts 2020;10.

[94] Saeidi S, Fazlollahi F, Najari S, Iranshahi D, Klemeš JJ, Baxter LL. Hydrogen production: perspectives, separation with special emphasis on kinetics of WGS reaction: a state-of-the-art review. J Ind Eng Chem 2017;49:1–25.

[95] Zhang N, Chen X, Chu B, Cao C, Jin Y, Cheng Y. Catalytic performance of Ni catalyst for steam methane reforming in a micro-channel reactor at high pressure. Chem Eng Process: Process Intensif 2017;118:19–25.

[96] Madeira JGF, Oliveira EM, Springer MV, Cabral HL, Barbeito DfdC, Souza APG, et al. Hydrogen production from swine manure biogas via steam reforming of methane (SRM) and water gas shift (WGS): A ecological, technical, and economic analysis. Int J Hydrogen Energy 2021; 46: 8961-8971.

[97] Osazuwa OU, Abidin SZ, Fan X, Amenaghawon AN, Azizan MT. An insight into the effects of synthesis methods on catalysts properties for methane reforming. J Environ Chem Eng 2021;9:105052.

[98] Wang Y-N, Rodrigues AE. Hydrogen production from steam methane reforming coupled with in situ CO_2 capture: conceptual parametric study. Fuel 2005;84:1778–89.

[99] Antzara A, Heracleous E, Bukur DB, Lemonidou AA. Thermodynamic analysis of hydrogen production via chemical looping steam methane reforming coupled with in situ CO_2 capture. Int J Greenh Gas Control 2015;32:115–28.

[100] Hakizimana P. Modellization of a microreactor for the catalytic partial oxidation of methane. Universitat Politècnica de Catalunya; 2019.

[101] Boyano A, Blanco-Marigorta AM, Morosuk T, Tsatsaronis G. Exergoenvironmental analysis of a steam methane reforming process for hydrogen production. Energy 2011;36:2202–14.

[102] Harrison DP. Sorption-enhanced hydrogen production: a review. Ind Eng Chem Res 2008;47:6486–501.

[103] Yu X, Shen Y, Guan Z, Zhang D, Tang Z, Li W. Multi-objective optimization of ANN-based PSA model for hydrogen purification from steam-methane reforming gas. Int J Hydrogen Energy 2021;46:11740–55.

[104] Xiao J, Peng Y, Bénard P, Chahine R. Thermal effects on breakthrough curves of pressure swing adsorption for hydrogen purification. Int J Hydrogen Energy 2016;41:8236–45.

[105] Turpeinen E, Raudaskoski R, Pongrácz E, Keiski RL. Thermodynamic analysis of conversion of alternative hydrocarbon-based feedstocks to hydrogen. Int J Hydrogen Energy 2008;33:6635–43.

[106] Wismann ST. Electrically heated steam methane reforming: Technical University of Denmark (DTU); PhD Thesis. 2019.

[107] Simsek E, Avci AK, Önsan ZI. Investigation of catalyst performance and microstructured reactor configuration for syngas production by methane steam reforming. Catalyst 2011;178:157–63.

[108] Neni A, Benguerba Y, Balsamo M, Erto A, Ernst B, Benachour D. Numerical study of sorption-enhanced methane steam reforming over Ni/Al_2O_3 catalyst in a fixed-bed reactor. Int J Heat Mass Tran 2021;165:120635.

[109] Shahhosseini HR, Saeidi S, Najari S, Gallucci F. Comparison of conventional and spherical reactor for the industrial auto-thermal reforming of methane to maximize synthesis gas and minimize CO_2. Int J Hydrogen Energy 2017;42:19798–809.

[110] Wang S, Nabavi SA, Clough PT. A review on bi/polymetallic catalysts for steam methane reforming. Int J Hydrogen Energy 2023;48:15879–93.

[111] Pistonesi C, Juan A, Irigoyen B, Amadeo N. Theoretical and experimental study of methane steam reforming reactions over nickel catalyst. Appl Surf Sci 2007;253:4427–37.

[112] Hou K, Hughes R. The kinetics of methane steam reforming over a Ni/α-Al_2O catalyst. J Chem Eng 2001;82:311–28.

[113] Wei J, Iglesia E. Reaction pathways and site requirements for the activation and chemical conversion of methane on Ru−based catalysts. J Phys Chem B 2004;108:7253–62.

[114] Ribeiro NFP, Neto RCR, Moya SF, Souza MMVM, Schmal M. Synthesis of $NiAl_2O_4$ with high surface area as precursor of Ni nanoparticles for hydrogen production. Int J Hydrogen Energy 2010;35:11725–32.

[115] Kim H, Lee Y-H, Lee H, Seo J-C, Lee K. Effect of Mg contents on catalytic activity and coke formation of mesoporous Ni/Mg-aluminate spinel catalyst for steam methane reforming. Catalysts 2020;10.

[116] Aghaali MH, Firoozi S. Enhancing the catalytic performance of Co substituted $NiAl_2O_4$ spinel by ultrasonic spray pyrolysis method for steam and dry reforming of methane. Int J Hydrogen Energy 2021;46:357–73.

[117] Salhi N, Boulahouache A, Petit C, Kiennemann A, Rabia C. Steam reforming of methane to syngas over $NiAl_2O_4$ spinel catalysts. Int J Hydrogen Energy 2011;36:11433–9.

[118] Zhou L, Guo Y, Chen J, Sakurai M, Kameyama H. Trace precious metal Pt doped plate-type anodic alumina Ni catalysts for methane reforming reaction. Fuel 2012;92:373–6.

[119] Baek S-C, Jun K-W, Lee Y-J, Kim JD, Park DY, Lee K-Y. $Ru/Ni/MgAl_2O_4$ catalysts for steam reforming of methane: effects of Ru content on self-activation property. Res Chem Intermed 2012;38:1225–36.

[120] Nawfal M, Gennequin C, Labaki M, Nsouli B, Aboukaïs A, Abi-Aad E. Hydrogen production by methane steam reforming over Ru supported on Ni–Mg–Al mixed oxides prepared via hydrotalcite route. Int J Hydrogen Energy 2015;40:1269–77.

[121] Obradović A, Likozar B, Levec J. Steam methane reforming over Ni-based pellet-type and $Pt/Ni/Al_2O_3$ structured plate-type catalyst: intrinsic kinetics study. Ind Eng Chem Res 2013;52:13597–606.

[122] Wu H, La Parola V, Pantaleo G, Puleo F, Venezia AM, Liotta LF. Ni-based catalysts for low temperature methane steam reforming: recent results on Ni-Au and comparison with other Bi-metallic systems. Catalysts 2013;3: 563-583.

[123] Parizotto NV, Rocha KO, Damyanova S, Passos FB, Zanchet D, Marques CMP, et al. Alumina-supported Ni catalysts modified with silver for the steam reforming of methane: effect of Ag on the control of coke formation. Appl Catal A-Gen 2007;330:12–22.

[124] Zarei-Jelyani F, Salahi F, Farsi M, Rahimpour MR. Synthesis and application of Ni-Co bimetallic catalysts supported on hollow sphere Al_2O_3 in steam methane reforming. Fuel 2022;324:124785.

[125] Zhang X, Su Y, Pei C, Zhao Z-J, Liu R, Gong J. Chemical looping steam reforming of methane over Ce-doped perovskites. Chem Eng Sci 2020;223:115707.

[126] Zhao K, Zhang R, Gao Y, Lin Y, Liu A, Wang X, et al. High syngas selectivity and near pure hydrogen production in perovskite oxygen carriers for chemical looping steam methane reforming. Fuel Process Technol 2022;236:107398.

[127] Liao X, Xiao H, Haribal V, Shi X, Huang Z, Zhu L, et al. Highly efficient reduction of O_2-containing CO_2 via chemical looping based on perovskite nanocomposites. Nano Energy 2020;78:105320.

[128] Yin X, Shen L, Wang S, Wang B, Shen C. Double adjustment of Co and Sr in $LaMnO_{3+\delta}$ perovskite oxygen carriers for chemical looping steam methane reforming. Appl Catal B Environ 2022;301:120816.

[129] Ganesh I. A review on magnesium aluminate ($MgAl_2O_4$) spinel: synthesis, processing and applications. Int Mater Rev 2013;58:63–112.

[130] Yoon Y, Kim H, Lee J. Enhanced catalytic behavior of Ni alloys in steam methane reforming. J Power Sources 2017;359:450–7.

[131] Yin X, Wang S, Wang B, Shen L. Chemical looping steam methane reforming using Al doped $LaMnO_{3+\delta}$ perovskites as oxygen carriers. Int J of Hydrogen Energy 2021:4633375–87.

[132] Cho E, Lee Y-H, Kim H, Jang EJ, Kwak JH, Lee K, et al. Ni catalysts for dry methane reforming prepared by A-site exsolution on mesoporous defect spinel magnesium aluminate. Appl Catal A-Gen 2020;602:117694.

[133] Basile F, Benito P, Fornasari G, Vaccari A. Hydrotalcite-type precursors of active catalysts for hydrogen production. Appl Clay Sci 2010;48:250–9.

[134] Fonseca A, Assaf EM. Production of the hydrogen by methane steam reforming over nickel catalysts prepared from hydrotalcite precursors. J Power Sources 2005;142:154–9.

[135] Matsumura Y, Nakamori T. Steam reforming of methane over nickel catalysts at low reaction temperature. Appl Catal A-Gen 2004;258:107–14.

[136] Li G, Hu L, Hill JM. Comparison of reducibility and stability of alumina-supported Ni catalysts prepared by impregnation and co-precipitation. Appl Catal A-Gen 2006;301:16–24.

[137] Zhou L, Guo Y, Zhang Q, Yagi M, Hatakeyama J, Li H, et al. A novel catalyst with plate-type anodic alumina supports, $Ni/NiAl_2O_4/\gamma\text{-}Al_2O_3$/alloy, for steam reforming of methane. Appl Catal A-Gen 2008;347:200–7.

[138] Rostrup-Nielsen JR. Production of synthesis gas. Catalyst 1993;18:305–24.

[139] Wei J, Iglesia E. Structural requirements and reaction pathways in methane activation and chemical conversion catalyzed by rhodium. J Catal 2004;225:116–27.

[140] Blaylock DW, Zhu Y-A, Green WH. Computational investigation of the thermochemistry and kinetics of steam methane reforming over a multi-faceted nickel catalyst. Top Catal 2011;54:828.

[141] Zhao K, Zheng A, Li H, He F, Huang Z, Wei G, et al. Exploration of the mechanism of chemical looping steam methane reforming using double perovskite-type oxides $La_{1.6}Sr_{0.4}FeCoO_6$. Appl Catal B Environ 2017;219:672–82.

[142] Rostrup-Nielsen JR, Sehested J, Nørskov JK. Hydrogen and synthesis gas by steam- and CO_2 reforming. Advances in Catalysis: Academic Press; 2002. p. 65–139.

[143] Kim H-W, Kang K-M, Kwak H-Y, Kim JH. Preparation of supported Ni catalysts on various metal oxides with core/shell structures and their tests for the steam reforming of methane. J Chem Eng 2011;168:775–83.

[144] Roh H-S, Jun K-W, Dong W-S, Park S-E, Baek Y-S. Highly stable Ni catalyst supported on $Ce\text{–}ZrO_2$ for oxy-steam reforming of methane. Catal Lett 2001;74:31–6.

[145] Di Giuliano A, Gallucci K. Sorption enhanced steam methane reforming based on nickel and calcium looping: a review. Chem Eng Process: Process Intensif 2018;130:240–52.

[146] You X, Wang X, Ma Y, Liu J, Liu W, Xu X, et al. $Ni\text{-}Co/Al_2O_3$ bimetallic catalysts for CH_4 steam reforming: elucidating the role of Co for improving coke resistance. ChemCatChem 2014;6:3377–86.

[147] Bartholomew CH. Mechanisms of catalyst deactivation. Appl Catal A-Gen 2001;212:17–60.

[148] Wei J, Iglesia E. Isotopic and kinetic assessment of the mechanism of reactions of CH_4 with CO_2 or H_2O to form synthesis gas and carbon on nickel catalysts. J Catal 2004;224:370–83.

[149] Sekine Y, Haraguchi M, Matsukata M, Kikuchi E. Low temperature steam reforming of methane over metal catalyst supported on $CexZr_{1-x}O_2$ in an electric field. Catalyst 2011;171:116–25.

[150] Bian Z, Das S, Wai MH, Hongmanorom P, Kawi S. A review on bimetallic nickel-based catalysts for CO_2 reforming of methane. ChemPhysChem 2017;18:3117–34.

[151] Pashchenko D, Makarov I. Carbon deposition in steam methane reforming over a Ni-based catalyst: experimental and thermodynamic analysis. Energy 2021;222:119993.

[152] Zeppieri M, Villa PL, Verdone N, Scarsella M, De Filippis P. Kinetic of methane steam reforming reaction over nickel- and rhodium-based catalysts. Appl Catal A-Gen 2010;387:147–54.

[153] Jones G, Jakobsen JG, Shim SS, Kleis J, Andersson MP, Rossmeisl J, et al. First principles calculations and experimental insight into methane steam reforming over transition metal catalysts. J Catal 2008;259:147–60.

[154] Wang Y, Wang H, Dam AH, Xiao L, Qi Y, Niu J, et al. Understanding effects of Ni particle size on steam methane reforming activity by combined experimental and theoretical analysis. Catalyst 2020;355:139–47.

[155] Wu C, Xiao Z, Wang L, Li G, Zhang X, Wang L. Modulating oxidation state of Ni/CeO_2 catalyst for steam methane reforming: a theoretical prediction with experimental verification. Catal Sci Technol 2021;11:1965–73.

[156] Ligthart DM, Pieterse JA, Hensen EJ. The role of promoters for Ni catalysts in low temperature (membrane) steam methane reforming. Appl Catal A-Gen 2011;405:108–19.

[157] Helveg S, Lopez-Cartes C, Sehested J, Hansen PL, Clausen BS, Rostrup-Nielsen JR, et al. Atomic-scale imaging of carbon nanofibre growth. Nature 2004;427:426–9.

[158] Maluf SS, Assaf EM. Ni catalysts with Mo promoter for methane steam reforming. Fuel 2009;88:1547–53.

[159] Xu J, Chen L, Tan KF, Borgna A, Saeys M. Effect of boron on the stability of Ni catalysts during steam methane reforming. J Catal 2009;261:158–65.

[160] Xu J, Saeys M. Improving the coking resistance of Ni-based catalysts by promotion with subsurface boron. J Catal 2006;242:217–26.

[161] Bengaard HS, Nørskov JK, Sehested J, Clausen B, Nielsen L, Molenbroek A, et al. Steam reforming and graphite formation on Ni catalysts. J Catal 2002;209:365–84.

[162] Nieva MA, Villaverde MM, Monzón A, Garetto TF, Marchi AJ. Steam-methane reforming at low temperature on nickel-based catalysts. J Chem Eng 2014;235:158–66.

[163] Rodemerck U, Schneider M, Linke D. Improved stability of Ni/SiO_2 catalysts in CO_2 and steam reforming of methane by preparation via a polymer-assisted route. Catal Commun 2017;102:98–102.

[164] Siang TJ, Danh HT, Singh S, Truong QD, Setiabudi HD, Vo D-VN. Syngas production from combined steam and carbon dioxide reforming of methane over Ce-modified silica-supported nickel catalysts. Chem. Eng. Trans 2017;56:1129–34.

[165] Ali S, Al-Marri MJ, Abdelmoneim AG, Kumar A, Khader MM. Catalytic evaluation of nickel nanoparticles in methane steam reforming. Int J Hydrogen Energy 2016;41:22876–85.

[166] Rogers JL, Mangarella MC, D'Amico AD, Gallagher JR, Dutzer MR, Stavitski E, et al. Differences in the nature of active sites for methane dry reforming and methane steam reforming over nickel aluminate catalysts. ACS Catal 2016;6:5873–86.

[167] Oh Y-S, Roh H-S, Jun K-W, Baek Y-S. A highly active catalyst, $Ni/Ce\text{–}ZrO_2/\theta\text{-}Al_2O_3$, for on-site H_2 generation by steam methane reforming: pretreatment effect. Int J Hydrogen Energy 2003;28:1387–92.

[168] Silveira EB, Rabelo-Neto RC, Noronha FB. Steam reforming of toluene, methane and mixtures over Ni/ZrO_2 catalysts. Catalyst 2017;289:289–301.

[169] Lertwittayanon K, Atong D, Aungkavattana P, Wasanapiarnpong T, Wada S, Sricharoenchaikul V. Effect of $CaO\text{–}ZrO_2$ addition to Ni supported on $\gamma\text{-}Al_2O_3$ by sequential impregnation in steam methane reforming. Int J Hydrogen Energy 2010;35:12277–85.

[170] Guo X, Sun Y, Yu Y, Zhu X, Liu C-j. Carbon formation and steam reforming of methane on silica supported nickel catalysts. Catal Commun 2012;19:61–5.

[171] Miura S, Umemura Y, Shiratori Y, Kitaoka T. In situ synthesis of Ni/MgO catalysts on inorganic paper-like matrix for methane steam reforming. J Chem Eng 2013;229:515–21.

[172] Shinde VM, Madras G. Catalytic performance of highly dispersed Ni/TiO_2 for dry and steam reforming of methane. RSC Adv 2014;4:4817–26.

[173] Andrade ML, Almeida L, do Carmo Rangel M, Pompeo F, Nichio N. Ni-catalysts supported on Gd-doped ceria for solid oxide fuel cells in methane steam reforming. Chem Eng Technol 2014;37:343–8.

[174] Zhang Y, Wang W, Wang Z, Zhou X, Wang Z, Liu C-J. Steam reforming of methane over Ni/SiO_2 catalyst with enhanced coke resistance at low steam to methane ratio. Catalyst 2015;256:130–6.

[175] Lim Z-Y, Wu C, Wang WG, Choy K-L, Yin H. Porosity effect on ZrO_2 hollow shells and hydrothermal stability for catalytic steam reforming of methane. J Mater Chem 2016;4:153–9.

[176] Mundhwa M, Thurgood CP. Methane steam reforming at low steam to carbon ratios over alumina and yttria-stabilized-zirconia supported nickel-spinel catalyst: experimental study and optimization of microkinetic model. Fuel Process Technol 2017;168:27–39.

[177] Yang X, Da J, Yu H, Wang H. Characterization and performance evaluation of Ni-based catalysts with Ce promoter for methane and hydrocarbons steam reforming process. Fuel 2016;179:353–61.

[178] Mei D, Glezakou V-A, Lebarbier V, Kovarik L, Wan H, Albrecht KO, et al. Highly active and stable $MgAl_2O_4$-supported Rh and Ir catalysts for methane steam reforming: a combined experimental and theoretical study. J Catal 2014;316:11–23.

[179] Lee SM, Won JM, Kim GJ, Lee SH, Kim SS, Hong SC. Improving carbon tolerance of Ni-YSZ catalytic porous membrane by palladium addition for low temperature steam methane reforming. Appl Surf Sci 2017;419:788–94.

[180] Niu J, Wang Y, Qi Y, Dam AH, Wang H, Zhu Y-A, et al. New mechanism insights into methane steam reforming on Pt/Ni from DFT and experimental kinetic study. Fuel 2020;266:117143.

[181] de Castro TP, Silveira EB, Rabelo-Neto RC, Borges LEP, Noronha FB. Study of the performance of Pt/Al_2O_3 and $Pt/CeO_2/Al_2O_3$ catalysts for steam reforming of toluene, methane and mixtures. Catalyst 2018;299:251–62.

[182] Duarte RB, Krumeich F, van Bokhoven JA. Structure, activity, and stability of atomically dispersed Rh in methane steam reforming. ACS Catal 2014;4:1279–86.

[183] Farmer JA, Campbell CT. Ceria maintains smaller metal catalyst particles by strong metal-support bonding. Science 2010;329:933.

[184] Borowiecki T, Denis A, Rawski M, Gołębiowski A, Stołecki K, Dmytrzyk J, et al. Studies of potassium-promoted nickel catalysts for methane steam reforming: effect of surface potassium location. Appl Surf Sci 2014;300:191–200.

[185] Lee SM, Hong SC. Effect of palladium addition on catalytic activity in steam methane reforming over Ni-YSZ porous membrane. Int J Hydrogen Energy 2014;39:21037–43.

[186] Kusakabe K, Sotowa K-I, Eda T, Iwamoto Y. Methane steam reforming over Ce–ZrO_2-supported noble metal catalysts at low temperature. Fuel Process Technol 2004;86:319–26.

[187] Vahid Shahed G, Taherian Z, Khataee A, Meshkani F, Orooji Y. Samarium-impregnated nickel catalysts over SBA-15 in steam reforming of CH_4 process. J Ind Eng Chem 2020;86:73–80.

[188] Lucrédio AF, Assaf EM. Cobalt catalysts prepared from hydrotalcite precursors and tested in methane steam reforming. J Power Sources 2006;159:667–72.

[189] Roy PS, Park CS, Raju ASK, Kim K. Steam-biogas reforming over a metal-foam-coated (Pd–Rh)/($CeZrO_2$–Al_2O_3) catalyst compared with pellet type alumina-supported Ru and Ni catalysts. J CO2 Util 2015;12:12–20.

[190] Wei Z, Sun J, Li Y, Datye AK, Wang Y. Bimetallic catalysts for hydrogen generation. Chem Soc Rev 2012;41:7994–8008.

[191] Jaiswar VK, Katheria S, Deo G, Kunzru D. Effect of Pt doping on activity and stability of Ni/$MgAl_2O_4$ catalyst for steam reforming of methane at ambient and high pressure condition. Int J Hydrogen Energy 2017;42:18968–76.

[192] Kim Y, Cho E, Ko CH. Preparation of Ni-based egg-shell-type catalyst on cylinder-shaped alumina pellets and its application for hydrogen production via steam methane reforming. Int J Hydrogen Energy 2019;44:5314–23.

[193] Cho EH, Koo KY, Lee HW, Park Y-K, Yoon WL, Ko CH. Preparation of egg-shell-type Ni/Ru bimetal alumina pellet catalysts: steam methane reforming for hydrogen production. Int J Hydrogen Energy 2017;42:18350–7.

[194] Zhang J, Wang H, Dalai AK. Effects of metal content on activity and stability of Ni-Co bimetallic catalysts for CO_2 reforming of CH_4. Appl Catal A-Gen 2008;339:121–9.

[195] Koh ACW, Chen L, Kee Leong W, Johnson BFG, Khimyak T, Lin J. Hydrogen or synthesis gas production via the partial oxidation of methane over supported nickel–cobalt catalysts. Int J Hydrogen Energy 2007;32:725–30.

[196] Chen L, Zhu Q, Wu R. Effect of Co–Ni ratio on the activity and stability of Co–Ni bimetallic aerogel catalyst for methane Oxy-CO_2 reforming. Int J Hydrogen Energy 2011;36:2128–36.

[197] Yu Y, Jin G, Wang Y, Guo X. Synthesis of natural gas from CO methanation over SiC supported Ni–Co bimetallic catalysts. Catal Commun 2013;31:5–10.

[198] Zhang J, Wang H, Dalai AK. Development of stable bimetallic catalysts for carbon dioxide reforming of methane. J Catal 2007;249:300–10.

[199] Wang M, Fu Z, Yang Z. Tuning the performance of Ni-based catalyst by doping coinage metal on steam reforming of methane and carbon-tolerance. Fuel Cell 2014;14:251–8.

[200] Homsi D, Aouad S, Gennequin C, Aboukaïs A, Abi-Aad E. A highly reactive and stable $Ru/Co_{6-x}Mg_xAl_2$ catalyst for hydrogen production via methane steam reforming. Int J Hydrogen Energy 2014;39:10101–7.

[201] Boudjeloud M, Boulahouache A, Rabia C, Salhi N. La-doped supported Ni catalysts for steam reforming of methane. Int J Hydrogen Energy 2019;44:9906–13.

[202] Itkulova SS, Nurmakanov Y, Kussanova S, Boleubaev Y. Production of a hydrogen-enriched syngas by combined CO_2-steam reforming of methane over Co-based catalysts supported on alumina modified with zirconia. Catalyst 2018;299:272–9.

[203] Ashraf MA, Sanz O, Montes M, Specchia S. Insights into the effect of catalyst loading on methane steam reforming and controlling regime for metallic catalytic monoliths. Int J Hydrogen Energy 2018;43:11778–92.

[204] Zhai X, Ding S, Liu Z, Jin Y, Cheng Y. Catalytic performance of Ni catalysts for steam reforming of methane at high space velocity. Int J Hydrogen Energy 2011;36:482–9.

[205] Lazar MD, Dan M, Mihet M, Almasan V, Rednic V, Borodi G. Hydrogen production by low temperature methane steam reforming using Ag and Au modified alumina supported nickel catalysts. Rev Roum Chem 2011;56:637–42.

[206] Shen Q, Jiang Y, Xia F, Wang B, Lv X, Ye W, et al. Hydrogen production by Co-based bimetallic nano-catalysts and their performance in methane steam reforming. Petrol Sci Technol 2020;38:618–25.

[207] Yoshida K, Begum N, Ito S-i, Tomishige K. Oxidative steam reforming of methane over Ni/α-Al_2O_3 modified with trace noble metals. Appl Catal A-Gen 2009;358:186–92.

[208] Miyata T, Li D, Shiraga M, Shishido T, Oumi Y, Sano T, et al. Promoting effect of Rh, Pd and Pt noble metals to the Ni/Mg(Al)O catalysts for the DSS-like operation in CH_4 steam reforming. Appl Catal A-Gen 2006;310:97–104.

[209] Mohamedali M, Henni A, Ibrahim H. Recent advances in supported metal catalysts for syngas production from methane. ChemEngineering 2018;2:1-23..

[210] Li B, Maruyama K, Nurunnabi M, Kunimori K, Tomishige K. Effect of Ni loading on catalyst bed temperature in oxidative steam reforming of methane over α-Al_2O_3-supported Ni catalysts. Ind Eng Chem Res 2005;44:485–94.

[211] Araújo JCS, Oton LF, Bessa B, Neto ABS, Oliveira AC, Lang R, et al. The role of Pt loading on La_2O_3-Al_2O_3 support for methane conversion reactions via partial oxidation and steam reforming. Fuel 2019;254:115681.

[212] Jaffar MM, Nahil MA, Williams PT. Synthetic natural gas production from the three stage (i) pyrolysis (ii) catalytic steam reforming (iii) catalytic hydrogenation of waste biomass. Fuel Process Technol 2020;208:106515.

[213] Athayde DD, Souza DF, Silva AMA, Vasconcelos D, Nunes EHM, Diniz da Costa JC, et al. Review of perovskite ceramic synthesis and membrane preparation methods. Ceram Int 2016;42:6555–71.

[214] Maneerung T, Hidajat K, Kawi S. Co-production of hydrogen and carbon nanofibers from catalytic decomposition of methane over $LaNi_{(1-x)}M_x\ O_{3-\alpha}$ perovskite (where M = Co, Fe and X = 0, 0.2, 0.5, 0.8, 1). Int J Hydrogen Energy 2015;40:13399–411.

[215] Abd Mutalib M, Aziz F, Ismail AF, Wan Salleh WN, Yusof N, Jaafar J, et al. Towards high performance perovskite solar cells: a review of morphological control and HTM development. Appl Mater Today 2018;13:69–82.

[216] Shi Z, Jayatissa AH. Perovskites-based solar cells: a review of recent progress, materials and processing methods. Mater 2018;11.

[217] Li L, Jiang B, Sun Z, Zhang Q, Li D, Tang D. Hydrogen production from chemical looping steam reforming of ethanol over perovskite-type oxygen carriers with bimetallic Co and Ni B-site substitution. Catalysts 2018;8.

[218] Parravano G. Ferroelectric transitions and heterogenous catalysis. J Chem Phys 1952;20:342–3.

[219] Yeo TY, Ashok J, Kawi S. Recent developments in sulphur-resilient catalytic systems for syngas production. Renew Sustain Energy Rev 2019;100:52–70.

[220] Oemar U, Ang PS, Hidajat K, Kawi S. Promotional effect of Fe on perovskite $LaNi_xFe_{1-x}O_3$ catalyst for hydrogen production via steam reforming of toluene. Int J Hydrogen Energy 2013;38:5525–34.

[221] Lin K-H, Wang C-B, Chien S-H. Catalytic performance of steam reforming of ethanol at low temperature over $LaNiO_3$ perovskite. Int J Hydrogen Energy 2013;38:3226–32.

[222] Urasaki K, Sekine Y, Kawabe S, Kikuchi E, Matsukata M. Catalytic activities and coking resistance of Ni/perovskites in steam reforming of methane. Appl Catal A-Gen 2005;286:23–9.

[223] Dama S, Ghodke S, Bobade R, Gurav H, Chilukuri S. Tuning the dimensionality of layered $Sr_{n+1}Ti_{n-x}Ni_xO_{3n+1}$ perovskite structures for improved activity in syngas generation. J Catal 2018;360:27–39.

[224] Yin X, Wang S, Wang B, Shen L. Perovskite-type $LaMn_{1-x}B_xO_{3+\delta}$ (B = Fe, Co and Ni) as oxygen carriers for chemical looping steam methane reforming. J Chem Eng 2021:128751.

[225] De Guido G, Compagnoni M, Pellegrini LA, Rossetti I. Mature versus emerging technologies for CO_2 capture in power plants: key open issues in post-combustion amine scrubbing and in chemical looping combustion. Front Chem Sci Eng 2018;12:315–25.

[226] Zhao K, He F, Huang Z, Zheng A, Li H, Zhao Z. Three-dimensionally ordered macroporous $LaFeO_3$ perovskites for chemical-looping steam reforming of methane. Int J Hydrogen Energy 2014;39:3243–52.

[227] Carrasco-Díaz MR, Castillejos-López E, Cerpa-Naranjo A, Rojas-Cervantes ML. Efficient removal of paracetamol using $LaCu_{1-x}M_xO_3$ (M=Mn, Ti) perovskites as heterogeneous Fenton-like catalysts. J Chem Eng 2016;304:408–18.

[228] Hong K, Sutanto SN, Lee JA, Hong J. Ni-based bimetallic nano-catalysts anchored on $BaZr_{0.4}Ce_{0.4}Y_{0.1}Yb_{0.1}O_{3-\delta}$ for internal steam reforming of methane in a low-temperature proton-conducting ceramic fuel cell. J Mater Chem 2021;9:6139–51.

[229] Huang Y-H, Liang G, Croft M, Lehtimäki M, Karppinen M, Goodenough JB. Double-perovskite anode materials Sr_2MMoO_6 (M = Co, Ni) for solid oxide fuel cells. Chem Mater 2009;21:2319–26.

[230] Tuza PV, Souza MM. Steam reforming of methane over catalyst derived from ordered double perovskite: effect of crystalline phase transformation. Catal Lett 2016;146:47–53.

[231] Mosayebi A, Nasabi M. Steam methane reforming on $LaNiO_3$ perovskite-type oxide for syngas production, activity tests, and kinetic modeling. Int J Energy Res 2020;44:5500–15.

[232] He F, Chen J, Liu S, Huang Z, Wei G, Wang G, et al. $La_{1-x}Sr_xFeO_3$ perovskite-type oxides for chemical-looping steam methane reforming: identification of the surface elements and redox cyclic performance. Int J Hydrogen Energy 2019;44:10265–76.

[233] Zhao K, He F, Huang Z, Wei G, Zheng A, Li H, et al. Perovskite-type $LaFe_{1-x}Mn_xO_3$ (x=0, 0.3, 0.5, 0.7, 1.0) oxygen carriers for chemical-looping steam methane reforming: oxidation activity and resistance to carbon formation. Kor J Chem Eng 2017;34:1651–60.
[234] Ding H, Luo C, Li X, Cao D, Shen Q, Zhang L. Development of BaSrCo-based perovskite for chemical-looping steam methane reforming: a study on synergistic effects of A-site elements and CeO_2 support. Fuel 2019;253:311–9.
[235] Ding H, Xu Y, Luo C, Wang Q, Shen C, Xu J, et al. A novel composite perovskite-based material for chemical-looping steam methane reforming to hydrogen and syngas. Energy Convers Manag 2018;171:12–9.
[236] Zhai X, Cheng Y, Zhang Z, Jin Y, Cheng Y. Steam reforming of methane over Ni catalyst in micro-channel reactor. Int J Hydrogen Energy 2011;36:7105–13.
[237] Stutz MJ, Hotz N, Poulikakos D. Optimization of methane reforming in a microreactor—effects of catalyst loading and geometry. Chem Eng Sci 2006;61:4027–40.
[238] Arzamendi G, Diéguez PM, Montes M, Odriozola JA, Sousa-Aguiar EF, Gandía LM. Methane steam reforming in a microchannel reactor for GTL intensification: a computational fluid dynamics simulation study. J Chem Eng 2009;154:168–73.
[239] Ashraf MA, Sanz O, Italiano C, Vita A, Montes M, Specchia S. Analysis of Ru/La-Al_2O_3 catalyst loading on alumina monoliths and controlling regimes in methane steam reforming. J Chem Eng 2018;334:1792–807.
[240] Karthik G, Buwa VV. Effect of particle shape on fluid flow and heat transfer for methane steam reforming reactions in a packed bed. AIChE J 2017;63:366–77.
[241] Karthik G, Buwa VV. A computational approach for the selection of optimal catalyst shape for solid-catalysed gas-phase reactions. React. Chem. Eng 2020;5:163–82.
[242] Pashchenko D. Experimental investigation of reforming and flow characteristics of a steam methane reformer filled with nickel catalyst of various shapes. Energy Convers Manag 2019;185:465–72.
[243] Han J-R, Park S-J, Kim H, Lee S, Lee JM. Centralized and distributed hydrogen production using steam reforming: challenges and perspectives. Sustain Energy Fuels 2022;6:1923-1939.
[244] Dunker AM, Ortmann JP. Kinetic modeling of hydrogen production by thermal decomposition of methane. Int J Hydrogen Energy 2006;31:1989–98.
[245] Damm DL, Fedorov AG. Comparative assessment of batch reactors for scalable hydrogen production. Ind Eng Chem Res 2008;47:4665–74.
[246] Salciccioli M, Stamatakis M, Caratzoulas S, Vlachos DG. A review of multiscale modeling of metal-catalyzed reactions: mechanism development for complexity and emergent behavior. Chem Eng Sci 2011;66:4319–55.
[247] Aparicio LM. Transient isotopic studies and microkinetic modeling of methane reforming over nickel catalysts. J Catal 1997;165:262–74.
[248] Wang Y, Yoshiba F, Kawase M, Watanabe T. Performance and effective kinetic models of methane steam reforming over Ni/YSZ anode of planar SOFC. Int J Hydrogen Energy 2009;34:3885–93.
[249] Batebi D, Abedini R, Mosayebi A. Kinetic modeling of combined steam and CO_2 reforming of methane over the Ni–Pd/Al_2O_3 catalyst using Langmuir–hinshelwood and Langmuir–freundlich isotherms. Ind Eng Chem Res 2021;60:851–63.
[250] Xu J, Froment GF. Methane steam reforming, methanation and water-gas shift: I. Intrinsic kinetics. AIChE J 1989;35:88–96.
[251] Ke C, Lin Z. Elementary reaction pathway study and a deduced macrokinetic model for the unified understanding of Ni-catalyzed steam methane reforming. React. Chem. Eng 2020;5:873–85.
[252] Zhu W, Yang B. First-Principles-based microkinetic modeling of methane steam reforming with improved description of product desorption. J Phys Chem C 2021;125:18743–51.
[253] Jalid F, Haider MA, Alam MI, Khan TS. Mechanistic insights into the dominant reaction route and catalyst deactivation in biogas reforming using ab initio microkinetic modeling. Catal Sci Technol 2021;11:2130–43.
[254] Kechagiopoulos PN, Angeli SD, Lemonidou AA. Low temperature steam reforming of methane: a combined isotopic and microkinetic study. Appl Catal B Environ 2017;205:238–53.
[255] Maier L, Schädel B, Delgado KH, Tischer S, Deutschmann O. Steam reforming of methane over nickel: development of a multi-step surface reaction mechanism. Top Catal 2011;54:845.
[256] Che F, Gray JT, Ha S, McEwen J-S. Reducing reaction temperature, steam requirements, and coke formation during methane steam reforming using electric fields: a microkinetic modeling and experimental study. ACS Catal 2017;7:6957–68.
[257] Chen D, Lødeng R, Svendsen H, Holmen A. Hierarchical multiscale modeling of methane steam reforming reactions. Ind Eng Chem Res 2011;50:2600–12.
[258] Fabrik M, Salama A, Ibrahim H. State-of-the-art in methane-reforming reactor modeling: challenges and new insights. Rev Chem Eng 2022; 38: 991-1022.
[259] Bhat SA, Sadhukhan J. Process intensification aspects for steam methane reforming: an overview. AIChE J 2009;55:408–22.
[260] de Jong M, Reinders AHME, Kok JBW, Westendorp G. Optimizing a steam-methane reformer for hydrogen production. Int J Hydrogen Energy 2009;34:285–92.
[261] Patil CS, van Sint Annaland M, Kuipers JAM. Fluidised bed membrane reactor for ultrapure hydrogen production via methane steam reforming: experimental demonstration and model validation. Chem Eng Sci 2007;62:2989–3007.
[262] Patil CS. Membrane reactor technology for ultrapure hydrogen production. University of Twente; Ph.D. Thesis; 2005.
[263] Barrio VL, Schaub G, Rohde M, Rabe S, Vogel F, Cambra JF, et al. Reactor modeling to simulate catalytic partial oxidation and steam reforming of methane. Comparison of temperature profiles and strategies for hot spot minimization. Int J Hydrogen Energy 2007;32:1421–8.
[264] Vo ND, Kang J-H, Oh M, Lee C-H. Dynamic model and performance of an integrated sorption-enhanced steam methane reforming process with separators for the simultaneous blue H_2 production and CO_2 capture. J Chem Eng 2021;423:130044.
[265] Assaf ME, Cdf dJ, Assaf JM. Mathematical modelling of methane steam reforming in a membrane reactor: an isothermic model. Braz J Chem Eng 1998;15.
[266] Singh CP, Saraf DN. Simulation of side fired steam-hydrocarbon reformers. Ind Eng Chem Process Des Dev 1979;18:1–7.
[267] Shu J, Grandjean BPA, Kaliaguine S. Methane steam reforming in asymmetric Pd- and Pd-Ag/porous SS membrane reactors. Appl Catal A-Gen 1994;119:305–25.
[268] Itoh N, Xu WC, Haraya K. Radial mixing diffusion of hydrogen in a packed-bed type of palladium membrane reactor. Ind Eng Chem Res 1994;33:197–202.
[269] Itoh N. Chapter III.4 simultaneous operation of reaction and separation by a membrane reactor. In: Misono M, Moro-oka Y, Kimura S, editors. Studies in surface science and catalysis. Elsevier; 1990. p. 268–83.
[270] Caxiano IN, de Sousa Santos L, Prata DM. Sensitivity analysis and optimization of a membrane reactor for hydrogen production through methane steam reforming. Revista Mundi Engenharia, Tecnologia e Gestão 2020:5. ISSN: 2525-4782.
[271] Vigneault A, Elnashaie SS, Grace JR. Simulation of a compact multichannel membrane reactor for the production of pure hydrogen via steam methane reforming. Chem Eng Technol 2012;35:1520–33.
[272] Rusten HK, Ochoa-Fernández E, Chen D, Jakobsen HA. Numerical investigation of sorption enhanced steam methane reforming using Li_2ZrO_3 as CO_2-acceptor. Ind Eng Chem Res 2007;46:4435–43.
[273] Froment GF, Bischoff KB, De Wilde J. Chemical reactor analysis and design. New York: Wiley; 1990.
[274] Fernandez JR, Abanades JC, Murillo R. Modeling of sorption enhanced steam methane reforming in an adiabatic fixed bed reactor. Chem Eng Sci 2012;84:1–11.
[275] Xiu G-h, Li P, Rodrigues A E. Sorption-enhanced reaction process with reactive regeneration. J Chem Eng 2002;57:3893–908.
[276] Lee DK, Baek IH, Yoon WL. Modeling and simulation for the methane steam reforming enhanced by in situ CO_2 removal utilizing the CaO carbonation for H_2 production. Chem Eng Sci 2004;59:931–42.
[277] Reijers HTJ, Boon J, Elzinga GD, Cobden PD, Haije WG, Brink RWvd. Modeling study of the sorption-enhanced reaction process for CO_2 capture. II. Application to steam-methane reforming. Ind Eng Chem Res 2009;48:6975–82.
[278] Solsvik J, Jakobsen HA. Modeling of multicomponent mass diffusion in porous spherical pellets: application to steam methane reforming and methanol synthesis. Chem Eng Sci 2011;66:1986–2000.
[279] Wang J, Wei S, Wang Q, Sundén B. Transient numerical modeling and model predictive control of an industrial-scale steam methane reforming reactor. Int J Hydrogen Energy 2021;46:15241–56.
[280] Laosiripojana N, Assabumrungrat S. Catalytic steam reforming of methane, methanol, and ethanol over Ni/YSZ: the possible use of these fuels in internal reforming SOFC. J Power Sources 2007;163:943–51.
[281] Khoja AH, Tahir M, Saidina Amin NA. Process optimization of DBD plasma dry reforming of methane over Ni/La_2O_3-$MgAl_2O_4$ using multiple response surface methodology. Int J Hydrogen Energy 2019;44:11774–87.
[282] Pérez-Moreno L, Soler J, Herguido J, Menéndez M. Stable hydrogen production by methane steam reforming in a two-zone fluidized-bed reactor: effect of the operating variables. Int J Hydrogen Energy 2013;38:7830–8.
[283] Ayodele BV, Mustapa SI, Mohd Yassin Myb, Abdullah S. Experimental and optimization studies of hydrogen production by steam methane reforming over lanthanum strontium cobalt ferrite supported Ni catalyst. Int J Energy Res 2019;43:8118–35.
[284] García-Lario AL, Aznar M, Grasa GS, García T, Murillo R. Study of nickel catalysts for hydrogen production in sorption enhanced reforming process. J Power Sources 2013;242:371–9.
[285] Pashchenko D. Experimental investigation of synthesis gas production by methane reforming with flue gas over a NiO-Al_2O_3 catalyst: reforming characteristics and pressure drop. Int J Hydrogen Energy 2019;44:7073–82.
[286] Chen C-H, Yu C-T, Chen W-H. Improvement of steam methane reforming via in-situ CO_2 sorption over a nickel-calcium composite catalyst. Int J Hydrogen Energy 2020;46:16655–66.
[287] Dewoolkar KD, Vaidya PD. Improved hydrogen production by sorption-enhanced steam methane reforming over hydrotalcite- and calcium-based hybrid materials. Energy Fuel 2015;29:3870–8.
[288] Wu Z, Wang J, Xie B, Yang J, Wang Q. Methane steam reforming with axial variable diameter particle structures in grille-sphere composite packed bed: a numerical study of hydrogen production performance. Energy Convers Manag 2021;240:114163.
[289] Angeli SD, Turchetti L, Monteleone G, Lemonidou AA. Catalyst development for steam reforming of methane and model biogas at low temperature. Appl Catal B Environ 2016;181:34–46.
[290] Challiwala MS, Ghouri MM, Linke P, El-Halwagi MM, Elbashir NO. A combined thermo-kinetic analysis of various methane reforming technologies: comparison with dry reforming. J CO2 Util 2017;17:99–111.
[291] Abbas SZ, Dupont V, Mahmud T. Kinetics study and modelling of steam methane reforming process over a NiO/Al_2O_3 catalyst in an adiabatic packed bed reactor. Int J Hydrogen Energy 2017;42:2889–903.
[292] Castillo JMV, Sato T, Itoh N. Effect of temperature and pressure on hydrogen production from steam reforming of biogas with Pd–Ag membrane reactor. Int J Hydrogen Energy 2015;40:3582–91.

[293] Abbas S, Dupont V, Mahmud T. Modelling of H_2 production via sorption enhanced steam methane reforming at reduced pressures for small scale applications. Int J Hydrogen Energy 2019;44:1505–13.
[294] Fernandez JR, Abanades JC, Grasa G. Modeling of sorption enhanced steam methane reforming—Part II: simulation within a novel Ca/Cu chemical loop process for hydrogen production. Chem Eng Sci 2012;84:12–20.
[295] Mokheimer EMA, Ibrar Hussain M, Ahmed S, Habib MA, Al-Qutub AA. On the modeling of steam methane reforming. J Energy Resour Technol 2014;137:012001-11.
[296] Park H-G, Han S-Y, Jun K-W, Woo Y, Park M-J, Kim SK. Bench-scale steam reforming of methane for hydrogen production. Catalysts 2019;9: 1-14.
[297] Hacarlioglu P, Gu Y, Oyama S. Studies of the methane steam reforming reaction at high pressure in a ceramic membrane reactor. J Nat Gas Chem 2006;15:73–81.
[298] Amiri TY, Ghasemzageh K, Iulianelli A. Membrane reactors for sustainable hydrogen production through steam reforming of hydrocarbons: a review. Chem Eng Process: Process Intensif 2020;157:108148.
[299] Minette F, de Almeida LC, Ratan S, De Wilde J. Pressure drop and heat transfer of ZoneFlowTM structured catalytic reactors and reference pellets for Steam Methane Reforming. J Chem Eng 2021;417:128080.
[300] Simpson AP, Lutz AE. Exergy analysis of hydrogen production via steam methane reforming. Int J Hydrogen Energy 2007;32:4811–20.
[301] Chai S-P, Seah C-M, Mohamed AR. A parametric study of methane decomposition into carbon nanotubes over 8Co-2Mo/Al_2O_3 catalyst. J Nat Gas Chem 2011;20:84–9.
[302] Nakisa Y, Reza GMH. Modeling the oxidative coupling of methane: heterogeneous chemistry coupled with 3D flow field simulation. J Nat Gas Chem 2009;18:39–44.
[303] Anzelmo B, Wilcox J, Liguori S. Hydrogen production via natural gas steam reforming in a Pd-Au membrane reactor. Investigation of reaction temperature and GHSV effects and long-term stability. J Membr Sci 2018;565:25–32.
[304] Radfarnia HR, Iliuta MC. Development of Al-stabilized CaO–nickel hybrid sorbent–catalyst for sorption-enhanced steam methane reforming. Chem Eng Sci 2014;109:212–9.
[305] Santos DBL, Oliveira ACP, Hori CE. Performance of Na_2CO_3-CaO sorbent in sorption-enhanced steam methane reforming. J CO2 Util 2021;51:101634.
[306] Palma V, Ricca A, Meloni E, Martino M, Miccio M, Ciambelli P. Experimental and numerical investigations on structured catalysts for methane steam reforming intensification. J Clean Prod 2016;111:217–30.
[307] Xie M, Zhou Z, Qi Y, Cheng Z, Yuan W. Sorption-enhanced steam methane reforming by in situ CO_2 capture on a CaO–$Ca_9Al_6O_{18}$ sorbent. J Chem Eng 2012;207–208:142–50.
[308] Großmann K, Treiber P, Karl J. Steam methane reforming at low S/C ratios for power-to-gas applications. Int J Hydrogen Energy 2016;41:17784–92.
[309] Maqbool F, Abbas SZ, Ramirez-Solis S, Dupont V, Mahmud T. Modelling of one-dimensional heterogeneous catalytic steam methane reforming over various catalysts in an adiabatic packed bed reactor. Int J Hydrogen Energy 2021;46:5112–30.
[310] Abbas SZ, Dupont V, Mahmud T. Modelling of H_2 production in a packed bed reactor via sorption enhanced steam methane reforming process. Int J Hydrogen Energy 2017;42:18910–21.
[311] Zhou Y, Haynes D, Baltrus J, Roy A, Shekhawat D, Spivey JJ. Methane steam reforming at low steam-to-carbon ratio: the effect of Y doping in Rh substituted lanthanum zirconates. Appl Catal A-Gen 2020;606:117802.
[312] Tzanetis KF, Martavaltzi CS, Lemonidou AA. Comparative exergy analysis of sorption enhanced and conventional methane steam reforming. Int J Hydrogen Energy 2012;37:16308–20.
[313] Chen K, Zhao Y, Zhang W, Feng D, Sun S. The intrinsic kinetics of methane steam reforming over a nickel-based catalyst in a micro fluidized bed reaction system. Int J Hydrogen Energy 2020;45:1615–28.
[314] Keil FJ. Process intensification. Rev Chem Eng 2018;34:135–200.
[315] Zhai X, Ding S, Cheng Y, Jin Y, Cheng Y. CFD simulation with detailed chemistry of steam reforming of methane for hydrogen production in an integrated micro-reactor. Int J Hydrogen Energy 2010;35:5383–92.
[316] Ngo SI, Lim Y-I, Kim W, Seo DJ, Yoon WL. Computational fluid dynamics and experimental validation of a compact steam methane reformer for hydrogen production from natural gas. Appl Energy 2019;236:340–53.
[317] Darvishi P, Zareie-Kordshouli F. A rigorous mathematical model for online prediction of tube skin temperature in an industrial top-fired steam methane reformer. Chem Eng Res Des 2017;126:32–44.
[318] Jiang Q, Zhang H, Cao Y, Hong H, Jin H. Solar hydrogen production via perovskite-based chemical-looping steam methane reforming. Energy Convers Manag 2019;187:523–36.
[319] Abbasi M, Farniaei M, Abbasi S. Enhancement of hydrogen production by fluidization in industrial-scale steam reformers. Theor Found Chem Eng 2018;52:416–28.
[320] Kim C-H, Han J-Y, Lim H, Kim D-W, Ryi S-K. Methane steam reforming in a membrane reactor using high-permeable and low-selective Pd-Ru membrane. Kor J Chem Eng 2017;34:1260–5.
[321] Patil C, Annaland MVS, Kuipers J. Experimental study of a membrane assisted fluidized bed reactor for H_2 production by steam reforming of CH_4. Chem Eng Res Des 2006;84:399–404.
[322] Chompupun T, Limtrakul S, Vatanatham T, Kanhari C, Ramachandran PA. Experiments, modeling and scaling-up of membrane reactors for hydrogen production via steam methane reforming. Chem Eng Process: Process Intensif 2018;134:124–40.
[323] Singh AP, Singh S, Ganguly S, Patwardhan AV. Steam reforming of methane and methanol in simulated macro & micro-scale membrane reactors: selective separation of hydrogen for optimum conversion. J. Nat. Gas Eng 2014;18:286–95.
[324] Gallucci F, Fernandez E, Corengia P, van Sint Annaland M. Recent advances on membranes and membrane reactors for hydrogen production. Chem Eng Sci 2013;92:40–66.
[325] Lee H, Kim A, Lee B, Lim H. Comparative numerical analysis for an efficient hydrogen production via a steam methane reforming with a packed-bed reactor, a membrane reactor, and a sorption-enhanced membrane reactor. Energy Convers Manag 2020;213:112839.
[326] Basile A, Iulianelli A, Longo T, Liguori S, De Falco M. Pd-Based selective membrane state-of-the-art. In: De De Falco M, Marrelli L, Iaquaniello G, editors. Membrane reactors for hydrogen production processes. London: Springer London; 2011. p. 21–55.
[327] Abu El Hawa HW, Paglieri SN, Morris CC, Harale A, Douglas Way J. Application of a Pd–Ru composite membrane to hydrogen production in a high temperature membrane reactor. Sep Purif Technol 2015;147:388–97.
[328] Acha E, Requies J, Barrio VL, Cambra JF, Güemez MB, Arias PL, et al. PdCu membrane integration and lifetime in the production of hydrogen from methane. Int J Hydrogen Energy 2013;38:7659–66.
[329] Abu El Hawa HW, Paglieri SN, Morris CC, Harale A, Douglas Way J. Identification of thermally stable Pd-alloy composite membranes for high temperature applications. J Membr Sci 2014;466:151–60.
[330] Conde JJ, Maroño M, Sánchez-Hervás JM. Pd-based membranes for hydrogen separation: review of alloying elements and their influence on membrane properties. Separ Purif Rev 2017;46:152–77.
[331] Iulianelli A, Manzolini G, De Falco M, Campanari S, Longo T, Liguori S, et al. H_2 production by low pressure methane steam reforming in a Pd–Ag membrane reactor over a Ni-based catalyst: experimental and modeling. Int J Hydrogen Energy 2010;35:11514–24.
[332] Shigarov AB, Meshcheryakov VD, Kirillov VA. Use of Pd membranes in catalytic reactors for steam methane reforming for pure hydrogen production. Theor Found Chem Eng 2011;45:595.
[333] Kim C-H, Han J-Y, Kim S, Lee B, Lim H, Lee K-Y, et al. Hydrogen production by steam methane reforming in a membrane reactor equipped with a Pd composite membrane deposited on a porous stainless steel. Int J Hydrogen Energy 2018;43:7684–92.
[334] Abu El Hawa HW, Lundin S-TB, Patki NS, Douglas Way J. Steam methane reforming in a Pd-Au membrane reactor: long-term assessment. Int J Hydrogen Energy 2016;41:10193–201.
[335] Kim C-H, Han J-Y, Lim H, Lee K-Y, Ryi S-K. Hydrogen production by steam methane reforming in membrane reactor equipped with Pd membrane deposited on NiO/YSZ/NiO multilayer-treated porous stainless steel. J Membr Sci 2018;563:75–82.
[336] Gascon J, Kapteijn F. Metal-organic framework membranes—high potential, bright future? Angew Chem Int Ed Engl 2010;49:1530–2.
[337] Dong J, Lin Y, Liu W. Multicomponent hydrogen/hydrocarbon separation by MFI-type zeolite membranes. AIChE J 2000;46:1957–66.
[338] Al-Mufachi N, Rees N, Steinberger-Wilkens R. Hydrogen selective membranes: a review of palladium-based dense metal membranes. Renew Sustain Energy Rev 2015;47:540–51.
[339] Wang M, Tan X, Motuzas J, Li J, Liu S. Hydrogen production by methane steam reforming using metallic nickel hollow fiber membranes. J Membr Sci 2021;620:118909.
[340] Wu H-C, Rui Z, Lin JYS. Hydrogen production with carbon dioxide capture by dual-phase ceramic-carbonate membrane reactor via steam reforming of methane. J Membr Sci 2020;598:117780.
[341] Ovalle-Encinia O, Wu H-C, Chen T, Lin JYS. CO_2-permselective membrane reactor for steam reforming of methane. J Membr Sci 2022;641:119914.
[342] Upadhyay M, Lee H, Kim A, Lee S-h, Lim H. CFD simulation of methane steam reforming in a membrane reactor: performance characteristics over range of operating window. Int J Hydrogen Energy 2021;46:30402–11.
[343] Sarić M, van Delft YC, Sumbharaju R, Meyer DF, de Groot A. Steam reforming of methane in a bench-scale membrane reactor at realistic working conditions. Catalyst 2012;193:74–80.
[344] Medrano JA, Fernandez E, Melendez J, Parco M, Tanaka DAP, van Sint Annaland M, et al. Pd-based metallic supported membranes: high-temperature stability and fluidized bed reactor testing. Int J Hydrogen Energy 2016;41:8706–18.
[345] Fernandez E, Helmi A, Medrano JA, Coenen K, Arratibel A, Melendez J, et al. Palladium based membranes and membrane reactors for hydrogen production and purification: an overview of research activities at Tecnalia and TU/e. Int J Hydrogen Energy 2017;42:13763–76.
[346] Anzelmo B, Wilcox J, Liguori S. Hydrogen production via natural gas steam reforming in a Pd-Au membrane reactor. Comparison between methane and natural gas steam reforming reactions. J Membr Sci 2018;568:113–20.
[347] Masoudi Soltani S, Lahiri A, Bahzad H, Clough P, Gorbounov M, Yan Y. Sorption-enhanced steam methane reforming for combined CO_2 capture and hydrogen production: a state-of-the-art review. Carbon Capture Science & Technology 2021;1:100003.
[348] Zeng X, Fang M, Lv T, Tian J, Xia Z, Cen J, et al. Hydrogen-rich gas production by catalytic steam gasification of rice husk using CeO_2-modified Ni-CaO sorption bifunctional catalysts. J Chem Eng 2022:136023.
[349] Yan Y, Thanganadar D, Clough PT, Mukherjee S, Patchigolla K, Manovic V, et al. Process simulations of blue hydrogen production by upgraded sorption enhanced

steam methane reforming (SE-SMR) processes. Energy Convers Manag 2020;222:113144.
[350] Vanga G, Gattia DM, Stendardo S, Scaccia S. Novel synthesis of combined CaO-$Ca_{12}Al_{14}O_{33}$-Ni sorbent-catalyst material for sorption enhanced steam reforming processes. Ceram Int 2019;45:7594–605.
[351] Dou B, Song Y, Wang C, Chen H, Yang M, Xu Y. Hydrogen production by enhanced-sorption chemical looping steam reforming of glycerol in moving-bed reactors. Appl Energy 2014;130:342–9.
[352] Wu Y-J, Li P, Yu J-G, Cunha AF, Rodrigues AE. Progress on sorption-enhanced reaction process for hydrogen production. J Chem Eng 2016;32:271–303.
[353] Rodrigues AE, Wu Y-j, Madeira LM, Faria R. Sorption enhanced reaction processes. World Scientific; 2017.
[354] Shokrollahi Yancheshmeh M, Radfarnia HR, Iliuta MC. High temperature CO_2 sorbents and their application for hydrogen production by sorption enhanced steam reforming process. J Chem Eng 2016;283:420–44.
[355] Navarro MV, López JM, García T, Grasa G, Murillo R. Catalyst evaluation for high-purity H_2 production by sorption-enhanced steam-methane reforming coupled to a Ca/Cu process. J Power Sources 2017;363:117–25.
[356] Barelli L, Bidini G, Gallorini F, Servili S. Hydrogen production through sorption-enhanced steam methane reforming and membrane technology: a review. Energy 2008;33:554–70.
[357] Ganesh I. Conversion of carbon dioxide into methanol – a potential liquid fuel: fundamental challenges and opportunities (a review). Renew Sustain Energy Rev 2014;31:221–57.
[358] Oliveira ELG, Grande CA, Rodrigues AE. Effect of catalyst activity in SMR-SERP for hydrogen production: commercial vs. large-pore catalyst. Chem Eng Sci 2011;66:342–54.
[359] Fernández JR, Alarcón JM, Abanades JC. Investigation of a fixed-bed reactor for the calcination of $CaCO_3$ by the simultaneous reduction of CuO with a fuel gas. Ind Eng Chem Res 2016;55:5128–32.
[360] Waldron WE, Hufton J, Sircar S. Production of hydrogen by cyclic sorption enhanced reaction process. AIChE J 2001;47:1477.
[361] García-Lario AL, Aznar M, Grasa GS, Murillo R. Evaluation of process variables on the performance of sorption enhanced methane reforming. J Power Sources 2015;285:90–9.
[362] Lysikov AI, Okunev AG, Netskina OV. Study of a nickel catalyst under conditions of the SER process: influence of RedOx cycling. Int J Hydrogen Energy 2013;38:10354–63.
[363] Martavaltzi CS, Lemonidou AA. Hydrogen production via sorption enhanced reforming of methane: development of a novel hybrid material—reforming catalyst and CO_2 sorbent. Chem Eng Sci 2010;65:4134–40.
[364] Arstad B, Prostak J, Blom R. Continuous hydrogen production by sorption enhanced steam methane reforming (SE-SMR) in a circulating fluidized bed reactor: sorbent to catalyst ratio dependencies. J Chem Eng 2012;189–190:413–21.
[365] Wang S, Fan S, Fan L, Zhao Y, Ma X. Effect of cerium oxide doping on the performance of CaO-based sorbents during calcium looping cycles. J. Environ. Sci. Technol 2015;49:5021–7.
[366] Wu G, Zhang C, Li S, Huang Z, Yan S, Wang S, et al. Sorption enhanced steam reforming of ethanol on Ni–CaO–Al_2O_3 multifunctional catalysts derived from hydrotalcite-like compounds. Energy Environ Sci 2012;5:8942–9.
[367] Iliuta I, Radfarnia HR, Iliuta MC. Hydrogen production by sorption-enhanced steam glycerol reforming: sorption kinetics and reactor simulation. AIChE J 2013;59:2105–18.
[368] Cesário MR, Barros BS, Courson C, Melo DMA, Kiennemann A. Catalytic performances of Ni–CaO–mayenite in CO_2 sorption enhanced steam methane reforming. Fuel Process Technol 2015;131:247–53.
[369] Li L, Wen X, Fu X, Wang F, Zhao N, Xiao F, et al. MgO/Al_2O_3 sorbent for CO_2 capture. Energy Fuel 2010;24:5773–80.
[370] Dou B, Wang C, Song Y, Chen H, Jiang B, Yang M, et al. Solid sorbents for in-situ CO_2 removal during sorption-enhanced steam reforming process: a review. Renew Sustain Energy Rev 2016;53:536–46.
[371] Montes-Hernandez G, Chiriac R, Toche F, Renard F. Gas–solid carbonation of Ca$(OH)_2$ and CaO particles under non-isothermal and isothermal conditions by using a thermogravimetric analyzer: implications for CO_2 capture. Int J Greenh Gas Control 2012;11:172–80.
[372] Ghungrud SA, Dewoolkar KD, Vaidya PD. Cerium-promoted bi-functional hybrid materials made of Ni, Co and hydrotalcite for sorption-enhanced steam methane reforming (SESMR). Int J Hydrogen Energy 2019;44:694–706.
[373] Dewoolkar KD, Vaidya PD. Tailored Ce- and Zr-doped Ni/hydrotalcite materials for superior sorption-enhanced steam methane reforming. Int J Hydrogen Energy 2017;42:21762–74.
[374] Wang N, Feng Y, Chen Y, Guo X. Lithium-based sorbent from rice husk materials for hydrogen production via sorption-enhanced steam reforming of ethanol. Fuel 2019;245:263–73.
[375] Rusten HK, Ochoa-Fernández E, Lindborg H, Chen D, Jakobsen HA. Hydrogen production by sorption-enhanced steam methane reforming using lithium oxides as CO_2-acceptor. Ind Eng Chem Res 2007;46:8729–37.
[376] Zhao M, Yang X, Church TL, Harris AT. Novel CaO–SiO_2 sorbent and bifunctional Ni/Co–CaO/SiO_2 complex for selective H_2 synthesis from cellulose. J. Environ. Sci. Technol 2012;46:2976–83.
[377] Iordanidis AA, Kechagiopoulos PN, Voutetakis SS, Lemonidou AA, Vasalos IA. Autothermal sorption-enhanced steam reforming of bio-oil/biogas mixture and energy generation by fuel cells: concept analysis and process simulation. Int J Hydrogen Energy 2006;31:1058–65.
[378] Alshafei FH, Minardi LT, Rosales D, Chen G, Simonetti Dante A. Improved sorption-enhanced steam methane reforming via calcium oxide–based sorbents with targeted morphology. Energy Technol 2019;7:1800807.
[379] Guo H, Wang S, Li C, Zhao Y, Sun Q, Ma X. Incorporation of Zr into calcium oxide for CO_2 capture by a simple and facile sol–gel method. Ind Eng Chem Res 2016;55:7873–9.
[380] Luo C, Zheng Y, Guo J, Feng B. Effect of sulfation on CO_2 capture of CaO-based sorbents during calcium looping cycle. Fuel 2014;127:124–30.
[381] Liu W, An H, Qin C, Yin J, Wang G, Feng B, et al. Performance enhancement of calcium oxide sorbents for cyclic CO_2 capture—a review. Energy Fuel 2012;26:2751–67.
[382] Wang S, Fan S, Fan L, Zhao Y, Ma X. Effect of cerium oxide doping on the performance of CaO-based sorbents during calcium looping cycles. Environ Sci Technol 2015;49:5021–7.
[383] Koirala R, Gunugunuri KR, Pratsinis SE, Smirniotis PG. Effect of zirconia doping on the structure and stability of CaO-based sorbents for CO_2 capture during extended operating cycles. J Phys Chem C 2011;115:24804–12.
[384] Broda M, Müller CR. Sol–gel-derived, CaO-based, ZrO_2-stabilized CO_2 sorbents. Fuel 2014;127:94–100.
[385] Ridha FN, Manovic V, Macchi A, Anthony EJ. High-temperature CO_2 capture cycles for CaO-based pellets with kaolin-based binders. Int J Greenh Gas Control 2012;6:164–70.
[386] Wu Y, Manovic V, He I, Anthony EJ. Modified lime-based pellet sorbents for high-temperature CO_2 capture: reactivity and attrition behavior. Fuel 2012;96:454–61.
[387] Gruene P, Belova AG, Yegulalp TM, Farrauto RJ, Castaldi MJ. Dispersed calcium oxide as a reversible and efficient CO_2−Sorbent at intermediate temperatures. Ind Eng Chem Res 2011;50:4042–9.
[388] Wu SF, Zhu YQ. Behavior of $CaTiO_3$/nano-CaO as a CO_2 reactive adsorbent. Ind Eng Chem Res 2010;49:2701–6.
[389] Zhou Z, Qi Y, Xie M, Cheng Z, Yuan W. Synthesis of CaO-based sorbents through incorporation of alumina/aluminate and their CO_2 capture performance. Chem Eng Sci 2012;74:172–80.
[390] Broda M, Kierzkowska AM, Baudouin D, Imtiaz Q, Copéret C, Müller CR. Sorbent-enhanced methane reforming over a Ni–Ca-based, bifunctional catalyst sorbent. ACS Catal 2012;2:1635–46.
[391] Jitianu M, Gunness DC, Aboagye DE, Zaharescu M, Jitianu A. Nanosized Ni–Al layered double hydroxides—structural characterization. Mater Res Bull 2013;48:1864–73.
[392] Ferreira RAR, Ávila-Neto CN, Noronha FB, Hori CE. Study of LPG steam reform using Ni/Mg/Al hydrotalcite-type precursors. Int J Hydrogen Energy 2019;44:24471–84.
[393] Sikander U, Sufian S, Salam MA. A review of hydrotalcite based catalysts for hydrogen production systems. Int J Hydrogen Energy 2017;42:19851–68.
[394] Phuakpunk K, Chalermsinsuwan B, Putivisutisak S, Assabumrungrat S. Parametric study of hydrogen production via sorption enhanced steam methane reforming in a circulating fluidized bed riser. Chem Eng Sci 2018;192:1041–57.
[395] Herce C, Cortés C, Stendardo S. Computationally efficient CFD model for scale-up of bubbling fluidized bed reactors applied to sorption-enhanced steam methane reforming. Fuel Process Technol 2017;167:747–61.
[396] Chanburanasiri N, Ribeiro AM, Rodrigues AE, Arpornwichanop A, Laosiripojana N, Praserthdam P, et al. Hydrogen production via sorption enhanced steam methane reforming process using Ni/CaO multifunctional catalyst. Ind Eng Chem Res 2011;50:13662–71.
[397] García-Lario AL, Aznar M, Martinez I, Grasa GS, Murillo R. Experimental study of the application of a NiO/$NiAl_2O_4$ catalyst and a CaO-based synthetic sorbent on the Sorption Enhanced Reforming process. Int J Hydrogen Energy 2015;40:219–32.
[398] Radfarnia HR, Iliuta MC. Hydrogen production by sorption-enhanced steam methane reforming process using CaO-Zr/Ni bifunctional sorbent–catalyst. Chem Eng Process: Process Intensif 2014;86:96–103.
[399] de Miguel N, Manzanedo J, Arias PL. Active and stable Ni-MgO catalyst coated on a metal monolith for methane steam reforming under low steam-to-carbon ratios. Chem Eng Technol 2012;35:2195–203.
[400] Ji G, Zhao M, Wang G. Computational fluid dynamic simulation of a sorption-enhanced palladium membrane reactor for enhancing hydrogen production from methane steam reforming. Energy 2018;147:884–95.
[401] Saeidi S, Amiri MT, Amin NAS, Rahimpour MR. Progress in reactors for high-temperature Fischer–Tropsch process: determination place of intensifier reactor perspective. Int J Chem React Eng 2014;12:639–64.
[402] Saeidi S, Nikoo MK, Mirvakili A, Bahrani S, Amin NAS, Rahimpour MR. Recent advances in reactors for low-temperature Fischer-Tropsch synthesis: process intensification perspective. Rev Chem Eng 2015;31:209–38.
[403] Elbadawi AH, Ge L, Li Z, Liu S, Wang S, Zhu Z. Catalytic partial oxidation of methane to syngas: review of perovskite catalysts and membrane reactors. Catal Rev Sci Eng 2021;63:1–67.
[404] Spallina V, Pandolfo D, Battistella A, Romano MC, Van Sint Annaland M, Gallucci F. Techno-economic assessment of membrane assisted fluidized bed reactors for pure H_2 production with CO_2 capture. Energy Convers Manag 2016;120:257–73.
[405] Di Carlo A, Aloisi I, Jand N, Stendardo S, Foscolo PU. Sorption enhanced steam methane reforming on catalyst-sorbent bifunctional particles: a CFD fluidized bed reactor model. Chem Eng Sci 2017;173:428–42.
[406] Gil MV, Fermoso J, Rubiera F, Chen D. H_2 production by sorption enhanced steam reforming of biomass-derived bio-oil in a fluidized bed reactor: an assessment of the effect of operation variables using response surface methodology. Catalyst 2015;242:19–34.

[407] Yang X, Wang S, He Y. Review of catalytic reforming for hydrogen production in a membrane-assisted fluidized bed reactor. Renew Sustain Energy Rev 2022;154:111832.
[408] Silva JM, Soria M, Madeira LM. Thermodynamic analysis of Glycerol Steam Reforming for hydrogen production with in situ hydrogen and carbon dioxide separation. J Power Sources 2015;273:423–30.
[409] Andres M-B, Boyd T, Grace JR, Lim CJ, Gulamhusein A, Wan B, et al. In-situ CO_2 capture in a pilot-scale fluidized-bed membrane reformer for ultra-pure hydrogen production. Int J Hydrogen Energy 2011;36:4038–55.
[410] Adanez J, Abad A, Garcia-Labiano F, Gayan P, de Diego LF. Progress in chemical-looping combustion and reforming technologies. Prog Energy Combust Sci 2012;38:215–82.
[411] Gallucci F, Van Sintannaland M, Kuipers J. Theoretical comparison of packed bed and fluidized bed membrane reactors for methane reforming. Int J Hydrogen Energy 2010;35:7142–50.
[412] Chao Z, Zhang Y, Wang Y, Jakobsen JP, Jakobsen HA. Modelling of binary fluidized bed reactors for the sorption-enhanced steam methane reforming process. Can J Chem Eng 2017;95:157–69.
[413] Roses L, Gallucci F, Manzolini G, van Sint Annaland M. Experimental study of steam methane reforming in a Pd-based fluidized bed membrane reactor. J Chem Eng 2013;222:307–20.
[414] Chen Y, Zhao Y, Zheng C, Zhang J. Numerical study of hydrogen production via sorption-enhanced steam methane reforming in a fluidized bed reactor at relatively low temperature. Chem Eng Sci 2013;92:67–80.
[415] Adris A, Elnashaie S, Hughes R. A fluidized bed membrane reactor for the steam reforming of methane. Can J Chem Eng 1991;69:1061–70.
[416] Papalas T, Antzaras AN, Lemonidou AA. Intensified steam methane reforming coupled with Ca-Ni looping in a dual fluidized bed reactor system: a conceptual design. J Chem Eng 2020;382:122993.
[417] Wen C, Yu Y. A generalized method for predicting the minimum fluidization velocity. AIChE J 1966;12:610–2.
[418] Ye JW, Xie DL, Yang ZH, Cao ZY. Simulation of fluidized bed oxygen permeable membrane reactors for hydrogen production from natural gas. Advanced Materials Research. Trans Tech Publ; 2013. p. 1467–71.
[419] Pruvost F, Cloete S, del Pozo CA, Zaabout A. Blue, green, and turquoise pathways for minimizing hydrogen production costs from steam methane reforming with CO_2 capture. Energy Convers Manag 2022;274:116458.
[420] Li X, Li Z, Lu C, Li D, Li Z, Gao J, et al. Enhanced performance of $LaFeO_3$ oxygen carriers by NiO for chemical looping partial oxidation of methane. Fuel Process Technol 2022;236:107396.
[421] Wang J, Li K, Wang H, Li Z, Zhu X. Sandwich Ni-phyllosilicate@doped-ceria for moderate-temperature chemical looping dry reforming of methane. Fuel Process Technol 2022;232:107268.
[422] He X, Wang Y, Li K, Wang H, Jiang L, Yuan K, Zheng Y. Modification of $LaFe_{1-x}Co_xO_3$ oxygen carrier by Silicalite-1 for chemical looping coupled with the reduction of CO_2. J CO_2 Util 2022;63:102124.
[423] Zeng D, Kang F, Qiu Y, Cui D, Li M, Ma L, et al. Iron oxides with gadolinium-doped cerium oxides as active supports for chemical looping hydrogen production. J Chem Eng 2020;396:125153.
[424] Hafizi A, Rahimpour MR, Hassanajili S. Calcium promoted Fe/Al_2O_3 oxygen carrier for hydrogen production via cyclic chemical looping steam methane reforming process. Int J Hydrogen Energy 2015;40:16159–68.
[425] Zheng Y, Wei Y, Li K, Zhu X, Wang H, Wang Y. Chemical-looping steam methane reforming over macroporous CeO_2–ZrO_2 solid solution: effect of calcination temperature. Int J Hydrogen Energy 2014;39:13361–8.
[426] Zhu L, Li L, Fan J. A modified process for overcoming the drawbacks of conventional steam methane reforming for hydrogen production: thermodynamic investigation. Chem Eng Res Des 2015;104:792–806.
[427] Zhu X, Li K, Wei Y, Wang H, Sun L. Chemical-looping steam methane reforming over a CeO_2–Fe_2O_3 oxygen carrier: evolution of its structure and reducibility. Energy Fuel 2014;28:754–60.
[428] Spallina V, Marinello B, Gallucci F, Romano MC, Annaland MVS. Chemical looping reforming in packed-bed reactors: modelling, experimental validation and large-scale reactor design. Fuel Process Technol 2017;156:156–70.
[429] Yin X, Wang S, Sun R, Jiang S, Shen L. A Ce–Fe oxygen carrier with a core–shell structure for chemical looping steam methane reforming. Ind Eng Chem Res 2020;59:9775–86.
[430] Garai MHS, Khosravi-Nikou MR, Shariati A. Chemical looping steam methane reforming via Ni-ferrite supported on cerium and zirconium oxides. Chem Eng Technol 2020;43:1813–22.
[431] Kuo Y-L, Hsu W-M, Chiu P-C, Tseng Y-H, Ku Y. Assessment of redox behavior of nickel ferrite as oxygen carriers for chemical looping process. Ceram Int 2013;39:5459–65.
[432] Evdou A, Zaspalis V, Nalbandian L. Ferrites as redox catalysts for chemical looping processes. Fuel 2016;165:367–78.
[433] Nazari M, Soltanieh M, Heydarinasab A, Maddah B. Synthesis of a new self-supported $Mg_y(Cu_xNi_{0.6-x}Mn_{0.4})_{1-y}Fe_2O_4$ oxygen carrier for chemical looping steam methane reforming process. Int J Hydrogen Energy 2021;46:19397–420.
[434] Hosseini SY, Khosravi-Nikou MR, Shariati A. Kinetic study of the reduction step for chemical looping steam methane reforming by CeO_2-Fe_2O_3 oxygen carriers. Chem Eng Technol 2020;43:540–52.
[435] Yang Z, Zheng Y, Li K, Wang Y, Wang Y, Wang H, et al. Chemical-looping reforming of methane over La-Mn-Fe-O oxygen carriers: effect of calcination temperature. Chem Eng Sci 2021;229:116085.
[436] Ortiz M, de Diego LF, Abad A, Garcia-Labiano F, Gayan P, Adanez J. Catalytic activity of Ni-based oxygen-carriers for steam methane reforming in chemical-looping processes. Energy Fuel 2012;26:791–800.
[437] Zhao K, He F, Huang Z, Wei G, Zheng A, Li H, et al. Perovskite-type oxides $LaFe_{1-x}Co_xO_3$ for chemical looping steam methane reforming to syngas and hydrogen co-production. Appl Energy 2016;168:193–203.
[438] Zheng Y, Li K, Wang H, Tian D, Wang Y, Zhu X, et al. Designed oxygen carriers from macroporous $LaFeO_3$ supported CeO_2 for chemical-looping reforming of methane. Appl Catal B Environ 2017;202:51–63.
[439] Zhu X, Wei Y, Wang H, Li K. Ce–Fe oxygen carriers for chemical-looping steam methane reforming. Int J Hydrogen Energy 2013;38:4492–501.
[440] Li K, Wang H, Wei Y, Yan D. Ce–Fe oxygen carriers for chemical-looping steam methane reforming. Int J Hydrogen Energy 2011;36:3471–82.
[441] Wang D, Jin L, Li Y, Yao D, Wang J, Hu H. Upgrading of vacuum residue with chemical looping partial oxidation over Ce doped Fe_2O_3. Energy 2018;162:542–53.
[442] Meshksar M, Daneshmand-Jahromi S, Rahimpour MR. Synthesis and characterization of cerium promoted Ni/SBA-16 oxygen carrier in cyclic chemical looping steam methane reforming. J Taiwan Inst Chem Eng 2017;76:73–82.
[443] Tang M, Xu L, Fan M. Progress in oxygen carrier development of methane-based chemical-looping reforming: a review. Appl Energy 2015;151:143–56.
[444] Shen Y, Zhao K, He F, Li H. The structure-reactivity relationships of using three-dimensionally ordered macroporous $LaFe_{1-x}Ni_xO_3$ perovskites for chemical-looping steam methane reforming. J Energy Inst 2019;92:239–46.
[445] Singh V, Buelens LC, Poelman H, Saeys M, Marin GB, Galvita VV. Intensifying blue hydrogen production by in situ CO_2 utilisation. J CO2 Util 2022;61:102014.
[446] Martini M, Druiff M, van Sint Annaland M, Gallucci F. Experimental demonstration of the Ca-Cu looping process. J Chem Eng 2021;418:129505.
[447] Hu J, Galvita VV, Poelman H, Detavernier C, Marin GB. Catalyst-assisted chemical looping auto-thermal dry reforming: spatial structuring effects on process efficiency. Appl Catal B Environ 2018;231:123–36.
[448] Yang Q, Yan M, Zhang L, Xia X, Zhu Y, Zhang C, et al. Thermodynamic analysis of chemical looping coupling process for coproducing syngas and hydrogen with in situ CO_2 utilization. Energy Convers Manag 2021;231:113845.
[449] Yang J, Bjørgum E, Chang H, Zhu K-K, Sui Z-J, Zhou X-G, et al. On the ensemble requirement of fully selective chemical looping methane partial oxidation over La-Fe-based perovskites. Appl Catal B Environ 2022;301:120788.
[450] Chen Z, Elnashaie SS. Bifurcation and its implications for a novel autothermal circulating fluidized bed membrane reformer for the efficient pure hydrogen production. Chem Eng Sci 2005;60:4287–309.
[451] Chen Z, Yan Y, Elnashaie SS. Novel circulating fast fluidized-bed membrane reformer for efficient production of hydrogen from steam reforming of methane. Chem Eng Sci 2003;58:4335–49.
[452] Bahzad H, Shah N, Dowell NM, Boot-Handford M, Soltani SM, Ho M, et al. Development and techno-economic analyses of a novel hydrogen production process via chemical looping. Int J Hydrogen Energy 2019;44:21251–63.
[453] Zhu L, Fan J. Thermodynamic analysis of H_2 production from CaO sorption-enhanced methane steam reforming thermally coupled with chemical looping combustion as a novel technology. Int J Energy Res 2015;39:356–69.
[454] Powell J, Wongsakulphasatch S, Kokoo R, Noppakun N, Prapainainar C, Aziz MAA, et al. Optimisation of a sorption-enhanced chemical looping steam methane reforming process. Chem Eng Res Des 2021;173:183–92.
[455] Fernández JR, Abanades JC. Sorption enhanced reforming of methane combined with an iron oxide chemical loop for the production of hydrogen with CO_2 capture: conceptual design and operation strategy. Appl Therm Eng 2017;125:811–22.
[456] Ipsakis D, Heracleous E, Silvester L, Bukur DB, Lemonidou AA. Kinetic modeling of NiO-based oxygen carriers for the sorption enhanced chemical looping steam CH_4 reforming. Mater Today Proc 2018;5:27353–61.
[457] Dai X, Cheng J, Li Z, Liu M, Ma Y, Zhang X. Reduction kinetics of lanthanum ferrite perovskite for the production of synthesis gas by chemical-looping methane reforming. Chem Eng Sci 2016;153:236–45.
[458] Ma S, Chen S, Soomro A, Xiang W. Effects of supports on hydrogen production and carbon deposition of Fe-based oxygen carriers in chemical looping hydrogen generation. Int J Hydrogen Energy 2017;42:11006–16.
[459] Osman M, Zaabout A, Cloete S, Amini S. Internally circulating fluidized-bed reactor for syngas production using chemical looping reforming. J Chem Eng 2019;377:120076.
[460] Chen S, Shi Q, Xue Z, Sun X, Xiang W. Experimental investigation of chemical-looping hydrogen generation using Al_2O_3 or TiO_2-supported iron oxides in a batch fluidized bed. Int J Hydrogen Energy 2011;36:8915–26.
[461] Richard DM. Development and testing of two lab-scale reactors for electrified steam methane reforming. UCLA; MSc thesis; 2021.
[462] Merkouri L-P, Reina TR, Duyar MS. Feasibility of switchable dual function materials as a flexible technology for CO_2 capture and utilisation and evidence of passive direct air capture. Nanoscale 2022;14:12620–37.
[463] Singh G, Lee J, Karakoti A, Bahadur R, Yi J, Zhao D, et al. Emerging trends in porous materials for CO_2 capture and conversion. Chem Soc Rev 2020;49:4360–404.
[464] Li N, Chen X, Ong W-J, MacFarlane DR, Zhao X, Cheetham AK, et al. Understanding of electrochemical mechanisms for CO_2 capture and conversion into hydrocarbon fuels in transition-metal carbides (MXenes). ACS Nano 2017;11:10825–33.
[465] Baldea M, Edgar TF, Stanley BL, Kiss AA. Modular manufacturing processes: status, challenges, and opportunities. AIChE J 2017;63:4262–72.

[466] De Falco M, Santoro G, Capocelli M, Caputo G, Giaconia A. Hydrogen production by solar steam methane reforming with molten salts as energy carriers: experimental and modelling analysis. Int J Hydrogen Energy 2021;46:10682–96.
[467] Calisan A, Ogulgonen CG, Yilmaz A, Uner D, Kincal S. Steam methane reforming over structured reactors under concentrated solar irradiation. Int J Hydrogen Energy 2019;44:18682–93.
[468] Song H, Luo S, Huang H, Deng B, Ye J. Solar-driven hydrogen production: recent advances, challenges, and future perspectives. ACS Energy Lett 2022;7:1043–65.
[469] Wörner A, Tamme R. CO_2 reforming of methane in a solar driven volumetric receiver–reactor. Catalyst 1998;46:165–74.
[470] Wang J, Wu J, Xu Z, Li M. Thermodynamic performance analysis of a fuel cell trigeneration system integrated with solar-assisted methanol reforming. Energy Convers Manag 2017;150:81–9.
[471] Siavashi M, Hosseini F, Talesh Bahrami HR. A new design with preheating and layered porous ceramic for hydrogen production through methane steam reforming process. Energy 2021;231:120952.
[472] Jin J, Wei X, Liu M, Yu Y, Li W, Kong H, et al. A solar methane reforming reactor design with enhanced efficiency. Appl Energy 2018;226:797–807.
[473] Shagdar E, Lougou BG, Shuai Y, Ganbold E, Chinonso OP, Tan H. Process analysis of solar steam reforming of methane for producing low-carbon hydrogen. RSC Adv 2020;10:12582–97.
[474] Giaconia A, de Falco M, Caputo G, Grena R, Tarquini P, Marrelli L. Solar steam reforming of natural gas for hydrogen production using molten salt heat carriers. AIChE J 2008;54:1932–44.
[475] Ma J, Jiang B, Li L, Yu K, Zhang Q, Lv Z, et al. A high temperature tubular reactor with hybrid concentrated solar and electric heat supply for steam methane reforming. J Chem Eng 2022;428:132073.
[476] Simakov DS, Wright MM, Ahmed S, Mokheimer EM, Román-Leshkov Y. Solar thermal catalytic reforming of natural gas: a review on chemistry, catalysis and system design. Catal Sci Technol 2015;5:1991–2016.
[477] Angeli SD, Monteleone G, Giaconia A, Lemonidou AA. State-of-the-art catalysts for CH_4 steam reforming at low temperature. Int J Hydrogen Energy 2014;39:1979–97.
[478] Böhmer M, Langnickel U, Sanchez M. Solar steam reforming of methane. Sol Energy Mater 1991;24:441–8.
[479] Said SAM, Waseeuddin M, Simakov DSA. A review on solar reforming systems. Renew Sustain Energy Rev 2016;59:149–59.
[480] Agrafiotis C, von Storch H, Roeb M, Sattler C. Solar thermal reforming of methane feedstocks for hydrogen and syngas production—a review. Renew Sustain Energy Rev 2014;29:656–82.
[481] Lu YR, Nikrityuk PA. Steam methane reforming driven by the Joule heating. Chem Eng Sci 2022;251:117446.
[482] Ambrosetti M, Beretta A, Groppi G, Tronconi E. A numerical investigation of electrically-heated methane steam reforming over structured catalysts. Front. Chem. Eng 2021:53.
[483] Balzarotti R, Ambrosetti M, Beretta A, Groppi G, Tronconi E. Recent advances in the development of highly conductive structured supports for the intensification of non-adiabatic catalytic processes: the methane steam reforming case study. Front. Chem. Eng 2022;3:89.
[484] Rieks M, Bellinghausen R, Kockmann N, Mleczko L. Experimental study of methane dry reforming in an electrically heated reactor. Int J Hydrogen Energy 2015;40:15940–51.
[485] Wismann ST, Engbæk JS, Vendelbo SB, Bendixen FB, Eriksen WL, Aasberg-Petersen K, et al. Electrified methane reforming: a compact approach to greener industrial hydrogen production. Science 2019;364:756–9.
[486] Wismann ST, Engbæk JS, Vendelbo SB, Eriksen WL, Frandsen C, Mortensen PM, et al. Electrified methane reforming: understanding the dynamic interplay. Ind Eng Chem Res 2019;58:23380–8.
[487] Wismann ST, Engbæk JS, Vendelbo SB, Eriksen WL, Frandsen C, Mortensen PM, et al. Electrified methane reforming: elucidating transient phenomena. J Chem Eng 2021;425:131509.
[488] Mortensen PM, Engbæk JS, Vendelbo SB, Hansen MF, Østberg M. Direct hysteresis heating of catalytically active Ni–Co nanoparticles as steam reforming catalyst. Ind Eng Chem Res 2017;56:14006–13.
[489] Wang W, Tuci G, Duong-Viet C, Liu Y, Rossin A, Luconi L, et al. Induction heating: an enabling technology for the heat management in catalytic processes. ACS Catal 2019;9:7921–35.
[490] Diab J, Fulcheri L, Hessel V, Rohani V, Frenklach M. Why turquoise hydrogen will Be a game changer for the energy transition. Int J Hydrogen Energy 2022;47:25831–48.
[491] Omodolor IS, Otor HO, Andonegui JA, Allen BJ, Alba-Rubio AC. Dual-function materials for CO_2 capture and conversion: a review. Ind Eng Chem Res 2020;59:17612–31.
[492] Jelmy E, Thomas N, Mathew DT, Louis J, Padmanabhan NT, Kumaravel V, et al. Impact of structure, doping and defect-engineering in 2D materials on CO_2 capture and conversion. React. Chem. Eng 2021;6:1701–38.
[493] Romero M, Steinfeld A. Concentrating solar thermal power and thermochemical fuels. Energy Environ Sci 2012;5:9234–45.
[494] Sarafraz MM, Tran NN, Nguyen H, Fulcheri L, Burton R, Wadewitz P, et al. Trifold process integration leveraging high-and low-temperature plasmas: from biomass to fertilizers with local energy and for local use. J. Adv. Manuf. Process. 2021;3:e10081.
[495] Tran NN, Tejada JO, Asrami MR, Srivastava A, Laad A, Mihailescu M, et al. Economic optimization of local australian ammonia production using plasma technologies with green/turquoise hydrogen. ACS Sustainable Chem Eng 2021;9:16304–15.
[496] Osorio-Tejada J, Tran NN, Hessel V. Techno-environmental assessment of small-scale Haber-Bosch and plasma-assisted ammonia supply chains. Sci Total Environ 2022;826:154162.
[497] Le TNQ, Hessel V, Tran QD, Tran NN, Priest C, Skinner W, et al. Critical elements: opportunities for microfluidic processing and potential for ESG-powered mining investments. Green Chem 2022.
[498] Uzodike UO. The role of regional economic communities in Africa's economic integration: prospects and constraints. Africa Insight 2009;39:26–42.
[499] Sarafraz M, Christo F, Tran N, Fulcheri L, Hessel V. Thermal plasma-aided chemical looping carbon dioxide dissociation for fuel production from aluminium particles. Energy Convers Manag 2022;257:115413.